Heterojunction Engineering of Functional Catalysts for Photoelectrochemical CO_2 Reduction

Xingmo Zhang

A thesis submitted to fulfil requirements for the degree of Doctor of Philosophy

This research reported in this thesis was supported by the award of a Research Training Program scholarship to the PhD Candidate.

Lead supervisor Jun Huang

Supervisor Rongkun Zheng

School of Chemical and Biomolecular Engineering

Faculty of Engineering

The University of Sydney

2024

Declaration of Originality

This declaration is to certify that the content of this thesis, to the best of my knowledge, is my own work. No content of this work was written by another person or be previously published or been submitted for any degree or other purposes.

I certify that the intellectual content of this thesis is the product of my own work, and any other person and institutions, that made contribution to prepare this thesis and sources, are clearly acknowledged.

Xingmo Zhang

27 June 2024

Acknowledgements

This thesis encapsulates my 3.5-year Ph.D. journey and serves as a testament to the unwavering support and kindness I have received throughout. The tumultuous period of the Covid-19 pandemic posed significant challenges for all of us; my research endeavours were no exception, disrupted by the lockdowns imposed by the University of Sydney and the city itself. Furthermore, the relocation of our labs and my lumbar treatment in China also impacted my research progress. However, with the collective support of my supervisors, family, friends, and the technical staff in the labs, I successfully navigated through these obstacles, for which I am deeply grateful.

First and foremost, I extend my heartfelt appreciation to my lead supervisor, Prof. Jun Huang, and my supervisor, Prof. Rongkun Zheng, for their meticulous guidance, invaluable advice, stimulating discussions, and unwavering support throughout my projects and manuscript preparations. Their mentorship has not only enriched my academic journey but also fostered a conducive research environment that facilitated my growth. I consider myself fortunate to have such supportive and compassionate supervisors. I am equally thankful to Dr. Feng Li and Dr. Rui Tang for their innovative insights into my research projects and their meticulous guidance during experiments and manuscript writing. Their friendship and support have been invaluable in overcoming the challenges of academic life.

I express my gratitude to the University of Sydney for awarding me the Research Training Program Stipend International Scholarship, which provided crucial financial support for my tuition fees and stipend. My heartfelt thanks also go out to my friends in Sydney, whose emotional support and companionship have been a source of solace during challenging times. Special mentions to Miss Sibei Zou for her infectious enthusiasm, Miss Haoyue Sun for her thoughtful discussions, Mr. Yuhang Liang for his unwavering assistance, Miss Xingxu Liu for her generosity, Mr. Zhisheng Lin, and Mr. Chunjing Su for their contributions to my research projects, along with all other friends in Prof. Jun Huang's and Prof. Rongkun Zheng's groups. I am immensely grateful to all the technical staff who have supported my research endeavours. I would like to thank the staff in Australian Centre for Microscopy and Microanalysis (ACMM) at the University of Sydney, especially Dr. Magnus Garbrecht, Dr. Jiangtao Qu, Dr. Asha Indiradevi, and Dr. Hanyu Li. I would like to thank the staff affiliated with the Sydney Analytical Core Research Facilities, especially Dr. Samuel Duyker and Dr.

Nicholas Proschogo. I would also like to thank the staff in the analytical lab in the School of Chemical and Biomolecular Engineering, especially Dr. Caroline Tao and Dr. Rachel Zhong. Their expertise and assistance have been invaluable.

Lastly, but most importantly, I wish to express my deepest love and gratitude to my family: my parents, Mr. Peng Zhang and Mrs. Li Xu, my grandmother, Mrs. Xianglan Wang, and my grandfather Mr. Jinglu Xu. I am profoundly grateful to them for bringing me into this world, nurturing me, and instilling in me the values of strength, kindness, happiness, and responsibility. During the 3.5 years I spent alone in Sydney, Australia, amidst the challenges of the Covid-19 pandemic, my parents spared no effort in supporting me. They diligently sent me necessary medicines and face masks from China, ensuring my well-being and safety. Their unwavering care and support have been my anchor during trying times. I also extend my heartfelt thanks to all my other family members for their love and support.

Thesis Authorship Attribution Statement

Partial of Chapter 1 of this thesis is published as:

Xingmo Zhang, Rui Tang,* Feng Li,* Rongkun Zheng,* and Jun Huang*

Tailoring Inorganic Halide Perovskite Photocatalysts toward Carbon Dioxide Reduction
Solar RRL, 6.6 (2022):2101058.

https://doi.org/10.1002/solr.202101058

I independently completed this work involving searching for literature and manuscript drafting. Jun Huang, Rongkun Zheng, Feng Li and Rui Tang conceived and designed the project and revised and corrected the manuscript.

Chapter 3 of this thesis is published as:

Xingmo Zhang, Rui Tang,* Haoyue Sun, Wenjie Yang, Weibin Liang, Feng Li,* Rongkun Zheng,* and Jun Huang*

Synergistically Interface-Engineered Inorganic Halide Perovskite Photocathodes for Photoelectrochemical CO2 Reduction

Energy & Fuels 37.23 (2023): 18163-18172.

https://doi.org/10.1021/acs.energyfuels.3c02613

I designed the study, synthesized the materials, carried out XRD, Absorption, SEM, and PEC characterizations, analysed the data, and wrote the drafts of the manuscript drafting. Rui Tang carried out TRPL tests, Haoyue Sun carried out XPS tests. Wenjie Yang and Weibin Liang suggested on the work. Jun Huang, Rongkun Zheng, Feng Li and Rui Tang conceived and designed the project and revised and corrected the manuscript.

Chapter 4 of this thesis is submitted as:

Xingmo Zhang, Rui Tang,* Haoyue Sun, Zhisheng Lin, Weibin Liang, Feng Li,* Rongkun Zheng,* and Jun Huang*

Copper-Tin Composite Bimetallic Nanoparticles on Bismuth Vanadate Nanoplate Photocathodes for Photoelectrochemical Carbon Dioxide Reduction

Submitted to ***Nano Letter*** (Under review)

I designed the study, synthesized the materials, carried out XRD, Absorption, SEM, TEM and PEC characterizations, analysed the data, and wrote the drafts of the manuscript drafting. Haoyue Sun carried out XPS tests. Zhisheng Lin carried out UV−vis DRS and NMR tests. Weibin Liang suggested on the work. Jun Huang, Rongkun Zheng, Feng Li and Rui Tang conceived and designed the project and revised and corrected the manuscript.

In addition to the statements above, in cases where I am not the corresponding author of a published item, permission to include the published material has been granted by the corresponding author(s).

Signed by Xingmo Zhang

27 June 2024

As supervisor for the candidature upon which this thesis is based, I can confirm that the authorship attribution statements above are correct.

Signed by Professor Jun Huang

27 June 2024

Table of Contents

Declaration of Originality.....2

Acknowledgements.....3

Thesis Authorship Attribution Statement.....5

Table of Contents.....7

List of Figures.....10

List of Tables.....16

Abstract.....17

Chapter 1 Introduction.....20

1.1 Principle of the photocatalytic CO_2 reduction reaction.....23

1.2 Methods to improve PVK-based PC/PEC performance.....24

1.2.1 Morphology Engineering.....25

1.2.2 Component engineering.....28

1.2.3 Interfacial heterojunction engineering.....33

1.2.4 Surface encapsulation.....45

1.3 Methods to improve Cu-based catalyst performance.....48

1.3.1 Metal Cu materials for CO_2RR.....48

1.3.2 Copper oxides for CO_2RR.....51

1.3.3 Cu alloys or bimetallic composites for CO_2RR.....53

1.3.4 Copper ions for CO_2RRs.....56

1.4 Conclusions and outlook.....57

Chapter 2 Methodology.....61

2.1 Growth methods.....61

2.1.1 Spin-coating method for thin-film samples.....61

2.1.2 Electroplating method.....61

2.2 Characterization.....62

2.2.1 Scanning electron microscopy (SEM) and Energy-dispersive X-ray spectroscopy (EDS, EDX, EDXS or XEDS).....62

2.2.2 High-resolution transmission electron microscopy (HRTEM) and high-angle annular dark filed image-scanning transmission electron microscopy (HAADF-STEM).....64

2.2.3 X-ray diffraction (XRD).....65

2.2.4 X-ray Photoelectron Spectroscopy (XPS).....66

2.2.5 UV-Vis spectroscopy.....66

2.2.6 Time-resolved photoluminescence (TRPL).....67

2.2.7 Space-charge-limited current (SCLC) measurement.....67

2.2.8 Photoelectrochemical (PEC) performance evaluation.....68

Chapter 3 Synergistically Interface-engineered Inorganic Halide Perovskite Photocathodes for Photoelectrochemical CO_2 Reduction.....69

3.1 Introduction.....69

3.2 Experimental section.....70

3.3 Results and discussions.....72

3.4 Conclusion.....93

Chapter 4 Copper-Tin Composite Bimetallic Nanoparticles on Bismuth Vanadate Nanoplate Photocathodes for Photoelectrochemical Carbon Dioxide Reduction.....95

4.1 Introduction.....95

4.2 Experimental section.....96

4.3 Results and discussions.....98

4.4 Conclusion.....115

Chapter 5 Electroplated Copper-Tin Composite on Copper foam for Photoelectrochemical Carbon Dioxide Reduction.....116

5.1 Introduction..... 116

5.2 Experimental section..... 117

5.3 Results and discussions..... 118

5.4 Conclusion..... 130

Chapter 6 Summary and Perspectives..... 131

6.1 Summary..... 131

6.2 Perspective..... 132

Reference..... 134

List of Figures

Figure 1 - 1. Band position of semiconductors for photocatalysts vs. NHE at pH = 7 (Bi_2WO_6,[21] TiO_2 Anatase,[22] WO_3,[23] ZnO,[24] Ag_3PO_4 cubic,[25] α-Fe_2O_3,[21] $SrTiO_3$,[26] $BiVO_4$,[27] Cu_2O,[28] MIL-125 (Ti),[29] ZnS,[30] CdS,[31] GaN,[32] g-C_3N_4,[33] Ta_3N_5,[34] $CsPbCl_3$,[35] $CsPbI_3$,[35] $CsPbBr_3$[35]) and the redox potential of CO_2RR vs. NHE (pH = 0).[36] 26

Figure 1 - 2. Classification of all-inorganic halide perovskite (PVK) - based photocatalysts. 28

Figure 1 - 3. a) CO_2RR yield of $CsPbBr_3$ QDs with different particle sizes. Reproduced with permission.[49] Copyright 2017, John Wiley and Sons. b) CO production of $CsPbBr_3$ nanocrystals and nanosheets. Adapted with permission.[72] Copyright 2021, John Wiley and Sons. c) The product yield of bulk $CsPbBr_3$, 3DOM CPB and 3DOM Au-CPB. Adapted with permission.[74] Copyright 2021, Elsevier. d) CO_2RR activity of four $CsPbBr_3$ nanorods. Reproduced with permission.[75] Copyright 2021, American Chemical Society 32

Figure 1 - 4. a) Schematic illustration of Fe(II)-doped $CsPbBr_3$ and the CH_4 and CO_2 production of Fe(II) acetate salt, $CsPbBr_3$ and Fe(II)-doped $CsPbBr_3$. Reproduced with permission.[78] Copyright 2019, American Chemical Society. b) Schematic illustration of $CsPbBr_3$-BF_4/Co and the stability test for 2 h cycles. Adapted with permission.[79] Copy right 2021, John Wiley and Sons 34

Figure 1 - 5. a) Yields of CO_2RR for $CsPb(Br_x/Cl_{1-x})_3$ (x = 1, 0.7, 0.5, 0.3, 0) nanocrystals. Adapted with permission.[80] Copyright 2019, Elsevier. b) CO evolution of 4 nm $CsPbBr_3$ nanosheets and $CsPbBr_{3-x}I_x$ nanosheets. Reproduced with permission.[72] Copyright 2021, John Wiley and Sons. c) CO_2RR performance of $Cs_2AgBiBr_6$ NCs. Adapted with permission.[83] Copyright 2018, John Wiley and Sons 36

Figure 1 - 6. a) CO yield of $Cs_3Bi_2Br_9$ and $Cs_3Bi_2Cl_9$. Reproduced with permission.[50] Copyright 2020, American Chemical Society. b) Crystal structure of $CsAgCl_2$ microcrystals. Adapted with permission.[85] Copyright 2021, American Chemical Society. c) CO_2RR performance of $CsAgCl_2$ microcrystals. Adapted with permission.[85] Copyright 2021, American Chemical Society. d) Crystal structure models of polyhedron-shaped non-cubes, hexapods, and cube-shaped $CsPbBr_3$ nanostructures and e) their CO_2RR yield. Adapted with permission.[86] Copyright 2020, American Chemical Society 37

Figure 1 - 7. The band diagram of a) the typical Schottky junction, b) the type-II heterojunction, c) the direct Z-scheme heterojunction and d) the Z-scheme heterojunction with conductors for PVK photocatalysts 40

Figure 1 - 8. a) The sketch of $CsPbBr_3$ nanocrystals/Pd nanosheets. Reproduced with permission.[95] Copyright 2018, American Chemical Society. b) Electron consumption rates of $CsPbBr_3$ nanocrystals/Pd nanosheets. Reproduced with permission.[95] Copyright 2018, American Chemical Society. c) The charge transfer sketch of 3DOM Au-CPB during the photocatalytic reaction. Adapted with permission.[74] Copyright 2021, Elsevier. d) The band diagram of $CsPbBr_3$ QDs/GO photocatalysts. Reproduced with permission.[2] Copyright 2017, American Chemical Society. e) Scheme of photocatalytic CO2 reduction on the Cs_4PbBr_6/rGO composites. Adapted with permission.[99] Copyright 2020, Elsevier. f) The schematic illustration of $Cs_2AgBiBr_6$ nanoplates@Cu-rGO. Reproduced with permission.[100] Copyright 2021, Royal Society of Chemistry..... 43

Figure 1 - 9. a) The band structure of $CsPbBr_3$ QDs-PCN with different QDs concentrations. Adapted with permission.[71] Copyright 2018, John Wiley and Sons. b) The schematic illustration of Cs_2SnI_6 nanocrystal/SnS_2 nanosheet photocatalysts. Adapted with permission.[103] Copyright 2019, American Chemical Society. c) The scheme of CPB/MS for photocatalytic CO_2 reduction. Adapted with permission.[104] Copyright 2021, Elsevier. d) Band diagram of x%-$CsPbBr_3$ QDs/UiO-66(NH_2). Reproduced with permission.[111] Copyright 2019, Elsevier. e) Energy band structure of NMF/CPB-NWs. Adapted with permission.[113] Copyright 2021, Elsevier. f) The bandgap information of $CsPbBr_3$/CuTCPP MOF. Adapted with permission.[114] Copyright 2021, John Wiley and Sons..... 46

Figure 1 - 10. The band diagram and photocatalytic performance of a-b) Z-Scheme α-Fe_2O_3/Amine-RGO/$CsPbBr_3$ hybrids. Adapted with permission.[115] Copyright 2020, Elsevier. c-d) $Cs_2AgBiBr_6$@g-C_3N_4 with Z-scheme (CABB@C_3N_4-82%)/type-II (CABB@C_3N_4-10%) heterojunction. Adapted with permission.[117] Copyright 2021, Elsevier. e-f) the 0D/2D Z-scheme heterojunction of $CsPbBr_3$ QDs/Bi_2WO_6 nanosheet. Adapted with permission.[118] Copyright 2020, American Chemical Society..... 48

Figure 1 - 11. The schematic illustration and CO_2RR performance of a-b) the a-TiO_2-encapsulated $CsPbBr_3$ nanocrystal. Adapted with permission.[120] Copyright 2018, John Wiley and Sons. c-d) the $CsPbBr_3$/ZIFs. Reproduced with permission.[121] Copyright 2018, American Chemical Society. e) Co doped $CsPbBr_3$@GDY. Reproduced with permission.[122] Copyright 2020, American Chemical Society. f-g) C_{60}/$CsPbBr_3$ composite. Adapted with permission.[123] Copyright 2021, Elsevier. h-i) P3HT/$CsPbBr_3$ composite. Adapted with permission.[124] Copyright 2021, Elsevier..... 52

Figure 1 - 12. Schematic diagram of CO_2 a) PC reduction over Cu/ILs/OVs-BMO in APMImBr aqueous solution.[127] b) photoreduction over $Bi_4O_5I_2$@Cu-0.5.[128] c) photoreduction on Cu/g-C_3N_4.[125] d) PEC reduction on Cu@porphyrin-COFs nanorods.[129] e) PC reduction on Cu NWs@HKUST-1 Mott-Schottky structure.[130] 56
Figure 1 - 13. a) Band alignment of CCZO,[131] b) different shape with different CO_2 reduction product of Cu/Cu_2O. [132] And the scheme of CO_2 PC reaction on c) CuO with different conformations, [133] d) the Ti/CFO/TiO_x film,[134] e) CuO-Pd/H_xMoO_{3-y} hybrids,[135] 58
Figure 1 - 14. Schematic illustration of CO_2 conversion mechanism of a) PC reaction on $Cu_{0.8}Ag_{0.2}/TiO_2$.[137] b) PEC reaction over Nt/Ti-10at.%Cu (A) and Nt/Ti-10at.%Cu (Q).[138] c) PC reduction on PdCu/BN,[139] and d) CTS-1.[140] 61
Figure 1 - 15. Mechanism scheme of CO_2 a) PC reduction on Cu-BiOCl,[64] b) reduction to HCHO over DAS-Sn_{75}-Cu_{25}/C_3N_4.[141] 62
Figure 2 - 1. Schematic diagram of spin-coating method 66
Figure 2 - 2. Schematic diagram of electroplating method 67
Figure 2 - 3. Structure diagram of a SEM machine.[154] 68
Figure 2 - 4. Diagram of the interaction of the electron with the sample surface.[155] 69
Figure 2 - 5. Schematic illustration of a TEM with STEM function.[157] 70
Figure 2 - 6. Diagram of signals produced from the interaction between a high-energy electron beam transmits a thin sample.[158] 70
Figure 2 - 7. Diagram of diffraction from lattice planes.[159] 71
Figure 2 - 8 Schematic illustration of a spectrometer for TRPL tests.[165][, #730] 72
Figure 3 - 1 Schematic illustration of the two-step spin-coating method to synthesize $CsPbBr_3$-based photocathodes 77
Figure 3 - 2. Top-view SEM images of a) CPB and b) CPB-F thin films on FTO/glass substrates. c) Cross-section SEM image of CPB thin film. d) XRD patterns of FTO/glass substrate, as well as CPB and CPB-F thin films grown on FTO/glass substrates 79
Figure 3 - 3 XPS survey of CPB and CPB-F thin films 80
Figure 3 - 4. High-resolution XPS spectra of a) Cs 3d, b) Pb 4f, c) Br 3d and d) F 1s (and fitted curve) of both CPB and CPB-F thin films. e) UV-vis absorption spectra and Tauc plots of CPB and CPB-F thin films. f) LSV curves of CPB and CPB-F photocathodes 81
Figure 3 - 5. SCLC behavior of the CPB and CPB-F thin films 83
Figure 3 - 6. *I-V* characteristic of CPB-AU, red line is Forward scan from 0 V to 3 V and the

black line is Reverse scan from 0 V to -3 V..... 84
Figure 3 - 7. XRD patterns of CPB-AU and CPB-F-AU thin films..... 84
Figure 3 - 8. SEM images of a) CPB-AU and b) CPB-F-AU. c) LSV curves of CPB, CPB-AU, and CPB-F-AU photocathodes..... 86
Figure 3 - 9. Top-view SEM images of a) CPB-N and b) CPB-F-N thin films..... 87
Figure 3 - 10. High-resolution TEM image of CPB-N. The darker part is CPB, and the brighter part is amorphous Nafion..... 88
Figure 3 - 11. a) HAADF image, and b-d) related EDS image of CPB-N, which are acquired on Spectra 60-300 S/TEM under 300 kV..... 88
Figure 3 - 12. XRD of CPB-N, CPB-N-AU, and CPB-F-N-AU thin films..... 89
Figure 3 - 13. High-resolution XPS spectra of a) Cs 3d, b) Pb 4f, c) Br 3d, and d) F 1s of CPB, CPB-N, and CPB-F-N thin films. e) UV-vis absorption spectra and Tauc plots of CPB-N and CPB-F-N thin films. f) LSV curves of CPB, CPB-N, and CPB-F-N photocathodes..... 91
Figure 3 - 14. XPS survey of CPB-N and CPB-F-N..... 91
Figure 3 - 15. SCLC behavior of the CPB, CPB-N and CPB-F-N thin films..... 92
Figure 3 - 16. a) SEM image of CPB-F-N-AU. b) Cross-section SEM image of CPB-F-N-AU. c) TRPL curves of CPB, CPB-F, CPB-N, CPB-F-N, and CPB-F-N-AU photocathodes. d) LSV curves of CPB, CPB-N-AU, and CPB-F-N-AU photocathodes..... 94
Figure 3 - 17. The equivalent circuit diagram (upper) and the Nyquist plots of CPB, CPB-F, CPB-AU, CPB-N, and CPB-F-N-AU (lower). Since we mainly focus on the R_{ct}, we simplified the equivalent circuit of R_s, CPE_1 and R_{bulk} to R_1..... 95
Figure 3 - 18. I-t curves of a) CPB, b) CPB-F, c) CPB-AU, d) CPB-N, e) CPB-F-N, and f) CPB-F-N-AU photocathodes, at -0.5 V vs $E_{Ag/AgCl}$ with chopped light illumination..... 97
Figure 3 - 19. The recycle test of LSV on CPB-F-N-AU..... 98
Figure 3 - 20. LSV curve of photocathode in Ar environment and in CO_2 environment..... 98
Figure 3 - 21. Repeated LSV tests of CPB, CPB-F, CPB-N, CPB-AU, CPB-N-AU and CPB-F-N-AU..... 99
Figure 3 - 22. VB-XPS of a) CPB, b) CPB-F-N, and c) schematic band structure and charge transfer of CPB-F-N-AU..... 100
Figure 4 - 1. a) Top-view SEM image of $BiVO_4$ nanoplate thin film. b) Cross-section SEM image of $BiVO_4$ nanoplate thin film, showing its thickness of 2.5 μm. c) Top-view SEM image of CuSn NPs@$BiVO_4$ photocathode..... 108

Figure 4 - 2. TEM image of a) Cu NPs and b) CuSn NPs. c,d) HAADF-STEM images of CuSn NPs. e-g) EDS mappings of O, Cu and Sn element in CuSn NPs as shown in d)..... 109
Figure 4 - 3. a) TEM image and b) the zoomed-in TEM image of CuSn NPs@$BiVO_4$. c-g) HAADF and EDS mappings of Bi, O, Cu and Sn element in CuSn NPs@$BiVO_4$.....110
Figure 4 - 4. a) XRD patterns of Cu NPs and CuSn NPs (The bottom two images are the simulated XRD peaks for Cu_2O and SnO_2). b) XRD of $BiVO_4$ nanoplate thin film and CuSn NPs@$BiVO_4$ (The bottom image is the simulated XRD peaks for $BiVO_4$). c) UV−Vis DRS and Tauc plots (inset) of $BiVO_4$ nanoplate film, Cu NPs@$BiVO_4$, and CuSn NPs@$BiVO_4$. 112
Figure 4 - 5. XPS survey and high-resolution XPS spectrum of Cu and Sn elements of a-c) Cu NPs and d-f) CuSn NPs.....113
Figure 4 - 6. a) LSV curves of $BiVO_4$, Cu NPs@$BiVO_4$, and CuSn NPs@$BiVO_4$. b) *I-t* curves of photocathodes at the applied voltage of -0.8 V vs. $E_{Ag/AgCl}$. c) Nyquist impedance plots of $BiVO_4$, Cu NPs@$BiVO_4$, and CuSn NPs@$BiVO_4$ under light illumination and CuSn NPs@$BiVO_4$ in the dark. Inset is the zoomed-in region from 0-400 Ω and the equivalent circuit.....115
Figure 4 - 7. LSV of $BiVO_4$ with Cu NPs, CuSn 4:1 NPs, CuSn 2:1 NPs (short for CuSn NPs), CuSn 1:1 NPs, and pure $BiVO_4$ photocathode.....117
Figure 4 - 8. LSV of $BiVO_4$ with 50/100/200 μl CuSn NPs solution..... 118
Figure 4 - 9. LSV tests of CuSn NPs@$BiVO_4$ in electrolyte bubbled with Ar/CO_2.....118
Figure 4 - 10. a-b) ^1H NMR spectrum of the electrolyte of the CuSn NPs@$BiVO_4$ photocathode after CO_2RR I-t test for 2 h, with the applied voltage of -0.8 V vs. $E_{Ag/AgCl}$. c) ^1H NMR spectrum of the electrolyte before and after the CO_2RR I-t test, and the pure D_2O solvent..... 120
Figure 4 - 11. a) VB-XPS of $BiVO_4$.b) Schematic diagram of CuSn NPs@$BiVO_4$ photocathodes under light irradiation and applied negative voltage.....122
Figure 4 - 12. a) VB-XPS of CuSn NPs. b) UV−vis absorption and Tauc plot (inset) of CuSn NPs..... 122
Figure 4 - 13. High-resolution XPS spectrum of a) Cu element in CuSn NPs, b) Sn element in CuSn NPs, c) Bi element in $BiVO_4$, and d-f) Cu, Sn, and Bi element in CuSn NPs@$BiVO_4$. 123
Figure 5 - 1. a) c) Top-view SEM image and b) d) Cross-section SEM image of Cu film and

Cu foam with CuSn (1:1 4 5), respectively.....130
Figure 5 - 2. a) Chopped LSV test and b) I-t test in the dark at -0.8 V vs $E_{Ag/AgCl}$ of Cu film and Cu foam with CuSn composite layers (1:1 -4 5). SEM images of c) Cu film and d) Cu foam with CuSn composite layers (1:1 -4 5) after the PEC tests.....132
Figure 5 - 3. SEM images with the inset EDS atomic fraction pictures of a) Cu foam, as well as Cu foam with CuSn composites with the ratios of b) (1:1 -8 20), c) (1:2 -8 20), and d) (2:1 -8 20), respectively.....133
Figure 5 - 4. a) XRD patterns of a series of samples; (inset shows the simulate XRD of Cu (Cubic, Fm-3m, 225)) b) UV-vis absorption and c) the calculated Tauc plots of the Cu foam and the Cu foam with CuSn CuSn composite layers with the ratios of (1:1 -8 20), (1:2 -8 20), and (2:1 -8 20), respectively.....136
Figure 5 - 5. a), c), e), g) Cu element and b), d), f), h) Sn element and i) XPS survey and j) VB-XPS of Cu foam and Cu foam with CuSn (1:1 -8 20), (1:2 -8 20) and (2:1 -8 20), respectively..... 138
Figure 5 - 6. a) Chopped LSV curves, b) photoresponse, c) I-t curves at -1 V vs $E_{Ag/AgCl}$ and d) EIS in the dark of Cu foam and Cu foam with CuSn (1:1 -8 20), (1:2 -8 20) and (2:1 -8 20), respectively..... 139
Figure 5 - 7. SEM images with the inset EDS atomic fraction pictures after PEC tests of a) Cu foam and Cu foam with CuSn b) (1:1 -8 20) c) (1:2 -8 20) and d) (2:1 -8 20).....140
Figure 5 - 8. a-c) GC peaks of the CO_2 gas and the gas product of photocathode after I-t test. d) IC peaks of the liquid product of the photocathode after the I-t test..... 142

List of Tables

Table 1 - 1. Half-cell equation of CO_2 reduction to different products with E^0 vs NHE, pH = 7. 28

Table 1 - 2. Summary of morphology-designed PVK photocatalysts and their CO_2RR performance.....31

Table 1 - 3. Summary of defect-engineered PVK photocatalysts and their CO_2RR performance.....36

Table 1 - 4. Summary of PVK photocatalysts with heterojunction structures and their CO_2RR performance.....47

Table 1 - 5. Summary of encapsulated PVK photocatalysts and their CO_2RR performance.. 52

Table 1 - 6. Summary of metal Cu catalysts and their CO_2RR performance.....55

Table 1 - 7. Summary of copper oxide catalysts and their CO_2RR performance..... 57

Table 1 - 8. Summary of copper-alloy or bimetallic composites and their CO_2RR performance. 60

Table 1 - 9. Summary of copper ions catalysts and their CO_2RR performance.....61

Table 3 - 1. The calculated atomic percentage of F, Pb, Cs and Br of CPB-F by XPS survey. 80

Table 3 - 2. The parameters related to lifetimes fitted from the TRPL curves of CPB, CPB-F, CPB-N, CPB-F-N, and CPB-F-N-AU photocathodes..... 92

Table 3 - 3. The fitted parameters of Nyquist plots of CPB, CPB-F, CPB-AU, CPB-N, and CPB-F-N-AU..... 94

Table 4 - 1. The fitted parameters of Nyquist plots of $BiVO_4$, Cu NPs@$BiVO_4$ and CuSn NPs@$BiVO_4$ under light illumination and CuSn NPs@$BiVO_4$ in the dark.....116

Table 5 - 1. The fitted parameters of Nyquist plots of Cu foam, Cu foam with CuSn (1:1 -8 20), (1:2 -8 20) and (2:1 -8 20)..... 139

Table 5 - 2. The IC tested concentrations of the Formate in the electrolyte of $KHCO_3$ and Cu foam, Cu foam with CuSn (1:1 -8 20), (1:2 -8 20) and (2:1 -8 20) after 0.5 h I-t test under light illumination..... 142

Abstract

In recent years, photoelectrochemically (PEC) CO_2 reduction reaction (CO_2RR) has emerged as one of the most promising methods to address global warming and the energy crisis by converting CO_2 into valuable chemicals utilizing solar energy. Halide perovskite (PVK) materials, which have been broadly used for developing high-performance photovoltaics, have also shown immense potential for photocatalytic CO_2 reduction, due to their excellent optoelectronic properties as well as their cost-effective raw materials and facile fabrication processing. However, the rational approach to directly applying this class of materials to photoelectrochemical (PEC) CO_2 reduction remains unclear, in particular, given that this class of materials normally suffers from instability issues in the aqueous solution. Among metal-based catalysts, copper-tin (CuSn) composites have been widely reported for electrochemically reducing CO_2RR to produce formic acid but have rarely been studied for PEC CO_2RR.

In this thesis, with the aim of addressing the above-mentioned challenges, exploring more promising candidate materials in the field of PEC CO_2RR, and gaining an in-depth understanding of the working mechanisms of these materials for PEC CO_2RR, I carried out systematic research on using halide perovskite materials and CuSn composites as the active mediums for PEC CO_2RR. In detail, I developed the facile solution-processed methods to grow the high-quality heterostructures and composts coupling the above-mentioned material systems with other functional materials and investigated the effect of interfaces on the material properties and the performance and stability of the related devices for PEC CO_2RR.

In **Chapter 1**, I provided a comprehensive overview of the recent progress on PC/PEC CO_2RR based on PVK-related catalysts and Cu-based catalysts. I summarized and discussed the main strategies for improving the PC/PEC CO2RR performance. After that, pointed out the currently faced challenges and future potential research directions of PVK-based and Cu-based catalysts for PC/PEC CO_2RR.

In **Chapter 2**, I introduced the main methodologies applied in this thesis, including the growth approaches for preparing various PVK-based and Cu-based composites and heterostructures, as well as the relevant characterization techniques, such as scanning electron microscopy (SEM) and energy-dispersive X-ray spectroscopy (EDS, EDX, EDXS or XEDS), high-resolution transmission electron microscopy (HRTEM) and high-angle annular dark

filed image-scanning transmission electron microscopy (HAADF-STEM), X-ray diffraction (XRD), X-ray Photoelectron Spectroscopy (XPS), UV-Vis spectroscopy, time-resolved photoluminescence (TRPL), space-charge-limited current (SCLC) measurement and photoelectrochemical (PEC) performance evaluation together with their mechanisms..

In **Chapter 3**, which details my first research work, I synthesized $CsPbBr_3$ (CPB) thin-film photocathode catalysts using a two-step spin-coating method and modified the perovskites with a synergistic combination of 5% fluorine (F)-doping, Nafion (N) solution, and a 15 nm Au-coating, based on the stepwise optimized interface-engineering strategy. It was demonstrated that, with the synergistic effect of the interface-engineering approaches, the optimal photocathode (CPB-F-N-AU) achieved greatly enhanced light absorption and charge carrier transfer capability compared with the pristine CPB-based one. As a result, the as-fabricated CPB-F-N-AU photocathode exhibited the maximum photocurrent of -0.23 mA cm^{-2} at a bias of -0.5 V vs $E_{Ag/AgCl}$ under the 4.13 mW cm^{-2} light illumination, which is twice that of the pristine CPB device. This work demonstrated the practicability of directly applying halide perovskites in PEC CO_2 reduction and proposed useful interface-engineering strategies for tuning the relevant device performance, which can also be extended to other fields like photovoltaics and photodetectors.

In **Chapter 4**, which covers my second research work, I chose the non-toxic and low-cost bismuth vanadate ($BiVO_4$) nanoplates as the light-absorbing substrate and applied CuSn nanoparticles (NPs) onto $BiVO_4$ nanoplates (CuSn NPs@$BiVO_4$) to form type-II heterojunctions. Under the negative applied voltage, photo-induced electrons could transport through band bending of $BiVO_4$ via the tunnelling and hopping effects, leading to the reduction reactions on the sample surface. The as-fabricated photocathodes showed the highest photocurrent of -0.774 mA cm^{-2} at the applied voltage of -0.95 V vs. $E_{Ag/AgCl}$, which is 3 times higher than the pristine $BiVO_4$ photocathodes. This work demonstrated the potential of Cu-Sn bimetallic NPs and $BiVO_4$ nanoplates for the high-performance PEC CO_2RR.

In **Chapter 5**, which presents my third work, I electroplated CuSn composite onto Cu foam substrates due to the higher specific surface area of Cu foam than the Cu film substrate, with the aim to further improving the efficiency and stability of the devices for PEC CO_2RR than those in my second research work. With different Cu:Sn ratios, the coated CuSn composite

layers showed different morphologies on the surface of the Cu foam substrates. The absorption properties of the oxidized state of the photocathodes' surface would ensure the photo-response of my photocathodes in the PEC tests under light illumination. The Cu foam with CuSn (2:1 -8 20) showed the highest current density during the PEC tests, while Cu foam with CuSn (1:1 -8 20) showed the most formate production of CO_2RR. This work provided the possibility of applying Cu foam with CuSn composite for effectively enhancing the PEC CO_2RR performance.

In **Chapter 6**, I summarized the main research endeavours explored in this thesis. Additionally, I provided perspectives on the potential of halide perovskite-based and Cu-based catalysts, emphasizing the importance of suitable composite and heterostructure engineering for achieving high-performance and high-stability in PEC CO_2RR.

In Summary, this whole project puts forward innovative strategies of heterojunction engineering of perovskite materials and CuSn composites as the catalysts for PEC CO_2RR. These include the development of synergistically interface-engineered inorganic halide perovskite photocathodes for photoelectrochemical CO_2 reduction, copper-tin composite bimetallic nanoparticles on bismuth vanadate nanoplate photocathodes for photoelectrochemical carbon dioxide reduction, and electroplated copper-tin composite on copper foam for photoelectrochemical carbon dioxide reduction. These findings hold promise for applications not only in PEC CO_2 reduction but also in related fields like photovoltaics and photodetectors.

Chapter 1 Introduction

Along with the superfluous usage of fossil fuels and unlimited emission of greenhouse gases CO_2, the energy shortage and climate change have attracted broad attention. Inspired by the photosynthesis reaction, which was first reported by Inove and Fujishima et al. in 1979, photocatalytic (PC) and photoelectrochemical (PEC) CO_2 reduction reactions (CO_2RR) have become one of the most promising strategies to transform CO_2 into sustainable and useful chemicals such as carbon monoxide (CO), methane (CH_4), methanol (CH_3OH).[1-3] In the PC reaction system, reduction reactions and oxidation reactions happen at the same time on the same photocatalyst, in which it is difficult to separate the reduction products and the possibility of the reoxidation of the product would be increased.[4] In the PEC reaction system, the reduction reactions and the oxidation reactions are separated by the ion-exchange membrane, and they occur on the photoelectrodes and the counter electrodes, in which it is easier to control the reaction procedure and collect the reaction product(s) as compared to PC reaction process.[4]

So far, a great number of semiconductor candidates have been reported as PC or PEC catalysts for solar-driven CO_2RR, which include metal oxides (TiO_2, Cu_2O, etc), sulphides (CdS, $CuIn_5S_8$, etc), nitrides (CoN, C_3N_4, etc), metal organic frameworks (MOFs), and perovskite-structured oxides.[5-15] The energy band alignments of some commonly applied semiconductor photocatalysts are shown in **Figure 1 - 1**. It is noted that effectively activating CO_2 into the intermediate CO_2^- requires driving energy of −1.4 V (vs. normal hydrogen electrode, NHE, pH = 0) (−1.90 V vs NHE, pH = 7), which is obviously greater than conduction band values of the most semiconductor catalysts.[16] In addition, the Gibbs Free Energy (ΔG^0) for CO_2 reduction into CO is 259 kJ mol^{-1}, which requires the bandgaps of semiconductors larger than 1.34 eV.[17] Although the enhanced PC/PEC CO_2RR applications have been evidenced, these materials are still suffering from some intrinsic drawbacks, such as poor stability, limited optical response, weak reaction activity, and high cost; additionally, most materials can only absorb ultraviolet (UV) light and have low selectivity for products.[18-20] Thus, to relieve the global warming issue and to realize a carbon-neutral energy cycle, it is still of great challenge to discover novel PC/PEC catalysts with a broad-range optical response.

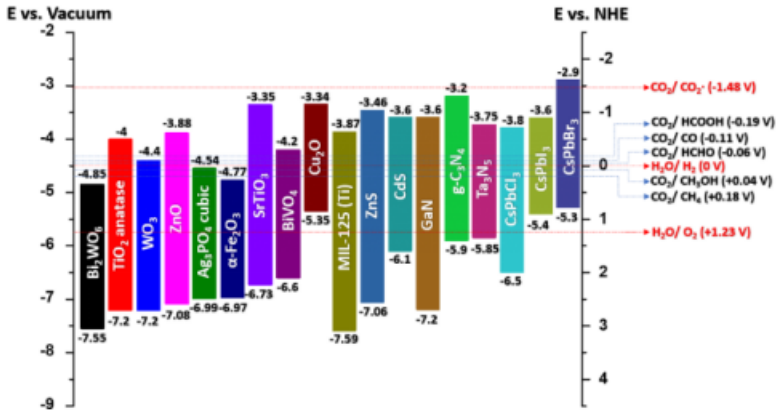

Figure 1 - 1. Band position of semiconductors for photocatalysts vs. NHE at pH = 7 (Bi_2WO_6,[21] TiO_2 Anatase,[22] WO_3,[23] ZnO,[24] Ag_3PO_4 cubic,[25] α-Fe_2O_3,[21] $SrTiO_3$,[26] $BiVO_4$,[27] Cu_2O,[28] MIL-125 (Ti),[29] ZnS,[30] CdS,[31] GaN,[32] g-C_3N_4,[33] Ta_3N_5,[34] $CsPbCl_3$,[35] $CsPbI_3$,[35] $CsPbBr_3$[35]) and the redox potential of CO_2RR vs. NHE (pH = 0).[36]

Halide perovskites (PVKs) are a class of ionic crystals with a similar structure to calcium titanium oxide ($CaTiO_3$), sharing the general chemical formula of ABX_3, where A represents monovalent cation (e.g. $CH_3NH_3^+$ (MA^+), $HC(NH_2)_2^+$ (FA^+), or Cs^+), B can be divalent cation (e.g. Pb^{2+}, Sn^{2+}), and X stands for halogen anion (Cl^-, Br^- or I^-).[37-38] In particular, when the A-site is occupied by a monovalent metallic cation, such as Cs^+, PVKs can be referred to as all-inorganic perovskite materials. The forms of PVKs include 3D cubic structure, orthorhombic structure, 2D nanosheets, 1D nanorods, nanowires, and 0D nanoparticles and quantum dots.[37] The controllable forms and structures of PVKs provide convenience for further structural designs and device fabrications. With the merits of large absorption coefficient, long carrier diffusion length, wide and tuneable bandgap from ultraviolet to near-infrared, high carrier mobility and lifetime, and excellent defect tolerance, the PVKs have been widely applied in solar cells, photodetectors, light-emitting diodes (LEDs) and field-effect transistors (FETs).[17, 39-48]

Additionally, PVKs possess the proper bandgaps for CO_2RR and relatively higher conduction bands (CB), which indicates that this family of materials have stronger reducibility and can satisfy the activation energy of CO_2 molecules. Their CO_2RR products also show good selectivity. In this regard, PVKs have great potential in photocatalysts for CO_2RR. In addition, modifications on the pure PVK materials could solve their issues of poor stability, limited optical response, weak reduction activity, and so on.[49] Moreover, Shen et al. demonstrated

that the adsorption model of the CO_2 reduction intermediates and the active sites of CO_2 are closely associated with the composition of the perovskite catalysts.[50] The regulation of halide ions in PVKs to improve the CO_2RR performance will be further introduced in the mix-component doping part.

Cu-based catalysts for PC/PEC CO_2RR have also attracted considerable attention due to their earth-abundant and low-cost nature.[51] Copper (Cu) is the only metal system that can produce hydrocarbons for the CO_2RR, due to their negative adsorption energy to *CO and positive adsorption energy to *H.[52-55] However, the product selectivity of Cu-based catalysts needs to be improved based on the binding strength of reduction intermediates.[52] Metal Cu and Cu-based alloys can be combined with light-absorbing semiconductors to enhance the PC/PEC capability.[56-58] In addition, the plasma resonance of Cu-based nanoparticles can induce visible light absorption.[59] With the narrow bandgap of 1.7 eV and 2.2 eV respectively, copper oxide (CuO) and cuprous oxide (Cu_2O) are also promising materials for PC/PEC CO_2RR.[60-63] Copper ions can also be doped into other functional semiconductors to change the lattice structure of the material systems and provide active sites for CO_2RR. [64]

Currently, there have been a lot of reports on the development of high-performance PVK-based and Cu-based catalysts for PC/PEC CO_2RR; however, few reports have systematically discussed the in-depth mechanism for improving the PC/PEC performance of PVK-based and Cu-based catalysts, which is of great importance for future investigation. In **Section 1.1**, I introduce the basic information on PC/PEC CO_2RR. In **Section 1.2**, I provide a comprehensive overview of the recent advances and ongoing progress on PC/PEC CO_2RR based on PVK-related catalysts from the structure-component engineering perspective to clarify its influence on the carrier transfer, stability, and product selectivity of PVK-based photocatalysts, as shown in **Figure 1 - 2**. After that, the Cu-based catalysts are classified according to the formations and the chemical states of Cu-based catalysts and are discussed in **Section 1.3**. Following Section 1.3, the current challenge and future potential research direction of PVK-based and Cu-based catalysts are also pointed out and highlighted (**Section 1.4**). This chapter could provide basic understanding and advanced knowledge on the design and synthesis of PVK-based and Cu-based catalysts, which could benefit not only the PC/PEC CO_2 field but also the related solar-energy conversion applications. In addition, the performed research works in other chapters of this thesis would be designed to address the

current challenges as detailed in **Section 1.4** of this Chapter.

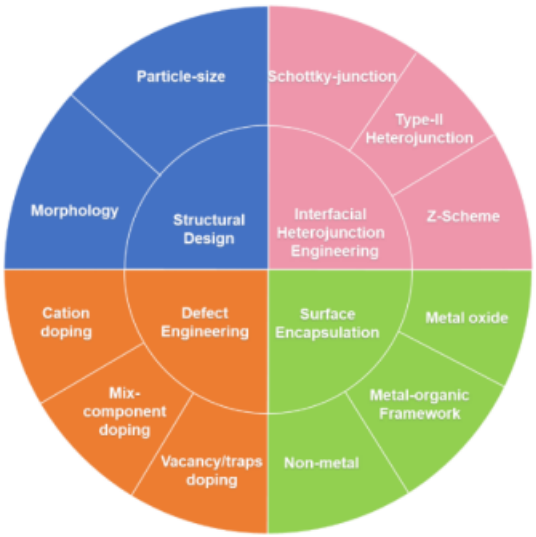

Figure 1 - 2. Classification of all-inorganic halide perovskite (PVK) - based photocatalysts.

1.1 Principle of the photocatalytic CO_2 reduction reaction

From the thermodynamic perspective, the CO_2 molecule is very stable with the C=O bond energy of 750 kJ mol^{-1}, which is higher than that of C−O (327 kJ mol^{-1}) bond, C−C bond (336 kJ mol^{-1}) and C−H bond (411 kJ mol^{-1}).[65-66] And the linear symmetric structure of CO_2 is averse to its activation. Therefore, the activation and conversion of the CO_2 molecule into a bent carbonate anion radical molecule (CO_2^-) is required by chemisorption on the surface of photocatalysts.[67] Kinetically, the multiple electrons involved in reactive steps make the CO_2RR quite sluggish. The complicated reaction intermediates adsorption/desorption can produce diverse reduction products.[68]

There are generally three procedures during a PC CO_2RR process: (1) the generation of light-induced electron-hole pairs by absorbing incident photons with the energy higher than the bandgap of the photocatalysts; (2) the separation of the electron-hole pairs, after which the electrons are excited to the conduction band (CB) and the holes left in the valence band (VB) and transfer to reaction sites; and (3) the oxidation and reduction reaction on the photocatalysts surface reaction sites with adsorbed CO_2.[38] While in a PEC reaction process, the higher CB can promise better reducibility. For a suitable material as a photocatalyst, its bandgap should be wide enough to cover the range of reduction and oxidation potentials. At the same time, the light-utilization efficiency requires the bandgap of the photocatalyst as

narrow as possible.[69] Based on the amount of electrons and protons reacted, the half CO_2RR equations to various products in water at pH = 7 are listed in **Table 1 - 1**, with the theoretical reduction potentials (E^0) vs the normal hydrogen electrode (NHE).[70] The multi-electron reaction steps indicate that the selectivity of diverse products should also be taken into consideration when designing suitable photocatalysts.[16]

On this basis, it can be concluded that the optical response, carrier transfer capability and the separation of photo-generated electron and hole pairs of the photocatalysts determine how many effective carriers can participate in the reduction reaction, which is one of the main factors for photocatalytic efficiency. Moreover, the activation of the CO_2 molecules is the rate-determining step of CO_2RR activity. By tailoring the intermediates' adsorption/desorption, selective photoreduction is promising to be realized. In addition, the reaction conditions can also influence the products of CO_2RR through the different solubility of CO_2 in different media.[71] Currently, the most reported PC/PEC CO_2 reduction products of PVK-based or Cu-based catalysts are CO, CH_4, and H_2, but the precise controls of the particular products still need to be further studied. In addition, the rational way to incorporate surface/interface-morphology engineering strategies of the PVK-based catalysts or the component modification of the Cu-based catalysts to improve the PC/PEC CO_2RR performance is still in its infancy and calls for further systematic investigations.

Table 1 - 1. Half-cell equation of CO_2 reduction to different products with E^0 vs NHE, pH = 7.

Equation	Product	E^0 (V)
$CO_2 + e^- = CO_2^-$	carbonate anion radical	−1.90
$CO_2 + 2H^+ + 2e^- = CO + H_2O$	Carbon monoxide	−0.53
$CO_2 + 2H^+ + 2e^- = HCOOH$	Formic acid	−0.61
$CO_2 + 4H^+ + 4e^- = HCHO + H_2O$	Formaldehyde	−0.48
$CO_2 + 6H^+ + 6e^- = CH_3OH + H_2O$	Methanol	−0.38
$CO_2 + 8H^+ + 8e^- = CH_4 + 2H_2O$	Methane	−0.24
$2CO_2 + 8H^+ + 8e^- = CH_3COOH + 2H_2O$	Acetic acid	−0.31
$2CO_2 + 14H^+ + 14e^- = C_2H_6 + 4H_2O$	Ethane	−0.51

1.2 Methods to improve PVK-based PC/PEC performance

Previous studies have confirmed that the photocatalytic CO_2RR performance of PVK-based catalysts is mainly hindered by three factors: the optical response capability, the carrier transfer behaviour, and the reaction intermediate adsorption capability. Based on these three points, a series of structure-component engineering strategies, such as structure design, defect engineering, interfacial heterojunction engineering, and surface encapsulation, have been reported to modify PVK-based catalysts and improve the photocatalytic CO_2RR performance.

1.2.1 Morphology Engineering

Despite a suitable bandgap for CO_2RR, pure PVK materials are still facing the issues of poor catalytic performance. To overcome the problems, different efforts have been reported to improve the quality of PVK catalysts, such as tuning the size and thickness to change the light absorption ability and changing the morphology of PVK catalysts to increase CO_2 reaction sites.

1.2.1.1 Size control

On account of the quantum confinement effect in the colloidal semiconductor QDs, PVK QDs have been reported as promising materials for widely ranged optoelectronic applications. Hou's group prepared colloidal $CsPbBr_3$ QDs with various sizes by tuning the temperature of the solution phase synthesis strategy.[49] The particle size was found to be increased with the increase of the reaction temperature, leading to the absorption edges and the photoluminescence (PL) peak being shifted to longer wavelengths. However, as for QDs, the reduced size can cause aggregation, while the larger size will result in a smaller surface area. Thus, from their PL decay results and CO_2RR yields, as shown in **Figure 1** - **3**a, 8.5 nm QDs show the optimized performance with the generation rate of CO 4.3 μmol g^{-1} h^{-1}, CH_4 1.5 μmol g^{-1} h^{-1} and H_2 0.1 μmol g^{-1} h^{-1} in ethyl acetate (EA) /water system under the AM 1.5 G 300 W Xe lamp illumination. In addition to the size of PVK QDs, the thickness of 2D PVK nanosheets has also been investigated for PC/PEC CO_2RR. As shown in **Figure 1** - **3**b, Wu et al. compared the 2D $CsPbBr_3$ (CPB) nanosheets with different thicknesses and found that, with the decrease of the thickness, the absorption and the PL peaks could show the tendency of blue-shift with the VB and the CB become more positive and more negative,

respectively.[72] The optimized thickness of 2D $CsPbBr_3$ nanosheets was evaluated to be 4 nm, with a CO formation rate of 21.6 μmol g^{-1} h^{-1} in the H_2O-electron donor system.

The size control method can tune the bandgap and light absorption properties of 0D and 2D PVK materials. However, the exciton peaks that appeared in the absorption spectrum indicated the low light-generated electron-hole pairs of the pure 0D/2D PVKs. Also, without additional protection materials, the stability of the pure PVKs needs further improvement. So, the combination of size control and other modification methods is a good strategy.

1.2.1.2 Morphology control

The modification of nanoparticle morphology can improve the mass transfer at the photocatalytic interface, which can facilitate CO_2 adsorption.[73] Tang et al. constructed a unique three-dimensionally ordered microporous (3DOM) structure $CsPbBr_3$ (3DOM CPB) and used them as suitable active materials for PC/PEC CO_2RR.[74] The ordered porous structure with the light scattering effect led to a better light-harvesting performance in comparison with bulk $CsPbBr_3$ single crystals and thin films. They also added Au particles as the sensitizers to enhance the performance of the resultant photocatalyst. In the ethyl alcohol (EA)-isopropanol system, under a 300-W Xe lamp with a 420 nm filter, the electron consumption rate was calculated to be 21.8 μmol g^{-1} h^{-1} for 3DOM CPB, as shown in **Figure 1 - 3**c. Apart from the 3DOM perovskite structure, orthorhombic phase spiral $CsPbBr_3$ nanorods with unusual anisotropy were reported by Pradhan's group.[75] By controlling the injection time of orthorhombic Cs_2CdBr_4 nanorods into the Pb(II) reaction system, four types of $CsPbBr_3$ nanorods were synthesized with structures of A (linear nanorod), B (spiral nanorod), C (spiral cutting to connected cubes), and D (spiral cutting to connected platelets). The CO_2 adsorption ability and the product evolution rate depended on the spiral nature of four sets of nanorods. The {110} and {002} facets created by spiralling led to the decrease of CO_2 adsorption and CH_4 desorption. After 2 h CO_2RR under 150 mW cm^{-2} illumination, the products were A (CH_4 74.45 μmol g^{-1}, CO 40.81 μmol g^{-1}), B (101.12 μmol g^{-1} in total), C (90.07 μmol g^{-1} in total) and D (72.59 μmol g^{-1} in total), as shown in **Figure 1 - 3**d.

The morphology control of PVKs can either increase the specific surface area for CO_2 activation and reaction or change the crystal facets for modifications of CO_2 adsorption and product desorption. However, the higher PL peak intensities of pure PVKs indicated the

increased recombination of photo-generated charges. Thus, controlling the morphology of PVKs by co-catalyst modification methods can significantly increase the product yield and stability of the photocatalysts.

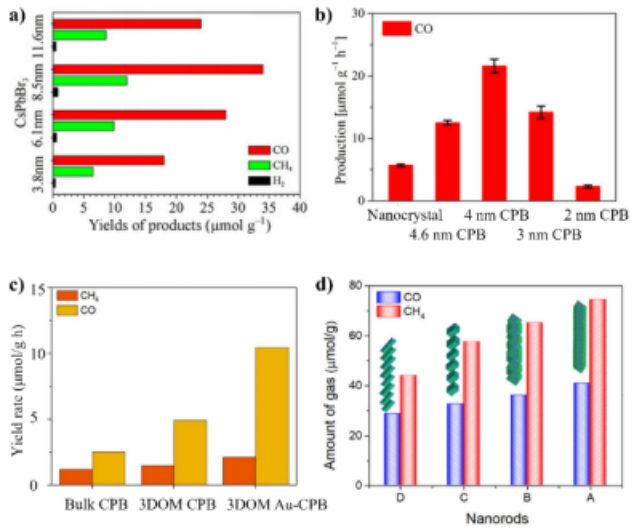

Figure 1 - 3. a) CO_2RR yield of $CsPbBr_3$ QDs with different particle sizes. Reproduced with permission.[49] Copyright 2017, John Wiley and Sons. b) CO production of $CsPbBr_3$ nanocrystals and nanosheets. Adapted with permission.[72] Copyright 2021, John Wiley and Sons. c) The product yield of bulk $CsPbBr_3$, 3DOM CPB and 3DOM Au-CPB. Adapted with permission.[74] Copyright 2021, Elsevier. d) CO_2RR activity of four $CsPbBr_3$ nanorods. Reproduced with permission.[75] Copyright 2021, American Chemical Society.

Table 1 - 2. Summary of morphology-designed PVK photocatalysts and their CO_2RR performance.

Type	Photocatalyst	Medium	Light source	Products	Reference
Size control	8.5 nm $CsPbBr_3$ QDs	EA with small amount of water	300 W Xe lamp, Standard AM 1.5G filter	CO 4.3 μmol $g^{-1}h^{-1}$ CH_4 1.5 μmol $g^{-1}h^{-1}$ H_2 0.1 μmol $g^{-1}h^{-1}$	49
	2D $CsPbBr_3$ nanosheets	H_2O-electron donor	100 mW cm^{-2}, 400 nm filter	CO 21.6 μmol $g^{-1}h^{-1}$	72
Morphology design	3DOM CPB	Isopropanol-EA	300 W Xe lamp, 420 nm filter	electron consumption rate ($R_{electron}$)	74

			21.8 μmol $g^{-1}h^{-1}$	
A type $CsPbBr_3$ nanorods	EA-water (300:1,v/v)	450 W Xe arc lamp 150 mW cm^{-2}	After 2 h, CO 40.81 μmol g^{-1} CH_4 74.45 μmol g^{-1}	[75]

1.2.2 Component engineering

In the field of PVK photovoltaics, it has been confirmed that the optical response and carrier transfer ability of the active PVKs can be affected through defect engineering, due to the introduction and tunability of the defect levels. However, in typical photocatalytic reactions, defect engineering is also regarded as an efficient strategy to promote the adsorption of the intermediate adsorbates, thus enhancing the resulting catalytic performance.[76] Therefore, it is promising to use defect engineering methods to modulate the photoreduction activity of PVK-based catalysts while simultaneously achieving selective product generation.

1.2.2.1 Metal-ion doping

Metal-ion doping on the B-site can promote the adsorption of the intermediate adsorbates and further enhance the catalytic performance, as well as the product selectivity.[77] In contrast to the pristine PVK materials, the doped PVKs would exhibit stronger CO_2^- adsorption energies, which include the first-step CO_2^- activation and are the most important factor of the catalytic efficiency. At the same time, the adsorption of the product is much weaker for the doped materials, facilitating the product desorption from the substrate. In addition, the reduced free energy barrier, which is caused by the metal-ion doping in the PVKs, promotes the selectivity of final catalytic products.[77]

Tang and co-workers simulated the photocatalytic CO_2RR by using $CsPbBr_3$ materials doped with Co, Fe, Ni, Cu, Ag, Mg, Mn, and Bi in benzene through density functional theory (DFT) calculations.[77] From their work, Co- and Fe-doped $CsPbBr_3$ materials were found to possess high selectivity of methane as the final product due to their stronger CO_2^- adsorption energy and weak CH_4^- adsorption ability. The simulation results were further proved in the experiments carried out by Pradhan's group.[78] They confirmed that Fe(II)-doped $CsPbBr_3$ has higher catalytic activities and higher CO_2-to-CH_4 selectivity with the yield of 6.1 μmol $g^{-1}h^{-1}$

CH_4 and 3.2 μmol g^{-1} h^{-1} CO in EA/water medium under the intensity of 150 mW cm^{-2} illumination, as shown in **Figure 1** - **4**a. Through two steps of the electrostatic self-assembly method, Wang et al. applied tetrafluoroborate salts (BF_4) as the defect treatment agent and realized the Co^{2+} doping into $CsPbBr_3$ materials, aiming to remove uncoordinated Pb adatoms, suppress charge recombination, enhance reduction activity and improve the performance of photocatalysts, as shown in **Figure 1** - **4**b.[79] With the optimum Co-loading amount of 2.0 μmol, the $CsPbBr_3$-BF_4/Co shows the photocatalytic activity of 83.8 μmol g^{-1} h^{-1} in EA/isopropyl alcohol (IPA) under a 100-mW cm^{-2} light illumination.

The dopped metal ions into perovskite materials as the catalysts could not only tune the CO_2RR product selectivity but also suppress the photo-generated electron-hole pairs recombination, enhance the photo-response ability and increase the stability of PVKs and related catalysts. The combination of DFT calculation predictions and experimental verifications can provide frontier ideas for photocatalysts' evolution.

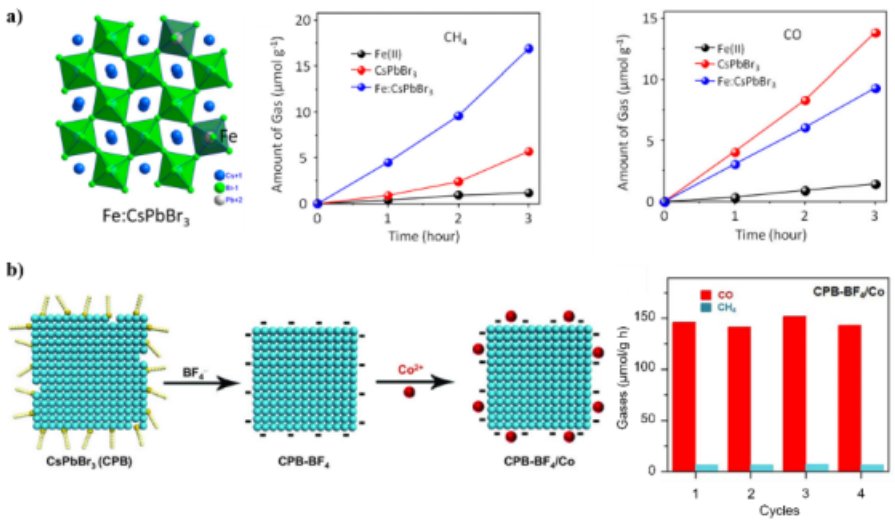

Figure 1 - **4.** a) Schematic illustration of Fe(II)-doped $CsPbBr_3$ and the CH_4 and CO_2 production of Fe(II) acetate salt, $CsPbBr_3$ and Fe(II)-doped $CsPbBr_3$. Reproduced with permission.[78] Copyright 2019, American Chemical Society. b) Schematic illustration of $CsPbBr_3$-BF_4/Co and the stability test for 2 h cycles. Adapted with permission.[79] Copy right 2021, John Wiley and Sons.

1.2.2.2 Mix-component doping

Tuning the B-site/C-site component of PVK materials can improve their photocatalytic activity, as that could effectively tune their band gaps and crystallinity, as well as lower their trap densities. From Guo's study, the PVK-based photocatalytic performance can also be improved by mixing halide components of the active perovskite materials.[80] It is found that in inorganic perovskite $CsPb(Br_x/Cl_{1-x})_3$, where x = 1, 0.7, 0.5, 0.3, 0, the increase of Cl concentration could lead to the increase in VB and very little change in CB of the materials. The obtained PVK material with x = 0.5 shows the highest CO and CH_4 catalytic yield of 875 μmol g^{-1} in EA for 9 h under AM 1.5 300 W Xe lamp, as shown in **Figure 1** - **5**a. Wu et al. also introduced I content in the inorganic PVKs and synthesized $CsPbBr_{3-x}I_x$ nanosheets (x = 0.3, 0.6, 0.9).[72] After comparison, the I-doped perovskite nanosheets with the I^--exchange could keep the similar morphology and crystal structure of pure $CsPbBr_3$ nanosheets and can result in the longer PL lifetime, as well as suppress the recombination of the photo-generated carriers. When x = 0.6, the CO formation rate can be as high as 43.9 μmol g^{-1} h^{-1} in the H_2O-electron donor system, as shown in **Figure 1** - **5**b.

The previous studies also showed that the poor distribution and inferior activity of Pb^{2+} in PVK materials could lead to the low performance of PVK-based photocatalysts.[81] The in-situ doping of metal ions can cause bulk doping in PVKs, which can increase the charge carrier recombination.[82] To overcome these problems, Cheng et al. partially replaced Br^- with acetate (Ac^-) to efficiently exchange B-site with Ni^{2+} ions, that is, Ni-coated $CsPbBr_{3-x}Ac_x$ ($Ni:CsPbBr_{3-x}Ac_x$) could be obtained to enhance the photocatalytic CO_2 reduction activity.[82] The weaker Pb-Ac bond than the Pb-Br bond facilitated the cation exchange and led to the higher Ni content in $Ni:CsPbBr_{3-x}Ac_x$. Under a 100-mW cm^{-2} illumination with a 400 nm filter, in the CO_2 and H_2O vapour environment, the $CsPbBr_{2.77}Ac_{0.23}$ and (0.59%) $Ni:CsPbBr_{2.77}Ac_{0.23}$ yielded 10.87 μmol g^{-1} h^{-1} CO and 44.09 μmol g^{-1} h^{-1} CO, respectively.

In order to avoid the toxicity of Pb element and to improve the stability of PVKs in moisture, Zhou and co-workers reported all-inorganic lead-free double PVK $Cs_2AgBiBr_6$ nanocrystal-photocatalysts for the first time.[83] Through synthesizing the active layers using hot-injection method and washing with absolute ethanol to reduce the ligand density, the as-prepared $Cs_2AgBiBr_6$ showed impressive electron consumption of 105 μmol g^{-1} in the treated EA under AM 1.5G illumination for 6 h (**Figure 1** - **5**) and remarkable stability in mild polar

solvent for 3 weeks, in 55% moisture for 90 d, under 70 mW cm^{-2} for 500 h or under 100 °C heating for 300 h, respectively.

Even though the components of PVKs have been modified via doping, the materials could still remain the perovskite structure. Mixing halide components in PVKs leads to their tuneable morphology, crystal structure, and bandgap. The replacement of Pb^{2+} with non-toxic metal ions can promote environmentally friendly material-development.

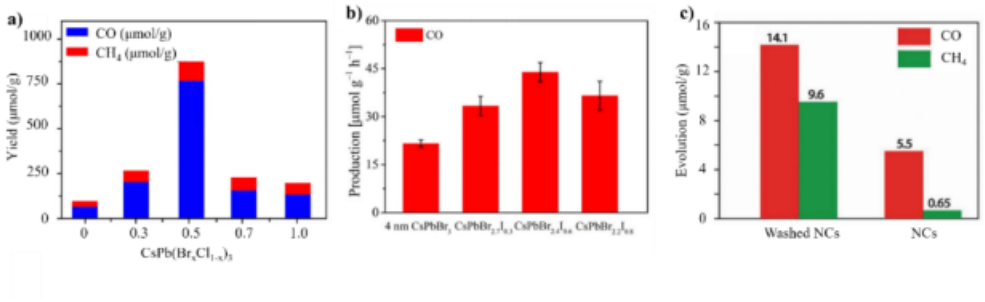

Figure 1 - 5. a) Yields of CO_2RR for $CsPb(Br_x/Cl_{1-x})_3$ (x = 1, 0.7, 0.5, 0.3, 0) nanocrystals. Adapted with permission.[80] Copyright 2019, Elsevier. b) CO evolution of 4 nm $CsPbBr_3$ nanosheets and $CsPbBr_{3-x}I_x$ nanosheets. Reproduced with permission.[72] Copyright 2021, John Wiley and Sons. c) CO_2RR performance of $Cs_2AgBiBr_6$ NCs. Adapted with permission.[83] Copyright 2018, John Wiley and Sons.

1.2.2.3 Vacancy or trap-state doping

Chen et al. performed DFT calculations to show that the halide defect engineering strategies in $Cs_2AgBiBr_6$ by doping halide-vacancy can promote the CO_2RR performance through chemically adsorbing CO_2 at Br-vacancy.[84] Supported by the in-situ diffuse reflectance infrared Fourier transform spectra (DRIFTS) and the DFT calculation, Dong's group have found that $Cs_3Bi_2Br_9$ possesses a higher CO_2RR performance than $Cs_3Bi_2Cl_9$ and $Cs_3Bi_2I_9$.[50] Because Br element can facilitate the charge carrier separation, narrow the bandgap, promote the directional electron delivery, lower the reaction energy of the intermediate COOH formed from CO_2 and the surface Br active site can change the CO_2 adsorption and activation modes. As shown in **Figure 1 - 6**a, the CO yield of $Cs_3Bi_2Br_9$ is 134.76 μmol g^{-1} with 98.7% selectivity in mixed CO_2 and H_2O vapour under AM 1.5G simulated solar irradiation for 5 h. Lead-free $CsAgCl_2$ microcrystals (**Figure 1 - 6**b and **Figure 1 - 6**c) were also synthesized by Wu et al., with the CO yield of 35.28 μmol g^{-1} in CO_2 after 5 h irradiation with long-term

stability in the air for over 2 months, under 100 °C heating in the air for 100 h or under UV lamp irradiation for 100 h.[85]

The combination of trap-state-control and facet control for PVKs is another effective strategy for producing better photocatalysts. Different facets of $CsPbBr_3$ nanocrystals with the shape of noncubic, hexapod, and cubic were investigated by Shyamal et al., as shown in **Figure 1** - **6**d.[86] Although with the identical absorption and the PL spectra, the poor-PL quantum yield (PLQY) emitting non-cubes showed a better CO_2RR performance due to their more and larger {112} and {102} facets than the {110} and {002} facets in cubic nanocrystals, which was further proved by the DFT study on the CO_2 adsorption and desorption energies on the surface. Also, the charge carriers were trapped by halide vacancy defects in non-cubes, leading to better photocurrents and catalytic performance. After 4 h CO_2RR in EA-water medium, the CO and CH_4 were formed 130.7 and 58.8 μmol g^{-1} for non-cube nanocrystals, as shown in Figure 1 - **6**e.

The vacancy doping can be achieved by modulation component or tuning the crystal facet of PVKs. With the doped vacancies, photo-generated charges can be trapped to facilitate the charge separation and transfer, and thus enhance the CO_2 adsorption ability of PVKs. Combining with DFT calculations, the mechanisms behind the induced vacancies can be discussed from CO_2 adsorption and desorption energies.

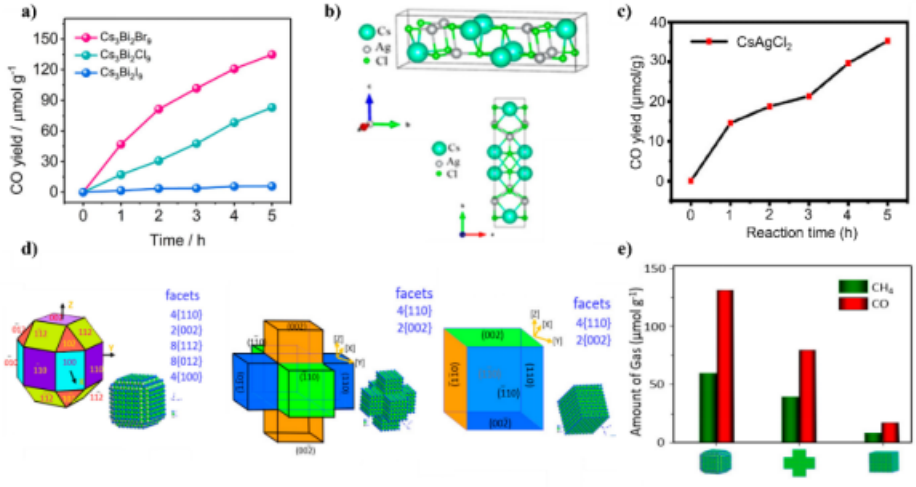

Figure 1 - 6. a) CO yield of $Cs_3Bi_2Br_9$ and $Cs_3Bi_2Cl_9$. Reproduced with permission.[50] Copyright 2020, American Chemical Society. b) Crystal structure of $CsAgCl_2$ microcrystals. Adapted with permission.[85] Copyright 2021, American Chemical Society. c) CO_2RR

performance of $CsAgCl_2$ microcrystals. Adapted with permission.[85] Copyright 2021, American Chemical Society. d) Crystal structure models of polyhedron-shaped non-cubes, hexapods, and cube-shaped $CsPbBr_3$ nanostructures and e) their CO_2RR yield. Adapted with permission.[86] Copyright 2020, American Chemical Society.

Table 1 - 3. Summary of defect-engineered PVK photocatalysts and their CO_2RR performance.

Type	Photocatalyst	Medium	Light source	Products	Reference
Metallic ion doping	Fe(II)-doped $CsPbBr_3$	EA/water medium	150 mW cm^{-2}	CO: 3.2 μmol g^{-1} CH_4: 6.1 μmol g^{-1}	[78]
	$CsPbBr_3$-BF_4/Co	EA/isopropyl alcohol (IPA) solution	300 W Xe lamp, 100 mW cm^{-2}	CO_2RR activity rate: 83.8 μmol g^{-1} h^{-1}	[79]
Mix component doping	$CsPb(Br_{0.5}/Cl_{0.5})_3$ nanocrystals	EA	300 W Xenon lamp with AM 1.5 filter	After 9 h, the total yield of CO and CH_4 875 μmol g^{-1}	[80]
	Ni:$CsPbBr_{2.77}Ac_{0.23}$	CO_2 and H_2O vapor	100 mW cm^{-2} with 400 nm filter	CO: 44.09 μmol $g^{-1}h^{-1}$	[82]
	$Cs_2AgBiBr_6$ nanocrystal	ethyl acetate which was HPLC grade and then pre-treated with 4A molecular sieve	AM 1.5G, 150 mW cm^{-2}	For 6 h, the total electron consumption: 150 μmol g^{-1}	[83]
Vacancies doping	$Cs_3Bi_2Br_9$ QDs	toluene	300 W Xenon lamp with AM 1.5 filter	After 5 h, CO: 134.76 μmol g^{-1} with 98.7% selectivity	[50]
	Non-cube $CsPbBr_3$	EA-water	450 W Xe lamp source	After 4 h,	[86]

	nanocrystals	medium	with 150 mW cm^{-2}	CO: 130.7 μmol g^{-1} CH_4: 58.8 μmol g^{-1}

1.2.3 Interfacial heterojunction engineering

Numerous reports have demonstrated effective strategies for improving the photocatalytic CO_2RR performance using PVKs as mono-photocatalysts. However, there still remained the great challenges to further improve the stability and photo-induced charge carrier separation efficiency of PVK materials. In the following part, I will introduce the recent advances in the PVKs with co-catalytic modifications to form Schottky-junctions, type-II heterojunctions, or Z-scheme heterojunctions, which can protect the PVK materials and facilitate the separation of photo-generated electron-hole pairs.

1.2.3.1 Principles of heterojunctions

To solve the serious carrier recombination issue, due to the high trap density of perovskite materials, which could lead to poor photocatalytic performance, researchers have tried to improve the carrier separation efficiency by constructing various interfacial heterojunctions, including type-II heterojunctions, Schottky-heterojunctions, and Z-scheme heterojunctions.

Typically, the Schottky-heterojunction refers to the Metal/Semiconductor interfacial region, as shown in **Figure 1** - 7a.[87-88] Generally, the fundamental reason for the formation of the Schottky barrier is the band-bending effect introduced by the contact of a metal and a semiconductor.[89-90] In a classic situation, the photo-generated electrons in the PVK material transfer to the metallic component through the Schottky-junction to join in the CO_2RR, and the photo-generated holes are left in the PVK for the photo-oxidation reaction. The additional charge transfer tunnel can efficiently suppress the charge recombination and thus improve the catalytic performance. Recently, some novel Schottky-junctions have also been constructed between semiconductors and MXene or graphene.[91-92]

As shown in **Figure 1** - 7b, the type-II heterojunction refers to two combined semiconductors with staggered bands and, under light illumination, the photogenerated electrons (holes) can transfer to the material with the lower CB (higher VB) to have the reduction (oxidation)

reaction.[37] With the light-harvesting ability of both semiconductors and the separated photo-reduction and -oxidation sites, the charge recombination in the photocatalysts can be greatly reduced and further improve the catalytic performance. By contrast, the type-I heterojunction also contains two semiconductors, but the bandgap of one semiconductor is completely contained within the bandgap of the other one.[93] Both oxidation and reduction reactions occur on the same semiconductor with lower CB, which can hinder the separation of photogenerated electron-hole pairs and reduce the reducing capability.[37]

Analogous to the type-II heterojunction, the Z-scheme heterojunction is also constructed with two conjunct semiconductors with staggered bands; however, under light illumination, the photogenerated electrons in the semiconductor with lower CB combine with the photogenerated holes in the semiconductor with the higher VB. The photoreduction (photooxidation) reaction occurs at the semiconductor with the higher CB (lower VB), which shows strong reduction (oxidation) potential, and further promotes the photocatalytic performance.[37] And the band diagram of direct Z-scheme structures and Z-scheme with conductors are shown in **Figure 1** - 7c and **Figure 1** - 7d.[94]

Therefore, proper interfacial heterojunction engineering can modify the charge transfer behaviour and reaction sites according to the designed mechanism, which can provide important strategies to enhance the photocatalytic CO_2RR performance of PVK-based photocatalysts and general catalysts.

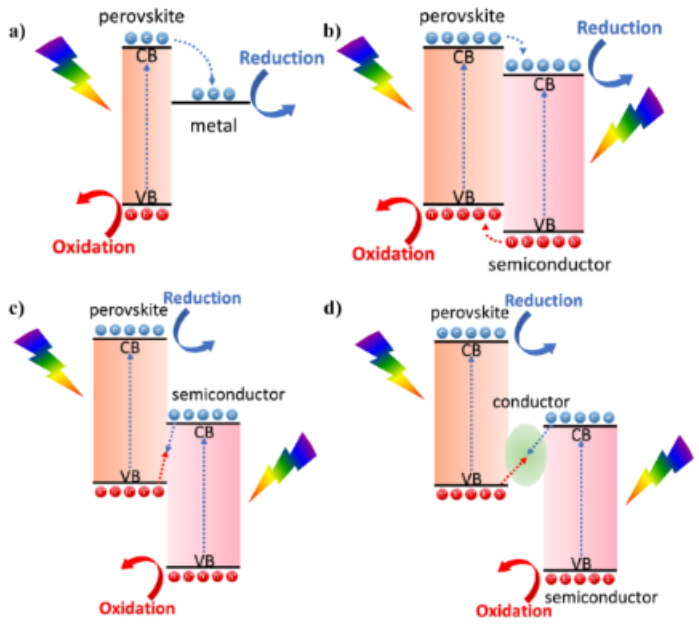

Figure 1 - 7. The band diagram of a) the typical Schottky junction, b) the type-II heterojunction, c) the direct Z-scheme heterojunction and d) the Z-scheme heterojunction with conductors for PVK photocatalysts.

1.2.3.2 Schottky Junctions

The formed Schottky-junction can not only accelerate the transfer of photoinduced electrons or holes from the semiconductor to the metal, but also introduce the catalytic reaction sites. A novel Schottky-junction-structure photocatalyst containing $CsPbBr_3$ nanocrystals/two-dimensional Pd nanosheets was introduced by Kuang's group, as shown in **Figure 1 - 8**a.[95] Acting as an electron reservoir, the Pd nanosheets can facilitate the separation of the photogenerated electron-hole pairs from the $CsPbBr_3$ nanocrystals through the Schottky contact and also provide CO_2RR sites. With adding Pd nanosheets, the photoelectron consumption rate of the $CsPbBr_3$ nanocrystals was increased from 9.86 to 33.79 μmol g^{-1} h^{-1} in a water vapour system under 150 mW cm^{-2} with a 420-nm cut-off filter. Chen and co-workers also decorated Pt on $CsPbBr_3$ PVK submicron single crystals to extract the photogenerated electrons through the Schottky barrier and to reduce the kinetic limitations of CO_2 activation and product generation.[96] In the ethyl acetate electrolyte, the $CsPbBr_3$/Pt composite doubled the electron yield rate to 5.6 μmol g^{-1} h^{-1} under the illumination of a 150-W Xe lamp with a 320-nm cut filter, as shown in **Figure 1 - 8**b.

The surface plasmon resonance (SPR) effect can be caused by the interaction between the incident photons and the conduction electrons of metal nanoparticles, which is also applied in the Schottky-junction structure.[97] In Chen's report, a lead-free $Cs_2AgInCl_6$ (CAIC) double PVK QDs decorated with Ag nanoparticles were synthesised for CO_2RR.[98] On account of the SPR effect of Ag nanoparticles, with the purification process treatment to regulate the surface ligand density, the optimised CAIC QDs@Ag composite showed the highest yield of 26.4 μmol g^{-1} CO and 28.9 μmol g^{-1} CH_4 with improved stability in the ethyl alcohol electrolyte under a 300-W xenon light illumination for 3 h. The Au-induced SPR effect was also proved to enhance the optical response in 3DOM Au-CPB by Tang and co-workers, as shown in **Figure 1 - 8**c.[74] When using light illumination with $\lambda < 530$ nm, the $CsPbBr_3$ parts absorb light, and the photogenerated electrons transfer to Au to have CO_2RR; when applying light illumination with 530 nm $< \lambda <$ 650 nm, due to the SPR effect, the Au parts generate hot

electrons, and which are transferred to $CsPbBr_3$ and to have CO_2RR. The electron consumption rate ($R_{electron}$) of 3DOM Au-CPB was increased to 38.0 μmol g^{-1} h^{-1} for 3DOM CPB, which is 2.6 folds of bulk $CsPbBr_3$ as illustrated in **Figure 1** - **3**c.

Instead of metals, conductive non-metallic materials can also construct Schottky-junctions with PVK materials for photocatalysts. Xu and co-workers first introduced the structure of the $CsPbBr_3$ QDs/graphene oxide (GO) complex to form a Schottky-junction structure, as shown in **Figure 1** - **8**d.[2] In addition to the inherent radiative channel in $CsPbBr_3$ QDs for excited-state electron transfer, the GO provided an additional energy-transfer channel due to the more positive Fermi Level of the conductive GO. With the improved stability and facilitated separation of the photogenerated electron-hole pairs, the electron consumption rate of $CsPbBr_3$ QDs improved from 23.7 to 29.8 μmol g^{-1} h^{-1} with the combination of GO, in EA solvent under AM 1.5 G illumination. Another derivative of graphene, reduced graphene oxide (rGO) with hole-in-microdisk Cs_4PbBr_6 was reported as photocatalysts by Zhu's group (**Figure 1** - **8**e).[99] Acting as an electron acceptor, the rGO improved the stability of the photocatalysts, and an excellent CO selectivity over 94.6% selectivity was of the formation of CO with the production rate of 11.4 μmol g^{-1} h^{-1} in the EA-water system under a 100 mW cm^{-2} light illumination with a 420 nm filter. Proved by DFT calculation, the surface oxygen defects in rGO served as trap centres for photogenerated electrons from the PVKs to facilitate the charge separation, and active sites to assist the CO_2 adsorption, activation, and reduction to CO. In Kumar's report, a Pb-free $Cs_2AgBiBr_6$ nanoplate with Cu-loaded reduced graphene oxide (Cu-rGO) (**Figure 1** - **8**f) was also synthesised for gas-phase CO_2RR.[100] The Cu-rGO not only promoted the photoinduced charge separation, enlarged the surface area of the photocatalyst, and improved the CO_2 adsorption, but also improved the reusability due to the hydrophobic character of rGO. With the important role of the added Cu, the CO_2-to-CH_4 selectivity was increased to 93.0 ± 0.5% with the total electron (e^-) consumption of 93 μmol e^- h^{-1} g^{-1} in a water vapor system at 1 sun.

Different from metal-ion doping, which can replace and change the component of PVKs, the Schottky-junctions are formed between PVKs and metals or conductive non-metallic materials. Both depositing PVKs on conductive films and decorating metal particles on PVKs can increase the CO_2 active sites and provide faster electron-transfer tunnels to enhance the photocatalytic performance of photocatalysts. The SPR effect in metal nanoparticles can

provide an additional improved optical response in Schottky-junction applications.

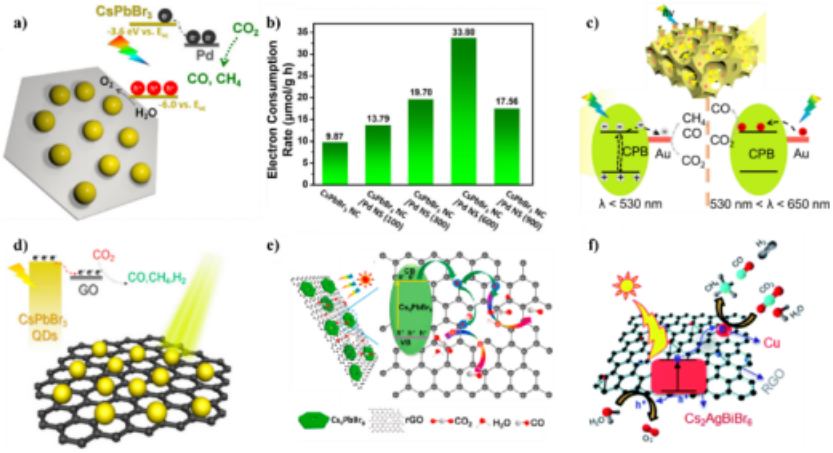

Figure 1 - 8. a) The sketch of $CsPbBr_3$ nanocrystals/Pd nanosheets. Reproduced with permission.[95] Copyright 2018, American Chemical Society. b) Electron consumption rates of $CsPbBr_3$ nanocrystals/Pd nanosheets. Reproduced with permission.[95] Copyright 2018, American Chemical Society. c) The charge transfer sketch of 3DOM Au-CPB during the photocatalytic reaction. Adapted with permission.[74] Copyright 2021, Elsevier. d) The band diagram of $CsPbBr_3$ QDs/GO photocatalysts. Reproduced with permission.[2] Copyright 2017, American Chemical Society. e) Scheme of photocatalytic CO2 reduction on the Cs_4PbBr_6/rGO composites. Adapted with permission.[99] Copyright 2020, Elsevier. f) The schematic illustration of $Cs_2AgBiBr_6$ nanoplates@Cu-rGO. Reproduced with permission.[100] Copyright 2021, Royal Society of Chemistry.

1.2.3.3 Type-II heterojunctions

The application of type-II heterojunction structure in the synthesis of photocatalysts can facilitate the separation of photogenerated charges, suppress the charge recombination, and extend light absorption ability and further improve the CO_2RR performance. Graphitic carbon nitride (g-C_3N_4) with a two-dimensional structure is reported to form a type-II heterostructure with PVK materials. Ou and co-workers anchored $CsPbBr_3$ QDs on NH_x-rich porous g-C_3N_4 nanosheets ($CsPbBr_3$ QDs-PCN), as shown in **Figure 1 - 9**a.[71] The unique N-Br chemical bond facilitated the charge separation and prolonged lifetime of the charge carriers, at the same time, it improved the stability of the photocatalyst by passivating the surface of the uncoordinated halides. The $CsPbBr_3$ QDs-PCN exhibited the highest CO_2-CO formation

rate of 148.9 μmol g^{-1} h^{-1}, which was around 3-fold/5-fold higher than that of PCN and $CsPbBr_3$ QDs, in acetonitrile/water solution under a 300 W Xe-lamp illumination with a 420-nm cut-off filter. Chen also reported $CsPbX_3$/g-C_3N_4 composite for CO_2RR with enhanced photoactivity caused by the solid bonding interfaces between PVK and g-C_3N_4.[101] Zhang's group utilized another strategy for synthesizing $CsPbBr_3$ nanocrystals with g-C_3N_4, containing titanium-oxide species ($CsPbBr_3$@TiO-CN) for photocatalytic CO_2RR.[102] The introduction of TiO-CN provided the increased active sites, a strong bonding interaction between NH_x and Br^- in $CsPbBr_3$@TiO-CN caused by the easily formed ionic bonding, and the red-shifted absorbance cut-off from 460 nm to 550 nm. In a CO_2-saturated ethyl acetate/water solution under the illumination of 100 mW cm^{-2} with a 400 nm filter, the as-prepared photocatalyst yielded 129 μmol g^{-1} CO after a 10-h light irradiation, which was 3/6-fold higher than that of $CsPbBr_3$/TiO-CN.

Kuang's group added SnS_2 nanosheets into a CsI precursor solution and synthesized a 0D Cs_2SnI_6 nanocrystal/2D SnS_2 nanosheet photocatalyst with the sharing of the Sn atoms, as shown in **Figure 1** - **9**b.[103] Forming a type-II heterojunction, the SnS_2 performed a prolonged photogenerated electron lifetime from 1290 ps to 3080 ps and an ultrafast hole transfer behaviour to Cs_2SnI_6 nanocrystal. The optimized photocatalyst exhibited a CH_4 production of 6.09 μmol g^{-1}, which was 5.4-fold higher than the pristine SnS_2 with improved stability in a CH_3OH/H_2O system under 150 mW cm^{-2} illumination with a 400-nm filter. The integration of $CsPbBr_3$ nanocrystals with monolayer MoS_2 nanosheet (CPB/MS) can also form a type-II heterojunction, as reported by Zhu's group (**Figure 1** - **9c**).[104] With the tight interaction of two photocatalysts, the CPB/MS possesses higher charge separation efficiency and a wider charge diffusion region than the pristine $CsPbBr_3$, which were proved by Surface photovoltage (SPV) spectroscopy technology and transient state photovoltage (TPV) spectrum, respectively. Under a 200-mW cm^{-2} light illumination, the highest photocatalytic yield was CO: 25.0 μmol $g^{-1}h^{-1}$ and CH_4: 12.8 μmol $g^{-1}h^{-1}$.

MOFs are made up of both metal ions/clusters and organic ligands with a porous crystalline structure, large surface area, and tuneable pore structure and composition.[105-106] As the MOF materials can accommodate nanoparticles and can be functionalized, they have been applied in gas adsorption/separation, biomedicine, and chemical sensors; meanwhile, they are another kind of materials to form the type-II heterojunction with PVKs.[107-110] As reported by Zhong's

group, possessing the increased electronegativity due to the existence of amino groups, UiO-66(NH_2) exhibits a great interaction with electropositive $CsPbBr_3$ QDs, which is much stronger in comparison to physical adsorption.[111] As illustrated in **Figure 1** - **9**d, the 15%-$CsPbBr_3$ QDs/UiO-66(NH_2) nanocomposites performed the yields of 8.21 μmol g^{-1} h^{-1} CO and 0.26 μmol g^{-1} h^{-1} CH_4 with good recyclability in the slight H_2O/EA system under a 300-W Xe lamp with a UV-cut filter (420 nm), on account of the large accessible specific surface area, enhanced CO_2RR activity and promoted visible light absorption capacity. MIL-100(Fe) was also reported to be composited with halide materials by Roeffaers's group.[112] The dual-phase $CsPbBr_3$/$CsPb_2Br_5$@MIL-100(Fe) micro-catalyst exhibited increased surface area, visible light absorption ability, good stability, and improved charge separation performance, with a yield of 20.4 μmol g^{-1} h^{-1} in the CO_2/H_2O vapour system under the light irradiation of a 300-W Xe lamp with a 420-cut-off filter. Combined with $CsPbBr_3$ nanomaterials, Ni-based and Cu-based 2D MOF materials also showed superior photocatalytic performance, and were reported by Xi's group and Li's group, respectively.[113-114] In Xi's work, they compared the properties of $CsPbBr_3$ nano-cubes, nanorods and nanowires, and they found that the charge carrier dynamics depend on the aspect ratio of the perovskites.[113] As shown in **Figure 1** - **9**e, the Ni-based MOF/$CsPbBr_3$ nanowires (NMF/CPB-NWs) exhibited the highest CO production rate of 81.0 μmol g^{-1} h^{-1}. Li and co-workers built the "cascade electron transfer" by combining $CsPbBr_3$ QDs and 2D Cu-based porphyrin MOF nanosheets ($CsPbBr_3$/CuTCPP MOF) to spur both interfacial and inner electron transfer (**Figure 1** - **9**f). [114] The optimized $CsPbBr_3$/CuTCPP MOF (0.1 wt% Cu) achieved a high yield of 11.8 and 2.95 μmol g^{-1} h^{-1} for CO and CH_4, respectively.

Various semiconductors have been combined with PVKs to form type-II heterojunctions, such as non-metallic semiconductors (g-C_3N_4), sulphides (SnS_2, MoS_2) and MOF materials (UiO-66(NH_2), MIL-100(Fe), Ni-based and Cu-based 2D MOF). [71,103,104,111,113,114] By modulating the morphology of these semiconductors and dispersing PVK nanoparticles, the CO_2 reaction sites can be efficiently enlarged, and the photogenerated charges can be quickly separated.

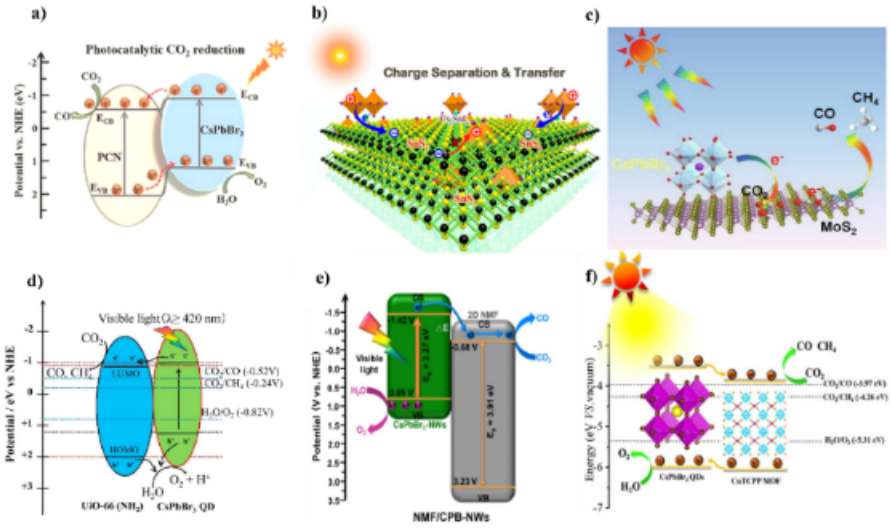

Figure 1 - 9. a) The band structure of $CsPbBr_3$ QDs-PCN with different QDs concentrations. Adapted with permission.[71] Copyright 2018, John Wiley and Sons. b) The schematic illustration of Cs_2SnI_6 nanocrystal/SnS_2 nanosheet photocatalysts. Adapted with permission.[103] Copyright 2019, American Chemical Society. c) The scheme of CPB/MS for photocatalytic CO_2 reduction. Adapted with permission.[104] Copyright 2021, Elsevier. d) Band diagram of x%-$CsPbBr_3$ QDs/UiO-66(NH_2). Reproduced with permission.[111] Copyright 2019, Elsevier. e) Energy band structure of NMF/CPB-NWs. Adapted with permission.[113] Copyright 2021, Elsevier. f) The bandgap information of $CsPbBr_3$/CuTCPP MOF. Adapted with permission.[114] Copyright 2021, John Wiley and Sons.

1.2.3.4 Z-scheme heterojunctions

Rather than sacrificing the reduction ability of photo-generated electrons caused by electron transfer in the formed type-II heterojunction, Z-scheme heterojunction can boost the charge separation and keep the high redox potential of photocatalysts. Kuang's group introduced a Z-scheme heterojunction (with conductors) structure using amine-functionalized reduced graphene oxide (Amine-RGO) coated between α-Fe_2O_3 and $CsPbBr_3$ nanocrystals, as shown in **Figure 1 - 10**a-b.[115] The amine groups on the surface of RGO provided more sites for $CsPbBr_3$ to grow and also prevented the superabundant growth and aggregation of $CsPbBr_3$. The Z-scheme structure was also proved by the electron spin resonance (ESR) test to exclude the type-II heterojunction. The photogenerated electrons in α-Fe_2O_3 and photogenerated holes in $CsPbBr_3$ recombined with the help of the amine-RGO, and the photoreduction happens

within $CsPbBr_3$ with the photooxidation happened in the added α-Fe_2O_3. With high recyclability, the as-prepared photocatalyst yielded the product of CH_4 (main) and CO with the $R_{electron}$ of 80.95 μmol g^{-1} h^{-1}, in a CO_2 and saturated H_2O vapour system under the 150-mW cm^{-2} illumination with a 420-nm optical filter. Lu's group also reported ultrathin and small-size graphene oxide (USGO) nanosheets in combination with α-Fe_2O_3 and $CsPbBr_3$ nanocrystals ($CsPbBr_3$/USGO/α-Fe_2O_3) composite with the formed Z-scheme structure.[116] The photocatalyst reached the CO yield of 73.8 μmol g^{-1} h^{-1} , which was about 19 times higher than that of the pristine $CsPbBr_3$ in the acetonitrile/deionized water-electrolyte under the light illumination of 100 mW cm^{-2} with a 400 nm filter.

Xu's group successfully synthesized and compared the lead-free PVK $Cs_2AgBiBr_6$@g-C_3N_4 (CABB@C_3N_4) with both direct Z-scheme structure and type-II heterojunction structure by tuning the solvent and the amount of g-C_3N_4, as shown in **Figure 1** - **10**c-d.[117] With suppressed charge recombination, enhanced CO_2RR activity, and stability, when the photoreduction happens in g-C_3N_4, the product showed high CH_4 selectivity of over 70% in CABB@C_3N_4-82% with the Z-scheme structure. On the contrary, when the photoreduction happens in $Cs_2AgBiBr_6$, the product shows high CO selectivity with the yield of 2.0 μmol g^{-1} h^{-1} in CABB@C_3N_4-10% with the type-II heterostructure.

Metal oxides are good candidates to form the direct Z-scheme heterojunction with PVKs. In Wang's report, 0D/2D $CsPbBr_3$ QDs/Bi_2WO_6 nanosheet can also form the direct Z-scheme heterojunction with the band diagram as shown in **Figure 1** - **10**e-f.[118] Under a 100-mW cm^{-2} visible light ($\lambda \geq 400$ nm), the main photoreduction product of Bi_2WO_6 ($CsPbBr_3$) is CH_4 (CO), hence the photoreduction product with high CO selectivity of the $CsPbBr_3$ QDs/Bi_2WO_6 nanosheet and the total electron-to-product rate of 114.4 μmol g^{-1} h^{-1} proved the successful formation of Z-scheme heterojunction structure. Lead-free $Cs_3Bi_2I_9$ nanocrystals on the surface of ultrathin Bi_2WO_6 nanosheets ($Cs_3Bi_2I_9$/Bi_2WO_6) were also reported to construct a direct Z-scheme heterojunction in Liu's report.[119] The in-situ growth of $Cs_3Bi_2I_9$/Bi_2WO_6 successfully shared the Bi atoms, which can effectively promote the electron cloud coupling between the two composites. In the system of water as the electron source, the photocatalytic CO conversion rate was 66 μmol g^{-1}, under a 100-mW cm^{-2} light illumination.

Both Z-scheme heterojunction structures with conductors and without conductors have been

reported to modify the structures and properties of PVK-based composites and heterostructures. Due to the highly efficient charge separation and the fact that the CO_2 reduction reaction occurs on the semiconductor with the higher CB, the reduction ability and product yield efficiency of the photocatalysts are higher than those with the type-II heterojunction structure.

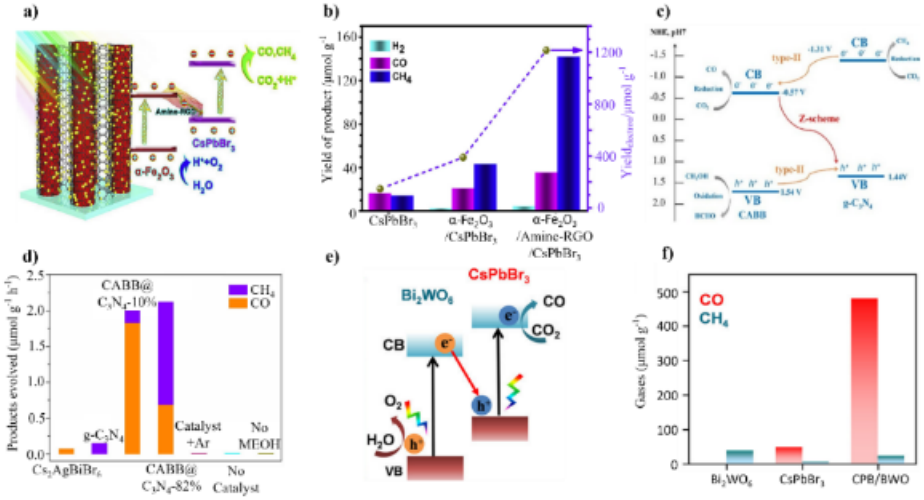

Figure 1 - 10. The band diagram and photocatalytic performance of a-b) Z-Scheme α-Fe_2O_3/Amine-RGO/$CsPbBr_3$ hybrids. Adapted with permission.[115] Copyright 2020, Elsevier. c-d) $Cs_2AgBiBr_6$@g-C_3N_4 with Z-scheme (CABB@C_3N_4-82%)/type-II (CABB@C_3N_4-10%) heterojunction. Adapted with permission.[117] Copyright 2021, Elsevier. e-f) the 0D/2D Z-scheme heterojunction of $CsPbBr_3$ QDs/Bi_2WO_6 nanosheet. Adapted with permission.[118] Copyright 2020, American Chemical Society.

Table 1 - 4. Summary of PVK photocatalysts with heterojunction structures and their CO_2RR performance.

Type	Photocatalyst	Medium	Light source	Products	Reference
Schottky-Junction	$CsPbBr_3$/ Pt nanosheet (600)	CO_2 and H_2O vapor	150 W Xe lamp with 420 nm filter 150 mW cm^{-2}	Electron consumption rate: 33.79 μmol g^{-1} h^{-1}	95
	CAIC QDs@Ag-2	EA	300 W Xe lamp	After 3 h, CO 14.58 μmol g^{-1}	98

				CH_4 13.99 μmol g^{-1}	
	3DOM Au-CPB	Isopropanol-EA	300 W Xe lamp, 420 nm filter	$R_{electron}$ 38.0 μmol g^{-1} h^{-1}	74
	$CsPbBr_3$ QD/ GO	EA	100 W Xe lamp AM 1.5G filter 150 mW cm^{-2}	electron consumption 29.8 μmol g^{-1} h^{-1}	2
	Cs_4PbBr_6/rGO	EA-water system	300 W Xe lamp with 420 nm filter 100 mW cm^{-2}	CO 11.4 μmol g^{-1} h^{-1}	99
	$Cs_2AgBiBr_6$-Cu-RGO	water vapor	1 sun	CO 1.9 (±0.3) μmol g^{-1} h^{-1}	100
				CH_4 10.7 (±0.6) μmol g^{-1} h^{-1}	
Type-II heterojunction	20 $CsPbBr_3$ QDs-PCN	acetonitrile/ water	300 W Xe lamp with 420 nm filter	CO 148.9 μmol g^{-1} h^{-1}	71
	Cs_2SnI_6(1.0)/ SnS_2	CH_3OH/H_2O system	150 mW cm^{-2}, 400 nm filter	After 3 h, CH_4: 6.09 μmol g^{-1}	103
	$CsPbBr_3$/MoS_2 (1.0 wt%)	EA	200 mW cm^{-2}	CO 25.0 μmol g^{-1} h^{-1}	104
				CH_4 12.8 μmol g^{-1} h^{-1}	
	15%-$CsPbBr_3$ QDs/UiO-66(NH_2)	slight H_2O/EA v:v 1:300	300 W Xe lamp with 420 nm filter	CO 8.21 μmol g^{-1} h^{-1}	111
				CH_4 0.26 μmol g^{-1} h^{-1}	
	NMF/$CsPbBr_3$ nanowires	EA/H_2O	100 mW cm^{-2} 420 nm filter	CO 81.0 μmol g^{-1} h^{-1}	113

	$CsPbBr_3$/Cu TCPP MOF (0.1 wt% Cu)	EA/H_2O	100 mW cm^{-2}	CO 11.8 μmol g^{-1} h^{-1} CH_4 2.95 μmol g^{-1} h^{-1}	[114]
Z-Scheme heterojunction	α-Fe_2O_3/Amine-RGO/$CsPbBr_3$	CO_2 and H_2O vapor	AM 1.5G, λ > 420 nm, 150 mW cm^{-2}	electron consumption rate ($R_{electron}$): 80.95 μmol g^{-1} h^{-1}	[115]
	$CsPbBr_3$/USGO/α-Fe_2O_3	acetonitrile/deionized water 200:1 v:v	300 W Xe lamp with 400 nm filter 100 mW cm^{-2}	CO 73.8 μmol g^{-1} h^{-1}	[116]
	$Cs_2AgBiBr_6$ @g-C_3N_4-82%	EA/methanol	AM 1.5 G 150 mW cm^{-2}	CO_2RR activity above 2.0 μmol g^{-1} h^{-1}	[117]
	$CsPbBr_3$ QDs/Bi_2WO_6 nanosheet	EA/water solution v:v 49:1	300 W Xe lamp with 400 nm filter 100 mW cm^{-2}	total yield of CH_4/CO is 503 μmol g^{-1} $R_{electron}$: 114.4 μmol g^{-1} h^{-1}	[118]
	$Cs_3Bi_2I_9$/Bi_2WO_6	40 μL deionized water	300 W Xe lamp with 400 nm filter 100 mW cm^{-2}	After 9 h CO: 66 μmol g^{-1}	[119]

1.2.4 Surface encapsulation

It is noted that the PVK materials are sensitive to aqueous, therefore the humid stability of PVK-based catalysts is vital to their practical photocatalytic performance. Currently, one of the most applied methods is encapsulating PVKs with other stable materials, including metal oxides, MOF, and non-metal materials. Therefore, how to rationally manipulate the species and thickness of the encapsulation layers, but without obviously weakening the light-harvesting and reaction activity of PVKs, still requires a lot of investigation.

1.2.4.1 Metal oxide encapsulation

The encapsulation can improve the stability of PVK materials by preventing their direct contact with the electrolyte, which also functions as the electron/hole acceptor to facilitate the charge carrier transfer. A novel amorphous-TiO_2 (α-TiO_2)-encapsulated $CsPbBr_3$ nanocrystalline photocatalyst was developed by Kuang's group through a solution processing strategy, as shown in **Figure 1** - **11**a-b.[120] The coupling of the α-TiO_2 matrix not only increased the stability of the PVK materials, but also improved the photocatalytic performance by quenching the intrinsic radiative recombination and enhancing the CO_2 adsorption and activation. With the optimized concentration of α-TiO_2, the photocatalysts consumed 193.36 μmol g^{-1} photoelectrons, which was 6.5-fold higher than that of the individual $CsPbBr_3$ nanocrystals, with the final products of CO, CH_4, and H_2.

1.2.4.2 MOF encapsulation

With the combination of MOFs, the stability of PVK photocatalysts in moisture can also be enhanced dramatically. An *in-situ* growth strategy to synthesize a zinc/cobalt-based zeolitic imidazolate framework (ZIF)-encapsulated $CsPbBr_3$ QDs (**Figure 1** - **11**c-d) was reported by Kong and co-workers.[121] The Co^{2+} centres in ZIF, under light illumination, can accept electrons to be activated, which can further act as the active centres for CO_2 activation and reduction. The synergetic action of $CsPbBr_3$ and ZIF coating not only facilitated the ability of CO_2 capture/activation ability and the efficiency of charge separation but also improved the moisture stability and photocatalytic recycling stability. With the light absorption ability, the ZIF-67-coated PVK possessed the electron consumption rate of 29.630 μmol g^{-1} h^{-1}, which was 2.66-fold higher than that of pure $CsPbBr_3$ photocatalyst, with the selected final product of CO and CH_4 under the solid-vapor reaction mode.

1.2.4.3 Non-metal encapsulation

Non-metallic materials have also been applied to encapsulate PVK materials. Su and co-workers successfully *in situ* coated thin graphdiyne (GDY) on $CsPbBr_3$ nanocrystals and then decorated Co^{2+} on the photocatalyst (**Figure 1** - **11**e).[122] The coated GDY improved the catalytic stability in the water-containing system and also acted as a hole-transfer layer, which could enhance the transfer of photogenerated holes in $CsPbBr_3$. It can also provide a

compatible platform for active sites Co^{2+} decoration to further facilitate the chemisorption of CO_2, with the photocatalytic activity of the CO_2-to-CO conversion as high as 27.7 μmol g^{-1} h^{-1}. The highly conjugated C_{60} is another promising candidate for $CsPbBr_3$ encapsulation, as shown in **Figure 1** - **11**f-g.[123] In Zhang's work, the high electrically conductive C_{60} acted as the efficient electron acceptor, enhancing the electron transfer process and also improving the photocatalytic cycling stability and the solvent stability of the photocatalyst. With the final product of CO and CH_4, the electron consumption rate of the C_{60}/$CsPbBr_3$ composite reached 90.2 μmol g^{-1} h^{-1} in the acetonitrile (water) system under a light illumination with the intensity of 150 mW cm^{-2} with a 420-nm cut-off filter. Acting as a protective layer, a hole transporter, and an electron donor, the conducting polymer poly(3-hexylthiophene-2,5-diyl) (P3HT) with the highly conjugated structure was combined with $CsPbBr_3$ to form an encapsulation structure, as reported in Li's report (**Figure 1** - **11**h-i).[124] Benefited from the p-p* type electron transfer of P3HT, the light absorption of P3HT/$CsPbBr_3$ system was obviously red-shifted compared with the pure $CsPbBr_3$. The P3HT/$CsPbBr_3$ composite photocatalysts exhibited the yields of 145.45 μmol g^{-1} h^{-1} CO and 23.05 μmol g^{-1} h^{-1} CH_4 in the acetonitrile (water) system under a 300-W Xe lamp with a 420-nm cut-off filter, and the calculated electron consumption was 475.3 μmol g^{-1} h^{-1}, which was 10 times higher than that of $CsPbBr_3$ QDs (46.95 μmol g^{-1} h^{-1}).

The encapsulation method is also designed to protect PVKs from decomposing in humidity. The conductive materials can assist in transferring photo-generated electrons to react with CO_2. However, the photogenerated-charge-recombination problems still need to be taken into consideration.

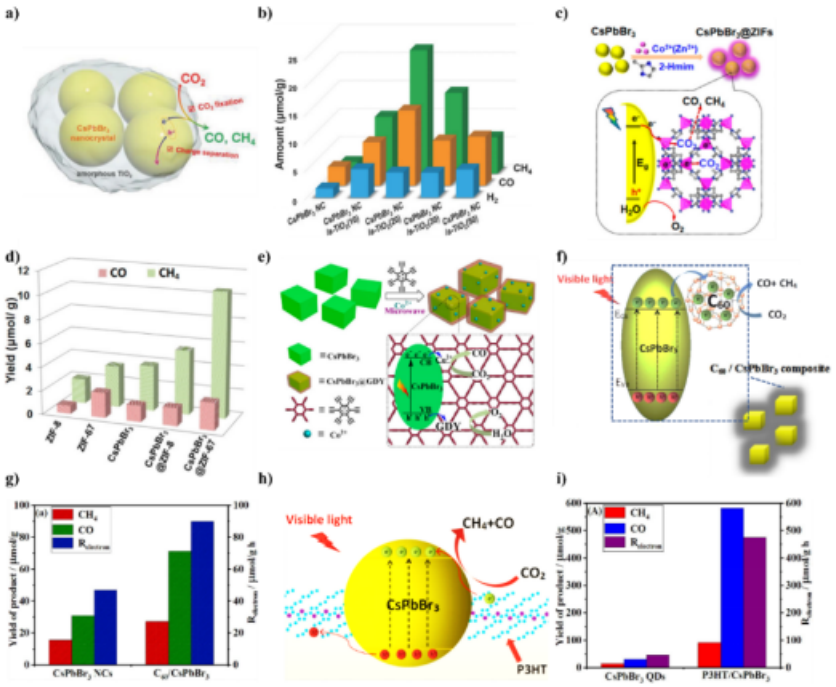

Figure 1 - 11. The schematic illustration and CO_2RR performance of a-b) the a-TiO_2-encapsulated $CsPbBr_3$ nanocrystal. Adapted with permission.[120] Copyright 2018, John Wiley and Sons. c-d) the $CsPbBr_3$/ZIFs. Reproduced with permission.[121] Copyright 2018, American Chemical Society. e) Co doped $CsPbBr_3$@GDY. Reproduced with permission.[122] Copyright 2020, American Chemical Society. f-g) C_{60}/$CsPbBr_3$ composite. Adapted with permission.[123] Copyright 2021, Elsevier. h-i) P3HT/$CsPbBr_3$ composite. Adapted with permission.[124] Copyright 2021, Elsevier.

Table 1 - 5. Summary of encapsulated PVK photocatalysts and their CO_2RR performance.

Type	Photocatalyst	Medium	Light source	Products	Reference
Metal oxide encapsulation	amorphous-TiO_2/$CsPbBr_3$ nanocrystal	EA/isopropanol	150 W Xe lamp AM 1.5G filter 150 mW cm^{-2}	After 3 h, the photoelectron consumption: 193.36 μmol g^{-1}	[120]
MOF encapsulation	$CsPbBr_3$@ZIF-67	CO_2 and H_2O vapor	100 W Xe lamp AM 1.5G filter 150 mW cm^{-2}	electron consumption rate: 29.630 μmol g^{-1} h^{-1}	[121]
Non-metal	$CsPbBr_3$@G	acetonitrile	300 W Xe	CO 27.7	[122]

encapsulation	$DY_{0.3}$-Co	and deionized water (200:1 v:v)	lamp with 400 nm filter 100 mW cm^{-2}	μmol g^{-1} h^{-1}	
	C_{60}/$CsPbBr_3$	acetonitrile and deionized water	300 W Xe lamp with 420 nm filter 150 mW cm^{-2}	After 4 h, CO: 71.3 μmol g^{-1} CH_4: 27.3 μmol g^{-1}	[123]
	P3HT/$CsPbBr_3$	acetonitrile and deionized water	300 W Xe lamp with a 420 nm cut-off filter	CO: 145.45 μmol g^{-1} h^{-1} CH_4: 23.05 μmol g^{-1} h^{-1}	[124]

1.3 Methods to improve Cu-based catalyst performance

In this section, I will classify the Cu-based catalysts by the modification of metal Cu, Cu oxides, Cu alloys and Cu ions. The metal Cu and Cu alloys don't have the light-response ability, so they are usually loaded on semiconductors to achieve PC/PEC reactions. The photocatalytic performance of copper oxides is improved by forming heterojunctions with other semiconductors. Cu ions can also be doped in semiconductors to increase active sites for CO_2 reduction.

1.3.1 Metal Cu materials for CO_2RR

Despite being unable to absorb light, metal Cu can also improve PC/PEC CO_2RR based on their excellent conductivity and work as electron capture agents or adsorption sites.[51, 125-126] Applying the wet impregnation method, Zhang and co-workers successfully modified the highly dispersed BMO with oxygen vacancies (OVs-BMO) with the Cu nanodots and then introduced efficient-CO_2 adsorbed amino-functionalized 1-ampropyl-3-methylimidazolium bromide (APMImBr) ionic liquids (ILs) into the reaction system.[127] The introduction of oxygen vacancies into BMO formed a defect energy level, narrowed the band gap, and improved the light response. The highly dispersed Cu nanodots not only provided more active sites, but also formed an effective charge transport channel with OVs-BMO through their close interaction and reduced the photoinduced electron transport distance to facilitate the

photogenerated charge carrier transport. The interface reactions of the electrolyte and the catalysts were optimized by adding ILs in the electrolyte, which could have a complexation reaction with CO_2 and reduced the activation energy of CO_2 intermediates and improved CO_2 reaction activity. With all the modifications above, the Cu/ILs/OVs-BMO showed the highest PC CO_2RR performance with the product of methanol 98.66 μmol g^{-1} h^{-1} and ethanol 95.74 μmol g^{-1} h^{-1}, which was 17.8 times higher than that of BMO, as shown in **Figure 1** - **12**a.

Huang and co-workers applied an *in-situ* photo-deposition method to embed Cu nanoparticles onto $Bi_4O_5I_2$ nanosheets assembled micron flowers and formed a plasmonic heterostructure, as shown in **Figure 1** - **12**b.[128] The Cu nanoparticles introduced the surface plasmon resonance (SPR) effect, which could improve the near-infrared (NIR) light absorption, generate hot electrons, and induce the migration of hot electrons across the $Bi_4O_5I_2$/Cu Schottky barrier and injected into the conduction band (CB) of $Bi_4O_5I_2$. In addition, the Schottky junction of $Bi_4O_5I_2$/Cu suppressed the electron backflow to Cu, as well as promoted the photogenerated holes transfer to Cu. The optimized 0.5% mass ratio of Cu nanoparticles on $Bi_4O_5I_2$ ($Bi_4O_5I_2$@Cu-0.5) showed the highest CO production rate of 7.34 μmol g^{-1} h^{-1} under visible light illumination, which was 13.1 times more than that of bare $Bi_4O_5I_2$. Yu's group modified layer g-C_3N_4 nanosheets with Cu nanoparticles via secondary calcination and microwave hydrothermal method, as shown in **Figure 1** - **12**c.[125] The optimized 6 wt.% Cu nanoparticles not only improved the light absorption ability of g-C_3N_4, but also promoted the separation of photo-generated electrons-hole pairs and increased the catalytic activity sites, with the CO_2RR product of 49.43 μmol g^{-1} CO in 0.1 M $KHCO_3$ solution under a 350 W xenon lamp illumination for 5 h.

Wang and co-workers first designed the Cu@porphyrin-COFs nanorods by electrodepositing Cu nanowires on the free-base porphyrin-COFs, as shown in **Figure 1** - **12**d.[129] The photo-induced electrons are trapped and absorbed by the nitrogen in porphyrins and the Cu to form high-active hydrogen atoms, which can reduce the CO_2 molecules trapped by porous COFs. In addition to supplying trapping sites for electrons and protons, the deposited Cu also improved the charge transfer and the electron-hole pair separation. The PEC CO_2RR products of Cu@porphyrin-COFs nanorods are methanol, ethanol, ethane-1,1-diol and acetone with the highest formation rate of 5352 μM $g^{-1}h^{-1}$ and the apparent Faradaic efficiency (AFE) of

452.75%. Li and co-workers coated MOFs on the surface of Cu nanowires (NWs) to synthesize a series of 1D dual-channel Cu NWs@MOFs with tuneable CO/H_2 products.[130] In the hetero-wire catalysts, MOFs show the functionality of the molecular and photon channels, and Cu NWs function as the electron channels and promote electronic transmission. They further replaced the insulator MOF with a semiconductor $Cu_3(BTC)_2$ (BTC = 1,3,5-benzene tricarboxylate) (HKUST-1) to form a 1D/1D Mott-Schottky heterojunction, which exhibits the superior catalytic activity with the CO_2RR product of CO 176.2 μmol h^{-1} g^{-1} with a small amount of C_2H_4 as shown in **Figure 1** - **12**e.

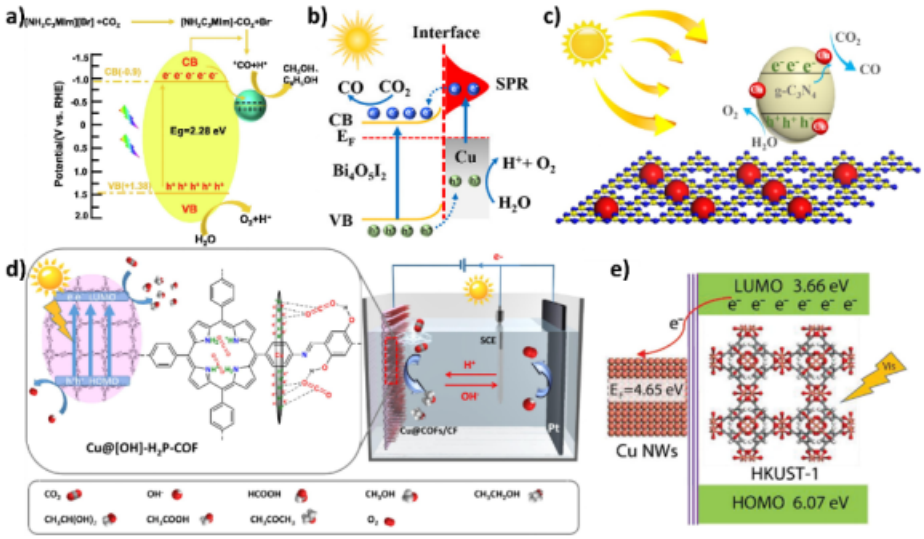

Figure 1 - **12.** Schematic diagram of CO_2 a) PC reduction over Cu/ILs/OVs-BMO in APMImBr aqueous solution.[127] b) photoreduction over $Bi_4O_5I_2$@Cu-0.5.[128] c) photoreduction on Cu/g-C_3N_4.[125] d) PEC reduction on Cu@porphyrin-COFs nanorods.[129] e) PC reduction on Cu NWs@HKUST-1 Mott-Schottky structure.[130]

Table 1 - **6.** Summary of metal Cu catalysts and their CO_2RR performance.

Type	Photocatalyst	Medium	Light source	Products	Reference
Cu nanodots	0.1%Cu/ILs/ OVs-BMO (Cu: ILs = 1:10)	7 wt% ILs-H_2O	A 300 W Xe lamp	Methanol 98.66 μmol g^{-1} h^{-1} Ethanol 95.74 μmol g^{-1} h^{-1}	127
Cu nanoparticles	$Bi_4O_5I_2$@Cu-0.5	Water vapour	A 300 W Xe lamp	CO 7.34 μmol g^{-1} h^{-1}	128
	6 wt.% Cu	0.1 M	A 350 W Xe	After 5 h,	125

	nanoparticle/ g-C_3N_4 nanosheets	$KHCO_3$ solution	lamp	CO 49.43 μmol g^{-1}	
Cu nanowires	Cu@porphyrin-COFs nanorods	CO_2 saturated 0.5 M $KHCO_3$ solution	A 300 W Xe lamp with 200 mW cm^{-2}	C1~C3 chemicals 5352 μM g^{-1} h^{-1}	129
	Cu NWs@HKUST-1	5 ml pure water with 0.1 MPa high purity CO_2	A 300 W Xe lamp with a 420 nm cutoff filter	CO 176.2 μmol h^{-1} g^{-1} C_2H_4 15.3 μ mol h^{-1} g^{-1}	130

1.3.2 Copper oxides for CO_2RR

Copper oxides have two chemical states, including cupric oxide (CuO) and cuprous oxide (Cu_2O). Both copper oxides have suitable bandgaps with light-absorbing ability and active sites for CO_2RR; however, the Cu_2O can be easily oxidized, and the photo-generated electron-hole pairs are easily recombined.[62] So the copper oxides are usually modified with other semiconductors to form heterojunctions to improve the charge carrier transfer.

Guo and co-workers introduced a chlorine (Cl)-modified Cu_2O/ZnO heterostructure (CCZO) photocathode via a facile two-step electrodeposition method, as shown in **Figure 1** - **13**a.[131] In the catalysts, the Cu_2O/ZnO heterojunction enhances the charge carrier separation with the Cl^- ions passively stabilizing the Cu^+ active sites on the catalyst surface. The CCZO reduces the energy barrier of *CO to *CHO, and favours *CO hydrogenation favours CO desorption. The PEC reduction product of CCZO is CH_4, with a yield of 1.04 μmol and a faradaic efficiency of 88.6% achieved under the applied voltage of - 0.6 V vs. RHE. Zheng et al. investigated Cu/Cu_2O photocatalysts with sphere and octahedron shapes via a solution-based chemical method, as shown in **Figure 1** - **13**b.[132] Based on the X g NaOH added in a 25-ml H_2O when synthesizing Cu/Cu_2O-X, Cu/Cu_2O-0.2 shows spherical shape with (111), (110) and (100) facets of Cu_2O, and Cu/Cu_2O-2.0 shows octahedral shape with only (111) facets. The multifaceted spherical Cu/Cu_2O-0.2 photocatalysts make electrons and holes prefer to move to the (100) and (111) facets, and increase the separation of photoinduced charge carriers, and thus show the PC CO_2 reduction performance with the products of

CO 87.7 μmol g^{-1} h^{-1}, CH_3OH 10.2 μmol g^{-1} h^{-1}, and H_2 5.4 μmol g^{-1} h^{-1}.

The CO_2 photoreduction abilities of CuO-based catalysts with different conformations are also compared by Ávila-López and co-workers, as shown in **Figure 1** - **13**c.[133] Compared to the CuO synthesize methods involving precipitation, sonochemical, microwave-hydrothermal, and spin-coating on thin film, the CuO microwave-coated on glass fibre exhibited the CO_2RR performance with 100% product selectivity and a rate of56.3 μmol g^{-1} h^{-1} CH_4. Park's group introduced a Ti layer/CuO/$CuFeO_2$/TiO_x particles (Ti/CFO/TiO_x) photocatalyst for O_2 evolution and ~100% selectivity of formate products for CO_2 PC reduction reaction, as shown in **Figure 1** - **13**d.[134] The metallic Ti underlayer shows high electric conductivity and working function, improving hole transfer, and robust the connection between CFO and FTO substrate. The Z-scheme of heterostructures between the CFO and the unsaturated Ti states in TiO_x facilitates the electron transfer. With the irradiated area of 0.5 × 0.5 cm^2, the Ti/CFO/TiO_x system produced the photocatalytic products of ~14 μmol h^{-1} formate and ~2.8 μmol h^{-1} O_2. Yin and Li applied a solution-processed impregnation-reduction method to synthesize CuO on Pd nanoparticles in situ grown on plasmonic H_xMoO_{3-y} nanosheets with oxygen vacancies (OVs) (CuO-Pd/H_xMoO_{3-y}) hybrids, as shown in **Figure 1** - **13**e.[135] The Cu-Pd sites in CuO-Pd could function as the highly active sites for CO selectivity, which could synergize with OVs in H_xMoO_{3-y} to further improve the selectivity by inducing the localized electrons transfer across Schottky junctions to CuO-Pd. At the reaction temperature of 100 °C under light illumination, the synergetic effect of light and heat promotes the formation of Cu_1O-Pd_5/H_xMoO_{3-y} heterostructures, showing the CO_2 PC reduction product of ~100% selectivity of CO (870 μmol g^{-1} h^{-1}).

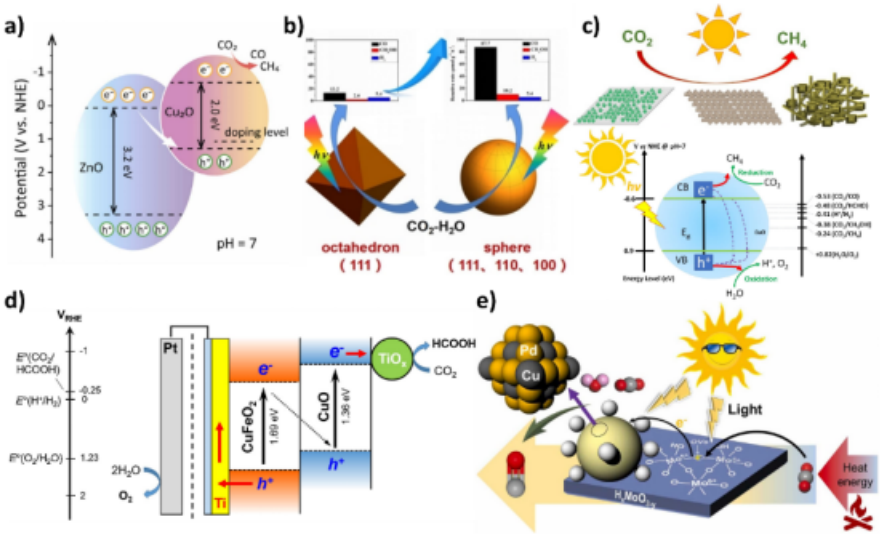

Figure 1 - 13. a) Band alignment of CCZO,[131] b) different shape with different CO_2 reduction product of Cu/Cu_2O. [132] And the scheme of CO_2 PC reaction on c) CuO with different conformations, [133] d) the $Ti/CFO/TiO_x$ film,[134] e) $CuO\text{-}Pd/H_xMoO_{3-y}$ hybrids,[135]

Table 1 - 7. Summary of copper oxide catalysts and their CO_2RR performance.

Type	Photocatalyst	Medium	Light source	Products	Reference
Cu_2O	CCZO	CO_2 saturated 0.1 M $KHCO_3$ solutions	A 300 W Xe lamp with a 420 nm cutoff filter	− 0.6 V vs. RHE CH_4 1.04 μmol	131
	spherical Cu/Cu_2O-0.2 photocatalyst	5.00 mL of ultrapure water with feed gas CO_2/Ar 15/85 flowed through a gas purifier	A 300 W Xe lamp (λ >400 nm)	CO 87.7 μmol g^{-1} h^{-1}, CH_3OH 10.2 μmol g^{-1} h^{-1}, H_2 5.4 μmol g^{-1} h^{-1}	132
CuO	CuO coated on glass fiber mesh	1 bar CO_2	150 mWcm^{-2}	CH_4 56.3 μmol g^{-1} h^{-1}	133
	$Ti/CFO/TiO_x$	0.1 M $KHCO_3$	A 150 W Xe arc lamp (AM 1.5 G; 100 mW cm^{-2})	Formate ~14 μmol h^{-1} O_2 ~2.8 μmol h^{-1}	134
	$Cu_1O\text{-}Pd_5/H_xMoO_{3-y}$	CO_2 with H_2O vapor at 100 °C	A 300 W Xe lamp	CO 870 μmol g^{-1} h^{-1}	135

1.3.3 Cu alloys or bimetallic composites for CO_2RR

The metal-oxygen (O) affinity and hydrogen (H) affinity decided the CO_2RR activity and selectivity via the binding strength of the reaction intermediates on the metal surface.[136] So, the selectivity of Cu-based catalysts can be improved by alloying or forming bimetallic composites with other metals with different O- and H- affinity.

Dong's group reported that the 49.1 ± 1.9% selectivity of C2 products in CO_2 PC reduction would be achieved by applying a stepwise photo-deposition method to modify TiO_2 with Cu-Ag alloy sub-nanoclusters (ASNC). Such a stepwise photo-deposition process can form a strong interfacial dielectric coupling interface state (IFS) with TiO_2 and lead to the formation of hot electrons in TiO_2 under visible light.[137] In synergistic Cu-Ag ASNC, Cu serves as CO_2 reduction active sites and has merits of good C_2H_4 adsorption ability, and Ag enhances the CO_2 adsorption on Cu sites and as well as promotes the migration of photogenerated electrons to Cu sites, and has excellent C-C coupling properties. With adding 0.8 at% Cu, the $Cu_{0.8}Ag_{0.2}/TiO_2$ shows the highest CO_2 PC reduction performance, with the production rate of C_2H_4 1110.6 ± 82.5 μmol g^{-1} h^{-1} and CH_4 1628.5 ± 108.3 μmol g^{-1} h^{-1}, as depicted in **Figure 1 - 14**a.

Rodrigues's group annealed (A) or annealed/quenched (Q) heat treatments of Ti-xCu (x = 0.5, 5.5 and 10 at. %) alloys and get the anodic product of self-organized nanotubular (Nt) oxides for CO_2 PEC reduction, as shown in **Figure 1 - 14**b.[138] In the Ti-xCu (A) samples, the Cu-rich phases distribute in the lamellar regions with a low defect density and homogeneous distribution of Cu^+ and Cu^{2+}, and the Cu ions and oxygen vacancies along the wall of the oxide nanotubes are favourable for the methanol formation. While, in the Ti-xCu (Q) samples, the Cu-rich phases assemble in the acicular substrate with high concentration of Cu^+ and oxygen vacancies near the bottom of the nanotubes, which increase the CO_2 adsorption active sites, stabilize CO_2 reduction intermediate radicals, and are favourable for the formation of ethanol. After 1 h illumination, the PEC CO_2RR products of the Nt/Ti-10at.%Cu (A) are 0.10 mmol L^{-1} methanol and 0.44 mmol L^{-1} acetone, and that of the Nt/Ti-10at.%Cu (Q) are 2.32 mmol L^{-1} ethanol and 0.43 mmol L^{-1} acetone.

Yang and co-workers applied palladium (Pd)-Cu nanocrystals on the carbon and oxygen co-doped ultra-micropores boron nitride (BN) (PdCu/BN), as illustrated in **Figure 1 - 14**c.[139]

The C and O co-doped BN absorbs CO_2 as bicarbonate species on the surface with a high CO_2 capture ability. The Pd/Cu alloy size and their distribution on the BN are related to the molar ratio of Pd and Cu. The PdCu/BN shows interfacial bidirectional absorptions of CO_2, making it easier for CO release. With uniform distribution of small Pd-Cu nanocrystals, the Pd_5Cu_1/BN owns more effective interfaces with the CO_2RR PC reaction products of 7.74 μmol g^{-1} h^{-1} CO and 1.38 μmol g^{-1} h^{-1} CH_4.

Yu's group introduced sulphur (S)-deficient in Cu_3SnS_4 (CTS) nanoparticles to induce the Cu (I) and Sn (II) sites and the electron enrichment around Sn (II) atoms, which enhanced the reduction ability of CTS and the selectivity of CH_4, as shown in **Figure 1** - **14**d.[140] On the Cu(I)-Sn(IV) (200) surface, the CTS possesses increased CO_2/H_2O adsorption and activation; while, with the Sn (II) 5p orbital dominating the CB of the CTS, it has enhanced electron reduction ability. With the 83.1% selectivity of CH_4, the CTS-1 exhibits the highest PC CO_2RR performance with the product of 18.42 μmol g^{-1} h^{-1} CO and 22.65 μmol g^{-1} h^{-1} CH_4.

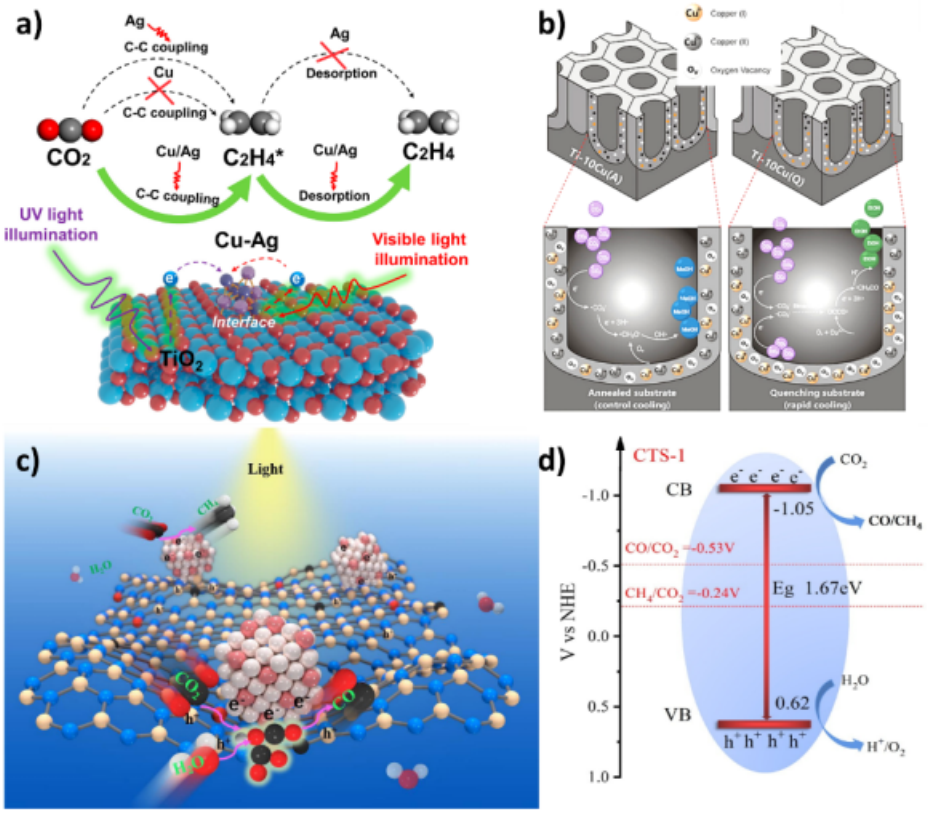

Figure 1 - **14.** Schematic illustration of CO_2 conversion mechanism of a) PC reaction on $Cu_{0.8}Ag_{0.2}/TiO_2$.[137] b) PEC reaction over Nt/Ti-10at.%Cu (A) and Nt/Ti-10at.%Cu (Q).[138] c)

PC reduction on PdCu/BN,[139] and d) CTS-1.[140]

Table 1 - 8. Summary of copper-alloy or bimetallic composites and their CO_2RR performance.

Type	Photocatalyst	Medium	Light source	Products	Reference
Cu-Ag	$Cu_{0.8}Ag_{0.2}/TiO_2$	High-purity CO_2 with 150 μL water	A 300 W Xe lamp with an AM 1.5G filter	C_2H_4 1110.6 ± 82.5 μmol g^{-1} h^{-1} CH_4 1628.5 ± 108.3 μmol g^{-1} h^{-1}	[137]
Cu-Ti	Nt/Ti-10at.%Cu (A) and Nt/Ti-10at.%Cu (Q)	0.10 mol L^{-1} $NaHCO_3$ saturated with CO_2	A 125 W high pressure Hg lamp ($\lambda \geq 365$ nm) was calibrated to 1 Sun (100 mW cm^{-2})	After 1 h Nt/Ti-10at.%Cu (A) methanol 0.10 mmol L^{-1} acetone 0.44 mmol L^{-1} Nt/Ti-10at.%Cu (Q) ethanol 2.32 mmol L^{-1} acetone 0.43 mmol L^{-1}	[138]
Cu-Pd	Pd_5Cu_1/BN	CO_2 with H_2O vapor	A 300 W Xe lamp	CO 7.74 μmol g^{-1} h^{-1} CH_4 1.38 μmol g^{-1} h^{-1}	[139]
Cu-Sn-S	Cu_3SnS_4-0.1 g Cu_2O	CO_2 with H_2O vapor	A 300 W Xe lamp with a 420 nm cutoff	CO 18.42 μmol g^{-1} h^{-1} CH_4 22.65 μmol g^{-1} h^{-1}	[140]

1.3.4 Copper ions for CO_2RRs

Copper ions can also be doped into the commonly used semiconductors to change their lattice structures, aiming to provide active sites for CO_2RR. He's group introduced Cu atomic dopants on the layered BiOCl nanosheets to fabricate the high-performance photocatalyst (Cu-BiOCl) via an impregnation method, as shown in **Figure 1 - 15**a.[64] Containing both Cu^+ and Cu^{2+}, the Cu elements could withdraw and migrate electrons from Bi through the Bi-O-Cu bond, slightly reduce the bandgap of BiOCl, and enhance the generation of photoinduced charge carriers, but slightly weaken the reduction ability. Moreover, the introduction of Cu can improve the CO_2 adsorption capability of BiOCl by reducing the CO_2 activation energy

barrier, favour the reaction dynamics by stabilizing the $COOH^*$ intermediate, and accelerate the CO_2 activation to CO desorption procedure. The reduction product of the optimized 1% mass ratio of Cu/BiOCl exhibits the CO_2RR performance of producing CO 38.3 μmol g^{-1} in H_2O after 4h illumination, which is 50% higher compared to the pristine BiOCl. Kim and coworkers introduced Sn (II) Cu (I) dual-atom-site (DAS) on C_3N_4 (DAS-Sn–Cu/C_3N_4) photocatalysts for CO_2 reduction to HCHO via the HCOOH reduction path.[141] The heteronuclear neighbouring Sn-Cu centres embedded in the C_3N_4 framework with the low valence states of Cu and Sn atoms formed by the anoxic reaction system and provided binding sites for CO_2 reduction activation, and the unique synergic action of the Sn-Cu combination contributed to the high selectivity of HCHO product. With the Sn:Cu precursor mass ratio of 3:1, the CO_2 photoreduction products are HCOOH and HCOH after a 24-h reaction, with the selectivity of 61% 259.1 μmol g^{-1} HCOH, as shown in **Figure 1** - **15**b.

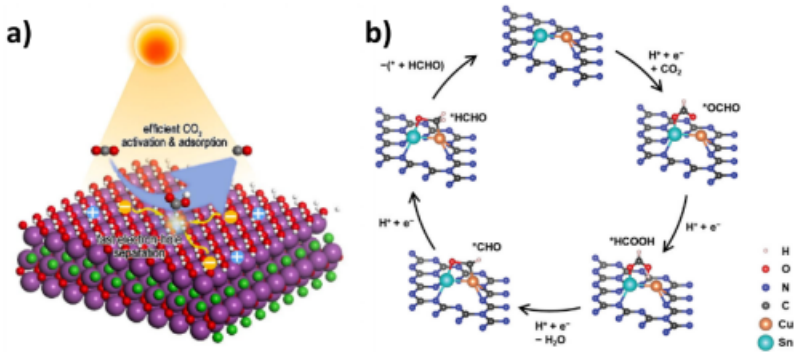

Figure 1 - **15.** Mechanism scheme of CO_2 a) PC reduction on Cu-BiOCl,[64] b) reduction to HCHO over DAS-Sn_{75}-Cu_{25}/C_3N_4.[141]

Table 1 - **9.** Summary of copper ions catalysts and their CO_2RR performance.

Type	Photocatalyst	Medium	Light source	Products	Reference
Atomic Cu	1 Cu-BiOCl	H_2O kept at 15 °C	A 300-W Xe lamp	After 4h, CO 38.3 μmol g^{-1}	64
	DAS-Sn_{75}-Cu_{25}/C_3N_4	CO_2-saturated 0.1 m $KHCO_3$ with 10 vol.% triethylamine (TEA)	A 300 W Xe lamp with a 420 nm cutoff filter	After 24 h, HCOH 259.1 μmol g^{-1} HCOOH 165.7 μmol g^{-1}	141

1.4 Conclusions and outlook

PVK-based materials have emerged as a new and highly promising class of solar-energy materials. Their extraordinary electrical and optical properties and suitable band structures combined with the abundance of raw materials, the simplicity of synthetic routes, and processing versatility make this family of materials ideal for cost-efficient, high-performance PC/PRC applications that span far beyond photovoltaics optoelectronics. Regarding Cu-based catalysts, Copper (Cu) stands out as the only metal system capable of producing hydrocarbons via the CO2RR. This unique capability is attributed to its negative adsorption energy to *CO and positive adsorption energy to *H. In this regard, applying PVK-based and Cu-based catalysts to perform the photocatalytic CO_2RR is a very effective way to mitigate the greenhouse effect issue and the energy crisis. However, the severe carrier recombination, poor reaction intermediate adsorption capability, and instability to the humid environment greatly limit the CO_2RR performance of the PVK-based and Cu-based catalysts. To conquer these problems, a series of structure-component engineering methods, including morphology design, defect engineering, interfacial heterojunction engineering, and active layer encapsulation have been developed, which are summarized and discussed in this Chapter. Therefore, to further improve the PC/PEC CO2RR performance and the stability of the catalysts, it is promising to achieve satisfying photocatalytic performance and stability by rationally modifying PVK-based and Cu-based catalysts.

While the PVK-based photocatalysts for CO2RR have been summarized in **Table 1** - **5**, the practical application of these catalysts necessitates further improvements, particularly in the development of lead-free PVK-based catalysts. This initiative aims to mitigate environmental pollution and minimize the risk of biological poisoning. In the meanwhile, other strategies are also highly encouraged, mainly including developing long-recycling humid stable PVK-based catalysts, applying defect engineering and in-situ detection method to further illustrate the intermediates adsorption/desorption and reaction pathway during the CO_2RR process. Specifically, the future research may focus on the developments as follows:

1) Due to environmental concerns, the toxicity of the Pb element cannot be neglected. As discussed above, a lot of attempts have been made to replace Pb element by using other

B-site cations with eco-friendly low-toxic or non-toxic nature, for instance, lead-free PVKs such as $Cs_2AgBiBr_6$ and $Cs_3Bi_2I_9$ with different structures and dimensions have been applied in CO_2RR photocatalysts.[83, 119] Other lead-free materials have also been synthesised, but their potential in photocatalytic CO_2RR have not been analysed yet, such as $M_3Sb_2I_9$ (M=Cs and Rb) nanocrystals, $CsSnI_3$, and $Cs_3Sb_2Br_9$.[142-144] So, the efforts can be taken to find stable lead-free candidates with higher photocatalytic performance.

2) The stability issues of PVK photocatalysts caused by thermal, moisture, UV light irradiation, self-segregation, or repeated catalytic cycles also impede their industrialization. The general ways to enhance the stability of PVKs are based on the physical confinement effect or the chemical bonding effect. The encapsulation strategy with an almost fully covered core-shell structure can reduce the direct contact of PVK and the environment. Also, the protecting layer can isolate PVK QDs from each other to enhance their tolerance to moisture.[145] The B-site metallic ion doping can enhance the interaction between the crystal frame and the ions, which can provide more stable crystal structures of PVK materials.[38] In addition, various kinds of heterojunction structures have been utilized for higher stability and different electrolytes and vapour systems have also been studied to improve the stability of photocatalysts. However, the mechanism of heterojunctions to improve the CO_2RR stability still needs further exploration. Stability issues can also be addressed by introducing surface defect (Wang et al.), surface ligand density control (Chen et al.), and so on.[79, 98-99]

3) To further improve the photocatalytic efficiency, there are several aspects to work on, such as increasing the specific surface area, introducing more active sites for CO_2 adsorption, facilitating the separation of photo-generated electron-hole pairs and suppressing the recombination of charges, improving the light-harvesting property of the photocatalysts, tailoring the surface property of PVKs, and so on. Strategies like defect engineering or cocatalyst modification could influence the reaction intermediate adsorption of PVK, which is promising to adjust the CO_2RR selectivity. However, the relative research is still rare, especially on the topic of defect engineering. Also, the mechanisms of the improvement of CO_2RR performance are not fully understood. For instance, in the defect and vacancies engineering method, no in-depth discussion about the position where the CO_2 is adsorbed. In-situ detection methods to further illustrate the

intermediates' adsorption/desorption and reaction pathways during the CO_2RR process are needed.

4) To deeply understand the mechanism behind photocatalysts, DFT calculations can be employed. Zhu's group used DFT calculations to identify the role of the residual oxygen defects in the rGO surface in improving the adsorption and activation of CO_2.[99] the electronic structures and interfacial properties of the Cs_2SnI_6/SnS_2 hybrid are investigated through DFT calculations in Wang's report.[103] Huang et al. simulated Gibbs free energy by DFT calculations to prove the near 100% CO selectivity of the photocatalytic final product.[146] Dong's group applied the spin-polarized DFT calculations to confirm that $COOH^-$ was the primary intermediate in the CO_2RR process.[50] More recently, Tang and co-workers investigated the reaction mechanisms of Co-doped and Fe-doped PVKs for CO_2RR through DFT calculations, providing theoretical support for the metal ion-doped PVKs as photocatalysts.[77] A variety of topics can be calculated by DFT calculations, such as the total energy, potential energy, and the energy spectra of the crystal structure, crystal molecular as well as organic complexes.[147] The band structure, effective masses of electrons and holes, band gaps, and optical transitions can also be calculated based on DFT simulations. More works combining theoretical DFT calculations with experimental verifications are in demand.

For the future development of Cu-based catalysts for PC/PEC CO_2RR: 1) According to the modification engineering on PVK-based catalysts, the structural design, interfacial heterojunction engineering, and defect engineering modification methods should also be future investigated on Cu-based catalysts. 2) To further control the product selectivity of Cu-based catalysts, mechanism, reaction active sites and reaction pathway calculations should also receive more attention. 3) The oxidation state of Cu-based bimetallic composite can be further investigated within the realm of PEC, and the combination of copper oxide with other elements can significantly enhance the selectivity of reduction products. 4) Different methods of modifications can also be applied within the same research project to synergistically improve the PC/PEC performance.

Chapter 2 Methodology

This chapter is devoted to introducing the principal methodologies employed in preparing PVK-based and Cu-based materials for photoelectrochemical CO_2 reduction reaction as well as the pertinent characterization methods.

2.1 Growth methods

2.1.1 Spin-coating method for thin-film samples

Spin-coating method (**Figure 2 - 1**) is designed for growing uniform thin sticky or hydrophobic material films on flat axis-symmetrical substrates.[148] The first step is to secure the axis-symmetrical substrate to the spinning stage via a vacuum pump or sticky material, and the non-axis-symmetric substrate will lead to the edge effect.[149] Then, the coating material with a particular volume is dropped to the centre of rotation with the substrate spinning at a specific speed to spread the liquid evenly over the substrate via centripetal acceleration force. The spin speed is also very important due to its determination functions on the film thicknesses. Choosing the suitable materials as the solvent is another key parameter, because their vaporization speed would determine the morphology and properties of the resulting films, and heating procedure is often applied after the spin-coating process to help the crystallization.[150]

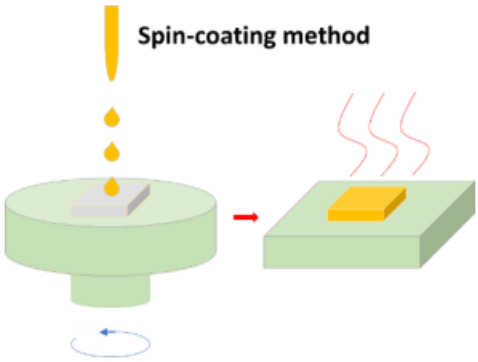

Figure 2 - 1. Schematic diagram of spin-coating method.

2.1.2 Electroplating method

The electroplating method (**Figure 2 - 2**) is used for reduction-coating metallic materials on the conductive substrate materials in the aqueous medium dissolved with target metallic ions

under the assistant of a negative external voltage.[151] There are three major procedures. The first step is to perform the pretreatments on the substrate to get a suitable surface with ideal roughness and cleanness, which can influence the bond strength between the substrate and the coated material. The second step is to set the appropriate coating parameters, such as the metallic ratio, the metal precursor solution, the concentration of metal ions, the applied negative current density and duration, etc. These parameters are based on the chemical, thermodynamical and kinetical influence on the electroplating procedure. The last step is to apply the post-treatment on the coated material, including cleaning, drying, and preserving process for further use.[152]

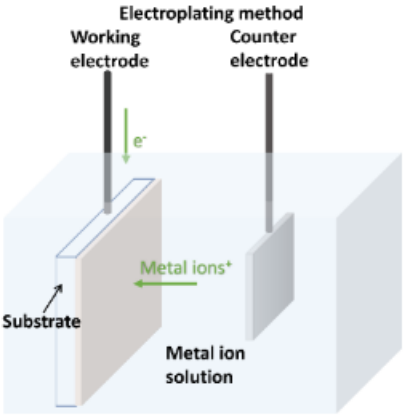

Figure 2 - 2. Schematic diagram of electroplating method.

2.2 Characterization

2.2.1 Scanning electron microscopy (SEM) and Energy-dispersive X-ray spectroscopy (EDS, EDX, EDXS or XEDS)

Scanning electron microscopy (SEM) is a characterization method to check the morphology properties of materials. Different from optical microscopy (OM), which uses light sources and shows the true colours of living cells or solid materials, SEM utilizes an electron beam source and is designed for dry and conductive materials and can provide more detailed grey-scale images with magnifications reaching 100 kx.[153] As shown in **Figure 2 - 3**, an SEM machine usually contains an electron gun source to generate high-energy electrons, a column to allow electrons transport through electromagnetic lenses, a deflection system composed of

scan cools, an electron detector, a vacuum sample chamber and a connection to the computer control system.[154]

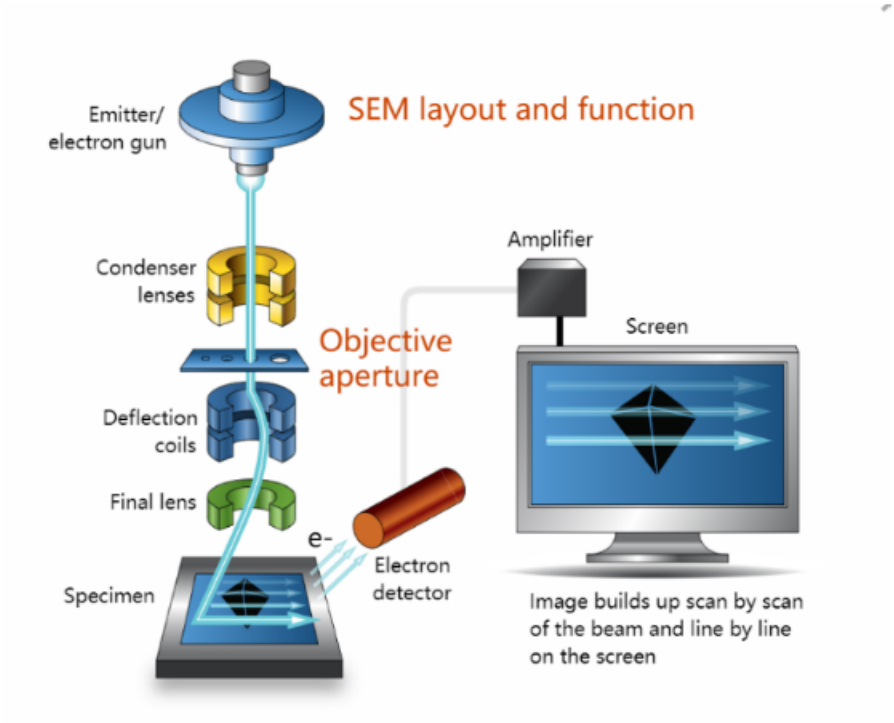

Figure 2 - 3. Structure diagram of a SEM machine.[154]

Usually, electrons are emitted and accelerated by the electron gun and are adjusted to a specific size, position and intensity via the electromagnetic lenses and the aperture systems and are focused on the sample surface in the vacuum chamber. As shown in **Figure 2 - 4**, the interaction between the electrons and the sample surface can generate a series of signals, including auger electrons (AE), secondary electrons (SE), backscattered electrons (BSE), characteristic X-rays and X-ray continuum.[155] The low-energy-SE signals are used for SEM image characterization and usually utilize the low accelerating voltage (5 kV) for detailed surface information.[153]

When entering the coulomb field of the specimen surface, the electrons will decelerate with the lost electron energy emitting as photons.[153] The X-ray photons with particular energy for different elements will also be emitted and can be detected for Energy-dispersive X-ray spectroscopy (EDS, EDX, EDXS or XEDS) testing. The EDS detector can separate the characteristic X-rays into energy spectrum and allow the software to determine the amplitude of each element to give the qualitative and quantitative chemical composition information

and mappings of the sample.[156] A higher accelerating voltage (20 kV) is needed for elemental EDS characterization, and a higher working distance of sample stage is needed for the insertion of the EDS detector.

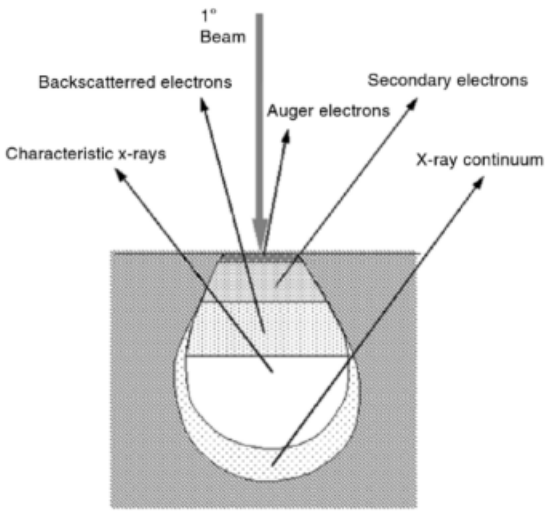

Figure 2 - 4. Diagram of the interaction of the electron with the sample surface.[155]

2.2.2 High-resolution transmission electron microscopy (HRTEM) and high-angle annular dark filed image-scanning transmission electron microscopy (HAADF-STEM)

High-resolution transmission electron microscopy (HRTEM) is a technique to transmit a high-energy electron beam through a thin sample and produce high-resolution and high-magnification electron diffraction images in a high-vacuum chamber. As shown in **Figure 2 - 5**, in a TEM machine, the electron gun system generates high-energy electrons via a filament or a field emission gun (FEG) and the electrons are accelerated by the gun accelerator to the column.[157] The beam is then focused on the sample by a series of electromagnetic condenser lenses and aperture, and the scattered radiation passes through objective lenses and apertures and is further magnified by the intermediate lens and projector lens and then projected on a screen or a CCD camera.

Similar to SEM equipment, scanning transmission electron microscopy (STEM) is used to scan the target sample pixel-by-pixel in a TEM machine by focusing the electron beam into a small probe. High-angle annular dark-field (HAADF)-STEM only collects electrons scattered through very large angles, which is related to the elemental mass; that is, the higher the

atomic number, the brighter the image area. Moreover, akin to the EDS function in SEM, the interaction between a high-energy electron beam and a thin sample can generate a series of signals (refer to **Figure 2 - 6**), where emitted X-rays can be detected for EDS characterization.[158]

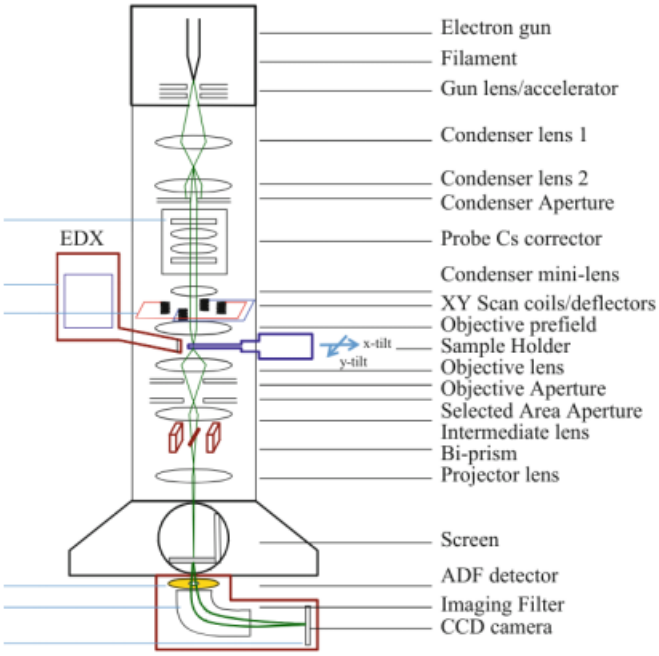

Figure 2 - 5. Schematic illustration of a TEM with STEM function.[157]

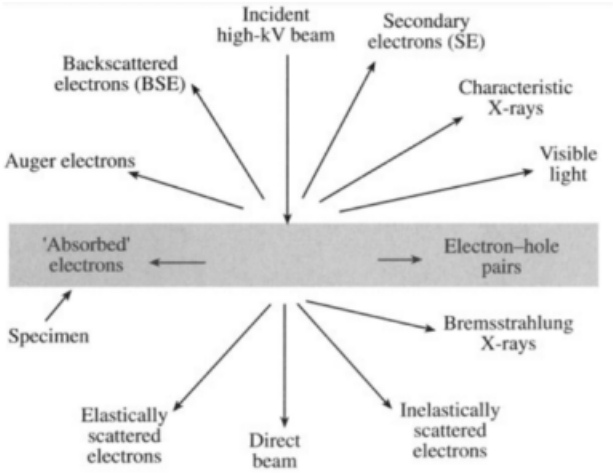

Figure 2 - 6. Diagram of signals produced from the interaction between a high-energy electron beam transmits a thin sample.[158]

2.2.3 X-ray diffraction (XRD)

X-ray diffraction (XRD) technology is designed for the precise study of crystal structure based on crystals diffracting X-rays in characteristic peaks. The position of the obtained diffraction peaks can be used to analyse the qualitative information of crystal lattice, space group, and chemical composition, and the peak intensity can show quantitative phase analyse, while the peak shape can indicate the nanocrystalline size.[159] When the X-ray photons reach periodic crystals, elastic scattering happens between the photons and the electrons around atom nuclei, generating constructive or destructive scattered radiations, which are characteristic diffraction peaks. The diffraction peaks follow the equation of Bragg's law (**Figure 2** - 7):[160]

$$n\lambda = 2*d_{hkl}*\sin\theta \quad (2.1)$$

where n is the order of diffraction, λ (unit: nm) is the incident beam wavelength, d_{hkl} (unit: nm) represents the lattice spacing, and θ (unit: degree) is the angle of the diffracted beam.

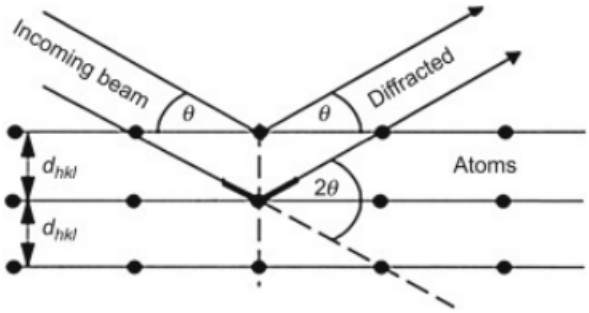

Figure 2 - 7. Diagram of diffraction from lattice planes.[159]

2.2.4 X-ray Photoelectron Spectroscopy (XPS)

X-ray Photoelectron Spectroscopy (XPS) technique is designed for checking the sample surface (only the top few atomic layers), aiming to gain the quantitative chemical analysis by irradiating the sample with monoenergetic soft X-rays in a vacuum environment.[161] Each element with a unique set of binding energies can form unique peaks in the XPS spectrum with the axis of the number of detected electrons vs kinetic energy, and the peak area or height can give the quantitative information, while the peak position and separation indicate chemical states and chemical potential and polarizability of the element in the compounds.[161]

2.2.5 UV-Vis spectroscopy

UV-Vis spectroscopy is designed to detect the wavelength of the light source absorbed by the sample and is based on the fact that the electrons in different bonding environments can absorb different photon energies and is promoted to higher energy states.[162] The intensity of the absorbance follows the Bouguer-Lambert-Beer law:[163]

$$A = \varepsilon * L * c = \log(I_0/I) \quad (2.2)$$

where A is the absorbance, ε is the extinction coefficient, c is the concentration of a sample, L is the path length, I_0 and I represent the intensity of the light before and after passing through the sample, respectively.

2.2.6 Time-resolved photoluminescence (TRPL)

Fluorescence is the relaxes of an orbital electron to its ground state at the same time emits a photon from an excited singlet state.[164] The excited materials can transfer energy to a secondary sensitized material. The time-resolved photoluminescence (TRPL) is designed to study the energy level and the fluorescence quenching lifetime of the excited state.[164] And as shown in **Figure 2 - 8**, a spectrometer for TRPL tests usually contains a pulsed light source, a monochromator or an optical filter and a photon-sensitive detector which can measure lifetimes in ps to ms scale.[165]

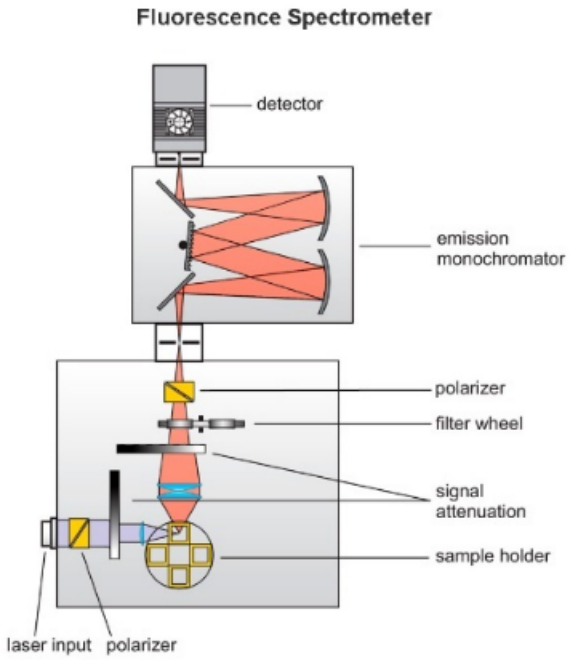

Figure 2 - 8 Schematic illustration of a spectrometer for TRPL tests.[165]

2.2.7 Space-charge-limited current (SCLC) measurement

Space-charge-limited current (SCLC) measurements is designed to test the trap-state densities or defect densities because the permittivity of the semiconductor can determine the space-charge density.[166] There are normally three regions in the measured current-voltage (I-V) curve: the Ohmic (linear, low-applied voltage) region, trap-filled region and the trap-free Child's region. At the intermediate voltages, the *I-V* curve has the slop larger than 2 in the log coordinate system, in which all the available trap states were filled by the injected carriers. The voltage started the trap filled region can be called trap-fill limit voltage V_{TFL}, which is proportional to the trap density n_{trap} according to the equation:[167]

$$n_{traps}=2\varepsilon\varepsilon_0 V_{\mathrm{TFL}}/ed^2 \quad (2.3)$$

where ε is the dielectric constant of the photoelectrode material, ε_0 is the vacuum permittivity, e means the electronic charge and d is the thickness of the material. And the charge carrier mobility can be calculated in the Child's region by the Mott-Gurney's law: [168]

$$\mu = 8Jd^3 / 9\varepsilon\varepsilon_0 V^2 \quad (2.4)$$

Where μ is the carrier mobility, J is current density and V is the corresponding applied voltage.

2.2.8 Photoelectrochemical (PEC) performance evaluation

Photoelectrochemical (PEC) tests are designed to acquire the quantitative and qualitative measurement of the light absorption ability and charge separation ability of photo-sensitive materials under the external applied voltage or current. PEC tests are usually conducted on an electrochemical workstation with a three-electrode system, which contains a working electrode, a counter electrode, and a reference electrode. A reference electrode provides a well-defined redox couple, with the only negligible current passed by, which is a reference for the working and counter electrodes. And the counter electrode is to complete the circuit of the reaction cell by passing all the current in the system and performing an opposite electrochemical process to the working electrode.[169]

Chapter 3 Synergistically Interface-engineered Inorganic Halide Perovskite Photocathodes for Photoelectrochemical CO_2 Reduction

To alleviate environmental problems, in this Chapter, I presented all-inorganic perovskite $CsPbBr_3$ (CPB)-base photocathodes for photoelectrochemical CO_2 reduction reaction, which are renowned for their exceptional optoelectronic properties, cost-efficiency, and ease of fabrication. And investigated the synergistic interfacial modification engineering of the photocathodes.

3.1 Introduction

The unlimited emission of carbon dioxide (CO_2), which is the main component of greenhouse gases, has become a severe global environmental issue due to rapid industrialization and fast population growth. Playing a key role in the natural carbon cycle, photosynthesis converts CO_2 and water into useful chemicals with the assistance of clean and infinite solar energy, which has inspired promising strategies to mitigate climate change and energy shortage.[170-171] Therefore, photocatalytic (PC) and photoelectrochemical (PEC) reduction of CO_2 by suitable semiconductors have attracted great attention in recent years.[172] In comparison to PC reactions, PEC cells can facilitate the separation of photo-generated electron-hole pairs and offer convenience for collecting oxidation and reduction products, respectively.[173]

Among various p-type semiconducting materials for PEC photocathodes, halide perovskite materials exhibit higher conduction bands with suitable bandgaps for CO_2 reduction reactions.[174] Their long charge carrier diffusion length and satisfying light-absorbing ability also make them promising candidates for photocathodes.[175] So far, there are only a few works reported applying halide perovskite materials in PEC CO_2 reductions. Jang and co-workers connected $CH_3NH_3PbI_3$ hybrid perovskite solar cells and photocathode in series to reduce CO_2.[176] Shen's group protected Br-based hybrid perovskite quantum dots with graphene oxide to synthesize photocathodes for CO_2 reduction.[177] Recently, sandwich-like perovskite photocathodes were reported by Zhang's group and Moore's team for PEC CO_2 reductions.[178-179] Nevertheless, how to enhance the PEC reduction performance based on halide perovskite materials is still challenging.[177, 179-180]

All-inorganic halide perovskite material, $CsPbBr_3$ (CPB), performs longer thermal-/aqueous-stability than that of organic-inorganic hybrid perovskite materials, which has been

intensively investigated as photocatalysts for CO_2 reduction.[181-184] However, the PEC CO_2 reduction performance tended to fluctuate among the publications, and the working mechanism still remains unclear. In addition, as a pristine semiconductor, the charge transport and light absorption properties of CPB in different forms are still waiting for further improvement. Up to now, various methods for enhancing light response and facilitating charge carrier transfer of pristine CPB have been reported in the photovoltaic and photocatalysis fields. Among these approaches, the halide doping is a widely used method, for example, fluorine (F)-doping,[185] through using the low-cost fluoride compounds, has been widely investigated to enhance the electronic performance of functional materials.[186] In addition, gold (Au)-coating is another effective strategy to enhance the photo-response ability and to facilitate the separation of photo-generated electron-hole pairs via forming a Schottky junction.[187] Depositing Au films onto perovskite materials for CO_2 photocatalytic reduction reaction is also reported by a lot of research groups.[188-191] Plus, applying the organic passivation layers, such as Nafion, can adjust their electronic properties through the coupling between organic and inorganic components.[192] However, the synergistic effect of these modification strategies on the PEC performance of CPB has rarely been studied before.

In this chapter, I demonstrated a prototype CPB-based photocathode through a facile spin-coating method and tuned their PEC CO_2 reduction performance by the rational interface-engineering strategy, which is to modify the obtained perovskite with 5% F-doping, Nafion, and 15 nm Au. It is demonstrated that separately applying F-doping can facilitate charge transfer, enhance interactions between perovskite elements and reduce the trap density of the material; adding Nafion can adjust the light absorbing ability of perovskite and passivate the material surface to further reduce the trap density; and constructing Au/$CsPbBr_3$ Schottky-junction can facilitate the photogenerated charge separation. Owing to the synergistic effect, the optimal CPB-F-N-AU system could achieve the champion performance with a photocurrent of -0.23 mA cm^{-2} at an applied voltage of -0.5 V vs $E_{Ag/AgCl}$ under a 4.13-mW cm^{-2} light illumination, which is twice of that of the pristine CPB photocathode. This work offered a practicable strategy to realise a satisfactory photo-activity for PEC CO_2 reduction based on halide perovskite materials.

3.2 Experimental section

Materials: Cesium bromide (CsBr, 99.9%), Lead bromide ($PbBr_2$, ≥98%), *N*,*N*'-

Dimethylformamide (DMF, 99.8%), Ammonium fluoride (NH_4F, ≥98%), Nafion perfluorinated resin solution (5 wt.% in lower aliphatic alcohols and water) were bought from Sigma-Aldrich P/L. The 704 Fixed High Temperature Resistant Silicon Rubber Insulated Sealing was bought from Hong Yue, China. Tetrabutylammonium Hexafluorophosphate ($C_{16}H_{36}F_6NP$, $TBAPF_6$ >98.0%) was purchased from TOKYO CHEMICAL INDUSTRY CO., LTD. Fluorine-doped tin oxide (FTO) glass (<14.0 Ohms/sq) was bought from Nippon Sheet Glass Co., Ltd. All the chemicals were used as received without further purification.

Growth of photocathodes: First, all the FTO glass substrates were cleaned in DI water, ethanol, acetone, and 2-propanol solvents ultrasonically for 10 min, respectively. Then, before being transferred into the glove box, all the pre-cleaned FTO substrates were further treated under a 20% O_2 plasma for 10 min. 1 $_M$ $PbBr_2$ solution was prepared in DMF solvent and was stirred at 70 °C for 30 min, and 1 ml solution was spin-coated onto FTO substrate at 2k rpm for 30 s. The $PbBr_2$ thin film was then heated on a hot plate at 90 °C for over 1 h. Thereafter, 0.07 $_M$ CsBr solution was prepared in methanol solvent and was stirred at room temperature. Subsequently, 1 ml CsBr solution was dropped onto $PbBr_2$ thin film and then spin-coated at 2k rpm for 30 s, followed by heating at 250 °C for 5 min, which was repeated for 4 times to synthesize the compact $CsPbBr_3$ thin films. Reserving the upper area for connecting the external circuit and an area of 1 cm × 1 cm on the thin film for PEC reaction, I covered the rest part and the side faces of the thin film with 704 silicon rubber. In order to dope F ions into CPB thin films, I prepared 0.07 $_M$ NH_4F into methanol, and mixed 5% NH_4F solution into CsBr solution during the 4-time spin-coating procedures. The 15-nm Au layer was prepared by sputtering Au in a Safematic CCU-010 Compact Coating Unit, with the process pressure of 5.0 Pa and process current of 30.0 mA. To add Nafion in CPB, I mixed a 100-μl Nafion solution into a 5-ml CsBr-methanol solution during the 4-times spin-coating procedures, including CsBr solution for 3 times and CsBr with Nafion for the last time.

Characterizations: The morphology of the obtained samples was characterized using a scanning electron microscope (SEM, Zeiss Sigma HD). The X-ray diffraction (XRD) data were acquired using a STOE STADI P with Mo $K\alpha 1$ (λ = 0.70926 Å). The *I-V* characterization of Schottky-junction and the space charge limited current (SCLC) were evaluated using a two-terminal probe station (EVERBEING INT'L CROP.) and a 4200A-

SCS PARAMETER ANALYZER in the dark condition at room temperature. Time-resolved photoluminescence (TRPL) measurements were analysed on a Microtime 200 STED instrument (Picoquant) with a 470 nm laser. X-ray photoelectron spectra (XPS) and the valence band (VB) were measured on a Thermo Fisher K-Alpha+.

Photoelectrochemical reactions: PEC measurements were conducted on a 3-electrode configuration (CHI 650E, Shanghai Chenhua) with a Pt foil as the counter electrode and Ag/AgCl (3 M KCl) as the reference electrode. The electrolyte was prepared using 0.01 M $TBAPF_6$ and 40 µl DI water in 80 ml Acetonitrile. Before testing, the electrolyte was bubbling with CO_2 for 15 min, and then immerse the photocathodes into the electrolyte. The light source was a LED torch with the tested light intensity of about 4.13 mW cm^{-2}. For Linear Sweep Voltammetry (LSV) scanning, I set the scan range from 0.5 V to -0.8 V vs. $E_{Ag/AgCl}$, with the scan rate of 0.01 V s^{-1} and chop the illuminated light every 5 s. Electrochemical impedance spectroscopy (EIS) was carried out with a frequency range of 1000 kHz to 1 Hz on the 3-electrode configuration in the dark.

3.3 Results and discussions

To acquire compact $CsPbBr_3$ thin films, I applied the two-step spin-coating method, as shown in **Figure 3 - 1**.[193] As descripted in the experimental section, I first spin-coated $PbBr_2$ films, and then spin-coated the CsBr-based precursor solutions for four times and added Fluorine or Nafion in the CsBr solution to obtain CPB-F and CPB-N films. Spin-coating the CsBr components four times can get the best crystallization in comparison to spin-coat it three times or five times, which is also verified in Duan's work.[193]

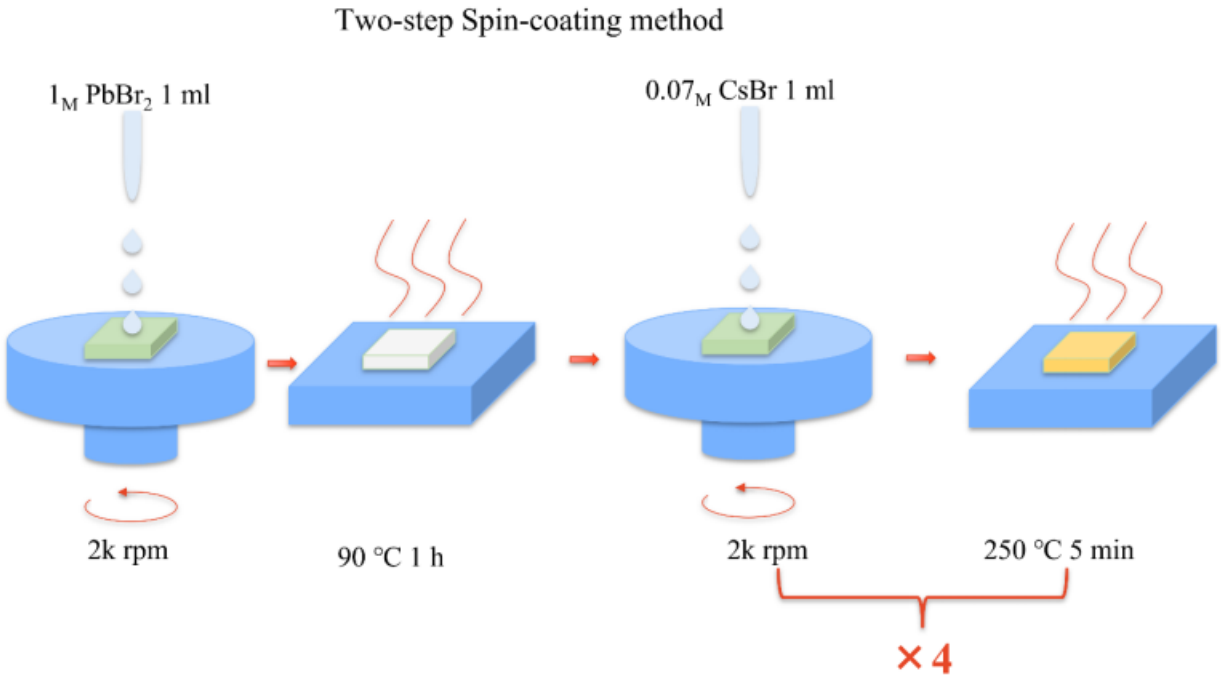

Figure 3 - 1 Schematic illustration of the two-step spin-coating method to synthesize $CsPbBr_3$-based photocathodes.

3.3.1 Light response enhancement by F-doping

Fluorine (F) doping strategy in improving the photocatalysis performance has been reported in various active materials, such as TiO_2, $SrTiO_3$, Bi_2WO_4, g-C_3N_4, due to their high electronegativity, excellent ability to improve photo-reactivity, and strong complexation with other materials.[194-198] We added 5% NH_4F in CsBr precursor when spin-coating the F-dopped $CsPbBr_3$ thin films (CPB-F). The top-view and cross-section scanning electron microscopy (SEM) images of the as-prepared $CsPbBr_3$ thin films (CPB) and CPB-F thin films are shown in **Figure 3 - 2**a-c, respectively. The thin films are compact with almost no pinholes and present the thickness of about 400 ~ 500 nm. There is no significant change in morphology after doping F ions in CPB. From the XRD pattern illustrated in **Figure 3 - 2**d, the CPB exhibits an orthorhombic phase (mp-567629, Pnma, 62) and the low dose of F-doping did not change the crystal structure. Due to the strong XRD signal from the FTO substrate, we only marked the position of orthorhombic $CsPbBr_3$ peaks.

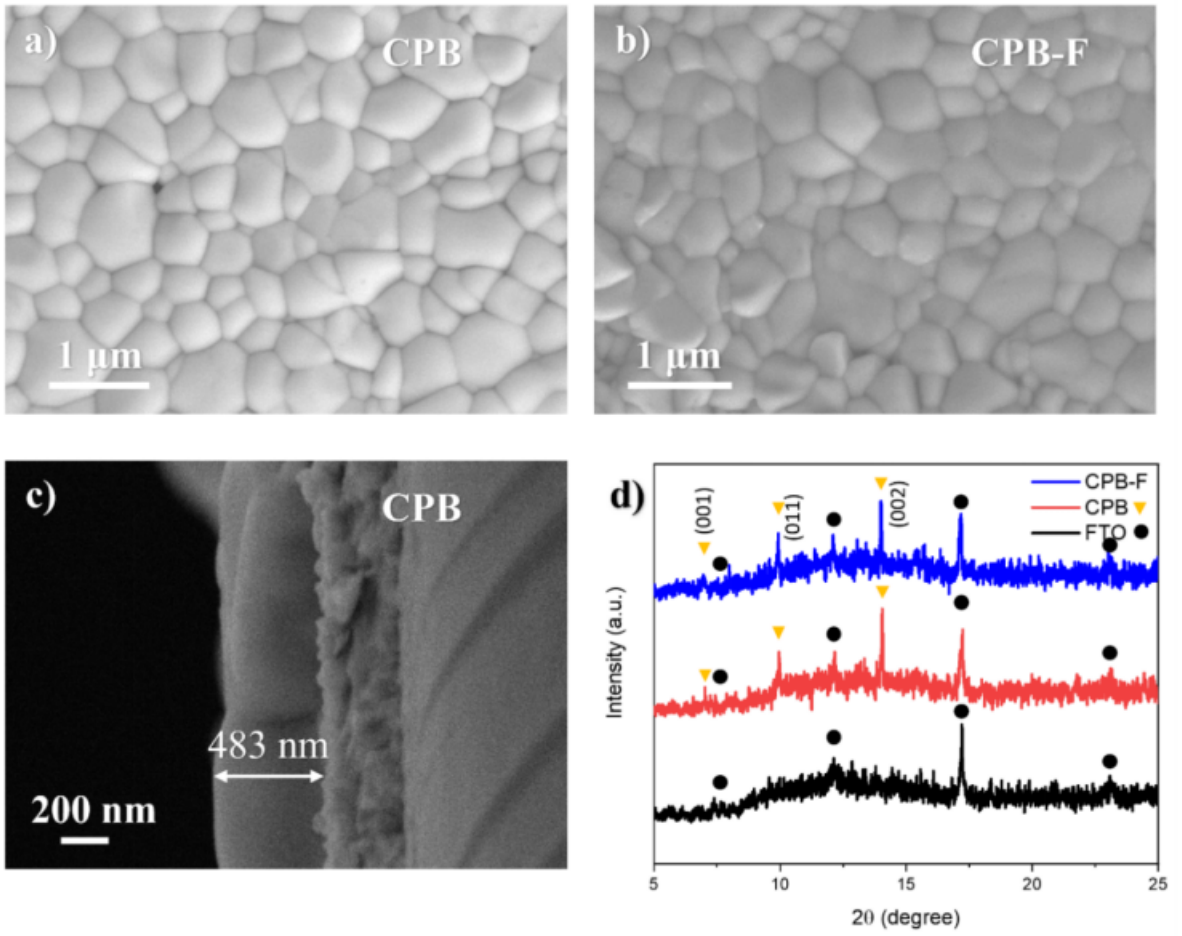

Figure 3 - 2. Top-view SEM images of a) CPB and b) CPB-F thin films on FTO/glass substrates. c) Cross-section SEM image of CPB thin film. d) XRD patterns of FTO/glass substrate, as well as CPB and CPB-F thin films grown on FTO/glass substrates.

To further confirm the composition of as-synthesized thin-film catalysts, the XPS spectra of as-synthesized catalysts were recorded, which can provide us with the information of chemical interaction and electron transfer.[199] Before the XPS tests, I scraped our samples from the FTO substrates and sticked them on carbon tapes. The XPS survey of the CPB and CPB-F sample is illustrated in **Figure 3 - 3**. To gain the detailed information, I analyzed the XPS of each element of the samples. It is pointed out that, compared with the pristine CPB, the CPB-F sample exhibited an obvious F peak. As shown in **Figure 3 - 4**a-c, the high-resolution XPS spectra of both CPB and CPB-F films clearly display the signals of Cs 3d, Pb 4f, and Br 3d elements. The additional F 1s signal in **Figure 3 - 4**d for CPB-F film illustrates the successful doping of F in CPB film. Moreover, compared with the pristine CPB film, Cs

$3d_{3/2}$ and $3d_{5/2}$ peaks, Pb $4f_{5/2}$ and $4f_{7/2}$ peaks, and Br $3d_{3/2}$ and $3d_{5/2}$ peaks of CPB-F film shift to the higher binding energy, indicating the stronger interactions between $CsPbBr_3$ elements after the F-doping, due to the lattice contraction and the redistribution of electron cloud density.[200] The atomic percentage of F doped in CPB-F can be calculated from XPS survey, which is about 0.72%, as shown in **Table 3 - 1**.

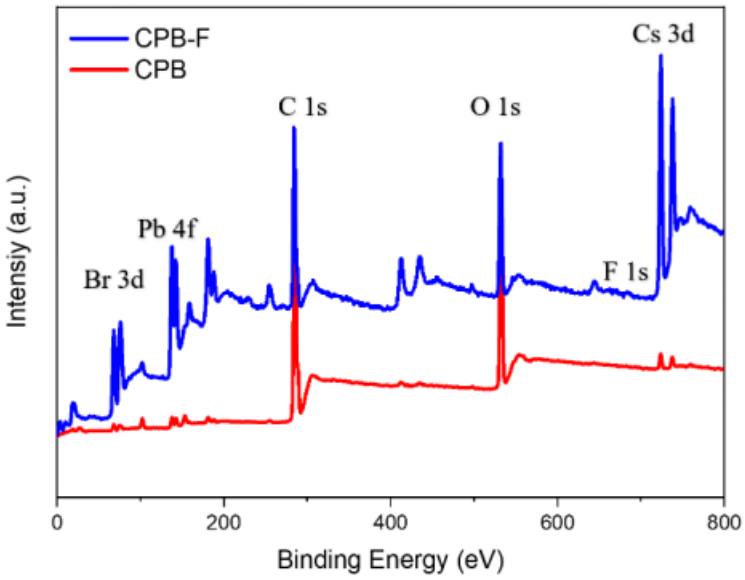

Figure 3 - 3 XPS survey of CPB and CPB-F thin films.

I further tested the UV-vis light absorption properties of both CPB and CPB-F films. As shown in **Figure 3 - 4**e, the absorption edge of CPB-F at 517.8 nm is blue-shifted in comparison to that of CPB film at 518.1 nm. The calculated Tauc plots also show a higher bandgap of CPB-F film (2.26 eV) than that of CPB film (2.25 eV). These indicate the F-doping slightly weaken the light absorbing range (or tune the band gap) of CPB.

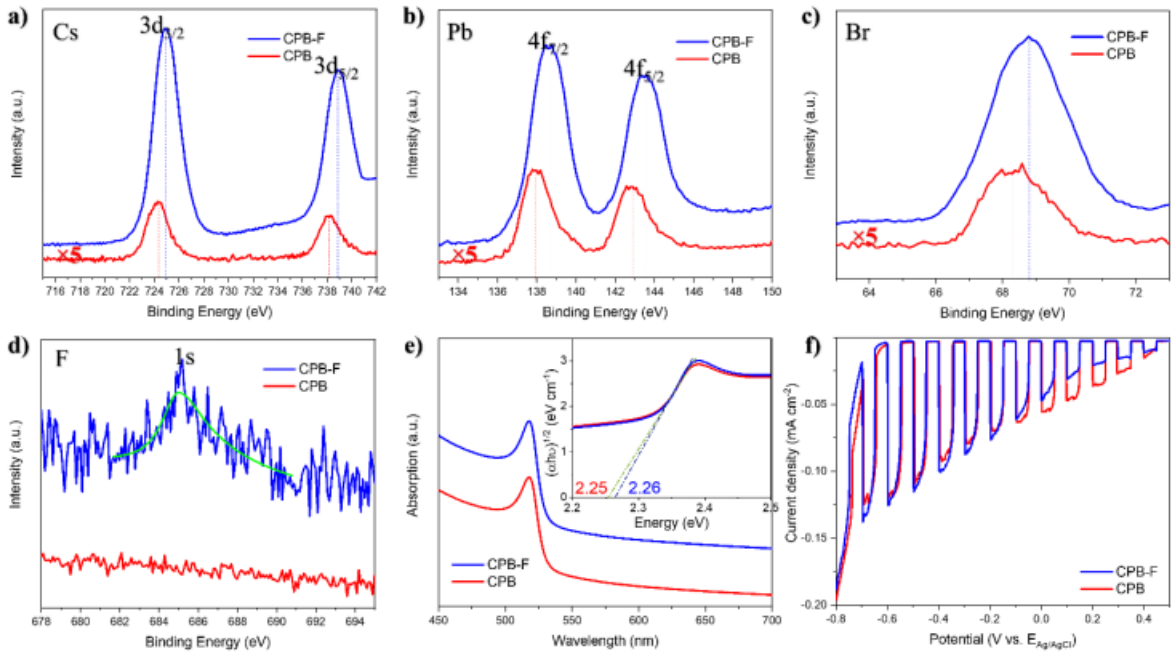

Figure 3 - 4. High-resolution XPS spectra of a) Cs 3d, b) Pb 4f, c) Br 3d and d) F 1s (and fitted curve) of both CPB and CPB-F thin films. e) UV-vis absorption spectra and Tauc plots of CPB and CPB-F thin films. f) LSV curves of CPB and CPB-F photocathodes.

Table 3 - 1. The calculated atomic percentage of F, Pb, Cs and Br of CPB-F by XPS survey.

Element	Peak binding energy (eV)	FWHM (eV)	Area (CPS.eV)	Atomic%
F 1s	685.17	4.30	5332.96	0.72
Pb 4f	137.54	2.12	1196517.91	13.38
Cs 3d	723.97	3.42	1371237.01	26.95
Br 3d	68.04	3.34	446274.34	58.95

I then compared the charge-transport properties of the photoelectrodes by performing the space-charge-limited current (SCLC) measurements in the dark condition.[201-203] There are normally three regions in the measured SCLC curve; at the intermediate voltages, the *I-V* curve has the slop larger than 2 in the log coordinate system, in which all the available trap

states were filled by the injected carriers. The voltage started the trap filled region can be called trap-fill limit voltage V_{TFL}, which is proportional to the trap density n_{trap} according to the equation:

$$n_{traps}=2\varepsilon\varepsilon_0 V_{\mathrm{TFL}}/ed^2 \quad (3.1)$$

where ε is the dielectric constant of the photoelectrode material, ε_0 is the vacuum permittivity, e means the electronic charge and d is the thickness of the material. From **Figure 3 - 5**, the V_{TFL} of CPB thin film is 1.39 V and that of CPB-F thin film is 1.22 V, indicating the less trap densities in the perovskite after doping Fluorine.

Instead of using a general strong sunlight simulator as the light source with a light intensity of 100 mW cm^{-2},[10] I used a light-emitting diode (LED) light as the light source, which could easily be found in daily life. When we keep the particular distance between the photocathode and the light source, the effective light intensity is about 4.13 mW cm^{-2}. As shown in the linear sweep voltammetry (LSV) curve in **Figure 3 - 4**f, when applying the positive voltage and low negative voltage, the photocurrent density of CPB thin film is higher than CPB-F thin film; when applying the higher negative voltage, the CPB-F film exhibits similar but slightly higher photocurrent density than that of CPB thin film due to the very low rate of F-doping. The highest photocurrent of -0.12 mA cm^{-2} of CPB-F thin film was obtained when applying a -0.6 V vs $E_{Ag/AgCl}$, and that of CPB was -0.11 mA cm^{-2}. If the applied voltage is lower than -0.7 V vs $E_{Ag/AgCl}$, the photocathode is trended to be damaged. Simply doping F into $CsPbBr_3$ increases the chemical interaction and reduces the trap density of the perovskite with little sacrifice of light absorbing ability, and the photo-response is almost the same as that of pure CPB, so I added Au layer to enhance the photocurrent of our photocathode.

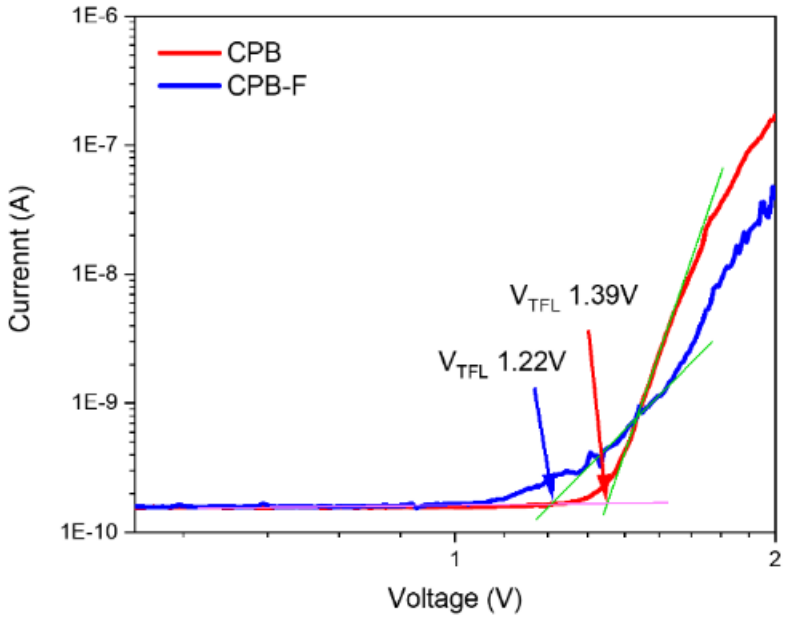

Figure 3 - 5. SCLC behavior of the CPB and CPB-F thin films.

3.3.2 Schottky heterojunction by Au-coating

The Schottky junctions created by the metal-semiconductor structures can prohibit photo-induced charge carrier recombination in the related devices.[204] I sputter-coated a 15 nm Au layer on the top of the CPB and CPB-F thin films and marked them as CPB-AU and CPB-F-AU, respectively. The *I-V* characteristic of CPB-AU, as shown in **Figure 3 - 6**, indicates the p-type Schottky heterojunction formed between CPB and Au.[205] The XRD patterns of CPB-AU and CPB-F-AU are shown in **Figure 3 - 7**, and Au signals (square marks) indicate successful Au-coating on CPB and CPB-F films. From the SEM images as shown in **Figure 3 - 8**a,b, it could be seen that the Au layer is rough and not too thick, from which I can be still found that there are the grain boundaries on the surfaces of both thin films. In comparison with CPB thin films, the Au-coated samples exhibit much larger photocurrent density in the tested potential window in LSV tests, confirming the formation of Schottky junction. However, when the applied voltage is negative, the Au-coated samples also exhibit higher dark current with obvious capacity current, so the retained photo-response of CPB-AU is similar to that of CPB, and this major issue does not help achieve enhanced PEC performance of the electrode, so, we applied Nafion component to the photocathode.

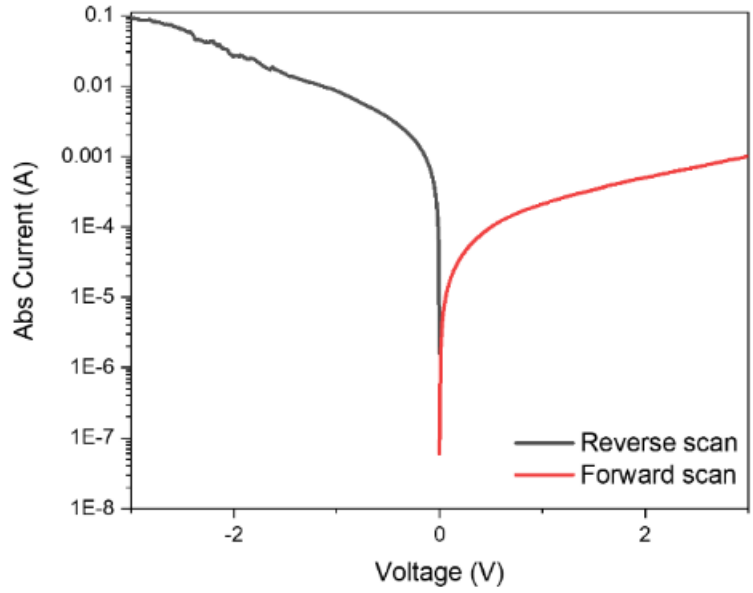

Figure 3 - 6. *I-V* characteristic of CPB-AU, red line is Forward scan from 0 V to 3 V and the black line is Reverse scan from 0 V to -3 V.

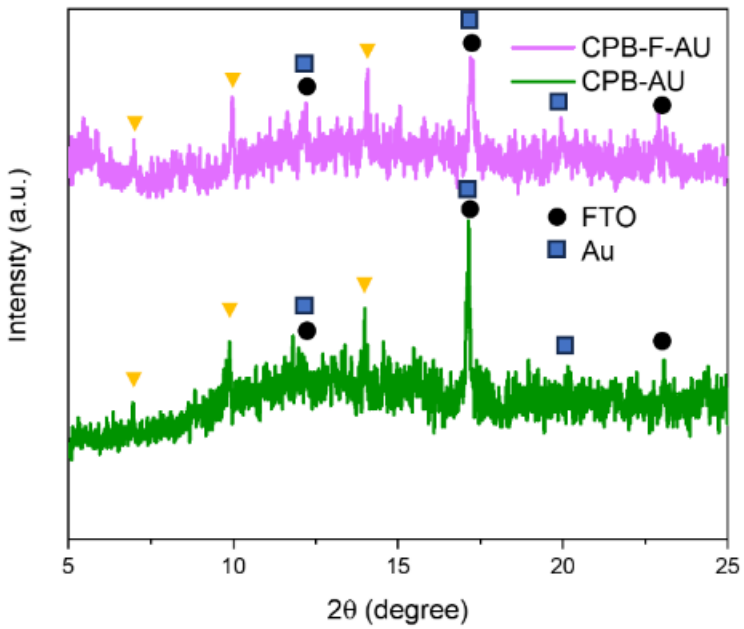

Figure 3 - 7. XRD patterns of CPB-AU and CPB-F-AU thin films.

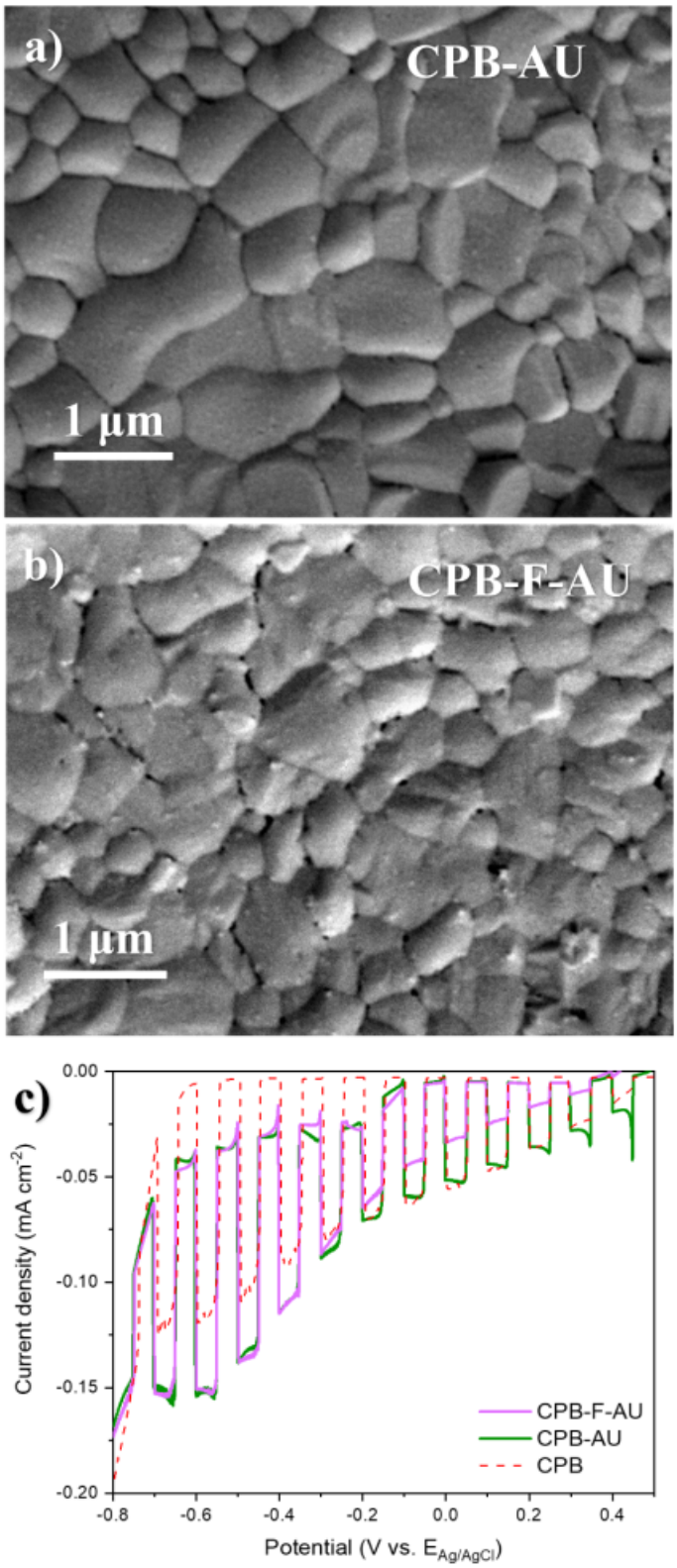

Figure 3 - 8. SEM images of a) CPB-AU and b) CPB-F-AU. c) LSV curves of CPB, CPB-AU, and CPB-F-AU photocathodes.

3.3.3 Surface-passivation by Nafion component

The organic component in Nafion can strongly couple with inorganic components of CPB and change their band structure, and passivate the surface of the photoelectrodes to reduce the surface trap states.[192] To further enhance the PEC performance of CPB, we added Nafion into CPB thin films to obtain CPB-N, by mixing 100 µl 5% Nafion solution in CsBr precursor, spin-coating CsBr for 3 times, and CsBr-Nafion for the last time. We also combined Nafion with F-doping and Au-coating CPB thin films, and the obtained samples were named as CPB-N-AU, CPB-F-N, and CPB-F-N-AU, respectively. As shown in **Figure 3 - 9**a,b, Nafion is partially covered on the top of CPB films. We also characterized the CPB-N by conducting the high-resolution TEM, HAADF, and EDS measurements, and the results are shown in **Figure 3 - 10** and **Figure 3 - 11**. We found that the Nafion component partially covered the perovskite surface. XRD of CPB-N is shown in **Figure 3 - 12**, which indicates that Nafion does not change the crystal structure of $CsPbBr_3$.

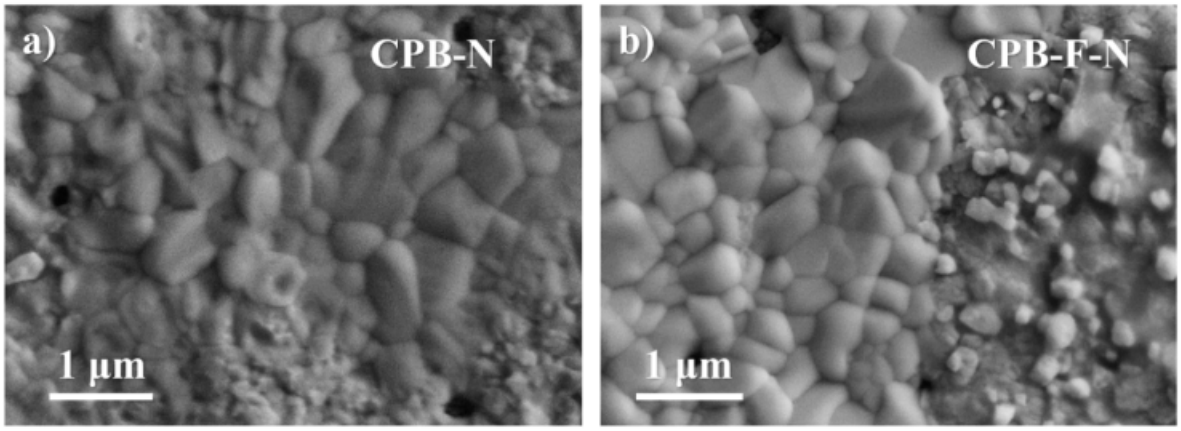

Figure 3 - 9. Top-view SEM images of a) CPB-N and b) CPB-F-N thin films.

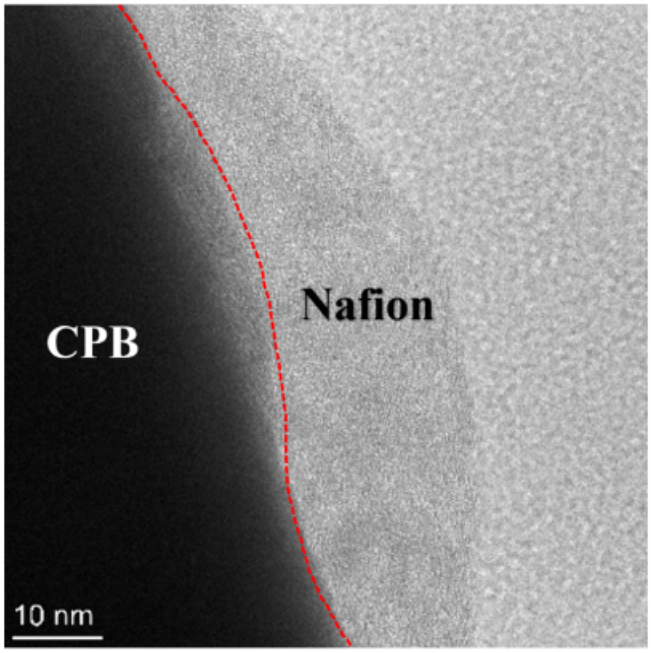

Figure 3 - 10. High-resolution TEM image of CPB-N. The darker part is CPB, and the brighter part is amorphous Nafion.

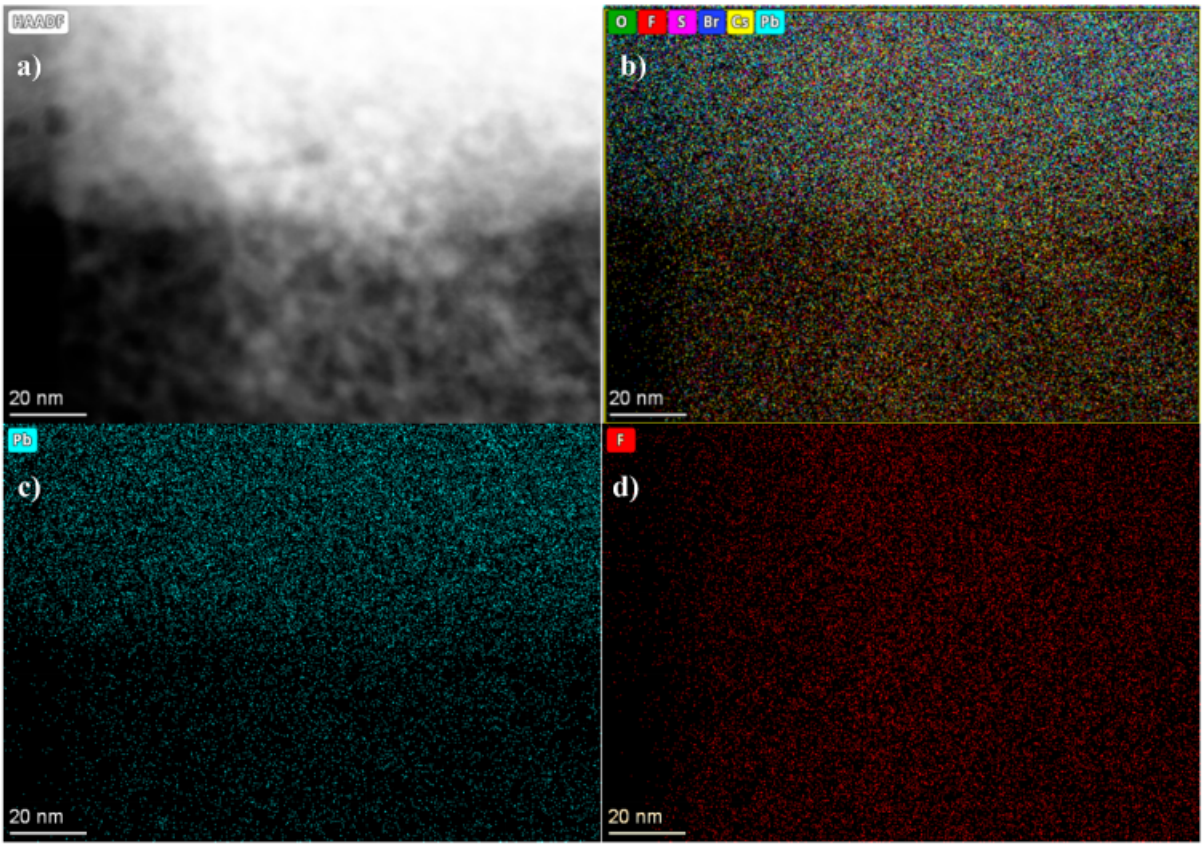

Figure 3 - 11. a) HAADF image, and b-d) related EDS image of CPB-N, which are acquired

on Spectra 60-300 S/TEM under 300 kV.

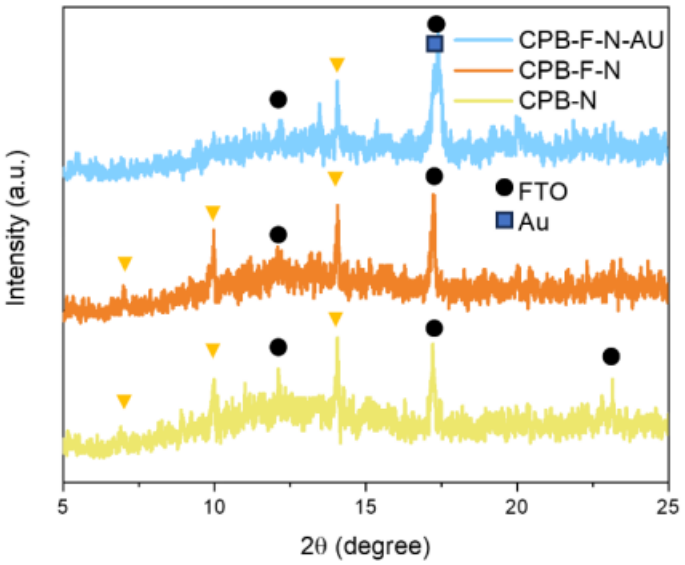

Figure 3 - 12. XRD of CPB-N, CPB-N-AU, and CPB-F-N-AU thin films.

We also compared the high-resolution XPS spectra of both the CPB-N and CPB-F-N thin films with the pure CPB thin film, which are shown in **Figure 3 - 13**a-d, while the XPS survey of both the CPB-N and CPB-F-N thin films are illustrated in **Figure 3 - 14**. Compared with CPB and CPB-F films, the addition of Nafion leads to the shift of Cs 3d, Pb 4f, and Br 3d peaks in CPB to lower the binding energy in the obtained CPB-N film, while the F component in the films with Nafion results in the shift of F 1s from 685.1 eV in CPB-F to 688.9 eV in the obtained CPB-F-N thin films. The shifts of elements in XPS indicate that a built-in electric field (BIEF) has been formed at the perovskite/Nafion interface.[199] The XPS peaks of Cs, Pb and Br in CPB-N contain peaks at original binding energy position and shifted binding energy position, which can be explained by Nafion partially covered the surface of CPB component (**Figure 3 - 9**b). Additionally, the introduction of F element in CPB-F-N induces peaks of all four elements shift to higher binding energy, indicating enhanced interactions between CPB-F-N elements. I also compared the SCLC behavior of CPB, CPB-N and CPB-F-N thin films, as shown in **Figure 3 - 15**. The V_{TFL} of CPB-N and CPB-F-N thin films are 1.28 V and 0.97 V, respectively, indicating the passivation of Nafion and F-doping on $CsPbBr_3$ can further reduce the trap density of the photocathode. From the UV-vis absorption curves (**Figure 3 - 13**e) and the calculated Tauc plot, Nafion can tune the bandgap of the modified CPB and CPB-F films to 2.24 eV, indicating an increased light-

absorbing range. However, the high resistance of the added Nafion impedes the photo-generated charge carriers in the perovskites being transferred to the electrolyte, resulting in the decreased photocurrent of -0.07 mA cm^{-2} for both CPB-N and CPB-F-N devices, as shown in **Figure 3** - **13**f. So, I further modified our photocathodes by combining the F element, Nafion component, and Au layer together.

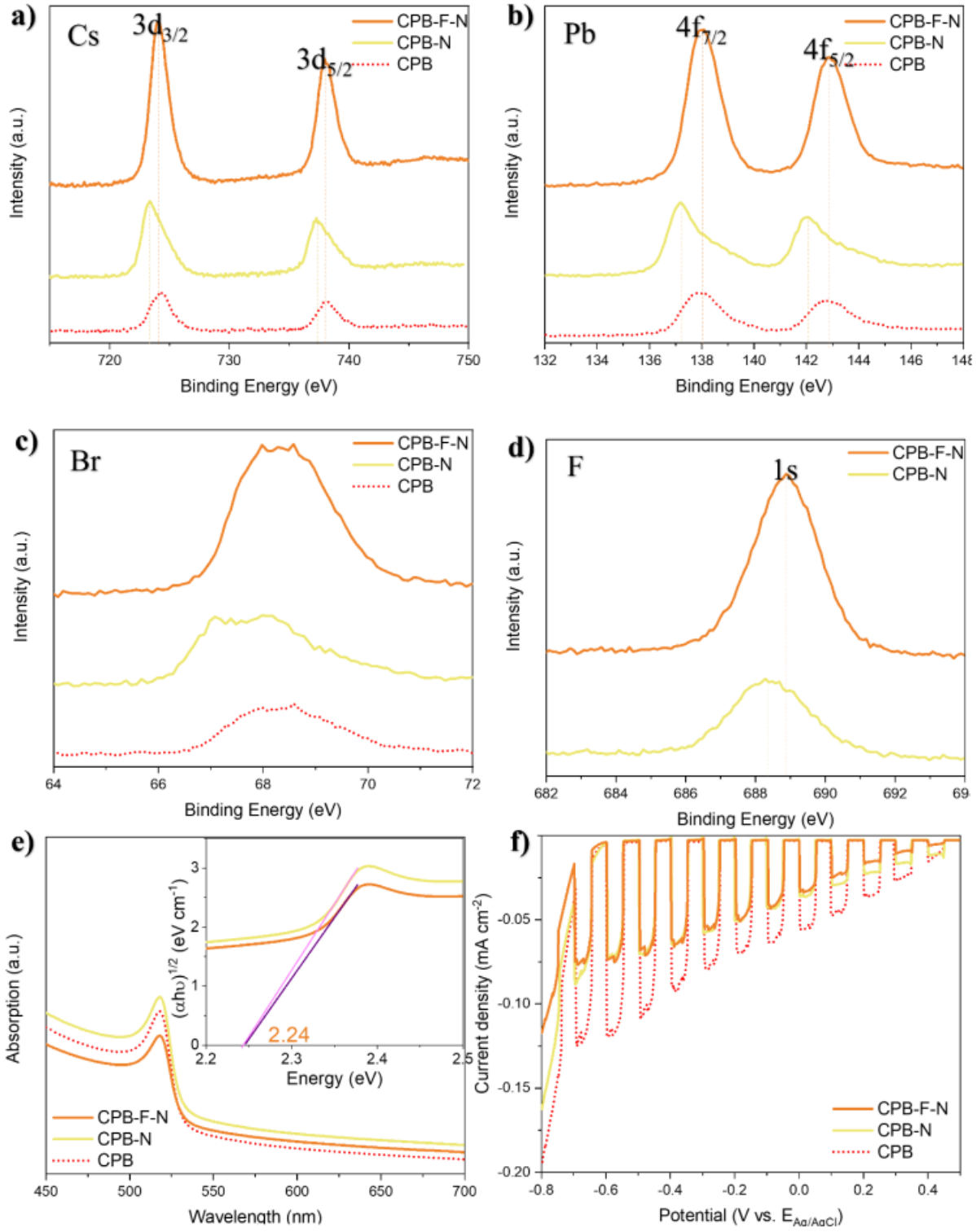

Figure 3 - 13. High-resolution XPS spectra of a) Cs 3d, b) Pb 4f, c) Br 3d, and d) F 1s of CPB, CPB-N, and CPB-F-N thin films. e) UV-vis absorption spectra and Tauc plots of CPB-N and CPB-F-N thin films. f) LSV curves of CPB, CPB-N, and CPB-F-N photocathodes.

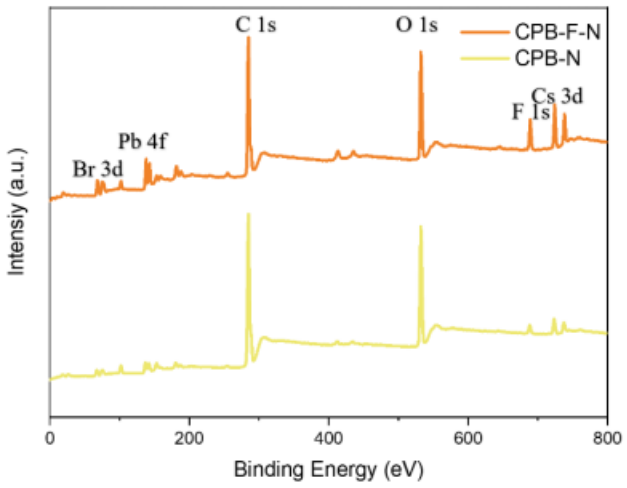

Figure 3 - 14. XPS survey of CPB-N and CPB-F-N.

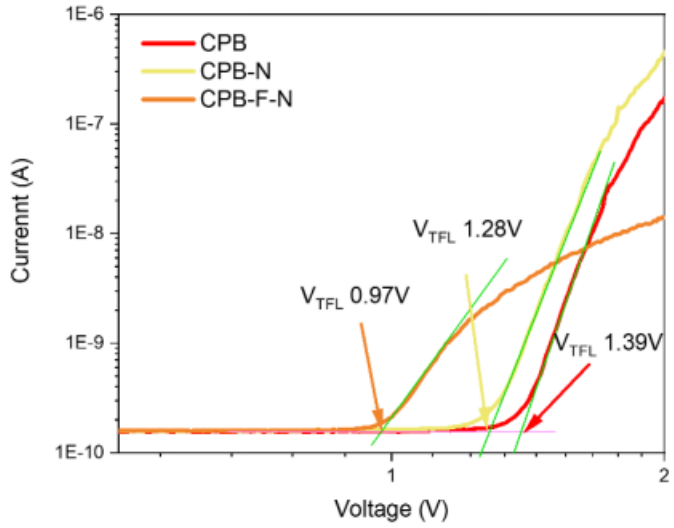

Figure 3 - 15. SCLC behavior of the CPB, CPB-N and CPB-F-N thin films.

3.3.4 Synergistic effect of F-doping, Nafion, and Au-coating

The PEC performance of photocathodes is determined by a series of key parameters, including the light-absorbing ability, the charge transfer ability, and the reactive sites.[206] As demonstrated in the above sections, employing F-doping, Nafion, and Au-coating, separately, can improve some particular aspect(s) of CPB samples and the related devices, but the individually applied method could also hinder the device performance, like may decrease the photocurrent density of the photocathodes. So, I thus applied F-doping, Nafion, and Au-coating methods together (leading to the CPB-F-N-AU thin films), as shown in **Figure 3** -

16a,b. In detail, the Au layer is uniformly coated on the thin film and does not contact the FTO substrate through the grain boundaries of the CPB film. I also compared their charge carrier transfer efficiencies by characterizing the time-resolved photoluminescence spectra (TRPL), as shown in **Figure 3** - **16**c. A bi-exponential decay model is applied to fit the TRPL curves, with the equation of:[207]

$$\Delta A_{decay} = A_1 e^{-\frac{t}{\tau_1}} + A_2 e^{-\frac{t}{\tau_2}} + \Delta A_0 \quad (3.2)$$

Where A_1 and A_2 are amplitudes, and τ_1 and τ_2 are fast and slow decay lifetimes, respectively. The calculated average carrier lifetime (τ_{ave}) is based on the following equation:

$$\tau_{ave} = \frac{A_1\tau_1^2 + A_2\tau_2^2}{A_1\tau_1 + A_2\tau_2} \quad (3.3)$$

All the obtained parameters fitted from TRPL are listed in **Table 3** - **2**. As compared to the high lifetime of 3.38 ns in pristine CPB caused by the charge recombination, F-doping can enhance the charge transfer efficiency of the modified CPB.[208] The Nafion layer hindered the charge transfer from the perovskite to the electrolyte, which increased τ_{ave} and charge recombination and thus decreased the photocurrent of the related devices (**Figure 3** - **13**f). However, the Schottky junction formed between perovskite and Au layer and the doping of F ions help the separation of Nafion-hindered photo-generated charge carriers and provide an additional pathway for electron transfer from CPB to Au, resulting in the shortest τ_{ave} of 3.12 ns in CPB-F-N-AU, which is consistent with the findings as shown in **Figure 3** - **16**d.[209] When applied -0.5 V vs $E_{Ag/AgCl}$, the photocurrent of CPB-N-AU is -0.18 mA cm^{-2}, and that of CPB-F-N-AU is -0.23 mA cm^{-2}, which are twice of that of the pristine CPB. At the same time, in comparison to the CPB-AU, the Nafion component also eliminates the capacitive current and reduces the dark current introduced by Au.

Table 3 - **2.** The parameters related to lifetimes fitted from the TRPL curves of CPB, CPB-F, CPB-N, CPB-F-N, and CPB-F-N-AU photocathodes.

Sample	τ_1 (ns)	τ_2 (ns)	τ_{ave} (ns)
CPB	4.40	0.80	3.38

CPB-F	4.10	1.00	3.26
CPB-N	5.00	1.06	3.99
CPB-F-N	4.90	1.13	3.86
CPB-F-N-AU	4.00	0.94	3.12

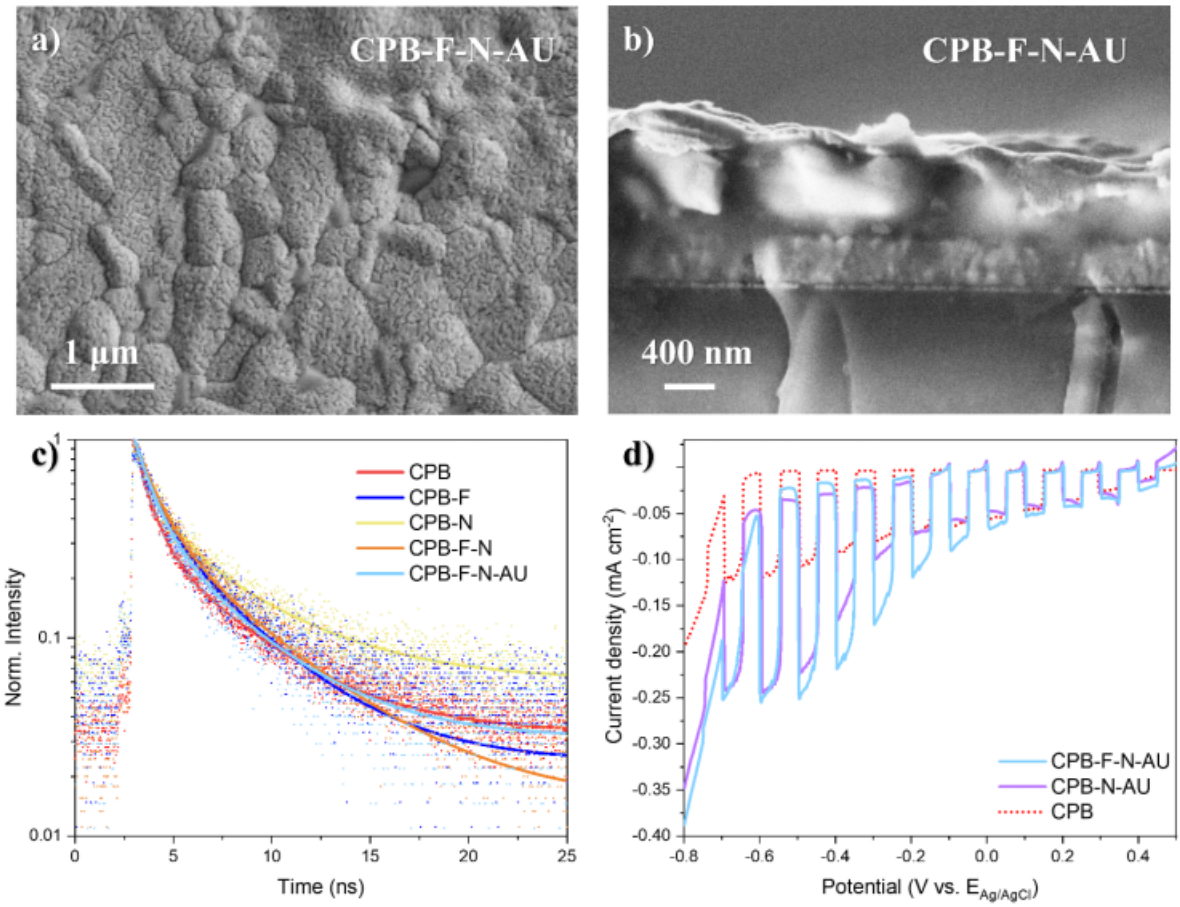

Figure 3 - 16. a) SEM image of CPB-F-N-AU. b) Cross-section SEM image of CPB-F-N-AU. c) TRPL curves of CPB, CPB-F, CPB-N, CPB-F-N, and CPB-F-N-AU photocathodes. d) LSV curves of CPB, CPB-N-AU, and CPB-F-N-AU photocathodes.

Additionally, I also tested the Nyquist plots under -0.5 V applied voltage in the dark in **Figure 3 - 17**. In the equivalent circuit diagram, R_s indicates the series resistance, CPE_{bulk} and R_{bulk} are related to the electron transport in the bulk and in the space charge, and CPE_2 and R_{ct} represent the charge transfer from the catalyst to the electrolyte.[210-211] The fitted parameters are shown in **Table 3 - 3**, from which I can find that CPB has the charge transfer resistance R_{ct} of 13457 Ω, the CPB-N exhibits the highest R_{ct} of 138230 Ω, and the Au-coated CPB-AU

has the smallest R_{ct} of 9387 Ω. The findings are in good consistency with our previous testing results.

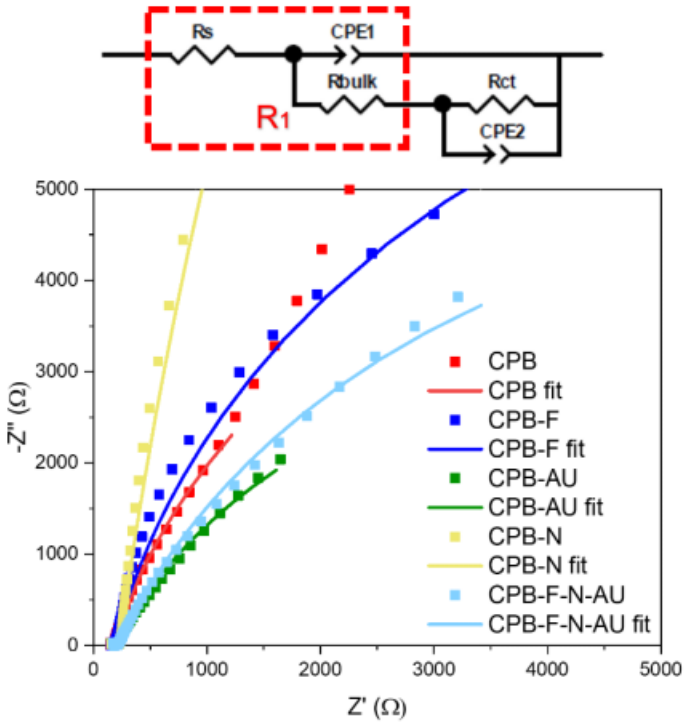

Figure 3 - 17. The equivalent circuit diagram (upper) and the Nyquist plots of CPB, CPB-F, CPB-AU, CPB-N, and CPB-F-N-AU (lower). Since we mainly focus on the R_{ct}, we simplified the equivalent circuit of R_s, CPE_1 and R_{bulk} to R_1.

Table 3 - 3. The fitted parameters of Nyquist plots of CPB, CPB-F, CPB-AU, CPB-N, and CPB-F-N-AU.

	R1 (Ω)	*Error%*	*Rct* (Ω)	*Error%*	*CPE2-T* (F)	*Error%*	*CPE2-P* (F)	*Error%*
CPB	175.4	0.43222	13457	6.9796	4.94E-06	2.4882	0.84656	0.41435
CPB-F	179.4	2.1123	16913	4.6002	6.75E-07	4.923	0.86871	0.69296
CPB-AU	182.7	0.42541	9387	6.5502	9.27E-06	1.8409	0.74424	0.56831

CPB-N	228.2	0.4784	138230	3.6762	4.03E-06	0.88816	0.93112	0.18553
CPB-F-N-AU	212	0.28953	13423	2.1716	4.00E-05	0.87841	0.77075	0.24707

I also tested the stability of these photocathodes via testing *I-t* curves at the applied voltage of -0.5 V vs $E_{Ag/AgCl}$ and chopped the light source every 5 s (**Figure 3 - 18**). The photocurrent values of the photocathodes are different, but the attenuation trends of the six photoelectrodes are similar. The recycle test of LSV on CPB-F-N-AU was also conducted and shown in **Figure 3 - 19**, and the 4^{th}-recycle LSV curve shows a much-reduced photo-response. I suspected that the water in the Ag/AgCl reference electrode can permeate into the acetonitrile electrolyte, which can decompose the perovskite photoelectrodes, so the stability issue still needs to be further improved in future research.

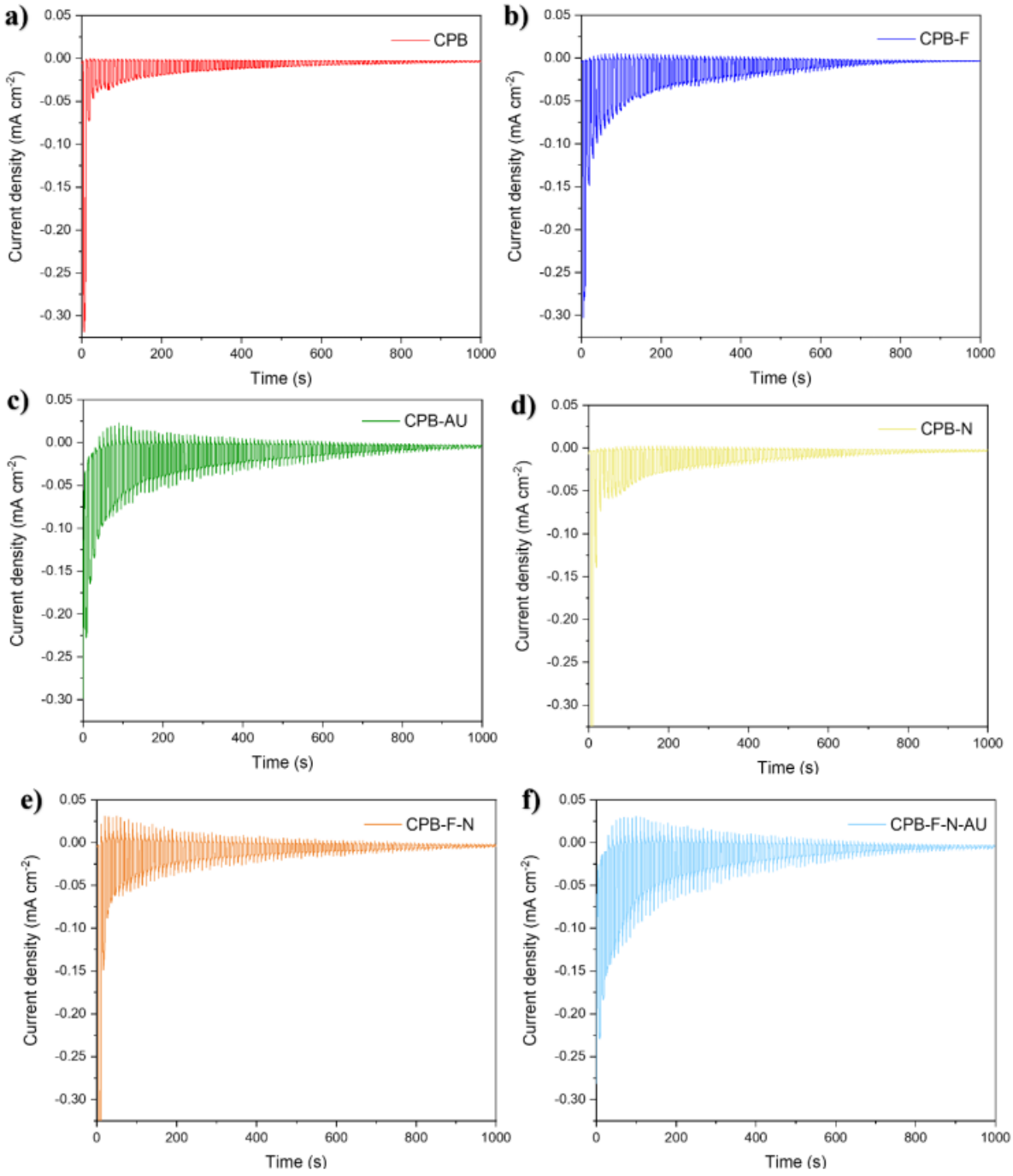

Figure 3 - 18. I-t curves of a) CPB, b) CPB-F, c) CPB-AU, d) CPB-N, e) CPB-F-N, and f) CPB-F-N-AU photocathodes, at -0.5 V vs $E_{Ag/AgCl}$ with chopped light illumination.

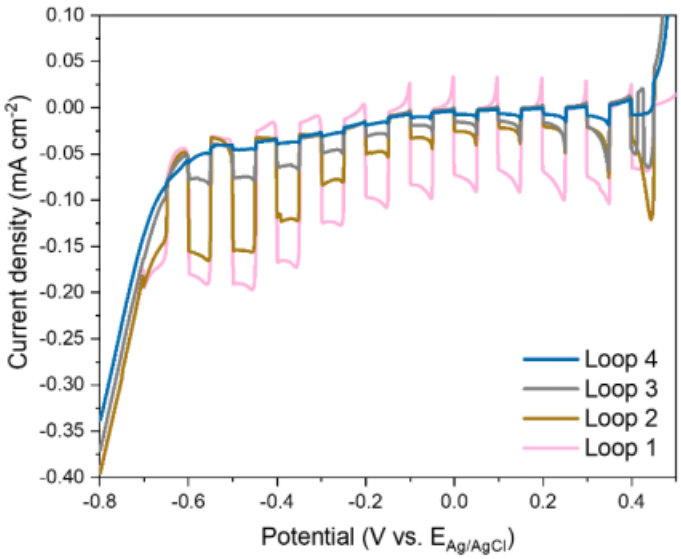

Figure 3 - 19. The recycle test of LSV on CPB-F-N-AU.

In addition, due to the stability issue, the total reaction time cannot provide us sufficient reaction products, so I tested the comparison experiments with the electrolyte purged with CO_2 and Ar, respectively (**Figure 3 - 20**). The obviously increased photocurrent indicates that CO_2 could indeed join in the PEC reduction reaction. I also repeated the LSV tests of all six sets of samples, as shown in **Figure 3 - 21**, which demonstrates good repeatability of our experiments.

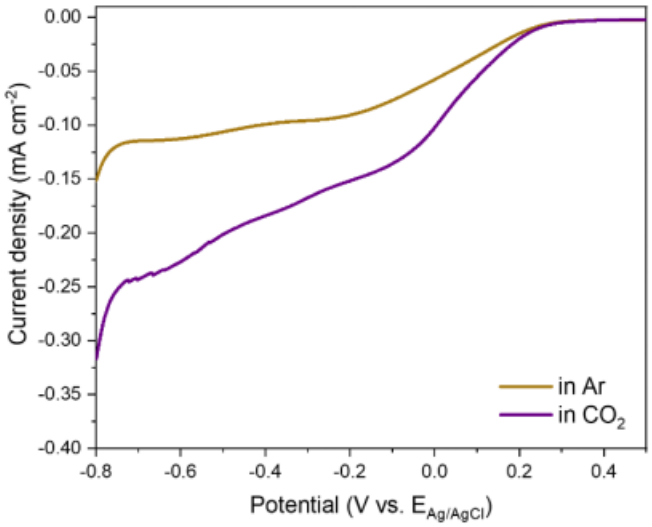

Figure 3 - 20. LSV curve of photocathode in Ar environment and in CO_2 environment.

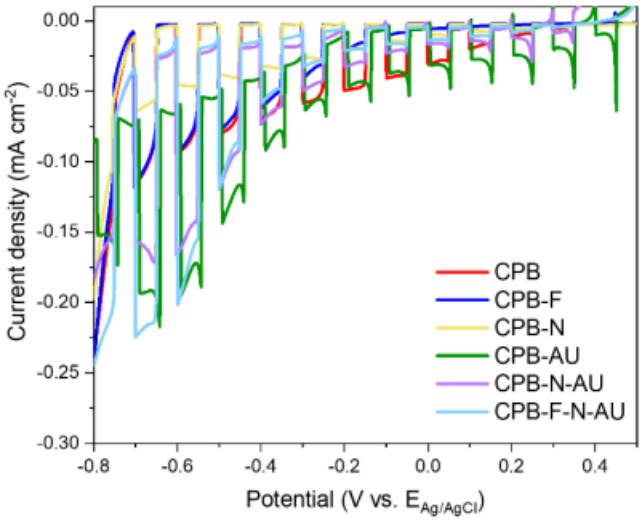

Figure 3 - 21. Repeated LSV tests of CPB, CPB-F, CPB-N, CPB-AU, CPB-N-AU and CPB-F-N-AU.

At last, I tested the valence bands (VB) of CPB, CPB-F-N, and drew the device structure and charge transfer illustration of CPB-F-N-Au, as shown in **Figure 3 - 22**. As shown in **Figure 3 - 22**a and b, with F and Nafion, the VB of CPB-F-N shifts to a more negative energy, with a smaller band gap than CPB, which is easier for CO_2 reduction reaction.[111] The Schottky junction formed between CPB-F-N and Au makes it easier for the transport of electrons and thus facilitates the separation of photo-generated electron-hole pairs.[212] Under light illumination, as shown in **Figure 3 - 22**c, the photo-induced electrons are excited to the conduction band (CB), the photo-induced holes left in VB are transmitted to external circuit through FTO substrate, and the electrons are easily transferred to Au layer due to the band bending formed by the Schottky junction between perovskite and Au, leading to having the reduction reaction of CO_2 at the electrode surface.

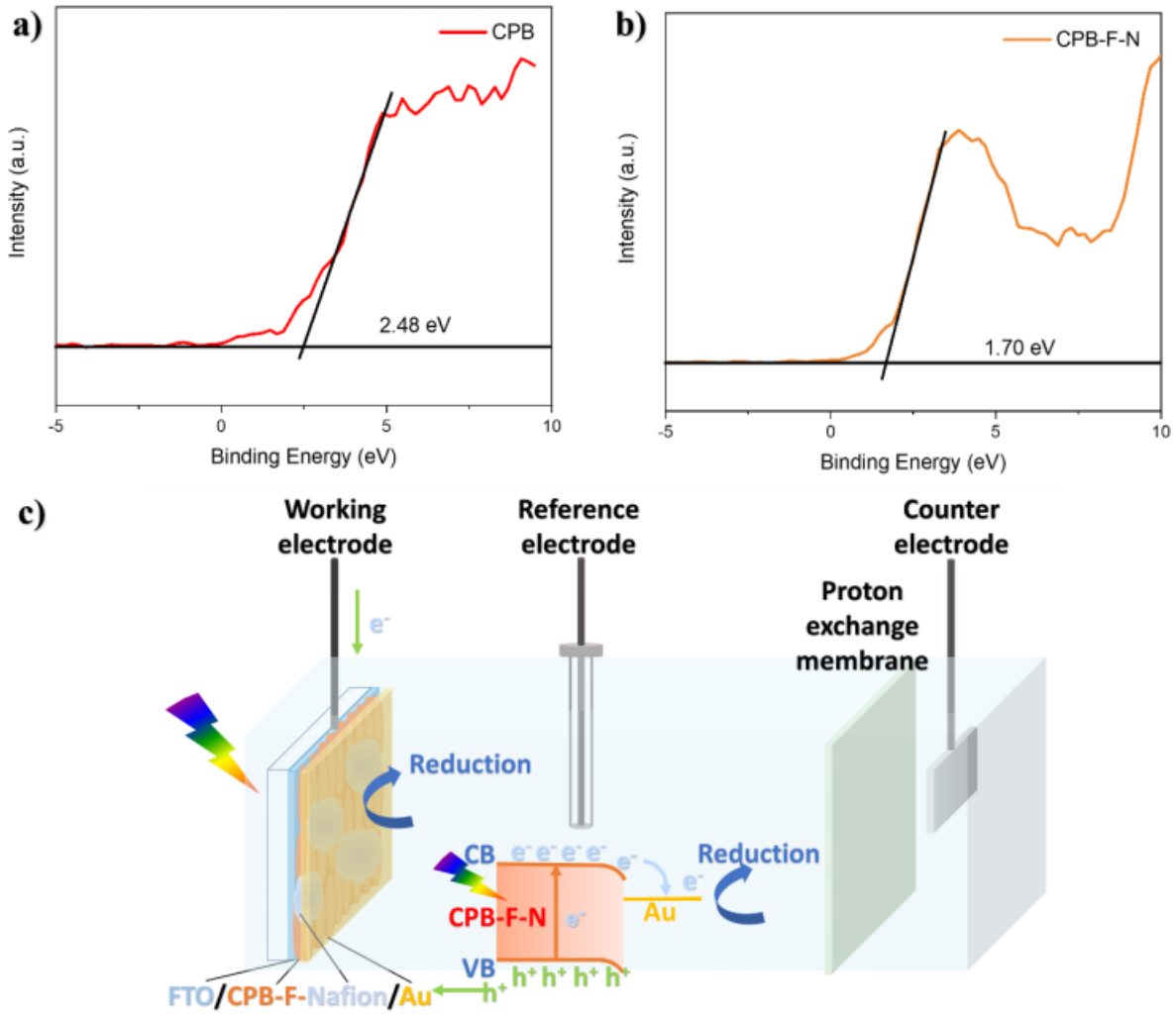

Figure 3 - 22. VB-XPS of a) CPB, b) CPB-F-N, and c) schematic band structure and charge transfer of CPB-F-N-AU.

3.4 Conclusion

In conclusion, to explore the possibility regarding applying halide perovskite-based PEC systems for CO_2 reduction, we utilized rational interface-engineered strategies to prepare the $CsPbBr_3$-based photocathodes by F-doping and sequence Nafion-adding, and Au-coating and systematically investigated their synergic effect on the device performance. It is found that, with F-doping ions in $CsPbBr_3$, the chemical interactions inside the perovskite active layers are enhanced and the trap density of the perovskites are reduced; however, the light absorbing ability is slightly reduced. Meanwhile, the introduction of Nafion tunes the bandgap of the photocathodes and passivate the material surface to further reduce the trap density but impedes charge carrier transfer and thus aggravates charge recombination within the

modified perovskites. Then, due to the formation of Au/$CsPbBr_3$ Schottky-junction, an obviously facilitated separation of photo-induced charge carriers in the resulting perovskite samples can be evidenced, however, the low resistance also introduced high dark current and capacitive current. When synergizing F-doping, Nafion, and Au-coating strategies together, the Au successfully offsets the impedance introduced by Nafion, meanwhile, retains their ability to tune the bandgap of photocathodes and reduce the dark current and the capacitive current, and with the help of F-doping, the chemical interactions within photocathodes are further enhanced. The obtained CPB-F-N-AU device shows the best PEC performance, mainly including the highest photocurrent of -0.23 mA cm^{-2} at a bias of -0.5 V vs $E_{Ag/AgCl}$ under a 4.13 mW cm^{-2} light illumination, which is twice of that of the pristine CPB photocathode. This work demonstrated the practicability of directly applying halide perovskite-based photocathode for CO_2 reduction with high efficiency and stability.

Chapter 4 Copper-Tin Composite Bimetallic Nanoparticles on Bismuth Vanadate Nanoplate Photocathodes for Photoelectrochemical Carbon Dioxide Reduction

Although the heterostructure-modified perovskites showed significantly improved photocurrents, the issue of poor stability cannot be ignored. Therefore, in this Chapter, I introduced Cu and Sn composite nanoparticles, which are known for their high stability properties during PEC CO_2RR.

4.1 Introduction

Carbon dioxide (CO_2) is regarded as the main greenhouse gas and has been increasingly and intensively emitted, due to the huge population and rapid industrial development.[213] Accordingly, seeking renewable energy resources, reducing the production of CO_2, and recycling CO_2 into useful chemicals have been intensively researched for ecologically sustainable development.[129, 214] Enlightened by photosynthesis in nature, photocatalytic (PC) and photoelectrochemically (PEC) CO_2 reduction reactions (CO_2RR) have emerged as the highly economical methods to convert solar energy into chemical energy.[215] In the PC reaction system, reduction reactions and oxidation reactions could happen at the same time on the same photocatalyst, in which it is difficult to separate the reduction products and the possibility of the reoxidation of the product would be increased.[4] In the PEC reaction system, the reduction reactions and the oxidation reactions are separated by the ion-exchange membrane, and they occur on the photoelectrode and the counter electrode, respectively, in which it is much easier to control the reaction procedure and collect the reaction product(s).[4]

Among various metal-based catalysts for CO_2RR, Copper (Cu)-based materials are regarded as the only metal system that can produce hydrocarbons during the reaction with reasonable efficiency, due to their negative adsorption energy to *CO and positive adsorption energy to *H.[52-55] However, the product selectivity of Cu-based catalysts needs to be improved based on the binding strength of reduction intermediates.[52] Cu-based bimetallic catalysts, such as Cu-Pd,[216-218] Cu-Au,[219-221] Cu-Zn,[222-223] Cu-In,[224-226] Cu-Ag,[227-229] have been reported with outstanding selectivity for CO_2RR. As the earth-abundant non-toxic low-cost metal element, Tin (Sn) has also been reported to have the selectivity of format based on its higher O affinity and lower H affinity than Cu.[52] In fact, Cu-Sn alloy catalysts have been widely investigated in the electrochemical CO_2RR, however, it is worth noting that they still haven't been studied for the PEC CO_2RR.[230-233] Moreover, among various oxide semiconductors as the light-

harvesting materials, bismuth vanadate ($BiVO_4$) materials have been widely applied in both the PC and PEC reactions, thanks to their nontoxicity, cost effectiveness, and suitable bandgaps;[234-241] however, they are rarely employed in the PEC photocathode applications.

In this Chapter, I applied $BiVO_4$ nanoplate thin films as the light-harvesting layer and loaded Cu nanoparticles (NPs) and Cu-Sn bimetallic NPs (CuSn NPs) on the surface of the thin films to fabricate the heterostructure photocathodes for the PEC CO_2RR. The systematic characterizations showed that the Cu NPs contain Cu(0) and Cu(II), while the CuSn NPs contain Cu(0), Cu(I), and Sn(IV). Under the negative applied voltage, light-induced electrons transport through band bending of $BiVO_4$ via the tunneling and hopping effects. With depositing the CuSn NPs onto the surface of $BiVO_4$ nanoplate thin films, type-II heterojunctions between CuSn NPs and BiVO4 nanoplates could be formed, which could facilitate the separation and the transfer photo-generated charge carriers. The resulting CuSn NPs@$BiVO_4$ photocathodes exhibit the highest photocurrent of -0.774 mA cm^{-2} at the applied voltage of -0.95 V vs $E_{Ag/AgCl}$, which is more than 3-time higher than that of pristine $BiVO_4$ or Cu NPs@$BiVO_4$.

4.2 Experimental section

4.2.1 Materials

Fluorine-doped tin oxide (FTO) glass (<14.0 Ohms/sq) was purchased from Nippon Sheet Glass Co., Ltd. Bismuth(III) nitrate pentahydrate ($Bi(NO_3)_3{\cdot}5H_2O$, 98%), Ethylenediaminetetra-acetic acid (EDTA, 99%), Ammonium hydroxide solution (30-33% NH_4 in H_2O), Copper(II) acetylacetonate ($Cu(acac)_2$, ≥99.9%), Oleylamine (70%), toluene (for analysis), methanol (for liquid chromatography), and Potassium bicarbonate ($KHCO_3$, 99.7%) were purchased from Sigma-Aldrich P/L. Ammonium metavanadate LR (H_4NO_3V, 98%) and Tin(II) chloride dihydrate AR ($SnCl_2{\cdot}2H_2O$, 98.0%) were purchased from ChemSupply Australia. The 704 fixed high-temperature resistant silicon rubber insulated sealing was purchased from Hong Yue, China. All the chemicals were used as received without further purification.

4.2.2 Preparation of photocathodes:

$BiVO_4$ seed films were prepared using spin-coating method.[242] The FTO/glass substrates were washed with deionized (DI) water, ethanol, and acetone in an ultrasonic machine for 10

min, respectively. Well-mixed 1 mmol $Bi(NO_3)_3 \cdot 5H_2O$ and 1.5 mmol EDTA in 15 ml DI water with 1 ml ammonium water, I labelled the solution as precursor solution A. Well-mixed 1 mmol H_4NO_3V and 0.5 mmol EDTA in 15 ml DI water with 1 ml ammonium water, I labelled the solution as precursor solution B. Next, the precursor solution B was added to the precursor solution A to form the spin-coating solution. Then, 1 ml solution was spin-coated on FTO substrate at low spin-coating speed and was calcined at 500 °C for 5 min. The spin-coat-and-calcine procedure was repeated for 3 times, and then the fresh samples were annealed at 500 °C for 1 h.

$BiVO_4$ thin films were synthesized using a hydrothermal method.[242] I mixed 0.6 mmol $Bi(NO_3)_3 \cdot 5H_2O$ and 0.9 mmol EDTA in a 30-ml DI water with a 3-ml 1 $_M$ NaOH and stirred the solution until it turned clear and transparent. Then a 0.6-mmol H_4NO_3V was added into the solution and was stirred to yellow and transparent. The as-prepared solution was added into a 50-ml autoclave with a 2.5 cm × 2 cm $BiVO_4$ seed film facing down. Thereafter, I heated the autoclave at 180 °C for 6 h. The $BiVO_4$ films were further calcined at 500 °C for 4 h.

Cu NPs and CuSn NPs were synthesized according to the previously reported synthesis method.[243] I first pre-heated a 10-ml oleylamine in a round-bottom flask with an oil bath at 180 °C and then added a 0.2-mmol $Cu(acac)_2$ into the flask under stirring. For CuSn NPs, I further added a 0.1-mmol $SnCl_2 \cdot 2H_2O$ after adding $Cu(acac)_2$ for 1 min. The flask was kept at 180 °C for 1 h. After the solution was cooled to room temperature, the NPs were washed and centrifuged with a 5-ml toluene and a 15-ml methanol mixture 3 times and were dispersed in a 10-ml toluene.

The $BiVO_4$ with Cu/CuSn NPs photocathodes were fabricated by removing unwanted $BiVO_4$ and exposing FTO substrates on the $BiVO_4$ nanoplate thin films, with 1 cm × 1 cm $BiVO_4$ area left. I then dropped a 50-µl NPs solvent on the thin films and heated the samples in an Ar atmosphere at 200 °C for 1 h. Next, I encapsulated the exposed FTO area with the 704-silicon rubber insulated sealing. Before the PEC testing and the characterization of the photocathodes, I washed the surface with 1 ml methanol, 1 ml ethanol, and DI water.

4.2.3 Characterizations:

The samples were characterized by using a scanning electron microscope (SEM) Zeiss Sigma

HD for SEM imaging and a transmission electron microscopy (TEM) FEI Themis-Z Double-corrected TEM for high-resolution TEM (HRTEM) imaging, aberration-corrected high-angle annular dark-field scanning TEM (HAADF-STEM) imaging, and energy-dispersive X-ray spectroscopy (EDS) testing under the operating voltage of 300 kV. The TEM samples of $BiVO_4$ with NPs were prepared by scratching off the samples, dispersing them into DI water, and dropping the solution on Ni grids. The X-ray diffraction (XRD) data of thin-film samples and NPs were acquired using a STOE STADI P with Mo *Kα1* (λ = 0.70926 Å) source. X-ray photoelectron spectra (XPS) and the valence band XPS (VB-XPS) were measured using a Thermo Fisher K-Alpha+. The ^1H nuclear magnetic resonance (NMR) spectra were recorded at a Bruker AVIII 600MHz NMR Spectrometer equipped with a high-resolution cryogenic triple nucleus probe-head (C/N/O). We mixed 25 µl 5 mmol l^{-1} Dimethyl sulfoxide (DMSO) into 0.1 ml electrolyte and 0.4 ml DI water and then mixed 125 µl mixture with 175 µl D_2O, and finally took 200 µl solution to perform the NMR measurements.

4.2.4 Photoelectrochemical reactions:

Photoelectrochemical (PEC) measurements were tested in a H-cell with a Nafion ion exchange membrane on a 3-electrode configuration (CHI 660E, Shanghai Chenhua) with a Pt foil as the counter electrode and Ag/AgCl (3 M KCl) as the reference electrode, and the 0.5 $_M$ $KHCO_3$ solution as the electrolyte. Before the tests, both sides of the H-cell were bubbled with CO_2 for 15 min, and the photocathodes were washed with methanol, ethanol, and DI water before being inserted into the container. The Linear Sweep Voltammetry (LSV) scanning was tested with the applied voltages from 0 V to -1 V vs. $E_{Ag/AgCl}$ with the scan rate of 0.01 V s^{-1} and the chopped light of every 5 s under a 300 W Xe lamp illumination. Electrochemical impedance spectroscopy (EIS) was tested under the applied voltage of -0.8 V vs. $E_{Ag/AgCl}$ with the frequency from 1000 kHz to 1 Hz using the 3-electrode configuration in the dark condition and under 1 Sun illumination.

4.3 Results and discussions

I fabricated the $BiVO_4$ nanoplate thin film as the light-harvesting layer using the seed-spin-coating method and the hydrothermal method.[242] **Figure 4 - 1**a,b shows the top-view scanning electron microscopy (SEM) image and cross-section SEM image of $BiVO_4$ nanoplate thin film substrate, respectively. The measurement results show that the thickness of the $BiVO_4$ nanoplates is 100 ~ 300 nm, while the vertical growth height of the formed thin

film is about 2.5 μm. The top SEM image and the zoom-in SEM image of the CuSn NPs@$BiVO_4$ photocathode are shown in **Figure 4** - **1**c. We can find that, even after washing with 1 ml methanol, 1 ml ethanol, and deionized (DI) water, there are still CuSn NPs on the surface of the $BiVO_4$ nanoplates, indicating the successful loading of CuSn NPs on the $BiVO_4$ nanoplate thin film.

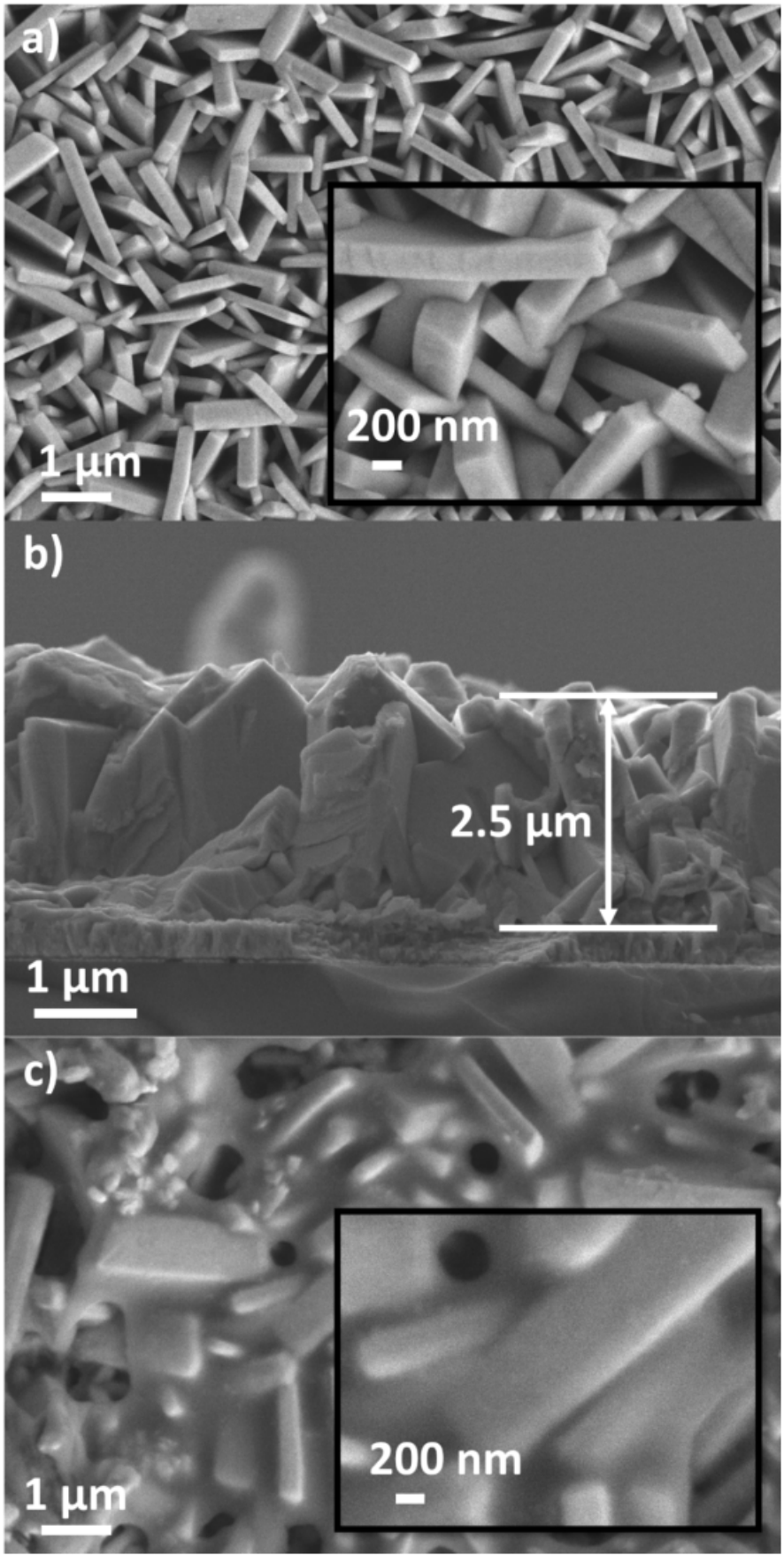
a)
200 nm
1 µm
b)
2.5 µm
1 µm
c)
200 nm
1 µm

Figure 4 - 1. a) Top-view SEM image of $BiVO_4$ nanoplate thin film. b) Cross-section SEM image of $BiVO_4$ nanoplate thin film, showing its thickness of 2.5 μm. c) Top-view SEM image of CuSn NPs@$BiVO_4$ photocathode.

The structure properties of Cu NPs and CuSn NPs were characterized by using high-resolution transmission electron microscopy (HRTEM) and aberration-corrected high-angle annular dark-field scanning TEM (HAADF-STEM) imaging measurements, as shown in **Figure 4 - 2**. Both Cu NPs and CuSn NPs are unavoidable oxidized, with the lattice spacing of 0.245 nm, 0.257 nm, and 0.341 nm, corresponding to the CuO (11-1) in Cu NPs and the SnO_2 (01-1) and (110) in CuSn NPs. From the HAADF-STEM image and energy-dispersive X-ray spectroscopy (EDS) element mappings of CuSn NPs, Cu and Sn elements are not uniformly distributed, and the elemental ratio of Cu/Sn is about 0.31 in CuSn NPs. I also carried out the HRTEM and EDS mapping measurements on the CuSn NPs@$BiVO_4$, of which the results are shown in **Figure 4 - 3**. It can be clearly found that CuSn NPs cover the whole surface of the $BiVO_4$ nanoplates, with lattice fringes of 0.477 nm, which corresponds to the (110) plane of $BiVO_4$ nanoplate.

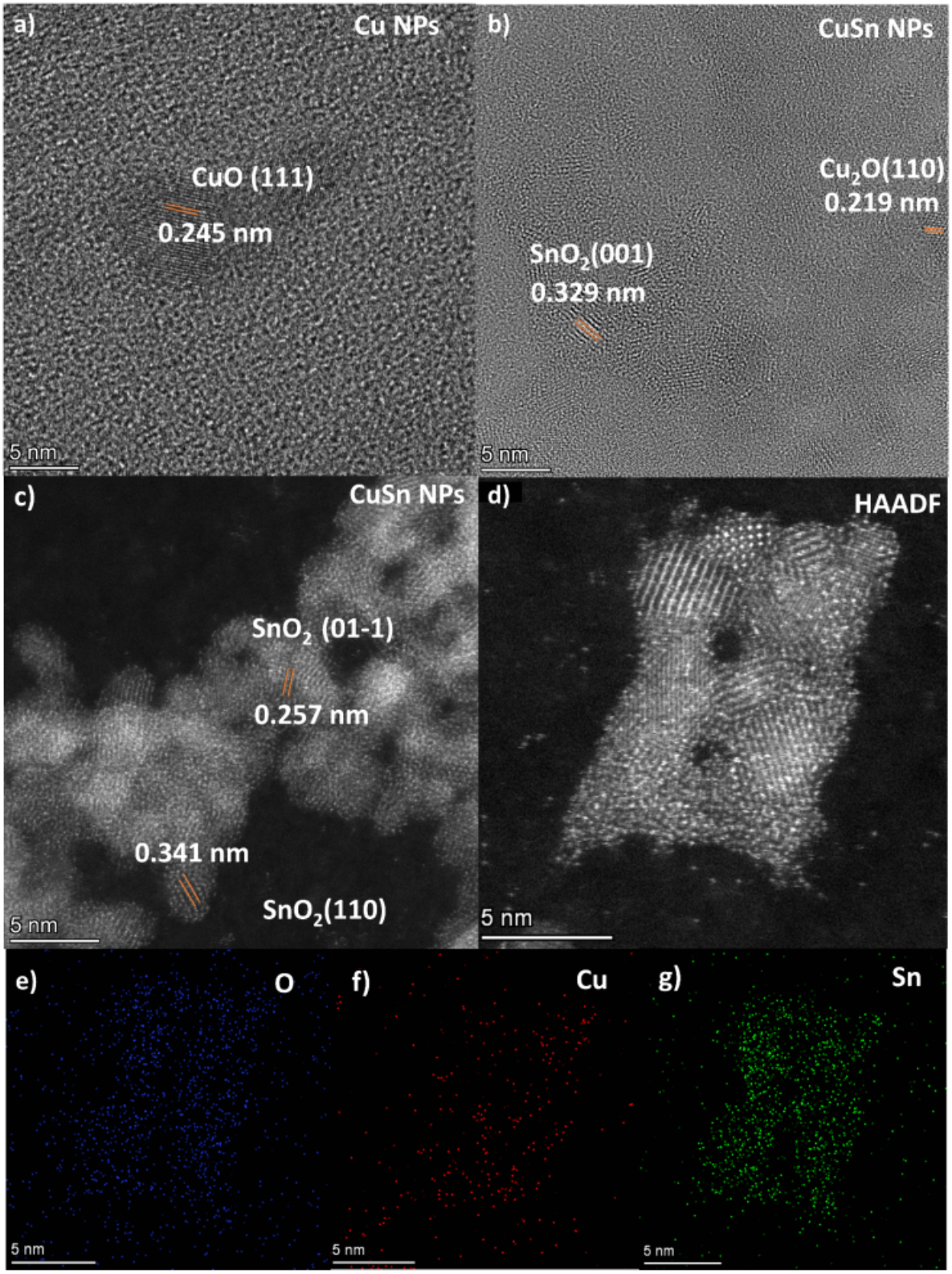

Figure 4 - 2. TEM image of a) Cu NPs and b) CuSn NPs. c,d) HAADF-STEM images of CuSn NPs. e-g) EDS mappings of O, Cu and Sn element in CuSn NPs as shown in d).

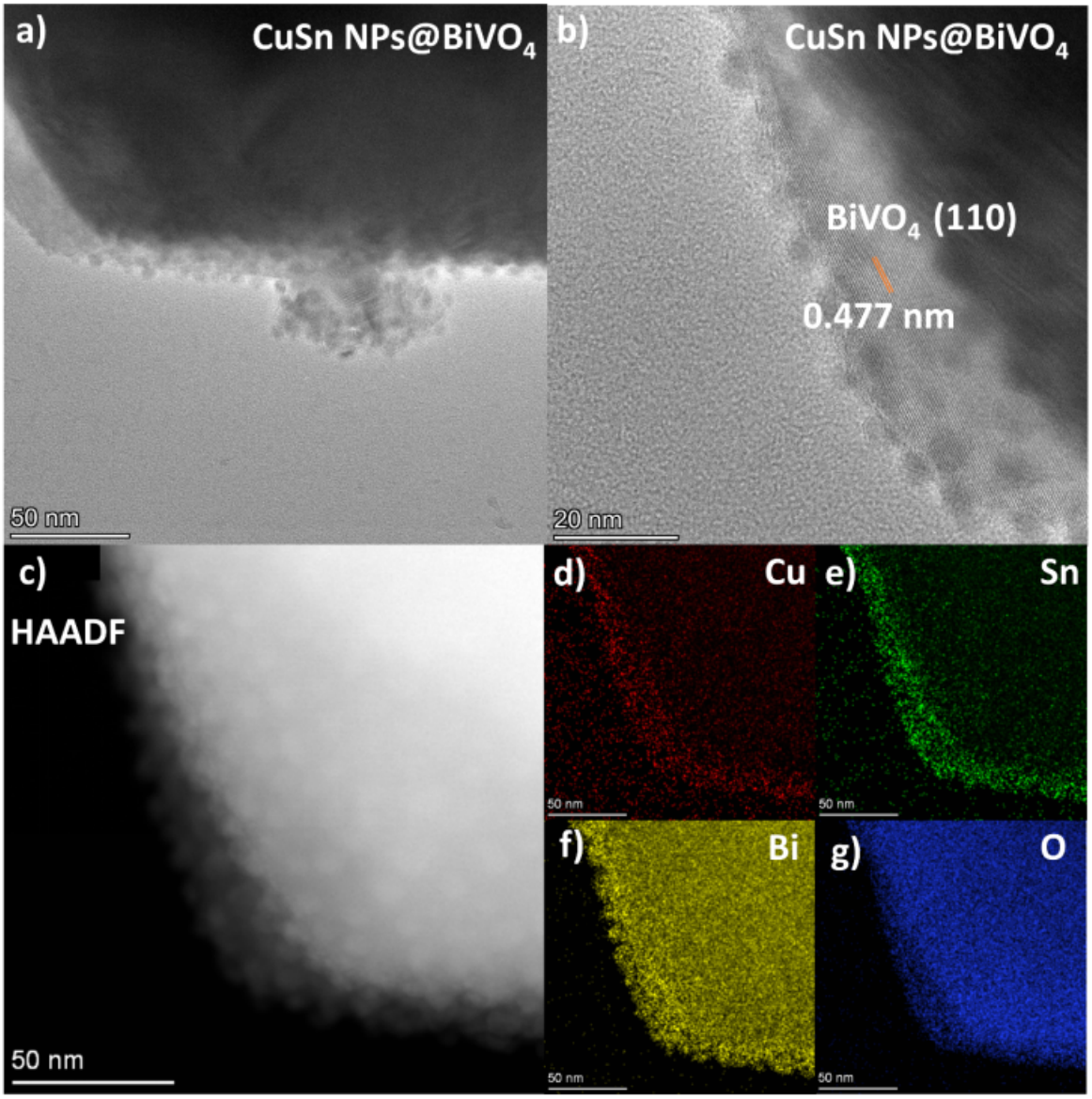

Figure 4 - 3. a) TEM image and b) the zoomed-in TEM image of CuSn NPs@$BiVO_4$. c-g) HAADF and EDS mappings of Bi, O, Cu and Sn element in CuSn NPs@$BiVO_4$.

To further confirm the crystal structure of Cu NPs and CuSn NPs, I performed X-ray diffraction (XRD) measurements, of which the results are shown in **Figure 4 - 4**a. The measurement results show that the smaller crystalline domain size would lead to the broader XRD peaks;[244] for the Cu NPs with the small size, I can only define Cu (Cubic, Fm-3m, 225) and CuO (Cubic, Fm-3m, 225) from the broad XRD peaks of Cu NPs. The CuSn NPs show the sharp XRD peaks, corresponding to Cu, Cu_2O, and SnO_2 (Tetragonal, P4_2/mnm, 136).

The measured XRD pattern of $BiVO_4$ nanoplates, as shown in **Figure 4** - **4**b, shows the good consistency with the simulated XRD pattern in the inset image, which is indexed to $BiVO_4$ (Monoclinic, C2/c, 15). Due to the small size and amount of CuSn NPs, the XRD peaks of CuSn NPs@$BiVO_4$ have the similar peaks as those of the pure $BiVO_4$ film.

UV-Vis diffuse reflectance spectroscopy (UV−Vis DRS) was adopted to test the optical properties of our photocathodes, of which the results are shown in **Figure 4** - **4**c. Using the Kubelka–Munk (K-M) formalism, the band gap of the samples can be calculated from the Tauc plot based on the following equation:[245-246]

$$F(R_\infty) = \frac{K}{S} = \frac{(1-R_\infty)^2}{2R_\infty}$$

(4.1)

Where $R_\infty = \frac{R_{sample}}{R_{standard}}$ is the reflectance (R) of the sample with infinity thickness, K is the K-M absorption, and S is the scattering coefficient.

$$(F(R)hv)^n = K(hv - E_g)$$

(4.2)

Where h is the Planck constant, v is the photon's frequency, K is a constant, for a direct band gap n = 1/2, and E_g is the band gap energy. I idealized the Tauc plot based on Zhong's research,[247] and the band gaps could be calculated to be 2.44 eV for both the $BiVO_4$ nanoplate and Cu NPs@$BiVO_4$, and 2.41 eV for the CuSn NPs@$BiVO_4$.

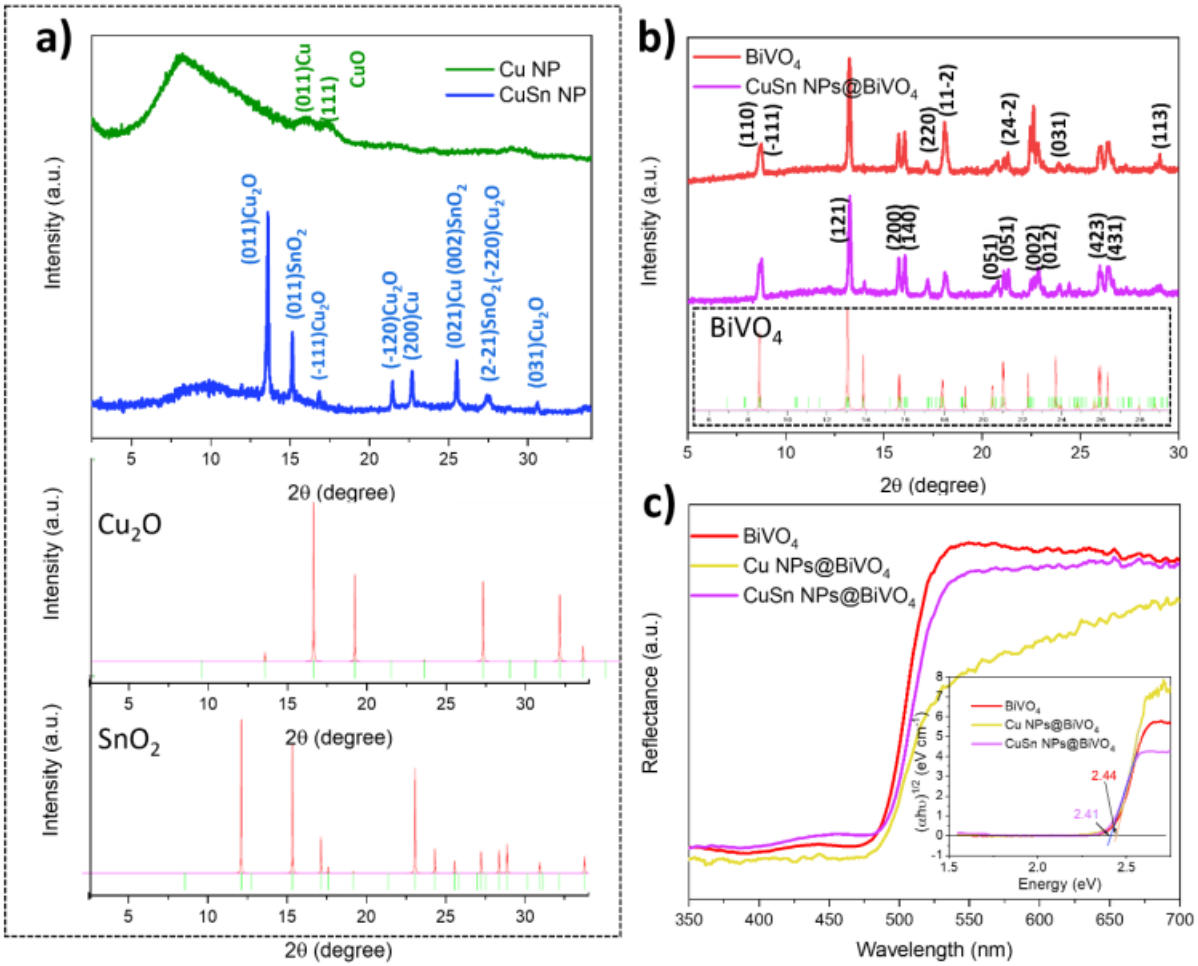

Figure 4 - 4. a) XRD patterns of Cu NPs and CuSn NPs (The bottom two images are the simulated XRD peaks for Cu_2O and SnO_2). b) XRD of $BiVO_4$ nanoplate thin film and CuSn NPs@$BiVO_4$ (The bottom image is the simulated XRD peaks for $BiVO_4$). c) UV−Vis DRS and Tauc plots (inset) of $BiVO_4$ nanoplate film, Cu NPs@$BiVO_4$, and CuSn NPs@$BiVO_4$.

To further investigate the chemical states of the Cu and Sn elements in both the NPs, I performed the high-resolution X-ray photoelectron spectroscopy (XPS) measurements. The obtained XPS survey and high-resolution XPS spectra are shown in **Figure 4 - 5**. The existence of the shake-up satellites in Cu 2p spectra of Cu NPs indicates the presence of Cu(II) ions.[248] The Cu $2p_{3/2}$ peaks at 933.0 eV and 934.5 eV are assigned to Cu(0) and Cu(II), respectively.[249] The Sn signal is not found in Cu NPs. In CuSn NPs, the Cu $2p_{3/2}$ peaks at 932.2 eV and 932.9 eV are assigned to Cu(I) and Cu(0), respectively, and no shake-up satellite peaks indicating no Cu(II) ions exist.[248] The less oxidation state of Cu in CuSn NPs is due to the higher O affinity of Sn than Cu, which is easier for the CO_2RR process via the

bidentate *OCHO intermediate.[52, 250] The Sn $3d_{5/2}$ peak at 486.6 eV can be assigned to Sn(IV) component, attributing to the SnO_2.[251] The XPS results show good consistency with the TEM lattice information and the XRD patterns.

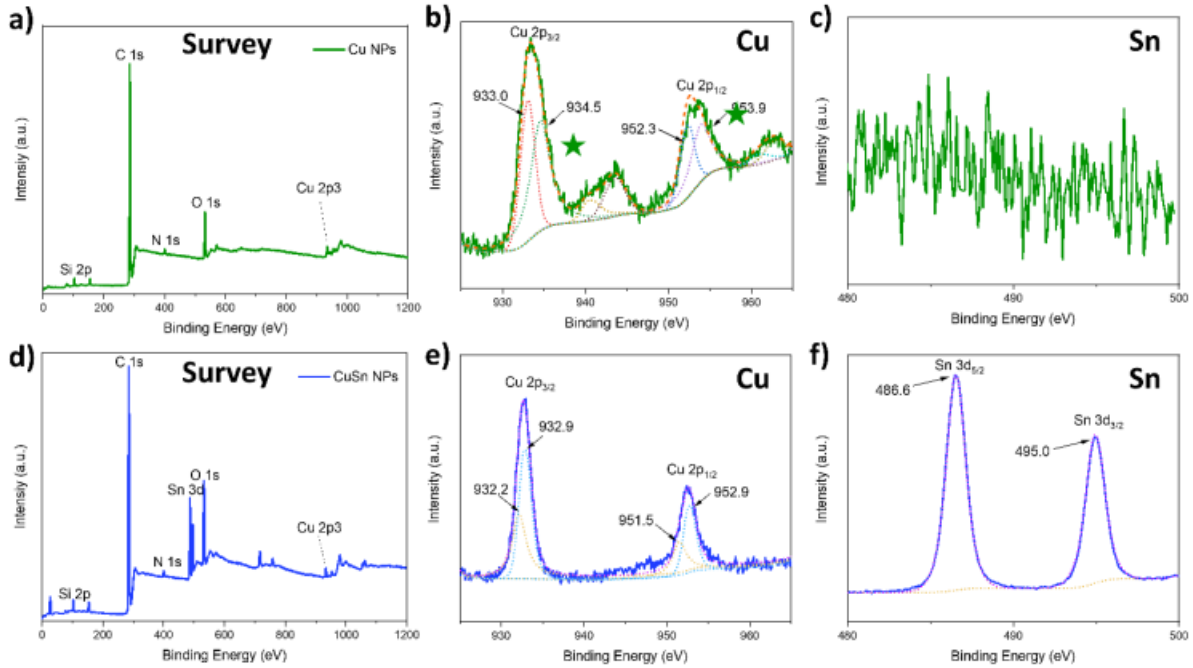

Figure 4 - 5. XPS survey and high-resolution XPS spectrum of Cu and Sn elements of a-c) Cu NPs and d-f) CuSn NPs.

The performance of the PEC CO_2RR of the relevant photocathodes were tested in a H-cell with a Nafion ion exchange membrane and 0.5 M $KHCO_3$ solution as the electrolyte, under a 100-mW cm^{-2} illumination. The measured results are shown in **Figure 4 - 6**. Before testing the linear sweep voltammetry (LSV) curves in **Figure 4 - 6**a, I bubbled the electrolyte with CO_2 for 15 min. The Cu NPs@$BiVO_4$ (-0.250 mA cm^{-2}) shows a little increased photocurrent than that of the pure $BiVO_4$ nanoplate photocathode (-0.217 mA cm^{-2}). Moreover, with coating CuSn NPs onto $BiVO_4$ nanoplate films, the fabricated photocathode shows the highest photocurrent of -0.774 mA cm^{-2} when the applied voltage is -0.95 V vs $E_{Ag/AgCl}$, which is more than 3 times higher than that of photocathodes based on pristine $BiVO_4$ or Cu NPs@$BiVO_4$. To examine the stability of the photocathodes, I tested current-time (I-t) curves with an applied constant voltage of -0.8 V vs. $E_{Ag/AgCl}$. The test results are shown in **Figure 4 - 6**b. Moreover, I also chopped the light several times to confirm the photo response. The three photocathodes can be relatively stable within 0.5 h, and the CuSn NPs@$BiVO_4$ shows

the highest photocurrent, which corresponds to the LSV results. Nyquist plots of the Electrochemical impedance spectroscopy (EIS) measurements of $BiVO_4$, Cu NPs@$BiVO_4$, and CuSn NPs@$BiVO_4$ under light illumination, as well as CuSn NPs@$BiVO_4$ in the dark condition, are shown in **Figure 4 - 6**c, with the fitted parameters listed in **Table 4 - 1**. The inset figure in **Figure 4 - 6**c shows the equivalent circuit of our photocathodes in the electrolyte, where *R*s means the solution resistance, the constant phase element (CPE) represents nonideal capacitances, *R*ct is the radius of the arc and represents the charge transfer resistance of the photocathode/electrolyte interface, and *R*1 means the charge diffusion resistance.[252-253] According to the fitted results, the CuSn NPs@$BiVO_4$ under light illumination shows the smallest *R*ct of 113.4 Ω than that of the other two types of photocathodes. In addition, the CuSn NPs@$BiVO_4$ under light illumination shows the much smaller *R*ct than the sample measured in the dark condition with the *R*ct of 1345 Ω, which is consistent with the PEC results.

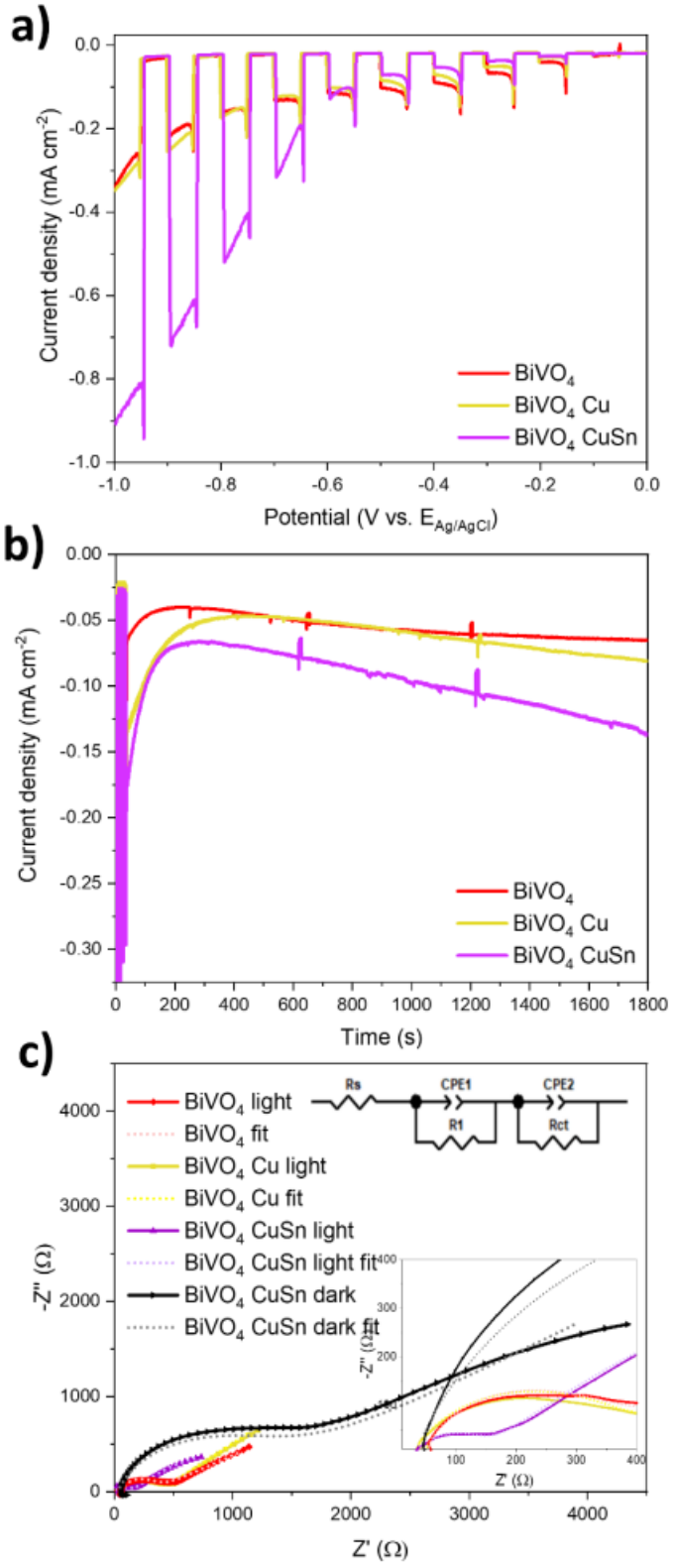

Figure 4 - 6. a) LSV curves of $BiVO_4$, Cu NPs@$BiVO_4$, and CuSn NPs@$BiVO_4$. b) *I-t* curves of photocathodes at the applied voltage of -0.8 V vs. $E_{Ag/AgCl}$. c) Nyquist impedance

plots of $BiVO_4$, Cu NPs@$BiVO_4$, and CuSn NPs@$BiVO_4$ under light illumination and CuSn NPs@$BiVO_4$ in the dark. Inset is the zoomed-in region from 0-400 Ω and the equivalent circuit.

Table 4 - 1. The fitted parameters of Nyquist plots of $BiVO_4$, Cu NPs@$BiVO_4$ and CuSn NPs@$BiVO_4$ under light illumination and CuSn NPs@$BiVO_4$ in the dark.

	$BiVO_4$ (light)	Cu NPs @$BiVO_4$ (light)	CuSn NPs @$BiVO_4$ (light)	CuSn NPs @$BiVO_4$ (dark)
Rs (Ω)	43.11	27.87	30.36	37.65
Error%	5.02	3.83	2.89	6.11
CPE1-T (F)	4.31E-04	4.09E-04	4.66E-04	5.10E-05
Error%	8.39	15.12	6.32	12.71
CPE1-P (F)	0.43	0.47	0.5	0.6
Error%	3.15	8.28	3.13	3.96
R1 (Ω)	3630	10633	2266	5945
Error%	10.34	26.98	4.1	12.31
CPE2-T (F)	9.51E-07	9.42E-07	3.94E-06	6.10E-07
Error%	10.36	16.36	18.49	10.39
CPE2-P (F)	0.8	0.75	0.71	0.83
Error%	1.15	2.02	2.48	1.22
Rct (Ω)	325.3	356.2	113.4	1345
Error%	7.62	4.27	3.96	11.05

I also compared the LSV curves of the CuSn NPs@$BiVO_4$ with different Cu:Sn ratios, of which the results are shown in **Figure 4 - 7**. It was found that the alloy NP device with Cu:Sn = 2:1 shows the highest LSV current density, so I used this bimetallic component as our

CuSn NPs to fabricate the device. I then compared the volume of the CuSn NPs solutions dropped on the surface of the $BiVO_4$ nanoplate films, as shown in **Figure 4 - 8**. The too thick layer of the toluene solvent is bad for the separation of photo-generated charge carriers and their transfer to the surface of the photocathode, so I further used 50 μl of the nanoparticles as the NPs layer of our photocathodes. In addition, I tested the LSV curves of the CuSn NPs@$BiVO_4$ sample in an electrolyte bubbled with Ar/CO_2. The measurement results are shown in **Figure 4 - 9**. The higher photocurrent of the photocathode in the CO_2 atmosphere than that in the Ar atmosphere could be obtained, which indicates that CO_2 participated in the reduction reaction.

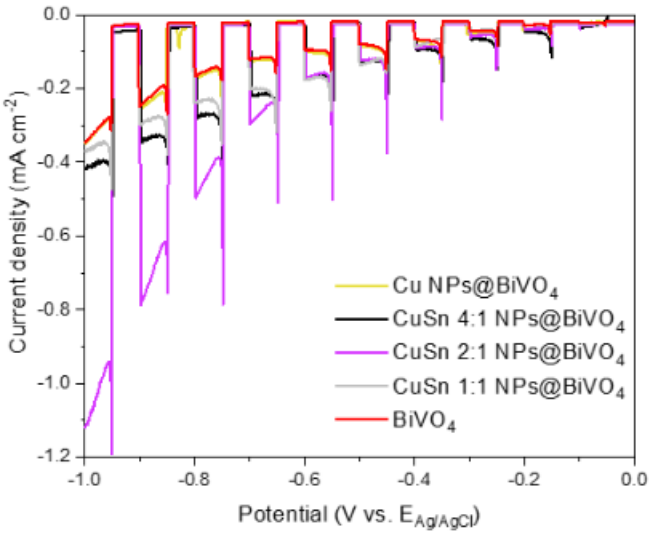

Figure 4 - 7. LSV of $BiVO_4$ with Cu NPs, CuSn 4:1 NPs, CuSn 2:1 NPs (short for CuSn NPs), CuSn 1:1 NPs, and pure $BiVO_4$ photocathode.

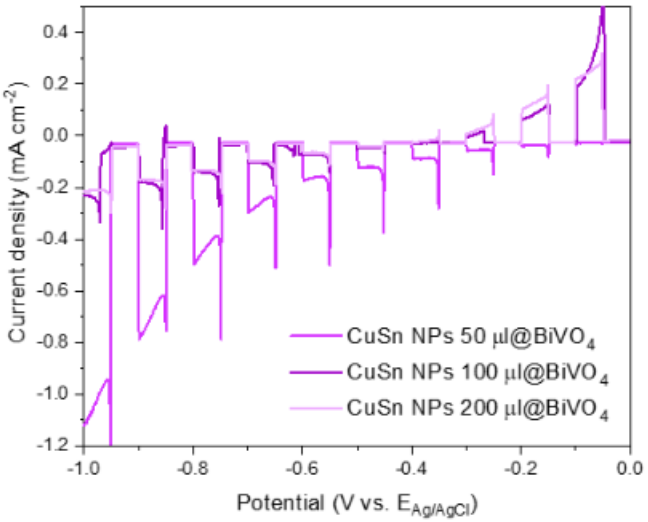

Figure 4 - 8. LSV of $BiVO_4$ with 50/100/200 µl CuSn NPs solution.

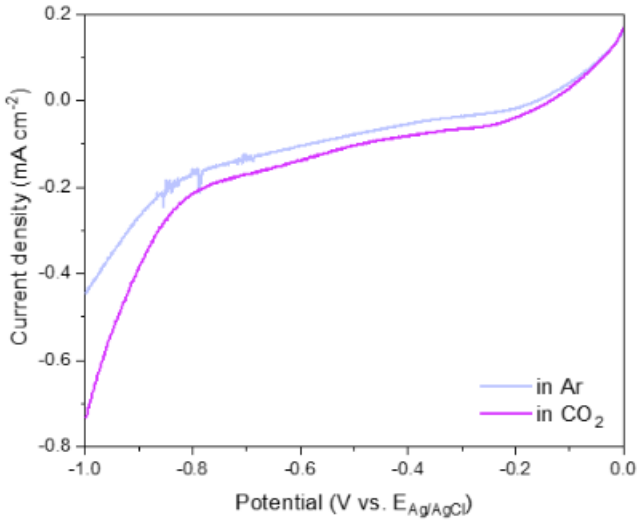

Figure 4 - 9. LSV tests of CuSn NPs@$BiVO_4$ in electrolyte bubbled with Ar/CO_2.

I then tested the gas chromatography (GC) and nuclear magnetic resonance (NMR) spectroscopy to confirm the product from the CO_2 reduction reaction. Theoretically, there should be CO and H_2 generated during the reduction reaction; however, due to the too small amount of the gas product, we can hardly detect any CO or H_2. The ^{1}H NMR spectrum of the electrolyte CuSn NPs@$BiVO_4$ photocathode before and after the CO_2RR I-t test and the pure D_2O solvent are shown in **Figure 4 - 10**a-c. The peak at 8.45 ppm can be assigned to $COOH^*$ formic acid, and the peak at 7.93 ppm can be assigned to $COOCH_3^*$ methyl formate.[232, 254] The formation of methyl formate is based on the reaction between the methanol and the formic acid.[255] The integration results of the formic acid, methyl formate, and the reference

DMSO peaks are listed in **Figure 4** - **10**b, and the calculated production of formic acid is 37.3 μmol/cm^2·h·l, and the production of methyl formate is 694.4 μmol/cm^2·h·l of our photocathode in the electrolyte.

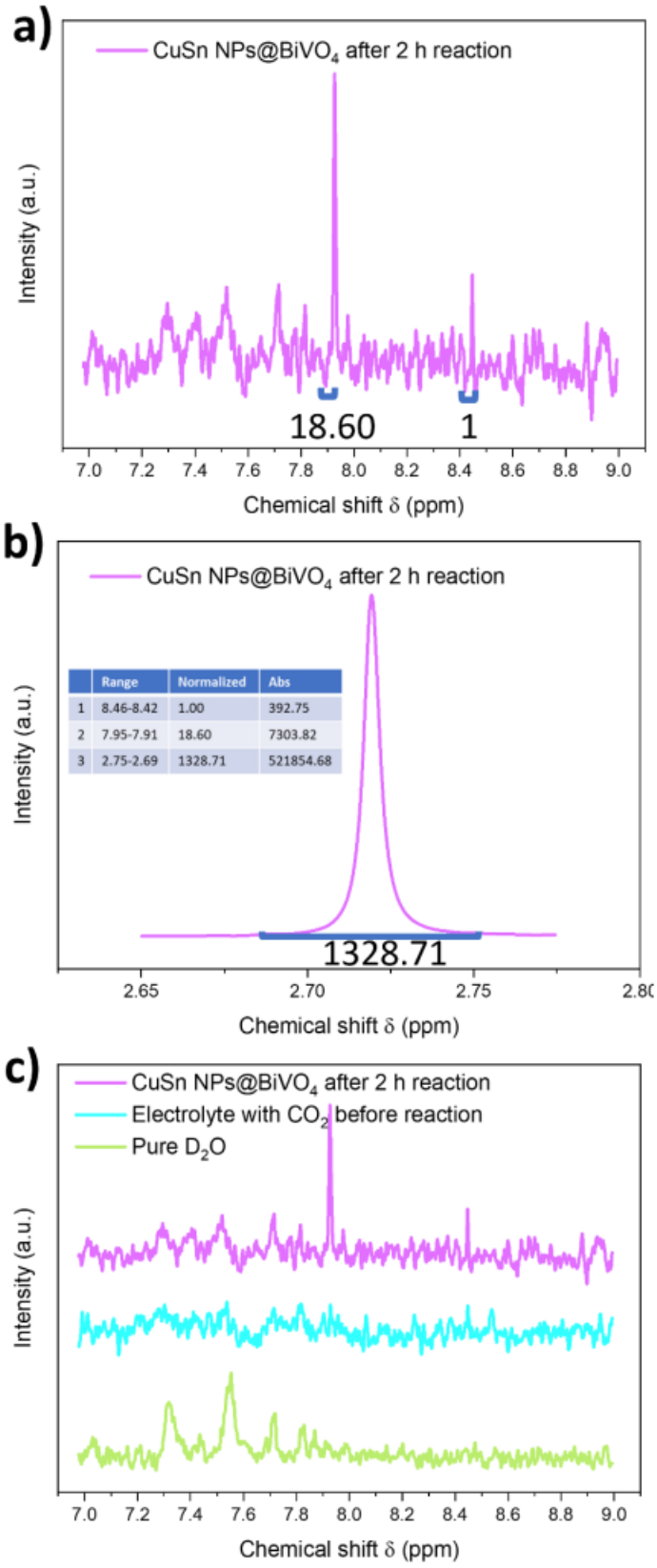

Figure 4 - 10. a-b) ^{1}H NMR spectrum of the electrolyte of the CuSn NPs@$BiVO_4$

photocathode after CO_2RR I-t test for 2 h, with the applied voltage of -0.8 V vs. $E_{Ag/AgCl}$. c) ^1H NMR spectrum of the electrolyte before and after the CO_2RR I-t test, and the pure D_2O solvent.

To get an in-depth insight into the band structure and the band alignment of the fabricated photocathodes, I measured the VB-XPS of $BiVO_4$ nanoplates (as shown in **Figure 4 - 11**a). Based on the above measurement results, the schematic diagram of the band alignment of the CuSn NPs@$BiVO_4$ photocathodes under light irradiation is shown in **Figure 4 - 11**b. The valence band (VB) of $BiVO_4$ was measured to be 1.6 eV (**Figure 4 - 11**a) and the bandgap was calculated, based on the band gap from the Tauc plot (see **Figure 4 - 4**c) to be 2.44 eV; then, the conduction band (CB) can be calculated to be -0.84 eV. However, when I tested the VB-XPS and the UV-Vis absorption of the CuSn NPs; the results are shown in **Figure 4 - 12**, which show a VB of 3.88 Ev and the calculated idealized bandgap of 3.0 eV from the Tauc plot, which can be assigned to the band structure of the SnO_2 component with the calculated CB of 0.88 eV.[256] The band structure of the Cu_2O component is unable to be tested due to the less composing proportion in the CuSn NPs, so I can only refer to references to get the approximate band structure of the Cu_2O.[62]

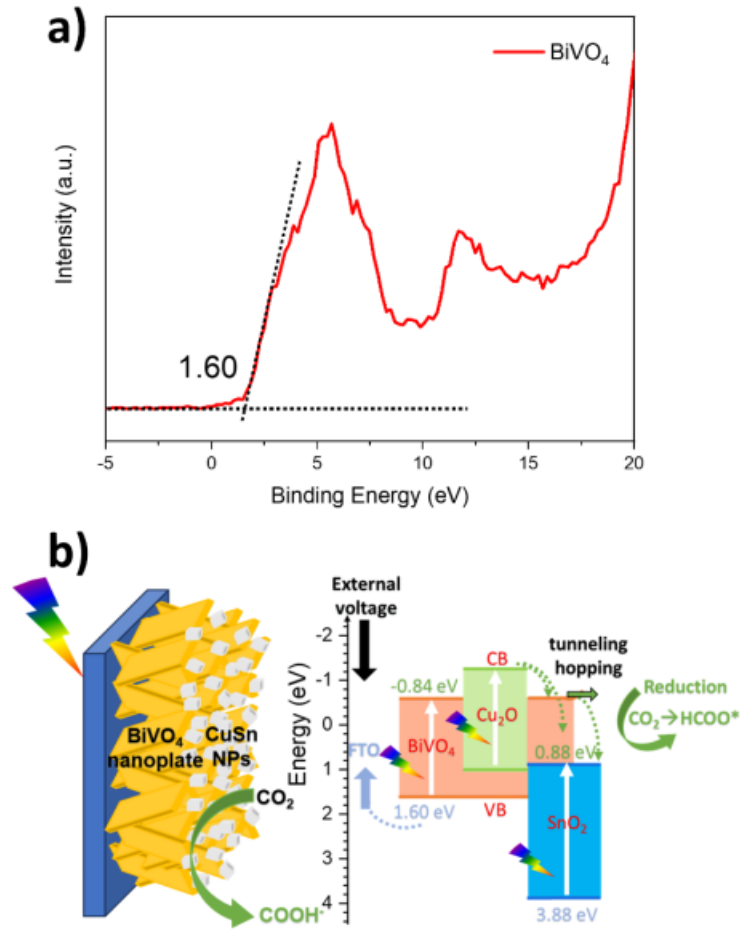

Figure 4 - 11. a) VB-XPS of $BiVO_4$.b) Schematic diagram of CuSn NPs@$BiVO_4$ photocathodes under light irradiation and applied negative voltage.

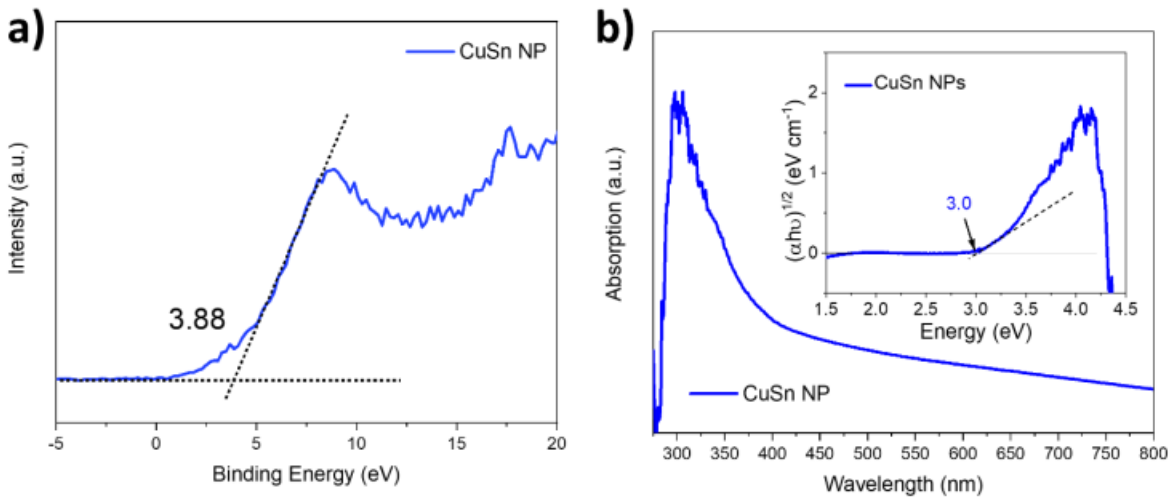

Figure 4 - 12. a) VB-XPS of CuSn NPs. b) UV−vis absorption and Tauc plot (inset) of CuSn

NPs.

I further compared the high-resolution XPS spectrum of Cu, Sn and Bi elements in CuSn NPs, $BiVO_4$ film and CuSn NPs@$BiVO_4$ (**Figure 4 - 13**). Both the Sn and Bi XPS peaks shifted to the lower binding energy, while the Cu peaks shifted to the higher binding energy in CuSn NPs@$BiVO_4$, indicating the electrons migrated from Cu_2O to SnO_2 and $BiVO_4$,[257] which means that the surface of the CuSn NPs@$BiVO_4$ photocathodes exhibits type-II heterojunction band structures and can facilitate photo-generated charge carrier transport and separation.[258] Even though $BiVO_4$ nanoplate is an n-type semiconductor, which has an upward band bending at the semiconductor-electrolyte interface,[259] with the effort of the external circuit, the applied negative voltage could lead to the tunnelling and hopping transport effects of the electrons through the band bending of the $BiVO_4$ to have reduction reaction, which can also explain why I observed photo-response on pure $BiVO_4$ film as shown in **Figure 4 - 6**a.[260-262] In addition, because of the higher O affinity of the Sn element, the SnO_2 can form a reaction path to the $HCOO^*$, which is the intermediate of HCOOH, increasing the selectivity of the reduction product of CO_2.[263]

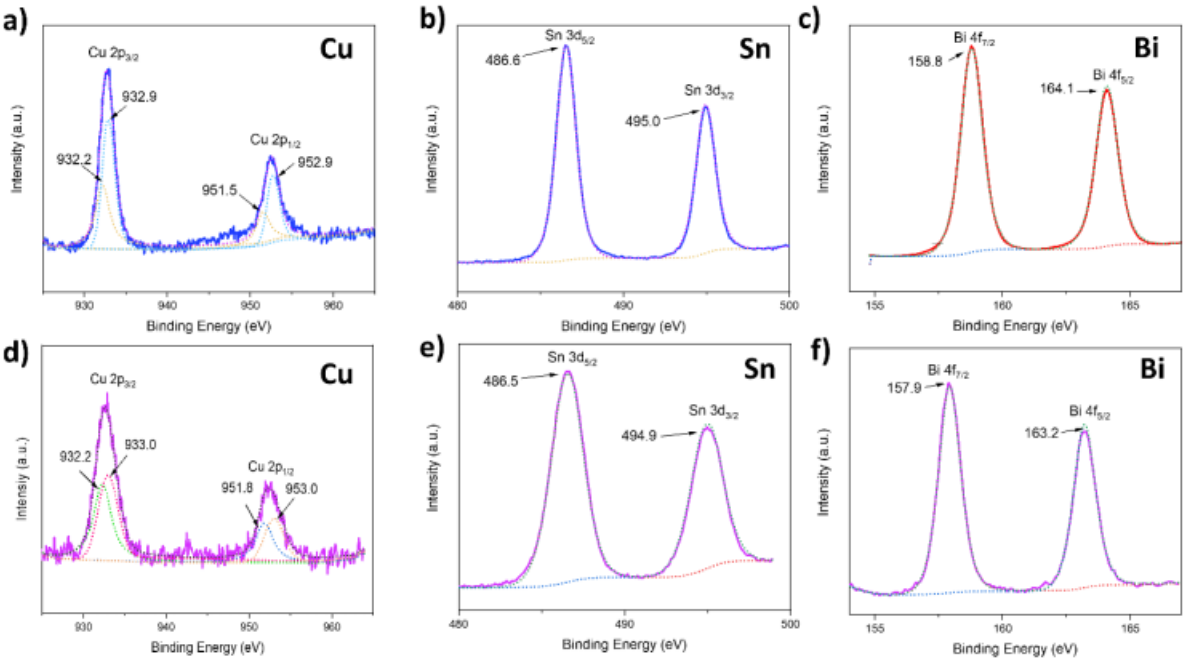

Figure 4 - 13. High-resolution XPS spectrum of a) Cu element in CuSn NPs, b) Sn element in CuSn NPs, c) Bi element in $BiVO_4$, and d-f) Cu, Sn, and Bi element in CuSn NPs@$BiVO_4$.

To sum up, the possible band structure of our photocathode samples under an applied

negative voltage and the light illumination can be schematically illustrated in **Figure 4 - 11**b. In detail, the photo-excited electrons will be generated in both $BiVO_4$ and CuSn NPs, and then the electrons transfer from the formed Cu_2O to $BiVO_4$ nanoplate films, due to the formation of type-II heterojunction between Cu_2O and $BiVO_4$, in which the photo-induced charge carriers are easier to be separated. Thereafter, the electrons transfer through the band bending of the $BiVO_4$ based on the external voltage-assisted tunnelling and hopping effects to the surface for the reduction reaction of CO_2 to the $COOH^*$ with the help of Sn element and the type-II heterojunction between $BiVO_4$ and SnO_2.

4.4 Conclusion

In this research work, I applied Cu NPs and CuSn bimetallic NPs on the surface of $BiVO_4$ nanoplate substrates to synthesize photocathodes for PEC CO_2RR. The Cu NPs contain Cu(0) and Cu(II), and the CuSn NPs contain Cu(0), Cu(I), and Sn(IV), which have been confirmed by the XRD and XPS measurement results. With the applied negative voltages, light-generated electrons transport through band bending of $BiVO_4$ via the tunnelling and hopping effects. With depositing CuSn NPs onto $BiVO_4$ nanoplates, the type-II heterojunctions are formed between $BiVO_4$ nanoplates and CuSn NPs, which could promote the separation of photo-induced charge carriers and their transfer to the sample surface for PEC CO_2RR. Thereby, as for the PEC measurement results, the CuSn NPs@$BiVO_4$ photocathodes show the highest photocurrent of -0.774 mA cm^{-2} at the applied voltage of -0.95 V vs $E_{Ag/AgCl}$, which is more than 3 times higher than that of the pristine $BiVO_4$ or the Cu NPs@$BiVO_4$ NPs. This work provides new strategies in PEC CO_2RR by introducing tunnelling and hopping effects, when applying the negative voltage on n-type semiconductors and forming type-II heterojunctions between $BiVO_4$ and CuSn NPs, which further expands the application of $BiVO_4$ and CuSn components in PEC CO_2RR.

Chapter 5 Electroplated Copper-Tin Composite on Copper foam for Photoelectrochemical Carbon Dioxide Reduction

The photo-response property and stability of the photocathodes can be further enhanced through the selection of a more stable substrate. Therefore, in this Chapter, we electroplated CuSn composite layers with varying parameters onto carefully chosen Cu foam substrates in order to improve the photo-response ability and stability.

5.1 Introduction

The massive and significantly increased usage of fossil fuels has caused energy shortages and environmental pollution issues, due to the burning product of hazards gases, such as NO_x, SO_2, and CO_2.[264] Notably, as the main greenhouse gas, the excessive emission of CO_2 can cause climate change, so it is critically important to develop effective strategies to artificially convert CO_2 into valuable chemicals, such as carbon monoxide (CO), methane (CH_4), methanol (CH_3OH), and formic acid (HCOOH).[265] Electrochemical (EC) carbon dioxide reduction reaction (CO_2RR) has attracted great attention due to its mild operating conditions in comparison to high-cost thermal-driven processes, and the light-assisted photoelectrochemical (PEC) CO_2RR can further improve the reaction efficiencies of the EC procedure.[265]

So far, a wide range of materials have been investigated for EC or PEC CO_2RR, among which transition metals with different forms are considered to be one of the most appealing research hotspots in the field of EC or PEC CO_2RR applications due to their superior features, such as their ability to absorb/activate CO_2 and their diverse catalytic properties on different faces.[266] The transition metals can be classified into four groups based on their different H-affinity and O- affinity and their different major products from the CO_2RR.[267] The earth-abundant copper (Cu) is the only metallic element that can produce hydrocarbons and CO. Cu possesses different oxidation states, including cuprous oxide (Cu_2O) and copper oxide (CuO) with narrow bandgaps of 2.2 eV and 1.7 eV, respectively.[60-61] However, Cu-based catalysts lack a relatively high product selectivity because a wide range of products is obtained from the CO_2RR based on Cu-based catalysts.[268] To increase the product selectivity, Cu-based materials have been combined with other metals to form bimetallic composites or alloys, such as Cu-Pd,[216-218] Cu-Au,[219-221] Cu-Zn,[222-223] Cu-In,[224-226] Cu-Ag,[227-229]. Another metallic element, Tin (Sn), which possesses a low H- affinity and high O- affinity, can inhibit the H_2

evolution and enhance the selectivity for the formation of formate acid.[265, 269] In this regard, Cu-Sn alloy catalysts have been widely applied in EC CO_2RR; however, such alloy catalysts have rarely been studied for the PEC CO_2RR.[230-233]

In Chapter 4, I presented my research on synthesizing Cu-Sn bimetallic nanoparticles (NPs) onto $BiVO_4$ nanoplate substrates and applying the resulting CuSn NPs@$BiVO_4$ photocathodes for photoelectrochemical (PEC) CO_2 reduction reaction (CO_2RR). This study has clearly demonstrated that Cu-Sn bimetallic systems are promising catalysts for PEC CO_2RR applications. To further enhance the efficiency and stability of Cu-Sn bimetallic catalysts for PEC CO_2RR, I electroplated Cu-Sn composites onto Cu foam substrates. The Cu foams, with their higher specific surface area compared to Cu thin-film substrates, improve the efficiency of the catalysts. By varying the Cu ratios, the synthesized Cu-Sn composite layers exhibit different morphologies on the Cu foam substrates. The absorption properties of the oxidized states on the surface of these photocathodes ensure sufficient photo-response in PEC tests under light illumination. Among the different compositions, the Cu foam with a CuSn composite ratio of 2:1 and the electroplate time of 20 min under -8 mA (2:1 -8 20) exhibited the highest current density during PEC measurements, while the Cu foam with a CuSn composite ratio of 1:1 (1:1 -8 20) demonstrated optimal production efficiency of formate from CO_2RR.

5.2 Experimental section

Materials: 0.5 mm-thick Cu foam substrates were bought from SuZhou KeShengHe, China. Copper(II) sulphate pentahydrate ($CuSO_4 \cdot 5H_2O$, ≥98%), Tin(II) sulphate ($SnSO_4$, ≥95%), Potassium pyrophosphate ($K_4P_2O_7$, 97%), Ammonium citrate dibasic ($HOC(CO_2H)(CH_2CO_2NH_4)_2$, ≥98%), Potassium bicarbonate ($KHCO_3$, 99.7%), and Hydrochloric acid solution (HCl, 1.0 N) were purchased from Sigma-Aldrich P/L. All the chemicals were used as received without further purification.

Growth of photocathodes: First, the Cu foam substrates were washed in deionized (DI) water, ethanol, and acetone for 10 min, respectively, in an ultrasonic machine. Before the deposition procedure of CuSn composite layers, the 2 cm × 1 cm Cu foam was rinsed with DI water, dried, and dipped in 1.0 N HCl solution for 60 s, rinsed with DI water again, and dried. The CuSn precursor was prepared with 0.5 mol L^{-1} $K_4P_2O_7$, 0.05 mol L^{-1} $C_6H_{14}N_2O_7$, 0.1 mol L^{-1} $CuSO_4 \cdot 5H_2O$ and 0.1 mol L^{-1} $SnSO_4$ and labelled as CuSn (1:1). The solution with 0.1 mol L^{-}

[1] $CuSO_4 \cdot 5H_2O$ and 0.2 mol L^{-1} $SnSO_4$ was labelled as CuSn (1:2), and the solution with 0.2 mol L^{-1} $CuSO_4 \cdot 5H_2O$ and 0.1 mol L^{-1} $SnSO_4$ is labelled as CuSn (2:1). The washed Cu foam substrates were then electroplated in the CuSn precursor under the applied current of -4 mA for 5 min (-4 5) or -8 mA for 20 min (-8 20) with a Pt electrode as the counter electrode. The as-electroplated photocathodes were rinsed with DI water and dried for PEC tests.

Characterizations: The fabricated photocathodes were analyzed using several techniques. Scanning electron microscopy (SEM) and energy-dispersive X-ray spectroscopy (EDS) were performed with a Zeiss Sigma HD. X-ray diffraction (XRD) data were obtained using a Rigaku SmartLAB SE powder diffractometer. Ultraviolet-visible (UV–vis) absorption properties were measured with a SHIMADZU UV-3600i Plus. X-ray photoelectron spectra (XPS) and valence band XPS (VB-XPS) measurements were carried out using a Thermo Fisher K-Alpha+. Gas chromatography (GC) was performed on an Agilent 7890B GC System, equipped with a 2m, 2mlD, 1/8-inch OD Silco HP column, with argon as the carrier gas. Ion chromatography (IC) was conducted using a Metrohm 930 Compact IC Flex 1, equipped with a Metrosep A Supp 19-150/4.0 column, under the following conditions: 25.6°C, 15.30 MPa, and a 0.700 mL/min flow rate for 20 minutes.

Photoelectrochemical reactions: PEC measurements were carried out on a 3-electrode configuration electrochemical workstation (CHI 660E, Shanghai Chenhua). In the reaction system, the reaction container was an H-cell with a Nafion ion exchange membrane. The counter electrode was a Pt foil, the reference electrode was Ag/AgCl (3M KCl), and the electrolyte was 0.5 mol L^{-1} $KHCO_3$. Before the PEC tests, both sides of the H-cell were bubbled with CO_2 (5 L h^{-1}) for 15 min. The Linear Sweep Voltammetry (LSV) scanning was performed from 0 V to -1.5 V vs $E_{Ag/AgCl}$ with a scan rate of 0.01 V s^{-1} under a 300 W Xe lamp illumination, which was chopped every 5 s. The current-time (I-t) tests were carried out at -1 V vs $E_{Ag/AgCl}$. Electrochemical impedance spectroscopy (EIS) measurements were conducted at an applied voltage of -1 V vs. $E_{Ag/AgCl}$ over a frequency range from 1000 kHz to 1 Hz in the dark condition.

5.3 Results and discussions

To grow CuSn composite layers onto the Cu substrates, I utilized both the general Cu thin film and Cu foam as the substrates. I prepared a precursor solution containing0.1 mol L^{-1}

$CuSO_4 \cdot 5H_2O$ and 0.1 mol L^{-1} $SnSO_4$ and electroplated the substrates under -4 mA cm^{-2} for 5 min. The resulting samples were labelled as Cu film/foam with CuSn (1:1 -4 5). The top-view scanning electron microscope (SEM) images and the cross-section SEM images of Cu film/foam with CuSn (1:1 -4 5) are shown in **Figure 5 - 1**. It can be clearly found that Cu film is much flatter than the porous Cu foam substrate. The cross-section SEM image (**Figure 5 - 1**b) reveals that the thickness of the Cu thin film substrate is approximately 350 μm, while the thickness of the porous Cu foam substrate is about 700 μm. Notably, the porous Cu foam substrate has a significantly higher specific surface area.

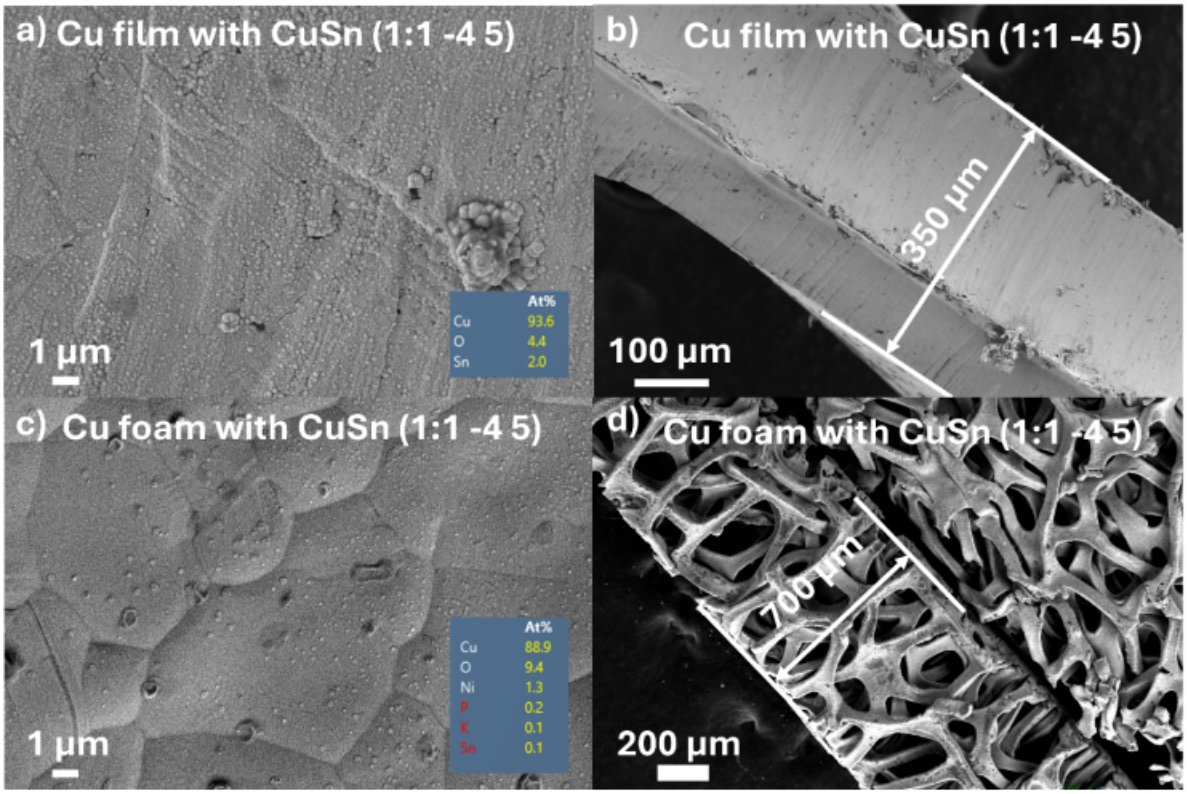

Figure 5 - 1. a) Top-view SEM image and b) Cross-section SEM image of Cu film with CuSn (1:1 -4 5). c) Top-view SEM image and d) Cross-section SEM image of Cu foam with CuSn (1:1 -4 5).I then compared the photoelectrochemical (PEC) properties of the CuSn composite catalysts deposited on the Cu thin film and Cu foam substrates by testing the chopped linear sweep voltammetry (LSV) and current-time (I-t) curves. The results are shown in **Figure 5 - 2**a,b. The current density of Cu foam substrate with CuSn composite layer (1:1 -4 5) is about -9 mA cm^{-2} at the applied voltage of -1 V vs $E_{Ag/AgCl}$, which is about nine times higher than that of the Cu thin film substrate with the same CuSn composite layer. The photo-response of the Cu foam-based CuSn composite catalyst is also significantly

stronger than that of the Cu film-based CuSn sample. In the I-t test, conducted at an applied voltage of -0.8 V vs. $E_{Ag/AgCl}$ under dark conditions, both the Cu film-based and Cu foam-based cathodes showed stable current densities during the 1-hour test. After the PEC tests, the electroplated CuSn composites remained on the Cu film/foam cathodes, as demonstrated by the SEM and corresponding energy-dispersive X-ray spectroscopy (EDS) results shown in **Figure 5** - 2c,d. Therefore, I chose Cu foam as the substrate for the photocathodes due to its stable and higher photo-response.

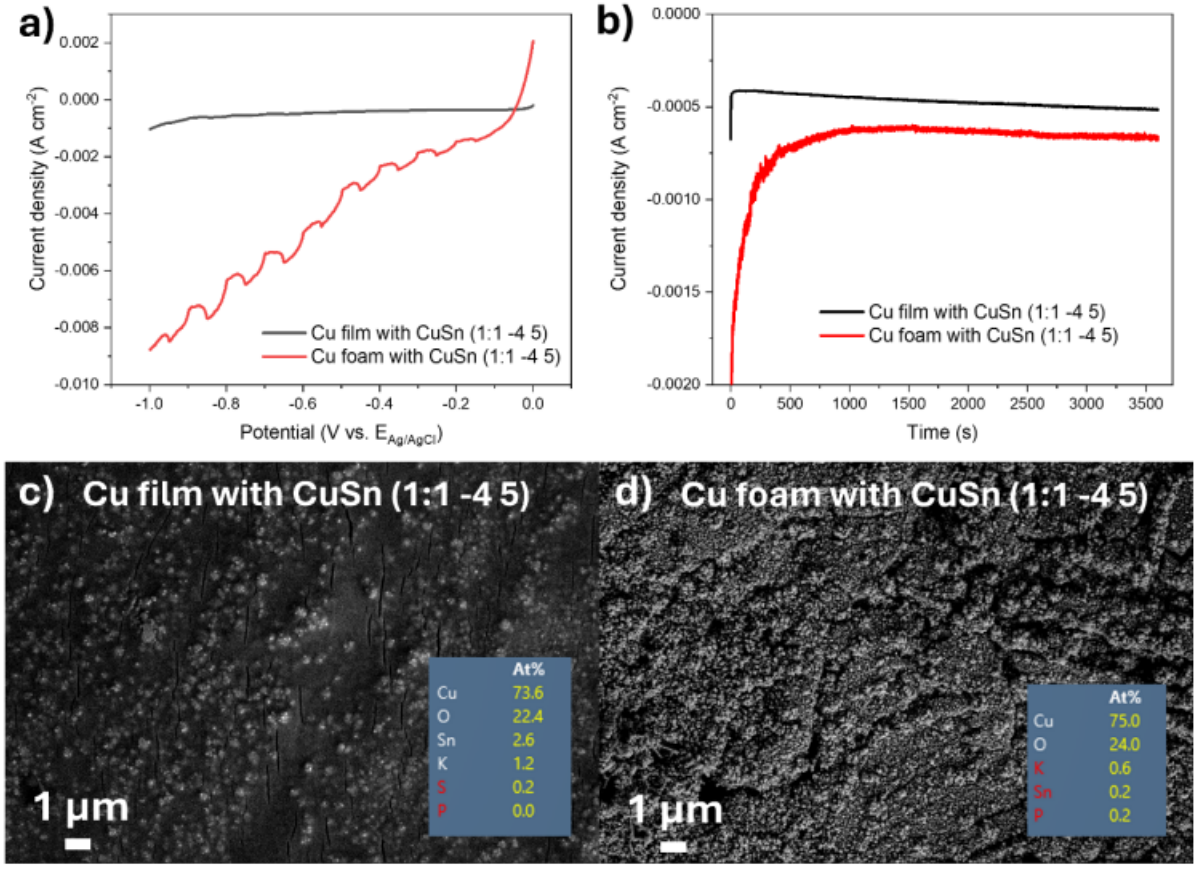

Figure 5 - 2. a) Chopped LSV test and b) I-t test in the dark at -0.8 V vs $E_{Ag/AgCl}$ of Cu film and Cu foam with CuSn composite layers (1:1 -4 5). SEM images and inset EDS results of c) Cu film and d) Cu foam with CuSn composite layers (1:1 -4 5) after the PEC tests.

I then applied the precursor with the Cu:Sn ratios of 1:1, 1:2, and 2:1, and increased the electroplating current density to -8 mA cm^{-2} and the electroplating time to 20 minutes. I compared the pure Cu foam and the Cu foam with CuSn composite photocathodes. The SEM images and corresponding EDS elemental atomic fraction images of the Cu foam and Cu

foam with CuSn composites in ratios of (1:1 -8 20), (1:2 -8 20), and (2:1 -8 20) are shown in **Figure 5 - 3**. The different Cu:Sn ratios resulted in photocathodes with varying surface morphologies, with the CuSn (2:1 -8 20) composite displaying the largest specific surface area. Due to the thinness of the CuSn composite layer, the EDS signals are primarily from the Cu foam substrate.

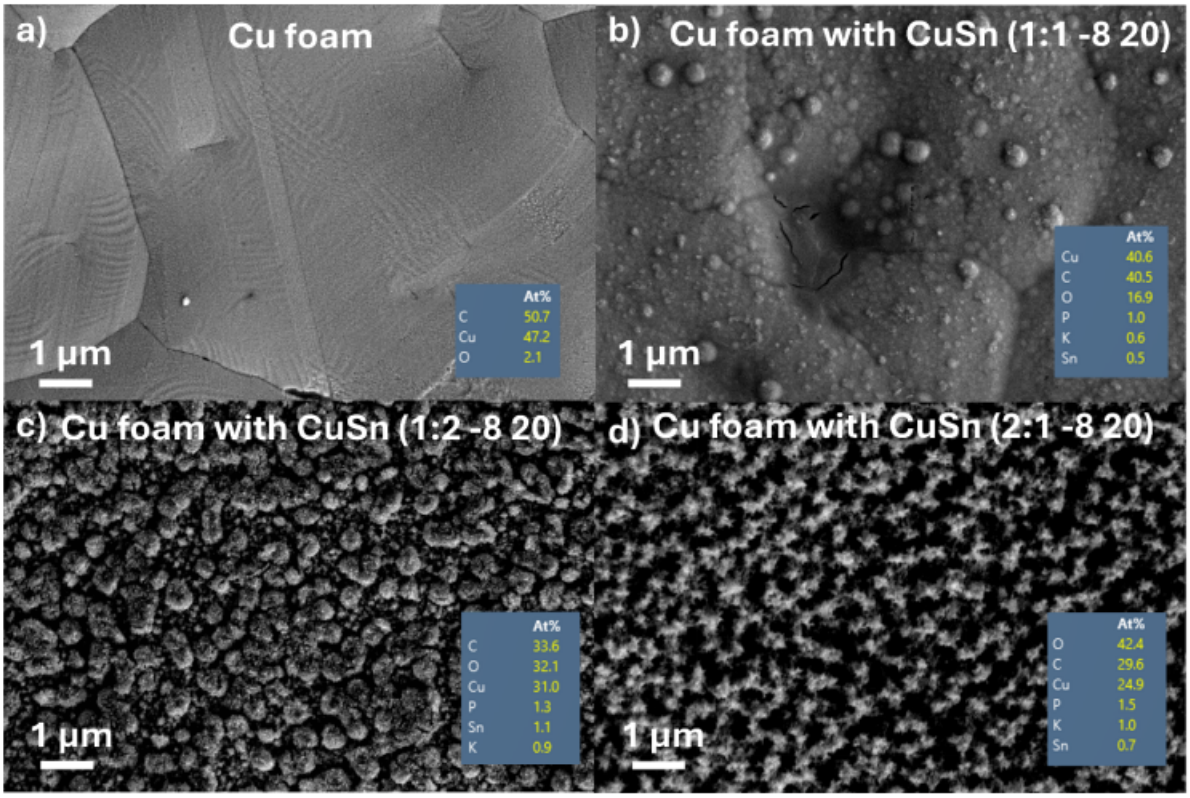

Figure 5 - 3. SEM images with the inset EDS atomic fraction pictures of a) Cu foam, as well as Cu foam with CuSn composites with the ratios of b) (1:1 -8 20), c) (1:2 -8 20), and d) (2:1 -8 20), respectively.

To verify the crystal structures of the CuSn composite layers deposited onto the Cu thin-film and Cu foam substrates, I performed X-ray diffraction (XRD) measurements on the fabricated photocathodes. The results are shown in **Figure 5 - 4**a. Due to the thinness of the CuSn composite layer, the XRD patterns of the four types of photocathodes mainly exhibit peaks related to Cu materials. The inset of **Figure 5 - 4**a shows the simulated XRD pattern for Cu (Cubic, Fm-3m, 225). The measured XRD patterns closely match the simulated results, indicating that the Cu substrates dominate in the photocathode systems.

I then tested the ultraviolet-visible (UV–vis) absorption properties of the fabricated

photocathodes, as shown in **Figure 5** - **4**b. Based on the UV–vis absorption data, I further calculated the optical bandgap values of the photocathodes from the Tauc plot curves, as shown in **Figure 5** - **4**c. Due to the strong background signals in the UV-Vis absorption plots, I idealized the Tauc plot curves based on the method reported by Zhong et al.[247] The bandgap values of the Cu foam and the Cu foam with CuSn composites with CuSn ratios of (1:1 -8 20), (1:2 -8 20), and (2:1 -8 20) are calculated to be 2.06 eV, 2.07 eV, 2.05 eV, and 2.02 eV, respectively.

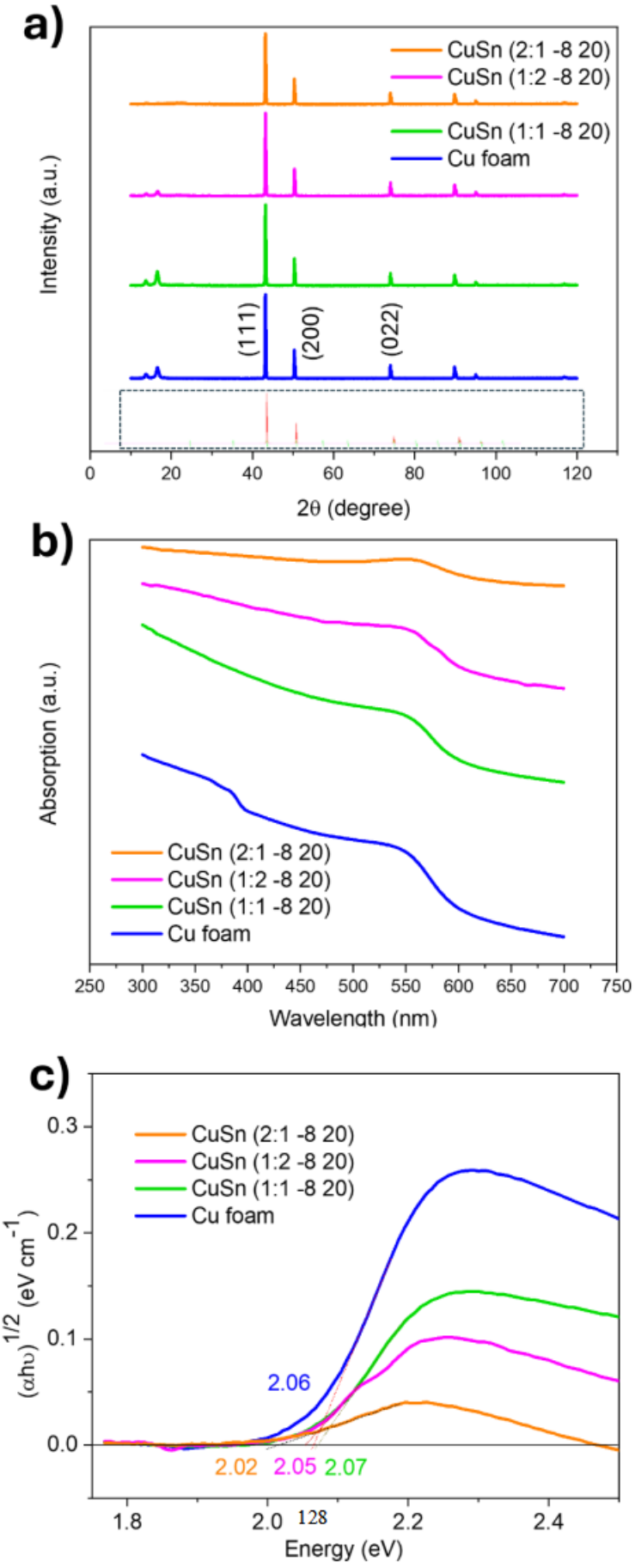
a)
CuSn (2:1 -8 20)
CuSn (1:2 -8 20)
CuSn (1:1 -8 20)
Cu foam
Intensity (a.u.)
(111)
(200)
(022)
0
20
40
60
80
100
120
2θ (degree)
b)
Absorption (a.u.)
CuSn (2:1 -8 20)
CuSn (1:2 -8 20)
CuSn (1:1 -8 20)
Cu foam
250
300
350
400
450
500
550
600
650
700
750
Wavelength (nm)
c)
CuSn (2:1 -8 20)
CuSn (1:2 -8 20)
CuSn (1:1 -8 20)
Cu foam
0.3
0.2
0.1
0.0
(αhυ)^1/2 (eV cm^-1)
2.06
2.02
2.05
2.07
1.8
2.0
2.2
2.4
Energy (eV)

Figure 5 - 4. a) XRD patterns of a series of samples; (inset shows the simulate XRD of Cu (Cubic, Fm-3m, 225)) b) UV-vis absorption and c) the calculated Tauc plots of the Cu foam and the Cu foam with CuSn CuSn composite layers with the ratios of (1:1 -8 20), (1:2 -8 20), and (2:1 -8 20), respectively.

X-ray photoelectron spectroscopy (XPS) characterizations were then conducted to investigate the chemical states of Cu and Sn elements in the photocathodes, as shown in **Figure 5 - 5**. In **Figure 5 - 5**a, the Cu $2p_{3/2}$ at 932.68 eV in Cu foam can be assigned to Cu(0), with the Cu $2p_{1/2}$ at 952.47 eV.[248] And the Cu $2p_{3/2}$ at 932.47 eV, 932.42 eV and 932.43 for Cu foam with CuSn (1:1 -8 20), (1:2 -8 20) and (2:1 -8 20) in **Figure 5 - 5**c, 5e, 5g can be assigned to Cu (I), with the Cu $2p_{1/2}$ at 952.26 eV, 952.22 eV and 952.24 eV, respectively.[248] The Cu foam does not show any Sn signal in **Figure 5 - 5**b, the Sn $3d_{5/2}$ signal for Cu foam with CuSn (1:1 -8 20), (1:2 -8 20) and (2:1 -8 20) in **Figure 5 - 5**d, 5f, 5h are 486.47 eV, 486.58 eV and 486.60 eV, with the Sn $3d_{3/2}$ at 494.92 eV, 494.98 eV and 495.05 eV, respectively, and can be assigned to Sn (IV).[270] The present of the shake-up satellites in Cu element are marked as stars in four photocathodes, indicating the presence of Cu(II), which is due to the surface oxidation after HCl treatment.[248] Compared with Cu foam with CuSn (1:1 -8 20), the Cu foam with CuSn (1:2 -8 20) and (2:1 -8 20) show lower binding energy for the Cu element and higher binding energy for the Sn element, indicating increased electron density for Cu(I) and decreased electron density for Sn(IV).[257] We also characterized the valence band (VB) of our photocathodes using VB-XPS, as shown in **Figure 5-5**j. The measured VB for Cu foam with CuSn composites (1:1 -8 20), (1:2 -8 20), and (2:1 -8 20) are similar, around 0.94 eV, while the VB of the oxidized Cu foam surface is 1.35 eV, consistent with the different chemical states of the Cu element in the XPS results.

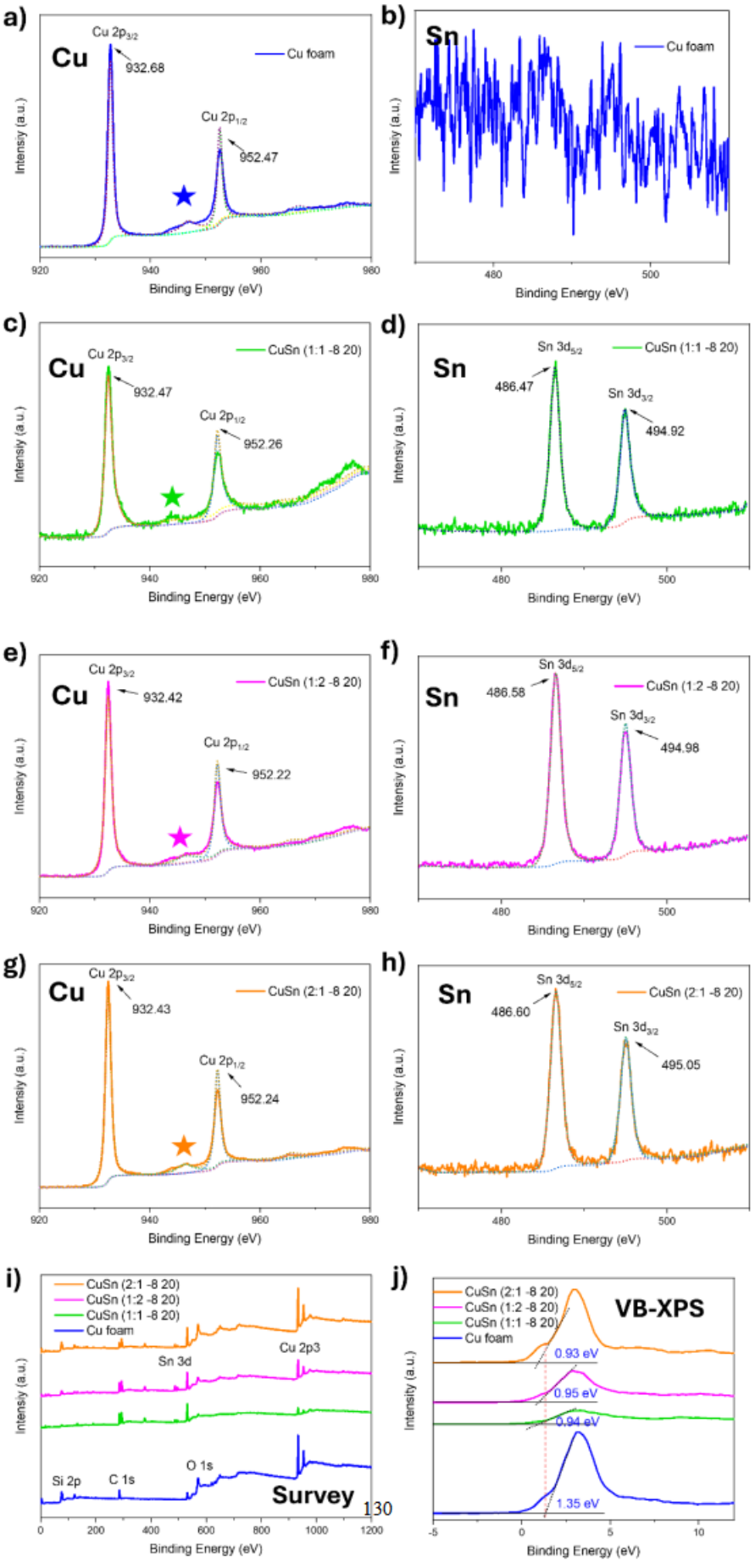
a)
Cu
Cu 2p3/2
932.68
Cu 2p1/2
952.47
Cu foam
Intensiy (a.u.)
Binding Energy (eV)
b)
Sn
Cu foam
Intensiy (a.u.)
Binding Energy (eV)
c)
Cu
Cu 2p3/2
932.47
Cu 2p1/2
952.26
CuSn (1:1 -8 20)
Intensiy (a.u.)
Binding Energy (eV)
d)
Sn
Sn 3d5/2
486.47
Sn 3d3/2
494.92
CuSn (1:1 -8 20)
Intensiy (a.u.)
Binding Energy (eV)
e)
Cu
Cu 2p3/2
932.42
Cu 2p1/2
952.22
CuSn (1:2 -8 20)
Intensiy (a.u.)
Binding Energy (eV)
f)
Sn
Sn 3d5/2
486.58
Sn 3d3/2
494.98
CuSn (1:2 -8 20)
Intensiy (a.u.)
Binding Energy (eV)
g)
Cu
Cu 2p3/2
932.43
Cu 2p1/2
952.24
CuSn (2:1 -8 20)
Intensiy (a.u.)
Binding Energy (eV)
h)
Sn
Sn 3d5/2
486.60
Sn 3d3/2
495.05
CuSn (2:1 -8 20)
Intensiy (a.u.)
Binding Energy (eV)
i)
CuSn (2:1 -8 20)
CuSn (1:2 -8 20)
CuSn (1:1 -8 20)
Cu foam
Cu 2p3
Sn 3d
O 1s
Si 2p
C 1s
Survey
Intensiy (a.u.)
Binding Energy (eV)
j)
CuSn (2:1 -8 20)
CuSn (1:2 -8 20)
CuSn (1:1 -8 20)
Cu foam
VB-XPS
0.93 eV
0.95 eV
0.94 eV
1.35 eV
Intensity (a.u.)
Binding Energy (eV)

Figure 5 - 5. a), c), e), g) Cu element and b), d), f), h) Sn element and i) XPS survey and j) VB-XPS of Cu foam and Cu foam with CuSn (1:1 -8 20), (1:2 -8 20) and (2:1 -8 20), respectively.

The PEC CO_2RR performance of the synthesized photocathodes was tested in a H-cell with a three-electrode system, using a 0.5 mol L^{-1} $KHCO_3$ solution as the electrolyte, an Ag/AgCl (3 mol L^{-1} KCl) as the reference electrode, and a Pt foil as the counter electrode. After bubbling the CO_2, under a 300 W Xe lamp illumination, the linear sweep voltammetry (LSV) curves were tested under the applied voltages ranging from 0 V to -1.5 V vs $E_{Ag/AgCl}$ with the speed of 0.01 V s^{-1} and the light was chopped at intervals of every 5 s, as shown in **Figure 5 - 6**a. All four types of photocathodes exhibited chopped photo-responses during the LSV tests, including the surface-oxidized Cu foam. I then calculated the photo-response by calculating the differences of the LSV curves measured in the dark condition and under light illumination, as shown in **Figure 5 - 6**b. It can be clearly found that the electroplated CuSn composite photocathodes show a higher photo-response than that of the pristine Cu foam. I then tested the current-time (I-t) curves under light illumination for 0.5 h. As shown in **Figure 5 - 6**c, all four types of photocathodes show relatively stable photo-induced current values, with the chopped photo response. The Cu foam deposited with CuSn composite layer with the ratio of (2:1 -8 20) shows the highest LSV current density of -35 mA cm^{-2} at an applied voltage of -1.5 V vs $E_{Ag/AgCl}$, as well as the highest I-t current density of -5 mA cm^{-2} at an applied voltage of -1 V vs $E_{Ag/AgCl}$ after 0.5 h reaction.

The Electrochemical impedance spectroscopy (EIS) measurements were carried out in the dark condition, and the Nyquist plots with the fitted results are shown in **Figure 5 - 6**d. In the inset figure of **Figure 5 - 6**d, the equivalent circuit represents the photocathode in the electrolyte, and the fitted parameters are listed in **Table 5 - 1**. As for the obtained Nyquist plots, *Rs* is the solution resistance, the radius of the arc is marked as *Rct* and represents the charge transfer resistance of the photocathode/electrolyte interface, the constant phase element (*CPE*) signifies the non-ideal capacitances, and *R1* is the charge diffusion resistance.[252, 271] The fitted results show that the Cu foam has the smallest *Rct* value of 5.080 Ω, and after electroplating with the CuSn composite layer, the resistance increased slightly to 5.829 Ω for CuSn composite layer (1:1 -8 20), 5.658 Ω for CuSn composite layer (1:2 -8 20), and 5.572 Ω for CuSn composite layer (2:1 -8 20). I then characterized the SEM images and

EDS atomic fractions of the photocathodes after the PEC tests, as shown in **Figure 5** - 7. From the measurement results, the CuSn composite layer remains on the photocathodes with the Sn signal on the surface, indicating the high stability of the CuSn composite photocathodes.

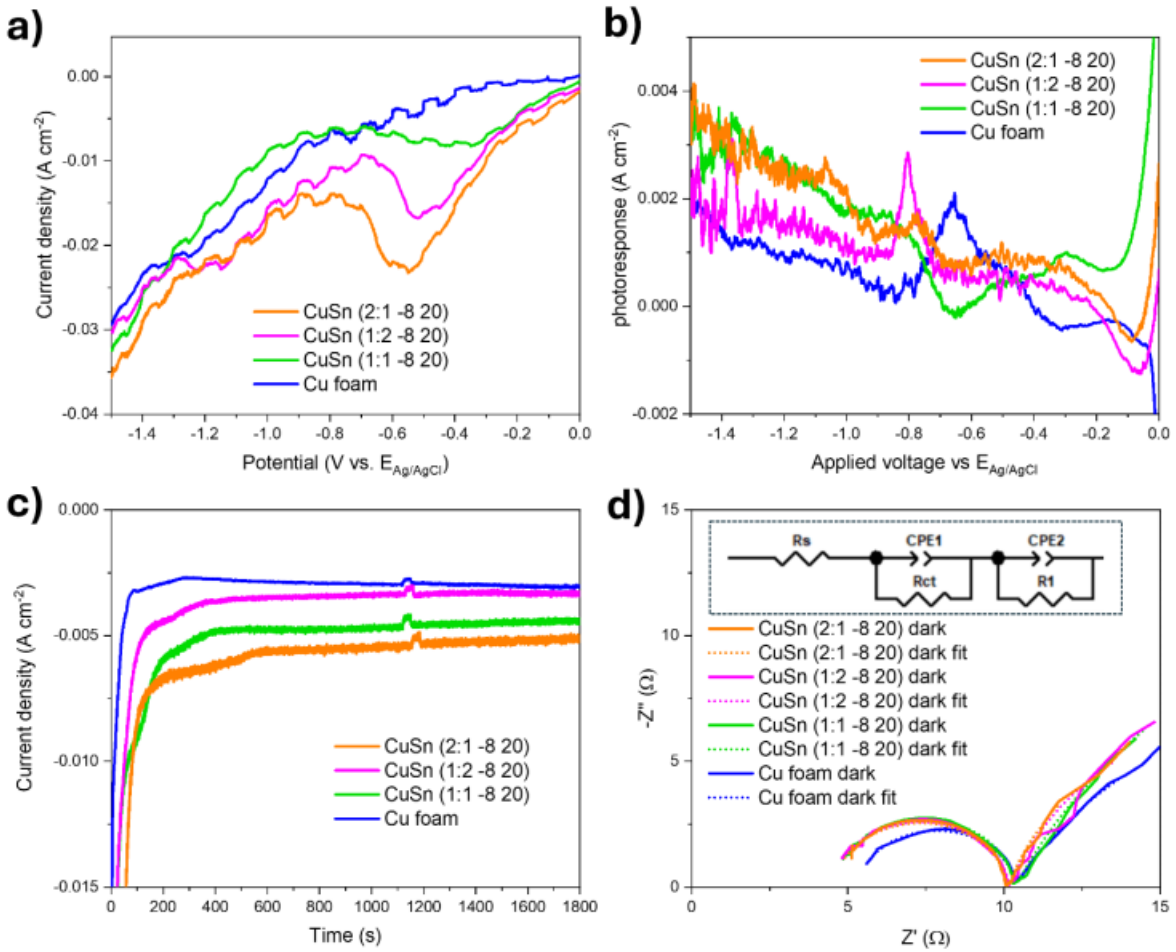

Figure 5 - 6. a) Chopped LSV curves, b) photoresponse, c) I-t curves at -1 V vs $E_{Ag/AgCl}$ and d) EIS in the dark of Cu foam and Cu foam with CuSn (1:1 -8 20), (1:2 -8 20) and (2:1 -8 20), respectively.

Table 5 - 1. The fitted parameters of Nyquist plots of Cu foam, Cu foam with CuSn (1:1 -8 20), (1:2 -8 20) and (2:1 -8 20).

	Rs (Ω)	*Error%*	*Rct* (Ω)	*Error%*	*CPE1-T* (F)	*Error%*	*CPE1-P* (F)	*Error%*

Cu foam	5.291	0.463	5.080	0.652	5.505E-07	7.698	0.920	0.647
CuSn (1:1 -8 20)	4.525	1.113	5.829	1.052	3.101E-07	13.745	0.946	1.113
CuSn (1:2 -8 20)	4.509	1.406	5.658	1.323	2.986E-07	16.984	0.945	1.378
CuSn (2:1 -8 20)	4.543	0.904	5.572	0.864	3.013E-07	11.024	0.944	0.896

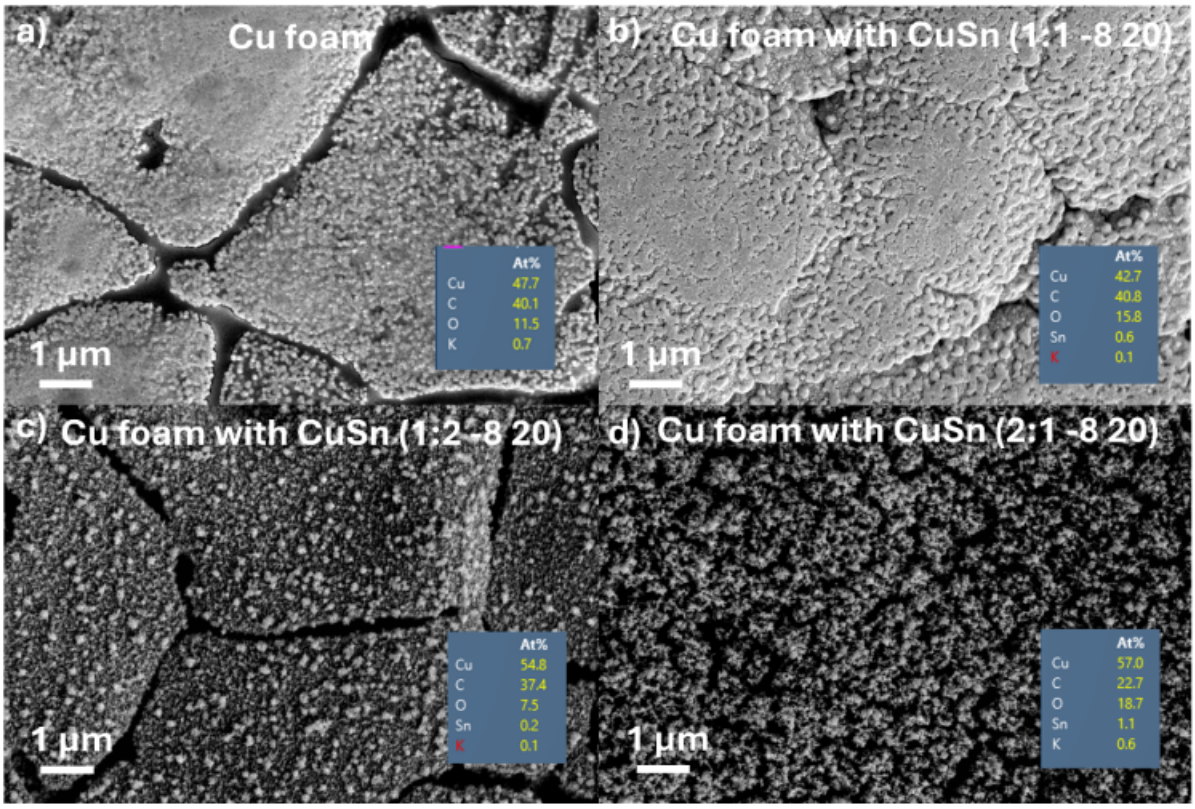

Figure 5 - 7. SEM images with the inset EDS atomic fraction pictures after PEC tests of a) Cu foam and Cu foam with CuSn b) (1:1 -8 20) c) (1:2 -8 20) and d) (2:1 -8 20).

I conducted gas chromatography (GC) and ion chromatography (IC) tests on the gas and liquid products, respectively, as shown in **Figure 5 - 8**. In the GC test, the N_2 signal at 0.99 min comes from the air in the container. Upon zooming into the gas figure post I-t test, I

observed peaks for H_2 at 0.56 min and CO at 1.16 min, absent in the pure CO_2 GC graph, indicating their production from the PEC CO_2RR. However, due to low yield, calculating total CO production proved challenging. In the IC tests, chloride from HCl treatment and sulphate from the CuSn precursor were detected. Next, I detailed the liquid formate production in $KHCO_3$ electrolyte with Cu foam, Cu foam with CuSn composites at ratios of (1:1 -8 20), (1:2 -8 20), and (2:1 -8 20) after a 0.5 h I-t test at -1 V vs $E_{Ag/AgCl}$ under light illumination. The obtained results are summarized in **Table 5 - 2**. It can be clearly found that the deposited CuSn composite layer increased the production of formate of the Cu foam, and the Cu foam with CuSn composite layer with the ratio of (1:1 -8 20) showed the highest production yield of formate of 3.968 ppm. At last, I depicted the structural schematic of Cu foam with CuSn composite photocathode for PEC CO_2RR in **Figure 5 - 8**e. The surface of Cu foam substrate is oxidized to Cu (II), and the CuSn composite is electroplated on the surface of the CuO exhibiting the oxidation state of Cu (I), Cu (II) and Sn (IV). Upon light illumination and application of negative applied voltage, the CuSn composite demonstrates high PEC CO_2RR product selectivity of $HCOO^*$.

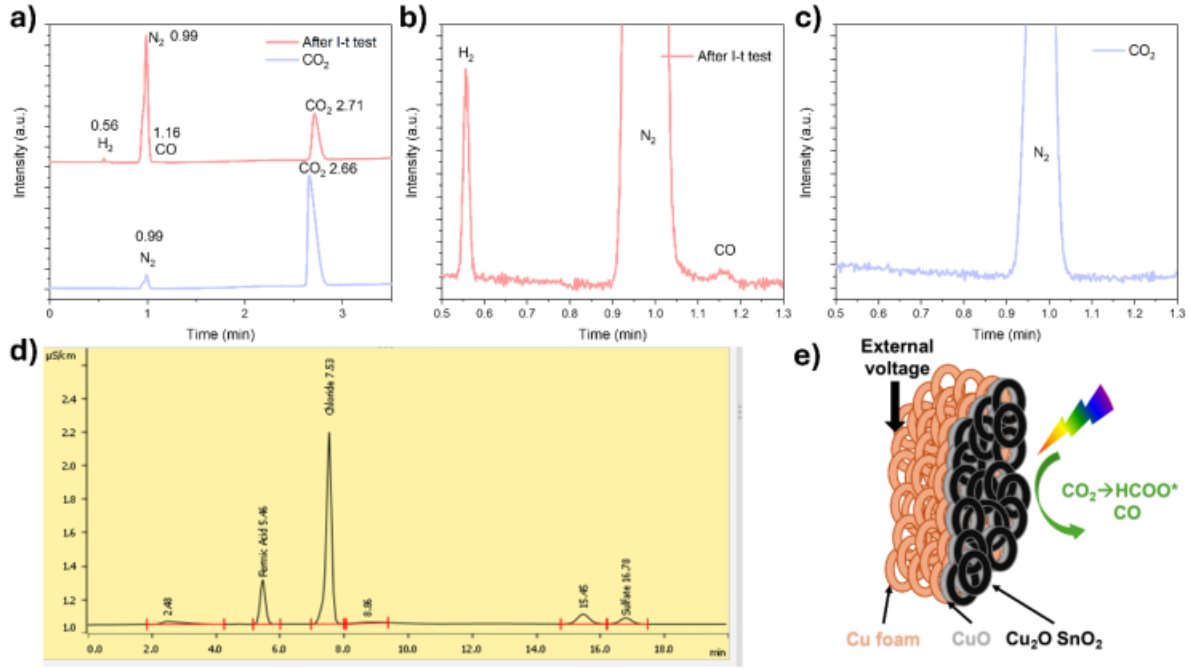

Figure 5 - 8. a-c) GC peaks of the CO_2 gas and the gas product of photocathode after I-t test. d) IC peaks of the liquid product of the photocathode after the I-t test. e) Structural schematic of Cu foam with CuSn composite photocathode for PEC CO_2RR.

Table 5 - 2. The IC tested concentrations of the Formate in the electrolyte of $KHCO_3$ and Cu foam, Cu foam with CuSn (1:1 -8 20), (1:2 -8 20) and (2:1 -8 20) after 0.5 h I-t test under light illumination.

	Formate (ppm)
$KHCO_3$	0.000
Cu foam	0.392
CuSn (1:1 -8 20)	3.968
CuSn (1:2 -8 20)	2.227
CuSn (2:1 -8 20)	3.314

5.4 Conclusion

In conclusion, I electroplated CuSn composites onto Cu foam substrates using varying parameters and employed these materials as catalysts in PEC CO2RR. Notably, Cu foam substrates exhibited a higher specific surface area compared to Cu thin-film substrates. The deposited CuSn composite layers displayed different morphological features on the Cu foam substrates, depending on the Cu:Sn ratios. Systematic characterizations revealed that Cu foam substrates exhibited Cu (0) and oxidized Cu (II) surface elements, while Cu foam substrates with CuSn composite layers exhibited Cu (I), oxidized Cu (II), and Sn (IV) peaks. UV-Vis absorption properties confirmed the photo-response of the fabricated photocathodes, demonstrating high performance in PEC tests under light illumination. Key findings include Cu foam with CuSn composite (2:1 -8 20) showing the highest LSV current density of -35 mA cm^{-2} at an applied voltage of -1.5 V vs $E_{Ag/AgCl}$ and the highest I-t current density of -5 mA cm^{-2} at an applied voltage of -1 V vs $E_{Ag/AgCl}$ after a 0.5 h reaction. Meanwhile, Cu foam with CuSn composite layer with the ratio of (1:1 -8 20) shows the most formate production yield of 3.968 ppm after a 0.5 h I-t test at an applied voltage of -1 V vs $E_{Ag/AgCl}$ under light illumination. This work demonstrates the great potential of Cu foam with CuSn composite layers for high-performance and highly stable PEC CO_2RR.

Chapter 6 Summary and Perspectives

6.1 Summary

In recent years, there has been growing interest in the photoelectrochemical (PEC) reduction of carbon dioxide (CO_2) as a promising approach to combat global warming and address energy shortages, leveraging solar energy to convert CO_2 into valuable chemicals. While halide perovskite (PVK) materials are renowned for their use in high-performance photovoltaics, they have also demonstrated potential for photocatalytic CO_2 reduction, thanks to their exceptional optoelectronic properties and cost-effective manufacturing processes. However, the direct application of these materials to PEC CO_2 reduction presents challenges, particularly due to their tendency to exhibit instability in aqueous solutions. While copper-tin (CuSn) composites have been extensively studied for electrochemical CO_2 reduction, focusing on formic acid production, their exploration in the realm of PEC CO_2 reduction has been limited. To address the environmental challenges associated with CO_2 emissions, I have proposed three strategies aimed at enhancing the efficiency of the photoelectrochemical CO_2 reduction reaction (PEC CO_2RR).

In the first work, I introduced all-inorganic perovskite $CsPbBr_3$ (CPB) materials, known for their outstanding optoelectronic properties, cost-effectiveness, and ease of processing. I explored various modification methods including 5% fluorine (F) doping, Nafion (N) solution treatment, and 15 nm Au-coating to create high-quality heterostructures and study their synergistic effects. The incorporation of F-doping ions into $CsPbBr_3$ enhanced chemical interactions within the perovskite layers and reduced trap densities, although it slightly diminished light absorption. Nafion treatment tuned the bandgap of the resulting photocathodes and passivated the material surface, further reducing trap densities but impeding charge carrier transfer, leading to increased charge recombination. On the other hand, the formation of Au/$CsPbBr_3$ Schottky junctions significantly improved the separation of photo-induced charge carriers but also introduced high dark current and capacitive current due to low resistance. By combining F-doping, Nafion, and Au-coating strategies, the Au layer effectively counteracted the impedance introduced by Nafion while retaining the ability to tune bandgaps and reduce dark and capacitive currents. F-doping further enhanced chemical interactions within the photocathodes. The resulting CPB-F-N-AU catalyst device exhibited superior PEC performance, notably achieving the highest photocurrent of -0.23 mA

cm^{-2} at a bias of -0.5 V vs $E_{Ag/AgCl}$ under 4.13 mW cm^{-2} light illumination, doubling that of the pristine CPB photocathode.

While the modified perovskites with the suitable heterostructure engineering strategy exhibited significantly improved photocurrents, the issue of poor stability cannot be overlooked. Therefore, in the second work, I employed cost-effective copper (Cu) and tin (Sn) composites, known for their high stability properties, as active materials for PEC CO_2RR. Cu-based catalysts are unique among metal-based catalysts in their ability to produce hydrocarbons due to their negative adsorption energy to *CO and positive adsorption energy to *H. On the other hand, Sn can enhance product selectivity towards formic acid due to its high affinity for oxygen and low affinity for hydrogen. Specifically, I deposited Cu nanoparticles (NPs) and CuSn bimetallic NPs onto $BiVO_4$ nanoplate substrates. The introduction of Sn in CuSn NPs altered the chemical states of Cu compared to pure Cu NPs. Under applied negative voltages, light-generated electrons were transported through band bending of BiVO4 via tunnelling and hopping effects. Notably, type-II heterojunctions were formed between BiVO4 nanoplates and CuSn NPs, promoting photo-induced charge carrier separation and transfer to the surface for PEC CO_2RR. The resulting CuSn NPs@$BiVO_4$ photocathodes exhibited the highest photocurrent of -0.774 mA cm^{-2} at an applied voltage of -0.95 V vs $E_{Ag/AgCl}$, surpassing that of pristine $BiVO_4$ or Cu NPs@$BiVO_4$ NPs by more than threefold.

It is worth noting that the photo-response property and the stability of the photocathodes can be further improved by choosing the more stable substrate, so, in the third work, I electroplated CuSn composite layers with different parameters onto the specially-selected Cu foam substrates. The Cu foam with CuSn composite layer with the ratio of (2:1 -8 20) shows the highest LSV current density of -35 mA cm^{-2} at the applied voltage of -1.5 V vs $E_{Ag/AgCl}$ and the highest I-t current density of -5 mA cm^{-2} at the applied voltage of -1 V vs $E_{Ag/AgCl}$ after a 0.5 h reaction. Meanwhile, Cu foam with CuSn composite layer with the ratio of (1:1 -8 20) shows the most formate production yield of 3.968 ppm after a 0.5 h I-t test at the applied voltage of -1 V vs $E_{Ag/AgCl}$ under light illumination. These results underscore the significance of substrate selection in improving both the photo-response and stability of photocathodes, with different CuSn composite ratios showcasing varying performance metrics.

6.2 Perspective

1) The efficiency and stability of the PEC CO_2RR can be further improved by developing more promising materials and their modifications. In the case of perovskite-based photocathodes, the decomposition of halide perovskite materials in aqueous solutions poses a significant challenge to the stability of relevant photoelectrodes. Consequently, it is crucial to devise new modification methods aimed at safeguarding the perovskite active layers in humid environments, for instance, exploring novel approaches to cultivate a dense charge transport layer on the surface of PVK, while also serving as a protective coating simultaneously.

2) When integrating bimetallic nanoparticles with light-absorbing materials for PEC CO_2RR, a primary concern is achieving a strong bond between the two materials without introducing excessive resistance. Nafion solution is commonly used as a conductive adhesive for nanoparticles on substrates, but it has been shown in previous research to impede charge carrier transfer. Therefore, further investigation is required to identify or develop ideal adhesive materials.

3) The $BiVO_4$ substrate we utilized is an n-type semiconductor, which is typically more suited for photoanodes. Hence, exploring different stable light-absorbing substrates could lead to improved light response and device stability for photocathodes.

4) While I successfully electroplated CuSn composite layers onto Cu foam substrates for PEC CO2RR, resulting in significantly improved device performance and stability, some challenges remain. Specifically, the coated layers exhibit unevenness, and they are prone to oxidation. It's essential to refine the coating conditions and parameters further to achieve superior bimetallic photocathodes.

5) Moreover, the mechanism study can be further supported by more advanced techniques, such as density functional theory (DFT) calculations and in-situ characterization techniques, to delve into the intricacies of reaction kinetics.

Reference

1. Mu, Y.-F.; Zhang, C.; Zhang, M.-R.; Zhang, W.; Zhang, M.; Lu, T.-B., Direct Z-Scheme Heterojunction of Ligand-Free FAPbBr3/α-Fe2O3 for Boosting Photocatalysis of CO2 Reduction Coupled with Water Oxidation. *ACS Applied Materials & Interfaces* **2021,** *13* (19), 22314-22322.

2. Xu, Y.-F.; Yang, M.-Z.; Chen, B.-X.; Wang, X.-D.; Chen, H.-Y.; Kuang, D.-B.; Su, C.-Y., A CsPbBr3 perovskite quantum dot/graphene oxide composite for photocatalytic CO2 reduction. *Journal of the American Chemical Society* **2017,** *139* (16), 5660-5663.

3. Inoue, T.; Fujishima, A.; Konishi, S.; Honda, K., Photoelectrocatalytic reduction of carbon dioxide in aqueous suspensions of semiconductor powders. *Nature* **1979,** *277* (5698), 637-638.

4. Chang, X.; Wang, T.; Yang, P.; Zhang, G.; Gong, J., The development of cocatalysts for photoelectrochemical CO2 reduction. *Advanced Materials* **2019,** *31* (31), 1804710.

5. Nguyen, T. P.; Nguyen, D. L. T.; Nguyen, V.-H.; Le, T.-H.; Vo, D.-V. N.; Trinh, Q. T.; Bae, S.-R.; Chae, S. Y.; Kim, S. Y.; Le, Q. V., Recent advances in TiO2-based photocatalysts for reduction of CO2 to fuels. *Nanomaterials* **2020,** *10* (2), 337.

6. Pu, Y.; Luo, Y.; Wei, X.; Sun, J.; Li, L.; Zou, W.; Dong, L., Synergistic effects of Cu2O-decorated CeO2 on photocatalytic CO2 reduction: Surface Lewis acid/base and oxygen defect. *Applied Catalysis B: Environmental* **2019,** *254*, 580-586.

7. Vu, N.-N.; Kaliaguine, S.; Do, T.-O., Synthesis of the g-C3N4/CdS nanocomposite with a chemically bonded interface for enhanced sunlight-driven CO2 photoreduction. *ACS Applied Energy Materials* **2020,** *3* (7), 6422-6433.

8. Li, X.; Sun, Y.; Xu, J.; Shao, Y.; Wu, J.; Xu, X.; Pan, Y.; Ju, H.; Zhu, J.; Xie, Y., Selective visible-light-driven photocatalytic CO 2 reduction to CH 4 mediated by atomically thin CuIn 5 S 8 layers. *Nature Energy* **2019,** *4* (8), 690-699.

9. Liang, L.; Li, X.; Zhang, J.; Ling, P.; Sun, Y.; Wang, C.; Zhang, Q.; Pan, Y.; Xu, Q.; Zhu, J., Efficient infrared light induced CO2 reduction with nearly 100% CO selectivity enabled by metallic CoN porous atomic layers. *Nano energy* **2020,** *69*, 104421.

10. Kuriki, R.; Yamamoto, M.; Higuchi, K.; Yamamoto, Y.; Akatsuka, M.; Lu, D.; Yagi, S.; Yoshida, T.; Ishitani, O.; Maeda, K., Robust binding between carbon nitride nanosheets and a binuclear ruthenium (II) complex enabling durable, selective CO2 reduction under visible light in aqueous solution. *Angewandte Chemie* **2017,** *129* (17), 4945-4949.

11. Xu, H.-Q.; Hu, J.; Wang, D.; Li, Z.; Zhang, Q.; Luo, Y.; Yu, S.-H.; Jiang, H.-L., Visible-light photoreduction of CO2 in a metal–organic framework: boosting electron–hole separation via electron trap states. *Journal of the American Chemical Society* **2015,** *137* (42), 13440-13443.

12. Li, P.; Ouyang, S.; Zhang, Y.; Kako, T.; Ye, J., Surface-coordination-induced selective synthesis of cubic and orthorhombic NaNbO 3 and their photocatalytic properties. *Journal of Materials Chemistry A* **2013,** *1* (4), 1185-1191.

13. Chand, H.; Choudhary, P.; Kumar, A.; Kumar, A.; Krishnan, V., Atmospheric pressure conversion of carbon dioxide to cyclic carbonates using a metal-free Lewis acid-base bifunctional heterogeneous catalyst. *Journal of CO2 Utilization* **2021,** *51*, 101646.

14. Singh, M.; Kumar, A.; Krishnan, V., Influence of different bismuth oxyhalides on the photocatalytic activity of graphitic carbon nitride: a comparative study under natural sunlight. *Materials Advances* **2020,** *1* (5), 1262-1272.

15. Chand, H.; Kumar, A.; Krishnan, V., Borophene and boron-based nanosheets: recent advances in synthesis strategies and applications in the field of environment and energy. *Advanced Materials Interfaces* **2021,** *8* (15), 2100045.

16. Liu, L.; Wang, S.; Huang, H.; Zhang, Y.; Ma, T., Surface sites engineering on semiconductors to boost photocatalytic CO2 reduction. *Nano Energy* **2020,** *75*, 104959.

17. Chen, J.; Dong, C.; Idriss, H.; Mohammed, O. F.; Bakr, O. M., Metal halide perovskites for solar-to-chemical fuel conversion. *Advanced Energy Materials* **2020,** *10* (13), 1902433.

18. Kweon, K. E.; Manogaran, D.; Hwang, G. S., Synergetic Role of Photogenerated Electrons and Holes in the Oxidation of CO to CO2 on Reduced TiO2 (110): A First-Principles Study. *Acs Catalysis* **2014,** *4* (11), 4051-4056.

19. White, J. L.; Baruch, M. F.; Pander III, J. E.; Hu, Y.; Fortmeyer, I. C.; Park, J. E.; Zhang, T.; Liao, K.; Gu, J.; Yan, Y., Light-driven heterogeneous reduction of carbon dioxide: photocatalysts and photoelectrodes. *Chemical reviews* **2015,** *115* (23), 12888-12935.

20. Wang, Z.; Wen, B.; Hao, Q.; Liu, L.-M.; Zhou, C.; Mao, X.; Lang, X.; Yin, W.-J.; Dai, D.; Selloni, A., Localized excitation of Ti3+ ions in the photoabsorption and photocatalytic activity of reduced rutile TiO2. *Journal of the American Chemical Society* **2015,** *137* (28), 9146-9152.

21. Wu, Q.-S.; Feng, Y.; Zhang, G.-Y.; Sun, Y.-Q.; Xu, Y.-Y.; Gao, D.-Z., α-Fe2O3

modified Bi2WO6 flower-like mesostructures with enhanced photocatalytic performance. *Materials Research Bulletin* **2014,** *49*, 440-447.

22. Ward, M. D.; White, J. R.; Bard, A. J., Electrochemical investigation of the energetics of particulate titanium dioxide photocatalysts. The methyl viologen-acetate system. *Journal of the American Chemical Society* **1983,** *105* (1), 27-31.

23. Hardee, K. L.; Bard, A. J., Semiconductor electrodes: X. Photoelectrochemical behavior of several polycrystalline metal oxide electrodes in aqueous solutions. *Journal of the Electrochemical Society* **1977,** *124* (2), 215.

24. Ferdosi, E.; Bahiraei, H.; Ghanbari, D., Investigation the photocatalytic activity of CoFe2O4/ZnO and CoFe2O4/ZnO/Ag nanocomposites for purification of dye pollutants. *Separation and Purification Technology* **2019,** *211*, 35-39.

25. Yi, Z.; Ye, J.; Kikugawa, N.; Kako, T.; Ouyang, S.; Stuart-Williams, H.; Yang, H.; Cao, J.; Luo, W.; Li, Z., An orthophosphate semiconductor with photooxidation properties under visible-light irradiation. *Nature materials* **2010,** *9* (7), 559-564.

26. Xia, Y.; He, Z.; Su, J.; Liu, Y.; Tang, B., Fabrication and photocatalytic property of novel SrTiO 3/Bi 5 O 7 I nanocomposites. *Nanoscale research letters* **2018,** *13* (1), 1-9.

27. Long, M.; Cai, W.; Kisch, H., Visible light induced photoelectrochemical properties of n-BiVO4 and n-BiVO4/p-Co3O4. *The Journal of Physical Chemistry C* **2008,** *112* (2), 548-554.

28. de Jongh, P. E.; Vanmaekelbergh, D.; Kelly, J. J., Cu 2 O: a catalyst for the photochemical decomposition of water? *Chemical Communications* **1999,** (12), 1069-1070.

29. Han, X.; Yang, X.; Liu, G.; Li, Z.; Shao, L., Boosting visible light photocatalytic activity via impregnation-induced RhB-sensitized MIL-125 (Ti). *Chemical Engineering Research and Design* **2019,** *143*, 90-99.

30. Zhang, H.; Wei, B.; Zhu, L.; Yu, J.; Sun, W.; Xu, L., Cation exchange synthesis of ZnS–Ag2S microspheric composites with enhanced photocatalytic activity. *Applied surface science* **2013,** *270*, 133-138.

31. Solakidou, M.; Giannakas, A.; Georgiou, Y.; Boukos, N.; Louloudi, M.; Deligiannakis, Y., Efficient photocatalytic water-splitting performance by ternary CdS/Pt-N-TiO2 and CdS/Pt-N, F-TiO2: interplay between CdS photo corrosion and TiO2-dopping. *Applied Catalysis B: Environmental* **2019,** *254*, 194-205.

32. Wang, D.; Zhang, M.; Zhuang, H.; Chen, X.; Wang, X.; Zheng, X.; Yang, J., The

photocatalytic properties of hollow (GaN) 1-x (ZnO) x composite nanofibers synthesized by electrospinning. *Applied Surface Science* **2017,** *396*, 888-896.

33. Wang, X.; Maeda, K.; Thomas, A.; Takanabe, K.; Xin, G.; Carlsson, J. M.; Domen, K.; Antonietti, M., A metal-free polymeric photocatalyst for hydrogen production from water under visible light. *Nature materials* **2009,** *8* (1), 76-80.

34. Chun, W.-J.; Ishikawa, A.; Fujisawa, H.; Takata, T.; Kondo, J. N.; Hara, M.; Kawai, M.; Matsumoto, Y.; Domen, K., Conduction and valence band positions of Ta2O5, TaON, and Ta3N5 by UPS and electrochemical methods. *The Journal of Physical Chemistry B* **2003,** *107* (8), 1798-1803.

35. Wang, J.; Liu, J.; Du, Z.; Li, Z., Recent advances in metal halide perovskite photocatalysts: Properties, synthesis and applications. *Journal of Energy Chemistry* **2021,** *54*, 770-785.

36. Wang, J.; Lin, S.; Tian, N.; Ma, T.; Zhang, Y.; Huang, H., Nanostructured Metal Sulfides: Classification, Modification Strategy, and Solar-Driven CO2 Reduction Application. *Advanced Functional Materials* **2021,** *31* (9), 2008008.

37. Pan, S.; Li, J.; Wen, Z.; Lu, R.; Zhang, Q.; Jin, H.; Zhang, L.; Chen, Y.; Wang, S., Halide Perovskite Materials for Photo (Electro) Chemical Applications: Dimensionality, Heterojunction, and Performance. *Advanced Energy Materials* **2021**, 2004002.

38. Huang, H.; Pradhan, B.; Hofkens, J.; Roeffaers, M. B.; Steele, J. A., Solar-driven metal halide perovskite photocatalysis: Design, stability, and performance. *ACS Energy Letters* **2020,** *5* (4), 1107-1123.

39. Shi, D.; Adinolfi, V.; Comin, R.; Yuan, M.; Alarousu, E.; Buin, A.; Chen, Y.; Hoogland, S.; Rothenberger, A.; Katsiev, K., Low trap-state density and long carrier diffusion in organolead trihalide perovskite single crystals. *Science* **2015,** *347* (6221), 519-522.

40. Yang, Y.; Yan, Y.; Yang, M.; Choi, S.; Zhu, K.; Luther, J. M.; Beard, M. C., Low surface recombination velocity in solution-grown CH 3 NH 3 PbBr 3 perovskite single crystal. *Nat. Commun.* **2015,** *6* (1), 1-6.

41. Alarousu, E.; El-Zohry, A. M.; Yin, J.; Zhumekenov, A. A.; Yang, C.; Alhabshi, E.; Gereige, I.; AlSaggaf, A.; Malko, A. V.; Bakr, O. M., Ultralong radiative states in hybrid perovskite crystals: compositions for submillimeter diffusion lengths. *The journal of physical chemistry letters* **2017,** *8* (18), 4386-4390.

42. Liu, J.; Song, K.; Shin, Y.; Liu, X.; Chen, J.; Yao, K. X.; Pan, J.; Yang, C.; Yin, J.; Xu, L.-J., Light-induced self-assembly of cubic CsPbBr3 perovskite nanocrystals into nanowires. *Chemistry of Materials* **2019,** *31* (17), 6642-6649.

43. Fu, Y.; Zhu, H.; Chen, J.; Hautzinger, M. P.; Zhu, X.-Y.; Jin, S., Metal halide perovskite nanostructures for optoelectronic applications and the study of physical properties. *Nature Reviews Materials* **2019,** *4* (3), 169-188.

44. Chen, Z.; Dong, Q.; Liu, Y.; Bao, C.; Fang, Y.; Lin, Y.; Tang, S.; Wang, Q.; Xiao, X.; Bai, Y., Thin single crystal perovskite solar cells to harvest below-bandgap light absorption. *Nat. Commun.* **2017,** *8* (1), 1-7.

45. Cao, Y.; Wang, N.; Tian, H.; Guo, J.; Wei, Y.; Chen, H.; Miao, Y.; Zou, W.; Pan, K.; He, Y., Perovskite light-emitting diodes based on spontaneously formed submicrometre-scale structures. *Nature* **2018,** *562* (7726), 249-253.

46. Zhang, Y.; Sun, R.; Ou, X.; Fu, K.; Chen, Q.; Ding, Y.; Xu, L.-J.; Liu, L.; Han, Y.; Malko, A. V., Metal halide perovskite nanosheet for X-ray high-resolution scintillation imaging screens. *ACS nano* **2019,** *13* (2), 2520-2525.

47. Chin, X. Y.; Cortecchia, D.; Yin, J.; Bruno, A.; Soci, C., Lead iodide perovskite light-emitting field-effect transistor. *Nat. Commun.* **2015,** *6* (1), 1-9.

48. Vassilakopoulou, A.; Papadatos, D.; Zakouras, I.; Koutselas, I., Mixtures of quasi-two and three dimensional hybrid organic-inorganic semiconducting perovskites for single layer LED. *Journal of Alloys and Compounds* **2017,** *692*, 589-598.

49. Hou, J.; Cao, S.; Wu, Y.; Gao, Z.; Liang, F.; Sun, Y.; Lin, Z.; Sun, L., Inorganic colloidal perovskite quantum dots for robust solar CO2 reduction. *Chemistry–A European Journal* **2017,** *23* (40), 9481-9485.

50. Sheng, J.; He, Y.; Li, J.; Yuan, C.; Huang, H.; Wang, S.; Sun, Y.; Wang, Z.; Dong, F., Identification of halogen-associated active sites on bismuth-based perovskite quantum dots for efficient and selective CO2-to-CO photoreduction. *ACS nano* **2020,** *14* (10), 13103-13114.

51. Wang, W.; Wang, L.; Su, W.; Xing, Y., Photocatalytic CO2 reduction over copper-based materials: A review. *Journal of CO2 Utilization* **2022,** *61*, 102056.

52. Vasileff, A.; Xu, C.; Jiao, Y.; Zheng, Y.; Qiao, S.-Z., Surface and interface engineering in copper-based bimetallic materials for selective CO2 electroreduction. *Chem* **2018,** *4* (8), 1809-1831.

53. Hori, Y.; Wakebe, H.; Tsukamoto, T.; Koga, O., Electrocatalytic process of CO

selectivity in electrochemical reduction of CO2 at metal electrodes in aqueous media. *Electrochimica Acta* **1994,** *39* (11-12), 1833-1839.

54. Xie, H.; Wang, T.; Liang, J.; Li, Q.; Sun, S., Cu-based nanocatalysts for electrochemical reduction of CO2. *Nano Today* **2018,** *21*, 41-54.

55. Nitopi, S.; Bertheussen, E.; Scott, S. B.; Liu, X.; Engstfeld, A. K.; Horch, S.; Seger, B.; Stephens, I. E.; Chan, K.; Hahn, C., Progress and perspectives of electrochemical CO2 reduction on copper in aqueous electrolyte. *Chemical reviews* **2019,** *119* (12), 7610-7672.

56. Zhang, M.; Cheng, J.; Xuan, X.; Zhou, J.; Cen, K., Pt/graphene aerogel deposited in Cu foam as a 3D binder-free cathode for CO2 reduction into liquid chemicals in a TiO2 photoanode-driven photoelectrochemical cell. *Chemical Engineering Journal* **2017,** *322*, 22-32.

57. Zhao, J.; Li, Y.; Zhu, Y.; Wang, Y.; Wang, C., Enhanced CO2 photoreduction activity of black TiO2− coated Cu nanoparticles under visible light irradiation: Role of metallic Cu. *Applied Catalysis A: General* **2016,** *510*, 34-41.

58. Shown, I.; Hsu, H.-C.; Chang, Y.-C.; Lin, C.-H.; Roy, P. K.; Ganguly, A.; Wang, C.-H.; Chang, J.-K.; Wu, C.-I.; Chen, L.-C., Highly efficient visible light photocatalytic reduction of CO2 to hydrocarbon fuels by Cu-nanoparticle decorated graphene oxide. *Nano letters* **2014,** *14* (11), 6097-6103.

59. Xie, H.; Wang, J.; Ithisuphalap, K.; Wu, G.; Li, Q., Recent advances in Cu-based nanocomposite photocatalysts for CO2 conversion to solar fuels. *Journal of energy chemistry* **2017,** *26* (6), 1039-1049.

60. Méndez-Medrano, M. G.; Kowalska, E.; Ohtani, B.; Bahena Uribe, D.; Colbeau-Justin, C.; Rau, S.; Rodríguez-López, J. L.; Remita, H., Heterojunction of CuO nanoclusters with TiO2 for photo-oxidation of organic compounds and for hydrogen production. *The Journal of Chemical Physics* **2020,** *153* (3).

61. Song, Y.; Ichimura, M., H 2 O 2 treatment of electrochemically deposited Cu 2 O thin films for enhancing optical absorption. *International Journal of Photoenergy* **2013,** *2013*.

62. Wang, J.-C.; Zhang, L.; Fang, W.-X.; Ren, J.; Li, Y.-Y.; Yao, H.-C.; Wang, J.-S.; Li, Z.-J., Enhanced photoreduction CO2 activity over direct Z-scheme α-Fe2O3/Cu2O heterostructures under visible light irradiation. *ACS applied materials & interfaces* **2015,** *7* (16), 8631-8639.

63. Wang, N.; Pan, Y.; Lu, T.; Li, X.; Wu, S.; Wu, J., A new ribbon-ignition method for

fabricating p-CuO/n-CeO2 heterojunction with enhanced photocatalytic activity. *Applied Surface Science* **2017,** *403*, 699-706.

64. Wang, Y.; Wang, H.; Guo, L.; He, T., Boosting the photocatalytic CO2 reduction reaction over BiOCl nanosheet via Cu modification. *Journal of Colloid and Interface Science* **2023**.

65. Kumaravel, V.; Bartlett, J.; Pillai, S. C., Photoelectrochemical conversion of carbon dioxide (CO2) into fuels and value-added products. *ACS Energy Letters* **2020,** *5* (2), 486-519.

66. Li, K.; Peng, B.; Peng, T., Recent advances in heterogeneous photocatalytic CO2 conversion to solar fuels. *ACS Catalysis* **2016,** *6* (11), 7485-7527.

67. Shyamal, S.; Pradhan, N., Halide perovskite nanocrystal photocatalysts for CO2 reduction: successes and challenges. *The Journal of Physical Chemistry Letters* **2020,** *11* (16), 6921-6934.

68. Hong, J.; Zhang, W.; Ren, J.; Xu, R., Photocatalytic reduction of CO 2: a brief review on product analysis and systematic methods. *Analytical methods* **2013,** *5* (5), 1086-1097.

69. Habisreutinger, S. N.; Schmidt-Mende, L.; Stolarczyk, J. K., Photocatalytic reduction of CO2 on TiO2 and other semiconductors. *Angewandte Chemie International Edition* **2013,** *52* (29), 7372-7408.

70. Hiragond, C. B.; Powar, N. S.; In, S.-I., Recent Developments in Lead and Lead-Free Halide Perovskite Nanostructures towards Photocatalytic CO2 Reduction. *Nanomaterials* **2020,** *10* (12), 2569.

71. Ou, M.; Tu, W.; Yin, S.; Xing, W.; Wu, S.; Wang, H.; Wan, S.; Zhong, Q.; Xu, R., Amino-assisted anchoring of CsPbBr3 perovskite quantum dots on porous g-C3N4 for enhanced photocatalytic CO2 reduction. *Angewandte Chemie* **2018,** *130* (41), 13758-13762.

72. Wu, L.-Y.; Zhang, M.-R.; Feng, Y.-X.; Zhang, W.; Zhang, M.; Lu, T.-B., 2D Metal Halide Perovskite Nanosheets for Efficient Photocatalytic CO2 Reduction. *Solar RRL* **2021,** *5(8)*, 2100263.

73. Wang, Y.; Wang, S.; Lou, X. W., Dispersed nickel cobalt oxyphosphide nanoparticles confined in multichannel hollow carbon fibers for photocatalytic CO2 reduction. *Angewandte Chemie International Edition* **2019,** *58* (48), 17236-17240.

74. Tang, R.; Sun, H.; Zhang, Z.; Liu, L.; Meng, F.; Zhang, X.; Yang, W.; Li, Z.; Zhao, Z.; Zheng, R., Incorporating plasmonic Au-nanoparticles into three-dimensionally ordered macroporous perovskite frameworks for efficient photocatalytic CO2 reduction. *Chemical*

Engineering Journal **2021**, 132137.

75. Bera, S.; Shyamal, S.; Pradhan, N., Chemically Spiraling CsPbBr3 Perovskite Nanorods. *Journal of the American Chemical Society* **2021**.

76. Bai, S.; Zhang, N.; Gao, C.; Xiong, Y., Defect engineering in photocatalytic materials. *Nano Energy* **2018,** *53*, 296-336.

77. Tang, C.; Chen, C.; Xu, W.; Xu, L., Design of doped cesium lead halide perovskite as a photo-catalytic CO 2 reduction catalyst. *Journal of Materials Chemistry A* **2019,** *7* (12), 6911-6919.

78. Shyamal, S.; Dutta, S. K.; Pradhan, N., Doping iron in CsPbBr3 perovskite nanocrystals for efficient and product selective CO2 reduction. *The journal of physical chemistry letters* **2019,** *10* (24), 7965-7969.

79. Wang, J.-C.; Li, N.; Idris, A. M.; Wang, J.; Du, X.; Pan, Z.; Li, Z., Surface Defect Engineering of CsPbBr3 Nanocrystals for High Efficient Photocatalytic CO2 Reduction. *Solar RRL* **2021**, 2100154.

80. Guo, S.-H.; Zhou, J.; Zhao, X.; Sun, C.-Y.; You, S.-Q.; Wang, X.-L.; Su, Z.-M., Enhanced CO2 photoreduction via tuning halides in perovskites. *Journal of Catalysis* **2019,** *369*, 201-208.

81. Han, C.; Zhu, X.; Martin, J. S.; Lin, Y.; Spears, S.; Yan, Y., Recent Progress in Engineering Metal Halide Perovskites for Efficient Visible-Light-Driven Photocatalysis. *ChemSusChem* **2020,** *13* (16), 4005-4025.

82. Cheng, J.; Mu, Y.; Wu, L.; Liu, Z.; Su, K.; Dong, G.; Zhang, M.; Lu, T., Acetate-assistant efficient cation-exchange of halide perovskite nanocrystals to boost the photocatalytic CO2 reduction. *Nano Research* **2021**, 1-8.

83. Zhou, L.; Xu, Y. F.; Chen, B. X.; Kuang, D. B.; Su, C. Y., Synthesis and Photocatalytic Application of Stable Lead-Free Cs2AgBiBr6 Perovskite Nanocrystals. *Small* **2018,** *14* (11), 1703762.

84. Chen, P.; Huang, Y.; Shi, Z.; Chen, X.; Li, N., Improving the Catalytic CO2 Reduction on Cs2AgBiBr6 by Halide Defect Engineering: A DFT Study. *Materials* **2021,** *14* (10), 2469.

85. Wu, D.; Zhou, J.; Kang, W.; An, K.; Yang, J.; Zhou, M.; He, P.; Huang, Q.; Tang, X., Ultrastable Lead-Free CsAgCl2 Perovskite Microcrystals for Photocatalytic CO2 Reduction. *The Journal of Physical Chemistry Letters* **2021,** *12*, 5110-5114.

86. Shyamal, S.; Dutta, S. K.; Das, T.; Sen, S.; Chakraborty, S.; Pradhan, N., Facets and defects in perovskite nanocrystals for photocatalytic CO2 reduction. *The journal of physical chemistry letters* **2020,** *11* (9), 3608-3614.

87. Li, X.; Zhu, H.; Wang, K.; Cao, A.; Wei, J.; Li, C.; Jia, Y.; Li, Z.; Li, X.; Wu, D., Graphene-on-silicon Schottky junction solar cells. *Advanced materials* **2010,** *22* (25), 2743-2748.

88. Zhang, L.; Jia, Y.; Wang, S.; Li, Z.; Ji, C.; Wei, J.; Zhu, H.; Wang, K.; Wu, D.; Shi, E., Carbon nanotube and CdSe nanobelt Schottky junction solar cells. *Nano letters* **2010,** *10* (9), 3583-3589.

89. Zhou, C.; Wang, S.; Zhao, Z.; Shi, Z.; Yan, S.; Zou, Z., A Facet-Dependent Schottky-Junction Electron Shuttle in a BiVO4 {010}–Au–Cu2O Z-Scheme Photocatalyst for Efficient Charge Separation. *Advanced Functional Materials* **2018,** *28* (31), 1801214.

90. Wang, X.; Long, R.; Liu, D.; Yang, D.; Wang, C.; Xiong, Y., Enhanced full-spectrum water splitting by confining plasmonic Au nanoparticles in N-doped TiO2 bowl nanoarrays. *Nano Energy* **2016,** *24*, 87-93.

91. Yang, Y.; Zeng, Z.; Zeng, G.; Huang, D.; Xiao, R.; Zhang, C.; Zhou, C.; Xiong, W.; Wang, W.; Cheng, M., Ti3C2 Mxene/porous g-C3N4 interfacial Schottky junction for boosting spatial charge separation in photocatalytic H2O2 production. *Applied Catalysis B: Environmental* **2019,** *258*, 117956.

92. Singh, R. S.; Nalla, V.; Chen, W.; Wee, A. T. S.; Ji, W., Laser patterning of epitaxial graphene for Schottky junction photodetectors. *ACS nano* **2011,** *5* (7), 5969-5975.

93. Wang, X.; He, J.; Li, J.; Lu, G.; Dong, F.; Majima, T.; Zhu, M., Immobilizing perovskite CsPbBr3 nanocrystals on Black phosphorus nanosheets for boosting charge separation and photocatalytic CO2 reduction. *Applied Catalysis B: Environmental* **2020,** *277*, 119230.

94. Trivedi, S.; Prochowicz, D.; Kalam, A.; Tavakoli, M.; Yadav, P., Development of all-inorganic lead halide perovskites for carbon dioxide photoreduction. *Renewable and Sustainable Energy Reviews* **2021,** *145*, 111047.

95. Xu, Y.-F.; Yang, M.-Z.; Chen, H.-Y.; Liao, J.-F.; Wang, X.-D.; Kuang, D.-B., Enhanced solar-driven gaseous CO2 conversion by CsPbBr3 nanocrystal/Pd nanosheet Schottky-junction photocatalyst. *ACS Applied Energy Materials* **2018,** *1* (9), 5083-5089.

96. Chen, Y.-X.; Xu, Y.-F.; Wang, X.-D.; Chen, H.-Y.; Kuang, D.-B., Solvent selection

and Pt decoration towards enhanced photocatalytic CO 2 reduction over CsPbBr 3 perovskite single crystals. *Sustainable Energy & Fuels* **2020,** *4* (5), 2249-2255.

97. Jana, J.; Ganguly, M.; Pal, T., Enlightening surface plasmon resonance effect of metal nanoparticles for practical spectroscopic application. *RSC advances* **2016,** *6* (89), 86174-86211.

98. Chen, T.; Zhou, M.; Chen, W.; Zhang, Y.; Ou, S.; Liu, Y., Cs2AgInCl6 Double Perovskite Quantum Dots Decorated with Ag Nanoparticles for Photocatalytic CO2 Reduction. *Sustainable Energy & Fuels* **2021**.

99. Wang, X.; Li, K.; He, J.; Yang, J.; Dong, F.; Mai, W.; Zhu, M., Defect in reduced graphene oxide tailored selectivity of photocatalytic CO2 reduction on Cs4PbBr6 pervoskite hole-in-microdisk structure. *Nano Energy* **2020,** *78*, 105388.

100. Kumar, S.; Hassan, I.; Regue, M.; Gonzalez-Carrero, S.; Rattner, E.; Isaacs, M. A.; Eslava, S., Mechanochemically synthesized Pb-free halide perovskite-based Cs 2 AgBiBr 6–Cu–RGO nanocomposite for photocatalytic CO 2 reduction. *Journal of Materials Chemistry A* **2021,** *9* (20), 12179-12187.

101. Cheng, R.; Jin, H.; Roeffaers, M. B.; Hofkens, J.; Debroye, E., Incorporation of Cesium Lead Halide Perovskites into g-C3N4 for Photocatalytic CO2 Reduction. *ACS omega* **2020,** *5* (38), 24495-24503.

102. Guo, X.-X.; Tang, S.-F.; Mu, Y.-F.; Wu, L.-Y.; Dong, G.-X.; Zhang, M., Engineering a CsPbBr 3-based nanocomposite for efficient photocatalytic CO 2 reduction: improved charge separation concomitant with increased activity sites. *RSC advances* **2019,** *9* (59), 34342-34348.

103. Wang, X.-D.; Huang, Y.-H.; Liao, J.-F.; Jiang, Y.; Zhou, L.; Zhang, X.-Y.; Chen, H.-Y.; Kuang, D.-B., In situ construction of a Cs2SnI6 perovskite nanocrystal/SnS2 nanosheet heterojunction with boosted interfacial charge transfer. *Journal of the American Chemical Society* **2019,** *141* (34), 13434-13441.

104. Wang, X.; He, J.; Mao, L.; Cai, X.; Sun, C.; Zhu, M., CsPbBr3 perovskite nanocrystals anchoring on monolayer MoS2 nanosheets for efficient photocatalytic CO2 reduction. *Chemical Engineering Journal* **2021,** *416*, 128077.

105. Yoon, J. W.; Kim, J. H.; Kim, C.; Jang, H. W.; Lee, J. H., MOF-Based Hybrids for Solar Fuel Production. *Advanced Energy Materials* **2021**, 2003052.

106. Wang, Z.; Li, X.; Xu, H.; Yang, Y.; Cui, Y.; Pan, H.; Wang, Z.; Chen, B.; Qian, G.,

Porous anatase TiO 2 constructed from a metal–organic framework for advanced lithium-ion battery anodes. *Journal of Materials Chemistry A* **2014,** *2* (31), 12571-12575.

107. Li, J.-R.; Kuppler, R. J.; Zhou, H.-C., Selective gas adsorption and separation in metal–organic frameworks. *Chemical Society Reviews* **2009,** *38* (5), 1477-1504.

108. Denny, M. S.; Moreton, J. C.; Benz, L.; Cohen, S. M., Metal–organic frameworks for membrane-based separations. *Nature Reviews Materials* **2016,** *1* (12), 1-17.

109. Hu, Z.; Deibert, B. J.; Li, J., Luminescent metal–organic frameworks for chemical sensing and explosive detection. *Chemical Society Reviews* **2014,** *43* (16), 5815-5840.

110. An, J.; Geib, S. J.; Rosi, N. L., Cation-triggered drug release from a porous zinc–adeninate metal– organic framework. *Journal of the American Chemical Society* **2009,** *131* (24), 8376-8377.

111. Wan, S.; Ou, M.; Zhong, Q.; Wang, X., Perovskite-type CsPbBr3 quantum dots/UiO-66 (NH2) nanojunction as efficient visible-light-driven photocatalyst for CO2 reduction. *Chemical Engineering Journal* **2019,** *358*, 1287-1295.

112. Cheng, R.; Debroye, E.; Hofkens, J.; Roeffaers, M. B., Efficient photocatalytic CO2 reduction with MIL-100 (Fe)-cspbbr3 composites. *Catalysts* **2020,** *10* (11), 1352.

113. Xi, Y.; Zhang, X.; Shen, Y.; Dong, W.; Fan, Z.; Wang, K.; Zhong, S.; Bai, S., Aspect ratio dependent photocatalytic enhancement of CsPbBr3 in CO2 reduction with two-dimensional metal organic framework as a cocatalyst. *Applied Catalysis B: Environmental* **2021,** *297*, 120411.

114. Li, N.; Zhai, X.-P.; Yan, W.-K.; Zhang, Y.-J.; Zhang, Z.-T.; Xiao, M.-J.; Zhang, X.-D.; Wang, Q.; Zhang, H.-L., Boosting Cascade Electron Transfer for Highly Efficient CO2 Photoreduction. *Solar RRL* **2021,** *5* (11), 2100558.

115. Jiang, Y.; Liao, J.-F.; Chen, H.-Y.; Zhang, H.-H.; Li, J.-Y.; Wang, X.-D.; Kuang, D.-B., All-solid-state Z-scheme α-Fe2O3/amine-RGO/CsPbBr3 hybrids for visible-light-driven photocatalytic CO2 reduction. *Chem* **2020,** *6* (3), 766-780.

116. Mu, Y. F.; Zhang, W.; Dong, G. X.; Su, K.; Zhang, M.; Lu, T. B., Ultrathin and Small-Size Graphene Oxide as an Electron Mediator for Perovskite-Based Z-Scheme System to Significantly Enhance Photocatalytic CO2 Reduction. *Small* **2020,** *16* (29), 2002140.

117. Wang, Y.; Huang, H.; Zhang, Z.; Wang, C.; Yang, Y.; Li, Q.; Xu, D., Lead-free perovskite Cs2AgBiBr6@ g-C3N4 Z-scheme system for improving CH4 production in photocatalytic CO2 reduction. *Applied Catalysis B: Environmental* **2021,** *282*, 119570.

118. Wang, J.; Wang, J.; Li, N.; Du, X.; Ma, J.; He, C.; Li, Z., Direct Z-scheme 0D/2D heterojunction of CsPbBr3 quantum dots/Bi2WO6 nanosheets for efficient photocatalytic CO2 reduction. *ACS Applied Materials & Interfaces* **2020,** *12* (28), 31477-31485.

119. Liu, Z.-L.; Liu, R.-R.; Mu, Y.-F.; Feng, Y.-X.; Dong, G.-X.; Zhang, M.; Lu, T.-B., In Situ Construction of Lead-Free Perovskite Direct Z-Scheme Heterojunction Cs3Bi2I9/Bi2WO6 for Efficient Photocatalysis of CO2 Reduction. *Solar RRL* **2021,** *5* (3), 2000691.

120. Xu, Y. F.; Wang, X. D.; Liao, J. F.; Chen, B. X.; Chen, H. Y.; Kuang, D. B., Amorphous-TiO2-Encapsulated CsPbBr3 Nanocrystal Composite Photocatalyst with Enhanced Charge Separation and CO2 Fixation. *Advanced materials interfaces* **2018,** *5* (22), 1801015.

121. Kong, Z.-C.; Liao, J.-F.; Dong, Y.-J.; Xu, Y.-F.; Chen, H.-Y.; Kuang, D.-B.; Su, C.-Y., Core@ shell CsPbBr3@ zeolitic imidazolate framework nanocomposite for efficient photocatalytic CO2 reduction. *ACS Energy Letters* **2018,** *3* (11), 2656-2662.

122. Su, K.; Dong, G.-X.; Zhang, W.; Liu, Z.-L.; Zhang, M.; Lu, T.-B., In situ coating CsPbBr3 nanocrystals with graphdiyne to boost the activity and stability of photocatalytic CO2 reduction. *ACS Applied Materials & Interfaces* **2020,** *12* (45), 50464-50471.

123. Zhang, Z.; Shu, M.; Jiang, Y.; Xu, J., Fullerene modified CsPbBr3 perovskite nanocrystals for efficient charge separation and photocatalytic CO2 reduction. *Chemical Engineering Journal* **2021,** *414*, 128889.

124. Li, L.; Zhang, Z.; Ding, C.; Xu, J., Boosting charge separation and photocatalytic CO2 reduction of CsPbBr3 perovskite quantum dots by hybridizing with P3HT. *Chemical Engineering Journal* **2021,** *419*, 129543.

125. Shi, G.; Yang, L.; Liu, Z.; Chen, X.; Zhou, J.; Yu, Y., Photocatalytic reduction of CO2 to CO over copper decorated g-C3N4 nanosheets with enhanced yield and selectivity. *Applied Surface Science* **2018,** *427*, 1165-1173.

126. Lan, Y.; Xie, Y.; Chen, J.; Hu, Z.; Cui, D., Selective photocatalytic CO 2 reduction on copper–titanium dioxide: A study of the relationship between CO production and H 2 suppression. *Chemical Communications* **2019,** *55* (56), 8068-8071.

127. Zhang, X.; Wang, H.; An, W.; Guo, H.; Liu, L.; Cui, W., Ionic liquid promotes the efficient photocatalytic reduction of CO2 by Cu nanodots modified oxygen-vacancy Bi2MoO6. *Applied Surface Science* **2023,** *641*, 158464.

128. Huang, Q.; Lin, J.; Yang, D.; Hu, Y.; Zhou, G.; Li, W.; Hu, J.; Yang, Z., Synergism of the Plasmonic Effect and Schottky Junction to Effectively Facilitate Photocatalytic CO2 Reduction of Bi4O5I2@ Cu. *ACS Sustainable Chemistry & Engineering* **2023**.

129. Wang, B.; Yang, F.; Dong, Y.; Cao, Y.; Wang, J.; Yang, B.; Wei, Y.; Wan, W.; Chen, J.; Jing, H., Cu@ porphyrin-COFs nanorods for efficiently photoelectrocatalytic reduction of CO2. *Chemical Engineering Journal* **2020,** *396*, 125255.

130. Li, B.; Liu, X.; Lei, B.; Luo, H.; Liu, X.; Liu, H.; Gu, Q.; Ma, J. G.; Cheng, P., Ultrastable Cu-Based Dual-Channel Heterowire for the Switchable Electro-/Photocatalytic Reduction of CO2. *Advanced Science* **2023,** *10* (26), 2302881.

131. Guo, S.-T.; Tang, Z.-Y.; Du, Y.-W.; Liu, T.; Ouyang, T.; Liu, Z.-Q., Chlorine anion stabilized Cu2O/ZnO photocathode for selective CO2 reduction to CH4. *Applied Catalysis B: Environmental* **2023,** *321*, 122035.

132. Zheng, Y.; Duan, Z.; Liang, R.; Lv, R.; Wang, C.; Zhang, Z.; Wan, S.; Wang, S.; Xiong, H.; Ngaw, C. K., Shape-Dependent Performance of Cu/Cu2O for Photocatalytic Reduction of CO2. *ChemSusChem* **2022,** *15* (10), e202200216.

133. Ávila-López, M. A.; Gavrielides, S.; Luo, X.; Ojoajogwu, A. E.; Tan, J. Z.; Luévano-Hipólito, E.; Torres-Martínez, L. M.; Maroto-Valer, M. M., Comparative study of CO2 photoreduction using different conformations of CuO photocatalyst: Powder, coating on mesh and thin film. *Journal of CO2 Utilization* **2021,** *50*, 101588.

134. Choi, S. Y.; Yoon, S. H.; Kang, U.; Han, D. S.; Park, H., Standalone photoconversion of CO2 using Ti and TiOx-sandwiched heterojunction photocatalyst of CuO and CuFeO2 films. *Applied Catalysis B: Environmental* **2021,** *288*, 119985.

135. Yin, H.; Li, J., New insight into photocatalytic CO2 conversion with nearly 100% CO selectivity by CuO-Pd/HxMoO3− y hybrids. *Applied Catalysis B: Environmental* **2023,** *320*, 121927.

136. Nørskov, J. K.; Abild-Pedersen, F.; Studt, F.; Bligaard, T., Density functional theory in surface chemistry and catalysis. *Proceedings of the National Academy of Sciences* **2011,** *108* (3), 937-943.

137. Yu, Y.; He, Y.; Yan, P.; Wang, S.; Dong, F., Boosted C–C coupling with Cu–Ag alloy sub-nanoclusters for CO2-to-C2H4 photosynthesis. *Proceedings of the National Academy of Sciences* **2023,** *120* (44), e2307320120.

138. de Almeida, J.; Câmara, S. H.; Bertazzoli, R.; Rajeshwar, K.; da Silva, R. A. G.; de

Arruda Rodrigues, C., Selective photoelectrocatalytic CO2 reduction to ethanol using nanotubular oxides grown on metastable Ti-Cu alloy. *Chemical Engineering Journal* **2023,** *477*, 147117.

139. Yang, Y.; Shen, Z.; Yang, H.; Zou, X.; Meng, Y.; Jiang, L.; Liu, Y.; Xia, Q.; Cao, Y.; Li, X., Construction adsorption and photocatalytic interfaces between C, O co-doped BN and Pd-Cu alloy nanocrystals for effective conversion of CO2 to CO. *Journal of Colloid and Interface Science* **2023,** *640*, 949-960.

140. Wang, J.; Bo, T.; Shao, B.; Zhang, Y.; Jia, L.; Tan, X.; Zhou, W.; Yu, T., Effect of S vacancy in Cu3SnS4 on high selectivity and activity of photocatalytic CO2 reduction. *Applied Catalysis B: Environmental* **2021,** *297*, 120498.

141. Kim, B.; Kwon, D.; Baeg, J. O.; Austeria P, M.; Gu, G. H.; Lee, J. H.; Jeong, J.; Kim, W.; Choi, W., Dual-Atom-Site Sn-Cu/C3N4 Photocatalyst Selectively Produces Formaldehyde from CO2 Reduction. *Advanced Functional Materials* **2023**, 2212453.

142. Pal, J.; Manna, S.; Mondal, A.; Das, S.; Adarsh, K.; Nag, A., Colloidal Synthesis and Photophysics of M3Sb2I9 (M= Cs and Rb) Nanocrystals: Lead-Free Perovskites. *Angewandte Chemie International Edition* **2017,** *56* (45), 14187-14191.

143. Chung, I.; Song, J.-H.; Im, J.; Androulakis, J.; Malliakas, C. D.; Li, H.; Freeman, A. J.; Kenney, J. T.; Kanatzidis, M. G., CsSnI3: semiconductor or metal? High electrical conductivity and strong near-infrared photoluminescence from a single material. High hole mobility and phase-transitions. *Journal of the American Chemical Society* **2012,** *134* (20), 8579-8587.

144. Zhang, J.; Yang, Y.; Deng, H.; Farooq, U.; Yang, X.; Khan, J.; Tang, J.; Song, H., High quantum yield blue emission from lead-free inorganic antimony halide perovskite colloidal quantum dots. *Acs Nano* **2017,** *11* (9), 9294-9302.

145. Zhang, Z.; Liu, L.; Huang, H.; Li, L.; Wang, Y.; Xu, J.; Xu, J., Encapsulation of CsPbBr3 perovskite quantum dots into PPy conducting polymer: Exceptional water stability and enhanced charge transport property. *Applied Surface Science* **2020,** *526*, 146735.

146. Huang, H.; Zhao, J.; Du, Y.; Zhou, C.; Zhang, M.; Wang, Z.; Weng, Y.; Long, J.; Hofkens, J.; Steele, J. A., Direct Z-Scheme Heterojunction of Semicoherent FAPbBr3/Bi2WO6 Interface for Photoredox Reaction with Large Driving Force. *ACS nano* **2020,** *14* (12), 16689-16697.

147. Schleder, G. R.; Padilha, A. C.; Acosta, C. M.; Costa, M.; Fazzio, A., From DFT to

machine learning: recent approaches to materials science–a review. *Journal of Physics: Materials* **2019,** *2* (3), 032001.

148. Augello, C.; Liu, H., Surface modification of magnesium by functional polymer coatings for neural applications. In *Surface Modification of Magnesium and Its Alloys for Biomedical Applications*, Elsevier: 2015; pp 335-353.

149. Pham, N. P.; Boellard, E.; Sarro, P. M.; Burghartz, J. N. In *Spin, spray coating and electrodeposition of photoresist for MEMS structures—A comparison*, Eurosensors, Citeseer: 2002; pp 81-86.

150. Kamanyi Jr, A. E.; Ngwa, W.; Luo, W.; Grill, W. In *Effects of solvent vapor pressure and spin-coating speed on morphology of thin polymer blend films*, Health Monitoring of Structural and Biological Systems 2008, SPIE: 2008; pp 598-604.

151. Kanani, N., *Electroplating: basic principles, processes and practice*. Elsevier: 2004.

152. Celis, J.-P.; De Bonte, M.; Roos, J., Electroplating technology. *Transactions of the IMF* **1994,** *72* (2), 89-93.

153. Mohammed, A.; Abdullah, A. In *Scanning electron microscopy (SEM): A review*, Proceedings of the 2018 International Conference on Hydraulics and Pneumatics—HERVEX, Băile Govora, Romania, 2018; pp 7-9.

154. Myscope training. https://myscope.training/.

155. Zhou, W.; Wang, Z. L., *Scanning microscopy for nanotechnology: techniques and applications*. Springer science & business media: 2007.

156. Goldstein, J. I.; Newbury, D. E.; Michael, J. R.; Ritchie, N. W.; Scott, J. H. J.; Joy, D. C., *Scanning electron microscopy and X-ray microanalysis*. springer: 2017.

157. Zuo, J. M.; Spence, J. C., *Advanced transmission electron microscopy*. Springer: 2017.

158. Williams, D. B.; Carter, C. B.; Williams, D. B.; Carter, C. B., *The transmission electron microscope*. Springer: 1996.

159. Epp, J., X-ray diffraction (XRD) techniques for materials characterization. In *Materials characterization using nondestructive evaluation (NDE) methods*, Elsevier: 2016; pp 81-124.

160. Bragg, W., The diffraction of short electromagnetic waves by a crystal: Proceedings of the Cambridge Philosophical Society. Cambridge: Proc. Camb. Philos. Soc., 1913; Vol. 17, pp 43-57.

161. Chastain, J.; King Jr, R. C., Handbook of X-ray photoelectron spectroscopy. *Perkin-*

Elmer Corporation **1992,** *40*, 221.

162. Tom, J., UV-Vis Spectroscopy: Principle, Strengths and Limitations and Applications Article Published: June 30, 2021.

163. Förster, H., UV/vis spectroscopy. *Characterization I: -/-* **2004**, 337-426.

164. PL / Steady-State & Time-Resolved Photoluminescence Spectroscopy. https://innovation-el.net/tool/pl-steady-state-time-resolved-photoluminescence-spectroscopy/.

165. Time-Resolved Photoluminescence (TRPL). https://www.picoquant.com/applications/category/materials-science/time-resolved-photoluminescence#:~:text=Time%2DResolved%20Photoluminescence%20(TRPL)%20is%20the%20tool%20of%20choice,few%20picoseconds%20up%20to%20nanoseconds.

166. Sajedi Alvar, M.; Blom, P. W.; Wetzelaer, G.-J. A., Space-charge-limited electron and hole currents in hybrid organic-inorganic perovskites. *Nat. Commun.* **2020,** *11* (1), 4023.

167. Saidaminov, M. I.; Abdelhady, A. L.; Murali, B.; Alarousu, E.; Burlakov, V. M.; Peng, W.; Dursun, I.; Wang, L.; He, Y.; Maculan, G., High-quality bulk hybrid perovskite single crystals within minutes by inverse temperature crystallization. *Nature communications* **2015,** *6*, 7586.

168. Zhang, Y.; Liu, Y.; Yang, Z.; Liu, S. F., High-quality perovskite MAPbI3 single crystals for broad-spectrum and rapid response integrate photodetector. *Journal of energy chemistry* **2018,** *27* (3), 722-727.

169. New electrochemistry SOP. https://berry.chem.wisc.edu/sites/berry.chem.wisc.edu/files/styles/medium/public/New%20electrochemistry%20SOP.pdf.

170. Battin, T. J.; Luyssaert, S.; Kaplan, L. A.; Aufdenkampe, A. K.; Richter, A.; Tranvik, L. J., The boundless carbon cycle. *Nature Geoscience* **2009,** *2* (9), 598-600.

171. Ding, P.; Jiang, T.; Han, N.; Li, Y., Photocathode engineering for efficient photoelectrochemical CO2 reduction. *Materials Today Nano* **2020,** *10*, 100077.

172. Cooper, J. K.; Zhang, Z.; Roychoudhury, S.; Jiang, C.-M.; Gul, S.; Liu, Y.-S.; Dhall, R.; Ceballos, A.; Yano, J.; Prendergast, D., CuBi2O4: Electronic structure, optical properties, and photoelectrochemical performance limitations of the photocathode. *Chemistry of Materials* **2021,** *33* (3), 934-945.

173. Cai, C.; Xu, Y.-F.; Chen, H.-Y.; Wang, X.-D.; Kuang, D.-B., Porous ZnO@ ZnSe nanosheet array for photoelectrochemical reduction of CO2. *Electrochimica Acta* **2018,** *274*,

298-305.

174. Zhang, X.; Tang, R.; Li, F.; Zheng, R.; Huang, J., Tailoring Inorganic Halide Perovskite Photocatalysts toward Carbon Dioxide Reduction. *Solar RRL* **2022**, 2101058.

175. Kazim, S.; Nazeeruddin, M. K.; Grätzel, M.; Ahmad, S., Perovskite as light harvester: a game changer in photovoltaics. *Angewandte Chemie International Edition* **2014,** *53* (11), 2812-2824.

176. Jang, Y. J.; Jeong, I.; Lee, J.; Lee, J.; Ko, M. J.; Lee, J. S., Unbiased sunlight-driven artificial photosynthesis of carbon monoxide from CO2 using a ZnTe-based photocathode and a perovskite solar cell in tandem. *ACS nano* **2016,** *10* (7), 6980-6987.

177. Wang, Q.; Tao, L.; Jiang, X.; Wang, M.; Shen, Y., Graphene oxide wrapped CH3NH3PbBr3 perovskite quantum dots hybrid for photoelectrochemical CO2 reduction in organic solvents. *Applied Surface Science* **2019,** *465*, 607-613.

178. Zhang, H.; Chen, Y.; Wang, H.; Wang, H.; Ma, W.; Zong, X.; Li, C., Carbon Encapsulation of Organic–Inorganic Hybrid Perovskite toward Efficient and Stable Photo-Electrochemical Carbon Dioxide Reduction. *Advanced Energy Materials* **2020,** *10* (44), 2002105.

179. Edwardes Moore, E.; Andrei, V.; Oliveira, A. R.; Coito, A. M.; Pereira, I. A.; Reisner, E., A Semi-artificial Photoelectrochemical Tandem Leaf with a CO2-to-Formate Efficiency Approaching 1%. *Angewandte Chemie International Edition* **2021,** *60* (50), 26303-26307.

180. Chen, J.; Yin, J.; Zheng, X.; Ait Ahsaine, H.; Zhou, Y.; Dong, C.; Mohammed, O. F.; Takanabe, K.; Bakr, O. M., Compositionally screened eutectic catalytic coatings on halide perovskite photocathodes for photoassisted selective CO2 reduction. *ACS Energy Letters* **2019,** *4* (6), 1279-1286.

181. Li, B.; Long, R.; Xia, Y.; Mi, Q., All-inorganic perovskite CsSnBr3 as a thermally stable, free-carrier semiconductor. *Angewandte Chemie International Edition* **2018,** *57* (40), 13154-13158.

182. Dong, Z.; Shi, Y.; Jiang, Y.; Yao, C.; Zhang, Z., In situ growth of CsPbBr3 quantum dots in mesoporous SnO2 frameworks as an efficient CO2-reduction photocatalyst. *Journal of CO2 Utilization* **2023,** *72*, 102480.

183. Wang, Y.; Wang, Q.; Jiang, G.; Zhang, Q.; Wang, J.; Li, Z., CsPbBr3 Nanocrystals Stabilized by Lead Oxysalts for Photocatalytic CO2 Reduction. *ACS Applied Nano Materials* **2023,** *6* (7), 5087-5092.

184. Wang, J.-C.; Li, N.; Idris, A. M.; Wang, J.; Du, X.; Pan, Z.; Li, Z., Surface defect engineering of CsPbBr3 nanocrystals for high efficient photocatalytic CO2 reduction. *Solar RRL* **2021,** *5* (7), 2100154.

185. Li, F.; Li, H.; Guan, L.-x.; Yao, M.-m., Nanocrystalline Co2+/F− codoped TiO2–SiO2 composite films for environmental applications. *Chemical Engineering Journal* **2014,** *252*, 1-10.

186. Yu, L.; Xiong, L.; Yu, Y., Cu2O homojunction solar cells: F-doped N-type thin film and highly improved efficiency. *The Journal of Physical Chemistry C* **2015,** *119* (40), 22803-22811.

187. Balakrishnan, S. K.; Kamat, P. V., Au–CsPbBr3 hybrid architecture: anchoring gold nanoparticles on cubic perovskite nanocrystals. *ACS Energy Letters* **2017,** *2* (1), 88-93.

188. Tang, R.; Sun, H.; Zhang, Z.; Liu, L.; Meng, F.; Zhang, X.; Yang, W.; Li, Z.; Zhao, Z.; Zheng, R., Incorporating plasmonic Au-nanoparticles into three-dimensionally ordered macroporous perovskite frameworks for efficient photocatalytic CO2 reduction. *Chemical Engineering Journal* **2022,** *429*, 132137.

189. Liao, J.-F.; Cai, Y.-T.; Li, J.-Y.; Jiang, Y.; Wang, X.-D.; Chen, H.-Y.; Kuang, D.-B., Plasmonic CsPbBr3–Au nanocomposite for excitation wavelength dependent photocatalytic CO2 reduction. *Journal of Energy Chemistry* **2021,** *53*, 309-315.

190. Huang, J.-N.; Dong, Y.-J.; Zhao, H.-B.; Chen, H.-Y.; Kuang, D.-B.; Su, C.-Y., Efficient encapsulation of CsPbBr 3 and Au nanocrystals in mesoporous metal–organic frameworks towards synergetic photocatalytic CO 2 reduction. *Journal of Materials Chemistry A* **2022,** *10* (47), 25212-25219.

191. Fu, H.; Liu, X.; Wu, Y.; Zhang, Q.; Wang, Z.; Zheng, Z.; Cheng, H.; Liu, Y.; Dai, Y.; Huang, B., Construction of a bismuth-based perovskite direct Z-scheme heterojunction Au-Cs3Bi2Br9/V2O5 for efficient photocatalytic CO2 reduction. *Applied Surface Science* **2023,** *622*, 156964.

192. Zheng, X. L.; Song, J. P.; Ling, T.; Hu, Z. P.; Yin, P. F.; Davey, K.; Du, X. W.; Qiao, S. Z., Strongly coupled nafion molecules and ordered porous CdS networks for enhanced visible-light photoelectrochemical hydrogen evolution. *Advanced Materials* **2016,** *28* (24), 4935-4942.

193. Duan, J.; Zhao, Y.; He, B.; Tang, Q., High-purity inorganic perovskite films for solar cells with 9.72% efficiency. *Angewandte Chemie* **2018,** *130* (14), 3849-3853.

194. Yu, J.; Wang, W.; Cheng, B.; Su, B.-L., Enhancement of photocatalytic activity of mesporous TiO2 powders by hydrothermal surface fluorination treatment. *The Journal of Physical Chemistry C* **2009,** *113* (16), 6743-6750.

195. Li, X.; Wu, X.; Liu, S.; Li, Y.; Fan, J.; Lv, K., Effects of fluorine on photocatalysis. *Chinese Journal of Catalysis* **2020,** *41* (10), 1451-1467.

196. Wang, J.; Yin, S.; Zhang, Q.; Saito, F.; Sato, T., Influences of the factors on photocatalysis of fluorine-doped SrTiO3 made by mechanochemical method. *Solid State Ionics* **2004,** *172* (1-4), 191-195.

197. Shi, R.; Huang, G.; Lin, J.; Zhu, Y., Photocatalytic activity enhancement for Bi2WO6 by fluorine substitution. *The Journal of Physical Chemistry C* **2009,** *113* (45), 19633-19638.

198. Sun, L.; Li, Y.; Feng, W., Gas-phase fluorination of g-C3N4 for enhanced photocatalytic hydrogen evolution. *Nanomaterials* **2021,** *12* (1), 37.

199. Dong, Z.; Zhang, Z.; Jiang, Y.; Chu, Y.; Xu, J., Embedding CsPbBr3 perovskite quantum dots into mesoporous TiO2 beads as an S-scheme heterojunction for CO2 photoreduction. *Chemical Engineering Journal* **2022,** *433*, 133762.

200. Li, X.; He, B.; Gong, Z.; Zhu, J.; Zhang, W.; Chen, H.; Duan, Y.; Tang, Q., Compositional engineering of Chloride Ion-Doped CsPbBr3 halides for highly efficient and stable all-inorganic perovskite solar cells. *Solar RRL* **2020,** *4* (10), 2000362.

201. Duijnstee, E. A.; Ball, J. M.; Le Corre, V. M.; Koster, L. J. A.; Snaith, H. J.; Lim, J., Toward understanding space-charge limited current measurements on metal halide perovskites. *ACS Energy Letters* **2020,** *5* (2), 376-384.

202. Bube, R. H., Trap density determination by space-charge-limited currents. *Journal of Applied Physics* **1962,** *33* (5), 1733-1737.

203. Zhang, X.; Zhang, R.; Yang, T.; Cheng, Y.; Li, F.; Li, W.; Huang, J.; Liu, H.; Zheng, R., Facile Fabrication of Hybrid Perovskite Single-Crystalline Photocathode for Photoelectrochemical Water Splitting. *Energy Technology* **2021,** *9* (5), 2000965.

204. Al-Hajji, L.; Ismail, A. A.; Bumajdad, A.; Alsaidi, M.; Ahmed, S.; Almutawa, F.; Al-Hazza, A., Construction of Au/TiO2 Heterojunction with high photocatalytic performances under UVA illumination. *Ceram. Int.* **2020,** *46* (12), 20155-20162.

205. Chen, H.-Y.; Lin, C.-Y.; Chen, M.-C.; Huang, C.-C.; Chien, C.-H., Nickel silicide formation using pulsed laser annealing for nMOSFET performance Improvement. *Journal of The Electrochemical Society* **2011,** *158* (8), H840.

206. Tang, R.; Zhou, S.; Zhang, Z.; Zheng, R.; Huang, J., Engineering nanostructure–interface of photoanode materials toward photoelectrochemical water oxidation. *Advanced Materials* **2021,** *33* (17), 2005389.

207. Xu, W.; Gao, W.; Meng, L.; Tian, W.; Li, L., Incorporation of sulfate anions and sulfur vacancies in ZnIn2S4 photoanode for enhanced photoelectrochemical water splitting. *Advanced Energy Materials* **2021,** *11* (26), 2101181.

208. Yu, H.; Lee, J. W.; Yun, J.; Lee, K.; Ryu, J.; Lee, J.; Hwang, D.; Kim, S. K.; Jang, J., Outstanding performance of hole-blocking layer-free perovskite solar cell using hierarchically porous fluorine-doped tin oxide substrate. *Advanced Energy Materials* **2017,** *7* (22), 1700749.

209. Sun, J.; Li, S.; Zhao, Q.; Huang, C.; Wu, Q.; Chen, W.; Xu, Q.; Yao, W., Atomically confined calcium in nitrogen-doped graphene as an efficient heterogeneous catalyst for hydrogen evolution. *Iscience* **2021,** *24* (7), 102728.

210. Joe, J.; Yang, H.; Bae, C.; Shin, H., Metal chalcogenides on silicon photocathodes for efficient water splitting: A mini overview. *Catalysts* **2019,** *9* (2), 149.

211. Lopes, T.; Andrade, L.; Le Formal, F.; Gratzel, M.; Sivula, K.; Mendes, A., Hematite photoelectrodes for water splitting: evaluation of the role of film thickness by impedance spectroscopy. *Physical Chemistry Chemical Physics* **2014,** *16* (31), 16515-16523.

212. Tong, G.; Li, H.; Li, D.; Zhu, Z.; Xu, E.; Li, G.; Yu, L.; Xu, J.; Jiang, Y., Dual-Phase CsPbBr3–CsPb2Br5 Perovskite Thin Films via Vapor Deposition for High-Performance Rigid and Flexible Photodetectors. *Small* **2018,** *14* (7), 1702523.

213. Cortes, M.; McMichael, S.; Hamilton, J. W. J.; Sharma, P. K.; Brown, A.; Byrne, J. A., Photoelectrochemical reduction of CO2 with TiNT. *Mater. Sci. Semicond. Process.* **2020,** *108*.

214. Perini, J. A. L.; Cardoso, J. C.; de Brito, J. F.; Zanoni, M. V. B., Contribution of thin films of ZrO2 on TiO2 nanotubes electrodes applied in the photoelectrocatalytic CO2 conversion. *Journal of CO2 Utilization* **2018,** *25*, 254-263.

215. Wang, Y.; He, D.; Chen, H.; Wang, D., Catalysts in electro-, photo-and photoelectrocatalytic CO2 reduction reactions. *Journal of Photochemistry and Photobiology C: Photochemistry Reviews* **2019,** *40*, 117-149.

216. Xie, J.-F.; Chen, J.-J.; Huang, Y.-X.; Zhang, X.; Wang, W.-K.; Huang, G.-X.; Yu, H.-Q., Selective electrochemical CO2 reduction on Cu-Pd heterostructure. *Applied Catalysis B:*

Environmental **2020,** *270*, 118864.

217. Jiang, X.; Koizumi, N.; Guo, X.; Song, C., Bimetallic Pd–Cu catalysts for selective CO2 hydrogenation to methanol. *Applied Catalysis B: Environmental* **2015,** *170*, 173-185.

218. Jiang, X.; Nie, X.; Wang, X.; Wang, H.; Koizumi, N.; Chen, Y.; Guo, X.; Song, C., Origin of Pd-Cu bimetallic effect for synergetic promotion of methanol formation from CO2 hydrogenation. *Journal of Catalysis* **2019,** *369*, 21-32.

219. Yu, Y.; Dong, X. a.; Chen, P.; Geng, Q.; Wang, H.; Li, J.; Zhou, Y.; Dong, F., Synergistic effect of Cu single atoms and Au–Cu alloy nanoparticles on TiO2 for efficient CO2 photoreduction. *ACS nano* **2021,** *15* (9), 14453-14464.

220. Liu, K.; Ma, M.; Wu, L.; Valenti, M.; Cardenas-Morcoso, D.; Hofmann, J. P.; Bisquert, J.; Gimenez, S.; Smith, W. A., Electronic effects determine the selectivity of planar Au–Cu bimetallic thin films for electrochemical CO2 reduction. *ACS applied materials & interfaces* **2019,** *11* (18), 16546-16555.

221. Liang, L.; Feng, Q.; Wang, X.; Hübner, J.; Gernert, U.; Heggen, M.; Wu, L.; Hellmann, T.; Hofmann, J. P.; Strasser, P., Electroreduction of CO2 on Au (310)@ Cu High-index Facets. *Angewandte Chemie International Edition* **2023,** *62* (12), e202218039.

222. Gao, P.; Li, F.; Zhang, L.; Zhao, N.; Xiao, F.; Wei, W.; Zhong, L.; Sun, Y., Influence of fluorine on the performance of fluorine-modified Cu/Zn/Al catalysts for CO2 hydrogenation to methanol. *Journal of CO2 Utilization* **2013,** *2*, 16-23.

223. Pasupulety, N.; Driss, H.; Alhamed, Y. A.; Alzahrani, A. A.; Daous, M. A.; Petrov, L., Studies on Au/Cu–Zn–Al catalyst for methanol synthesis from CO2. *Applied Catalysis A: General* **2015,** *504*, 308-318.

224. Wang, X.; Ng, D.; Du, H.; Hornung, C. H.; Polyzos, A.; Seeber, A.; Li, H.; Huo, Y.; Xie, Z., Copper decorated indium oxide rods for photocatalytic CO2 conversion under simulated sun light. *Journal of CO2 Utilization* **2022,** *58*, 101909.

225. Luo, W.; Xie, W.; Mutschler, R.; Oveisi, E.; De Gregorio, G. L.; Buonsanti, R.; Züttel, A., Selective and stable electroreduction of CO2 to CO at the copper/indium interface. *Acs Catalysis* **2018,** *8* (7), 6571-6581.

226. Yan, L.; Su, W.; Cao, X.; Zhang, P.; Fan, Y., Copper-indium hybrid derived from indium-based metal-organic frameworks grown on oxidized copper foils promotes the efficient electroreduction of CO2 to CO. *Chemical Engineering Journal* **2021,** *412*, 128718.

227. Banda-Alemán, J. A.; Orozco, G.; Bustos, E.; Sepúlveda, S.; Manríquez, J., Double-

layer effect on the kinetics of CO2 electroreduction at cathodes bearing Ag, Cu, and Ag/Cu nano-arrays electrodeposited by potentiostatic double-pulse. *Journal of CO2 Utilization* **2018,** *27*, 459-471.

228. Liu, Y.; Qiu, H.; Li, J.; Guo, L.; Ager, J. W., Tandem electrocatalytic CO2 reduction with efficient intermediate conversion over pyramid-textured Cu–Ag catalysts. *ACS applied materials & interfaces* **2021,** *13* (34), 40513-40521.

229. Iyengar, P.; Kolb, M. J.; Pankhurst, J. R.; Calle-Vallejo, F.; Buonsanti, R., Elucidating the facet-dependent selectivity for CO2 electroreduction to ethanol of Cu–Ag tandem catalysts. *Acs Catalysis* **2021,** *11* (8), 4456-4463.

230. Yoo, C. J.; Dong, W. J.; Park, J. Y.; Lim, J. W.; Kim, S.; Choi, K. S.; Odongo Ngome, F. O.; Choi, S.-Y.; Lee, J.-L., Compositional and geometrical effects of bimetallic Cu–Sn catalysts on selective electrochemical CO2 reduction to CO. *ACS Applied Energy Materials* **2020,** *3* (5), 4466-4473.

231. Li, D.; Huang, L.; Tian, Y.; Liu, T.; Zhen, L.; Feng, Y., Facile synthesis of porous Cu-Sn alloy electrode with prior selectivity of formate in a wide potential range for CO2 electrochemical reduction. *Applied Catalysis B: Environmental* **2021,** *292*, 120119.

232. Ju, W.; Jiang, F.; Ma, H.; Pan, Z.; Zhao, Y. B.; Pagani, F.; Rentsch, D.; Wang, J.; Battaglia, C., Electrocatalytic reduction of gaseous CO2 to CO on Sn/Cu-Nanofiber-Based gas diffusion electrodes. *Advanced Energy Materials* **2019,** *9* (32), 1901514.

233. Zhang, M.; Zhang, Z.; Zhao, Z.; Huang, H.; Anjum, D. H.; Wang, D.; He, J.-h.; Huang, K.-W., Tunable selectivity for electrochemical CO2 reduction by bimetallic Cu–Sn catalysts: elucidating the roles of Cu and Sn. *ACS Catalysis* **2021,** *11* (17), 11103-11108.

234. Lv, Y.-R.; Liu, C.-J.; He, R.-K.; Li, X.; Xu, Y.-H., BiVO4/TiO2 heterojunction with enhanced photocatalytic activities and photoelectochemistry performances under visible light illumination. *Materials Research Bulletin* **2019,** *117*, 35-40.

235. Zhu, Z.; Yang, C.-X.; Hwang, Y.-T.; Lin, Y.-C.; Wu, R.-J., Fuel generation through photoreduction of CO2 on novel Cu/BiVO4. *Materials Research Bulletin* **2020,** *130*, 110955.

236. Prajapati, P. K.; Saini, S.; Nandal, N.; Jain, S. L., Photochemical fixation of carbon dioxide for N-formylation of amine using Cu (II) embedded BiVO4 nanocomposite under visible light. *Journal of CO2 Utilization* **2021,** *45*, 101402.

237. Liu, L.-X.; Fu, J.; Jiang, L.-P.; Zhang, J.-R.; Zhu, W.; Lin, Y., Highly efficient photoelectrochemical reduction of CO2 at low applied voltage using 3D Co-Pi/BiVO4/SnO2

nanosheet array photoanodes. *ACS Applied Materials & Interfaces* **2019,** *11* (29), 26024-26031.

238. Kim, J. H.; Magesh, G.; Kang, H. J.; Banu, M.; Kim, J. H.; Lee, J.; Lee, J. S., Carbonate-coordinated cobalt co-catalyzed BiVO4/WO3 composite photoanode tailored for CO2 reduction to fuels. *Nano Energy* **2015,** *15*, 153-163.

239. Wang, F.; Ding, Q.; Ding, J.; Bai, Y.; Bai, H.; Fan, W., Frustrated Lewis pairs boosting photoelectrochemical nitrate reduction over ZnIn2S4/BiVO4 heterostructure. *Chemical Engineering Journal* **2022,** *450*, 138260.

240. Bai, H.; Wang, F.; Ding, Q.; Xie, W.; Li, H.; Zheng, G.; Fan, W., Construction of frustrated lewis pair sites in CeO2–C/BiVO4 for photoelectrochemical nitrate reduction. *Inorg. Chem.* **2023,** *62* (5), 2394-2403.

241. Liu, L.; Bai, Y.; Huang, Z.; Wang, G.; Cui, J.; Bai, H.; Fan, W., Understanding the role of Ce sites for boosting PEC-NIRR without externally applied potentials. *Inorganic Chemistry Frontiers* **2023,** *10* (7), 2060-2066.

242. Gao, B.; Wang, T.; Fan, X.; Gong, H.; Meng, X.; Li, P.; Feng, Y.; Huang, X.; He, J.; Ye, J., Selective deposition of Ag3PO4 on specific facet of BiVO4 nanoplate for enhanced photoelectrochemical performance. *Solar Rrl* **2018,** *2* (9), 1800102.

243. Chen, D.; Yao, Q.; Cui, P.; Liu, H.; Xie, J.; Yang, J., Tailoring the selectivity of bimetallic copper–palladium nanoalloys for electrocatalytic reduction of CO2 to CO. *ACS Applied Energy Materials* **2018,** *1* (2), 883-890.

244. Holder, C. F.; Schaak, R. E., Tutorial on powder X-ray diffraction for characterizing nanoscale materials. ACS Publications: 2019; Vol. 13, pp 7359-7365.

245. Jubu, P. R.; Obaseki, O.; Nathan-Abutu, A.; Yam, F.; Yusof, Y.; Ochang, M., Dispensability of the conventional Tauc's plot for accurate bandgap determination from UV–vis optical diffuse reflectance data. *Results in Optics* **2022,** *9*, 100273.

246. Yoong, L.; Chong, F. K.; Dutta, B. K., Development of copper-doped TiO2 photocatalyst for hydrogen production under visible light. *Energy* **2009,** *34* (10), 1652-1661.

247. Zhong, H.; Pan, F.; Yue, S.; Qin, C.; Hadjiev, V.; Tian, F.; Liu, X.; Lin, F.; Wang, Z.; Bao, J., Idealizing Tauc plot for accurate bandgap determination of semiconductor with ultraviolet–visible spectroscopy: a case study for cubic boron arsenide. *The Journal of Physical Chemistry Letters* **2023,** *14* (29), 6702-6708.

248. Biesinger, M. C.; Lau, L. W.; Gerson, A. R.; Smart, R. S. C., Resolving surface

chemical states in XPS analysis of first row transition metals, oxides and hydroxides: Sc, Ti, V, Cu and Zn. *Applied surface science* **2010,** *257* (3), 887-898.

249. Jung, C.; Han, J.; Nam, S.; Lim, T.-H.; Hong, S.-A.; Lee, H.-I., Selective oxidation of CO over CuO-CeO2 catalyst: effect of calcination temperature. *Catal. Today* **2004,** *93*, 183-190.

250. Feaster, J. T.; Shi, C.; Cave, E. R.; Hatsukade, T.; Abram, D. N.; Kuhl, K. P.; Hahn, C.; Nørskov, J. K.; Jaramillo, T. F., Understanding selectivity for the electrochemical reduction of carbon dioxide to formic acid and carbon monoxide on metal electrodes. *Acs Catalysis* **2017,** *7* (7), 4822-4827.

251. Naille, S.; Dedryvère, R.; Martinez, H.; Leroy, S.; Lippens, P.-E.; Jumas, J.-C.; Gonbeau, D., XPS study of electrode/electrolyte interfaces of η-Cu6Sn5 electrodes in Li-ion batteries. *Journal of Power Sources* **2007,** *174* (2), 1086-1090.

252. Zhao, Y.; Tenhaeff, W. E., Thermally and oxidatively stable polymer electrolyte for lithium batteries enabled by phthalate plasticization. *ACS Applied Polymer Materials* **2019,** *2* (1), 80-90.

253. Zhang, X.; Tang, R.; Sun, H.; Yang, W.; Liang, W.; Li, F.; Zheng, R.; Huang, J., Synergistically Interface-Engineered Inorganic Halide Perovskite Photocathodes for Photoelectrochemical CO2 Reduction. *Energy Fuels* **2023**.

254. Zhao, Z.; Yao, X.; Hou, G., Reaction Pathways of Methanol Reforming over Pt/α-MoC Catalysts Revealed by In Situ High-Pressure MAS NMR. *ACS Catalysis* **2023,** *13*, 7978-7986.

255. Saeki, T.; Hashimoto, K.; Kimura, N.; Omata, K.; Fujishima, A., Electrochemical reduction of CO2 with high current density in a CO2+ methanol medium at various metal electrodes. *J. Electroanal. Chem.* **1996,** *404* (2), 299-302.

256. Babu, B.; Reddy, I. N.; Yoo, K.; Kim, D.; Shim, J., Bandgap tuning and XPS study of SnO2 quantum dots. *Materials Letters* **2018,** *221*, 211-215.

257. Wang, L.; Cheng, B.; Zhang, L.; Yu, J., In situ irradiated XPS investigation on S-scheme TiO2@ ZnIn2S4 photocatalyst for efficient photocatalytic CO2 reduction. *Small* **2021,** *17* (41), 2103447.

258. Zhang, X.; Tang, R.; Li, F.; Zheng, R.; Huang, J., Tailoring inorganic halide perovskite photocatalysts toward carbon dioxide reduction. *Solar RRL* **2022,** *6* (6), 2101058.

259. Kibria, M.; Zhao, S.; Chowdhury, F.; Wang, Q.; Nguyen, H.; Trudeau, M.; Guo, H.;

Mi, Z., Tuning the surface Fermi level on p-type gallium nitride nanowires for efficient overall water splitting. *Nat. Commun.* **2014,** *5* (1), 1-6.

260. Srivastava, P. K.; Hassan, Y.; Gebredingle, Y.; Jung, J.; Kang, B.; Yoo, W. J.; Singh, B.; Lee, C., Van der Waals broken-gap p–n heterojunction tunnel diode based on black phosphorus and rhenium disulfide. *ACS applied materials & interfaces* **2019,** *11* (8), 8266-8275.

261. Olejnik, A.; Dec, B.; Goddard III, W. A.; Bogdanowicz, R., Hopping or tunneling? tailoring the electron transport mechanisms through hydrogen bonding geometry in the boron-doped diamond molecular junctions. *The Journal of Physical Chemistry Letters* **2022,** *13* (34), 7972-7979.

262. Song, X.; Yu, X.; Hu, W., Model Study on the Ideal Current–Voltage Characteristics and Rectification Performance of a Molecular Rectifier under Single-Level-Based Tunneling and Hopping Transport. *The Journal of Physical Chemistry C* **2020,** *124* (44), 24408-24419.

263. Li, Q.; Fu, J.; Zhu, W.; Chen, Z.; Shen, B.; Wu, L.; Xi, Z.; Wang, T.; Lu, G.; Zhu, J.-j., Tuning Sn-catalysis for electrochemical reduction of CO2 to CO via the core/shell Cu/SnO2 structure. *Journal of the American chemical society* **2017,** *139* (12), 4290-4293.

264. Rhimi, B.; Zhou, M.; Yan, Z.; Cai, X.; Jiang, Z., Cu-Based Materials for Enhanced C2+ Product Selectivity in Photo-/Electro-Catalytic CO2 Reduction: Challenges and Prospects. *Nano-Micro Letters* **2024,** *16* (1), 64.

265. Gong, Y.; Wang, Y.; He, T., Insights into selectivity modulation of electrochemical CO2 reduction reactions over Cu-based catalysts in terms of the key intermediates. *Catalysis Reviews* **2023**, 1-42.

266. Liu, C.; Cundari, T. R.; Wilson, A. K., CO2 reduction on transition metal (Fe, Co, Ni, and Cu) surfaces: In comparison with homogeneous catalysis. *The Journal of Physical Chemistry C* **2012,** *116* (9), 5681-5688.

267. Hori, Y.; Murata, A.; Takahashi, R., Formation of hydrocarbons in the electrochemical reduction of carbon dioxide at a copper electrode in aqueous solution. *Journal of the Chemical Society, Faraday Transactions 1: Physical Chemistry in Condensed Phases* **1989,** *85* (8), 2309-2326.

268. Rihm, S. D.; Kovalev, M. K.; Lapkin, A. A.; Ager, J. W.; Kraft, M., On the role of C 4 and C 5 products in electrochemical CO 2 reduction via copper-based catalysts. *Energy & Environmental Science* **2023,** *16* (4), 1697-1710.

269. Hoffman, Z. B.; Gray, T. S.; Moraveck, K. B.; Gunnoe, T. B.; Zangari, G., Electrochemical reduction of carbon dioxide to syngas and formate at dendritic copper–indium electrocatalysts. *ACS Catalysis* **2017,** *7* (8), 5381-5390.

270. Xia, W.; Wang, H.; Zeng, X.; Han, J.; Zhu, J.; Zhou, M.; Wu, S., High-efficiency photocatalytic activity of type II SnO/Sn 3 O 4 heterostructures via interfacial charge transfer. *CrystEngComm* **2014,** *16* (30), 6841-6847.

271. Zhang, X.; Tang, R.; Sun, H.; Yang, W.; Liang, W.; Li, F.; Zheng, R.; Huang, J., Synergistically interface-engineered inorganic halide perovskite photocathodes for photoelectrochemical CO2 reduction. *Energy Fuels* **2023,** *37* (23), 18163-18172.